Self-organisation in magnetised plasmas

Author: David Cambon Silva

Supervisors: Dr. Paul Bryant, Dr. Kirsty McKay, Prof. James Bradley

Department of Electrical Engineering and Electronics

University of Liverpool

2022

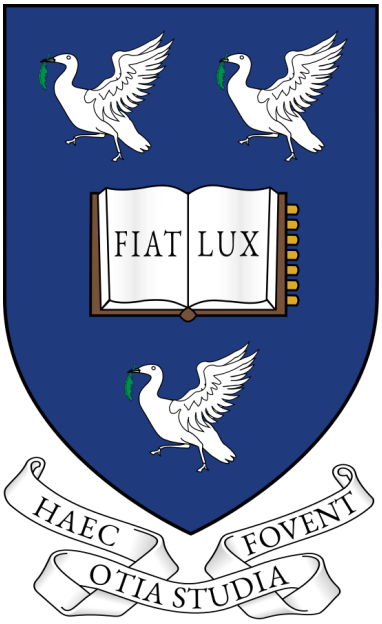

Declaration

I declare that I have read and understood the University's Academic Integrity Policy.

I declare that I have acted honestly, ethically and professionally in conduct leading to assessment for the program of study.

I declare that I have not copied material from another source nor committed plagiarism nor fabricated, falsified or embellished data when completing the attached piece of work. I confirm that I have not copied material from another source, nor colluded with any other student in the preparation and production of this work. Further sources of information have been used other than the references cited.

I declare that this thesis has not been submitted to any other university or institution for any other degree or qualification.

David Cambon Silva

31/05/22

Abstract

Turbulent rotating plasmas under the influence of magnetic fields tend naturally to the formation of regular patterns. The interplay between small-scale fluctuations and large-scale flows can lead to phenomena categorised as self-organisation. In these cases the turbulence regulates itself improving the plasma performance. However, these regimes can become unstable and trigger explosive events. These mechanisms remain unclear and require further investigation. This thesis has the aim of analysing different forms of self-organisation *e.g.* characterise coherent structures, study transitions between regimes and identify patterns in the context of tokamak plasma phenomena.

Data from probe measurements in COMPASS was analysed with the purpose of studying density transitions of the scrape-off layer, also known as shoulders. A statistical analysis was implemented for the characterisation of blobs. Results on blobs features are in agreement with AUG blobs previous to shoulder formation. Unfortunately, the requirements were not sufficient to observe the formation of shoulders.

A 2D imaging analysis on MAST was planned, combining beam emission spectroscopy data and fast camera frames. A recent tomographic inversion technique was employed to extract the ELM-filaments features prior to plasma ejections. However, the identification of pedestal fluctuations from camera frames using the Elzar code produced erroneous filament identifications.

An alternative consisted in executing a spectral analysis applied to beam emission spectroscopy and magnetic coil signals. The use of wavelet transforms provided accurate results of the ELM-precursor activity. Toroidal mode numbers from cross correlation spectra and bicoherence coupling modes agree with the other tokamaks' findings that associate the precursors with peeling-ballooning instabilities.

Acknowledgements

I want to express my sincere gratitude to Dr. Paul Bryant for accepting to join the supervisory team during a complicated period in 2020. I would also like to thank Dr. Kirsty McKay and Prof. James Bradley for their supervision during the initial period of this thesis. Thanks as well to my EEE colleagues, to the Fusion-CDT for the opportunity and the training, and to EPSRC for funding this project.

I also thank Dr. Jiri Adamek and Dr. Karel Kovarik who accepted to supervise my collaboratory project. I have to thank Dr. Jordan Cavalier for organising the SUMTRAIC (2019) course. I would further mention Dr. Martin Imrisek for his help during my stay, and Steven Thomas for his help during SUMTRAIC.

I would like to thank Dr. Fulvio Militello and Dr. Anthony Field for giving me the opportunity to participate in the scientific research at CCFE. Thanks to Dr. Nick Walkden for his guidance at the beginning of the project, and specially to Dr. Tom Farley for his help and patience when he clearly did not have time.

I would like to mention Anurag, Donatas, Han, Martin, Shao-feng, and Thom for making my time at Liverpool more enjoyable. I thank specially Leo Hernandez for resonating with me since the very first second we met, Raymond Maejima for his intermittent visits to Oxford, and Enrique Miralles for our conversations, our triad, our conversion. I cannot forget the support from Alessandro Di Siena and Rosaria Cercola, when I arrived at York with no clue, and in countless circumstances all along these years. I have to mention Anna, Andrea-Marco, Domenico, Francesco, Ludovico, Luca and Stefano, even if our relationship was mostly parasocial. At last, I will never be able to express how much I owe Marco Guarguaglini, thank you.

I must thank Daniel Vazquez for his generosity, without his help everything would have been more difficult.

Thanks to my father and specially my mother for their sacrifice and patience.

UNE CONSTELLATION

froide d'oubli et de désuétude

pas tant

qu'elle n'énumère

sur quelque surface vacante et supérieure

le heurt successif

sidéralement

d'un compte total en formation

veillant

doutant

roulant

brillant et méditant

avant de s'arrêter

à quelque point dernier qui le sacre —

Toute Pensée émet un Coup de Dés

Un Coup de Dés jamais n'abolira le Hasard

Stéphane Mallarmé

Contents

Chapter 1

Introduction

1.1 World energy crisis

At the start of this thesis, humanity's demand was dramatically exceeding the Earth's biocapacity of regenerating its resources annually. The planet's biocapacity is equivalent to the ecological footprint due to human's activities which is measured in global hectares (gha). This unit corresponds to the world's amount of resources involved in the cycle of production, consumption and waste assimilation. In 2018 the humanity's ecological footprint was estimated to be 2.8 gha per capita which surpasses the available world's biocapacity of 1.7 gha per capita [1]. In the context of the COVID-19 pandemic, global CO_2 emissions abruptly decreased by an 8.8 % in the first half of 2020 compared to the same period in 2019, nonetheless emissions due to important industrial activities from China and several European countries did not significantly drop. For instance emissions from China's steel production representing 42 % of the country's industrial emissions from fuel combustion remained the same as in 2019 [2]. The year 2021 was characterised with a comeback on a high energy demand. This generated a rapid response activating the global supply chain which had a significant rebound on the rising rates of CO_2 emissions and erasing the slight reduction effect from the lockdown period. Recently the prices of natural gas, oil and coal have dramatically increased in Europe and

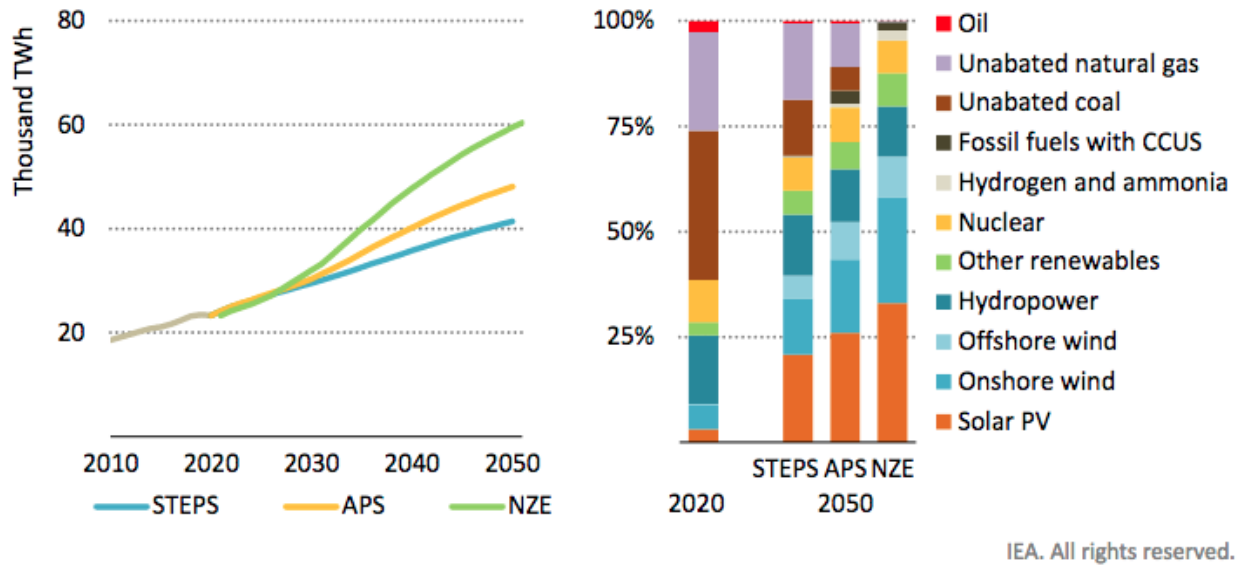

Figure 1.1: Electricity demand from IEA report [3]

Asia (before the war in Ukraine). In parallel the prices of copper, lithium, nickel, and cobalt have also risen because of its widespread use in a foreseeable future on new technologies, specially in the communications and energy sectors. Several explanations point to the stimulus spending from the demand after lockdown, the voluntary supply reduction in order to overvalue the prices, or the starting point of scarcity of these resources. Meanwhile, the COP26 kept the commitment signed in the Paris Agreement from 2015 which promises to maintain the limit of the global temperature increase up to 1.5 °C in a Net Zero Emissions (NZE) scenario as shown in Fig. 1.1. Abandoning the use of fossil fuels requires then to switch to new forms of generating energy. The predictions on the electricity demand for 2050 will double or even triple in a Net Zero Emissions scenario [3]. However, renewable energies such as wind, solar, or hydro power are still insufficient to cover the electricity demand for the moment. Although nuclear fission does not contribute with a carbon footprint, this option has become unpopular during the last decade due to the management of radioactive waste and the accident of Fukushima in 2011. While Germany had decided to shut down their nuclear plants, France has recently approved the construction of new fission reactors to satisfy the demand by 2035 as a medium-term solution. Therefore, there is an urgency to develop an alternative to conventional energy sources which needs to be affordable and sustainable with the environment.

1.2 Nuclear fusion

Nuclear fusion is one of the most promising options of energy supply in the long term. The D−T reaction involves light deuterium (D, ^{2}H) and tritium (T, ^{3}H) nuclei and proceeds according to the reaction:

$$\mathrm{D} + \mathrm{T} \rightarrow {}^4\mathrm{He}\ (3.5\ \mathrm{MeV}) + \mathrm{n}\ (14.1\ \mathrm{MeV}) \tag{1.1}$$

The reactions' products are a heavier nuclei ^{4}He (or α particle), and a neutron. Large amounts of energy are released during the reaction as a result of mass m being converted to energy E according to Einstein's equation:

$$\Delta E = \Delta m\ c^2 \tag{1.2}$$

The binding energy is the energy needed to split the nucleus into protons and neutrons which then recombine to produce heavier nuclei through strong nuclear force. In other words the binding energy ΔE is equivalent to the mass defect (or deficit) Δm resulting from the reaction. In Fig. 1.2 the binding energy per nucleon curve shows the lowest energy threshold corresponds to the lightest nuclei (H, He), whereas heaviest nuclei from (C, O) require a higher energy level. Hence fusion reactions are attractive for extracting higher energies from lower masses. In the D-T reaction the mass deficit is:

$$\Delta m = m_D + m_T - (m_{He} + m_n) = 0.01875\ m_H \tag{1.3}$$

with the mass of hydrogen being $m_H = 1.6727 \times 10^{-27}$ kg, the released energy is equal to $\Delta E = 17.6$ MeV. For 1 kg of D−T fuel this would correspond to 10^8 kWh of released energy and 1 GW of electrical power for a day [4]. In order to enable fusion the kinetic energy of reacting nuclei need to overcome the potential energy barrier of the order of 1 MeV due to the Coulomb repulsion force between particles. The only possible mechanism, which allows a small number of reactions to take place, is through quantum tunnelling for which kinetic energies around $10 - 20$ keV are sufficient. The collision rate $\mathcal{R}$, between these energetic nuclei, is given by:

$$\mathcal{R} = n_D n_T \langle \sigma v \rangle \tag{1.4}$$

with n_D, n_T the densities of deuterium and tritium respectively, being proportional to the cross section σ which estimates the probability of collision between two particles, the fusion reactivity [5] being a sixfold

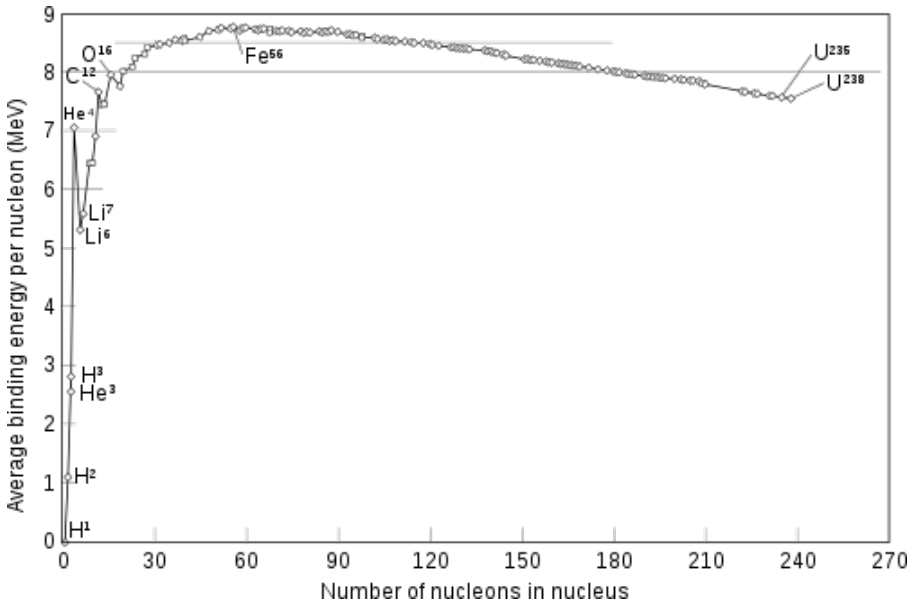

Figure 1.2: Average binding energies per nuclei [6]

integral of the distribution function of relative velocities at states (i, j) of a particle:

$$\langle \sigma v \rangle = \int_0^\infty \int_0^\infty f(v_i) f(v_j) \sigma(|v_i - v_j|) |v_i - v_j| dv_i dv_j \tag{1.5}$$

The reaction rates for different reactions are presented in Fig. 1.3 [4]. Among the possible reactions, the D−T reaction has the highest reaction rate of 10^{-21} m^{-3} s^{-1} at a temperature of 100 keV. Other reactions (D−D and D−^{3}He) are unpractical: their reaction rates are substantially lower and require a higher temperature above 100 keV for reaching a maxima. Therefore the D-T reaction has become the most promising scheme to achieve experimental controlled fusion. Deuterium is abundant in nature, being extracted from seawater, however tritium is not. This issue is solved by breeding tritium from a lithium blanket on the reactor walls. This is possible because the highly energetic neutrons are able to escape the plasma, being unaffected by the magnetic field, allowing two possible reactions:

$$^6\text{Li} + \text{n} \rightarrow {}^3\text{T} + {}^4\text{He} + 4.8 \text{ MeV} \tag{1.6}$$

$$^7\text{Li} + \text{n} \rightarrow {}^3\text{T} + {}^4\text{He} + n - 2.5 \text{ MeV} \tag{1.7}$$

producing tritium and self-sustaining the reaction back to the formula in (1.1). It is estimated that lithium reserves correspond approximately to 13.5 million tonnes without counting the limitless amount of lithium

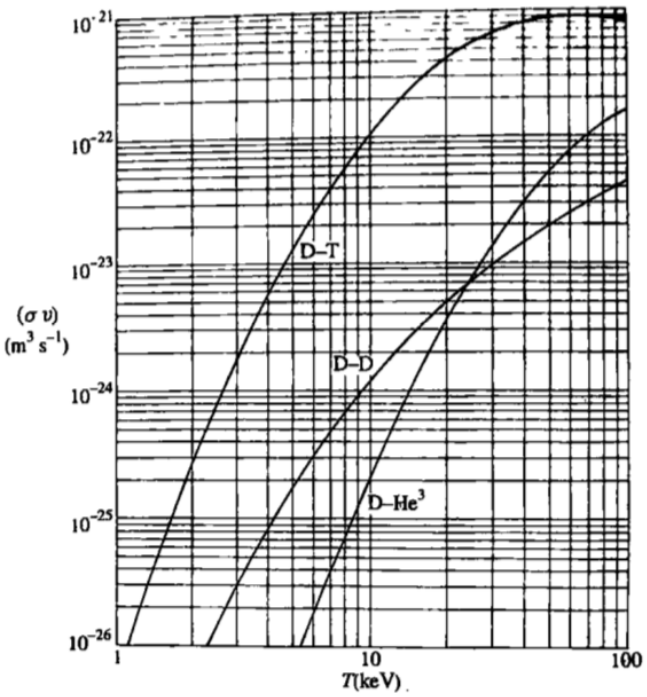

Figure 1.3: $\langle \sigma v \rangle$ reactivity function of the plasma temperature T in keV [4]

present in seawater [7]. In addition neutrons have the role of heating a water blanket located in between the vacuum vessel and the superconducting magnets. The kinetic energy of these neutrons is being extracted by the cooling water, which also help to protect the external components. The resulting steam would be used to drive turbines converting the energy into electricity. In astrophysical plasmas, such as starts including our Sun, these reactions are possible because of the immense gravitational force that confines the particles and drives the fusion reactions. Unlike stars, laboratory plasmas require a different type of confinement for controlling the fusion process. The two most favourable options are the inertial confinement fusion [8] by means of high-power lasers compressing rapidly a capsule of D−T fuel, or the magnetic confinement fusion [4] in thermonuclear reactors by means of strong magnetic fields.

1.3 Plasmas

The term *plasma* refers etymologically to *shape*, *body* or *molded figure* from the greek language [9]. Its first use was in the field of low pressure mercury arcs in vacuum tubes for describing glowing ionised gases and

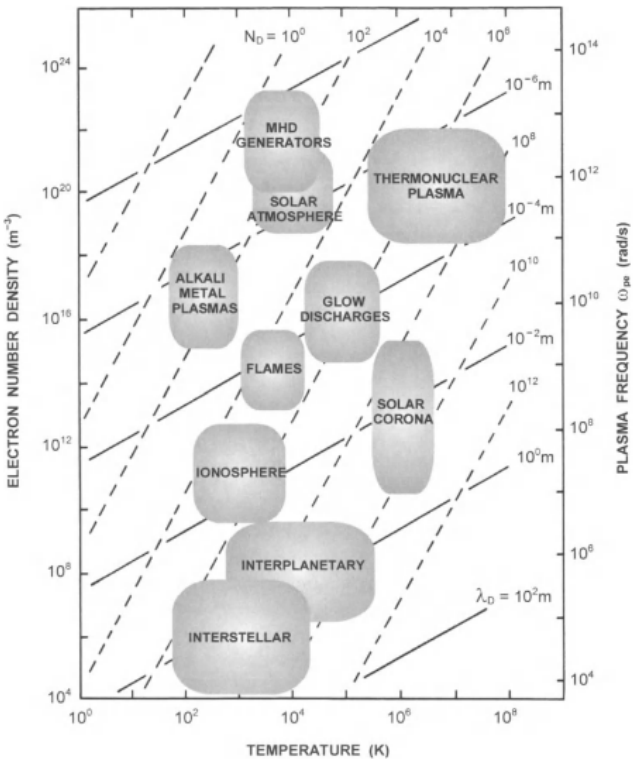

Figure 1.4: Diagram of plasmas in function of the temperature, the density and the plasma frequency [13]

was attributed to Irving Langmuir [10, 11]. This came purely as a necessity of distinguishing the main part of the discharge from the dark space (or sheath) region at the electrodes. This main part was at that time described by terms such as "complete charge space neutralization", "highly conductive" and being "unaffected by any imposed potential difference" [11]. Tonks clarified decades later that the analogy with the protoplasm image of a cellular jelly present in the blood was not intended [12]. Since then the term plasma has been associated with the fourth state of matter [13], even if this phase transition is misleading in comparison with the classic states of matter. The solid-liquid-gas cycle is characterised by first-order phase transitions which happen at fixed temperature points. Plasmas are instead meta-stable states that rely on combined requirements, not only by internal properties such as the density, but also by external factors such as the fields [14]. The generation of a plasma requires an energy input using different methods such as photo-ionisation or thermal-ionisation via electromagnetic radiation, as well as collisions in order to overcome the atom-electron binding forces. This phase transition is not immediate from 'neutral' to 'fully ionised', it depends on a temperature range and the system's dimensions. Plasma research covers all

types of ionised gases, from laboratory discharges to inter-stellar and inter-planetary as well as earth bound plasmas and ionospheres around planets. A diagram including these different types of plasmas is presented in Fig. 1.4. In order to categorise them macroscopic models are conceived taking into account macroscopic variables such as temperature, density, and pressure. These are thermodynamic state variables that describe the system's macroscopic state but are a result of a large amount of particles interacting in the microscopic scale. The additional complexity with plasmas is that the system contains many particles all moving with their own velocity (unlike a solid) and also their charges interacting via long range Coulomb forces (unlike a gas). The particles respond to external electric, magnetic and gravitational forces. Such a system cannot be described in a few macroscopic variables. The resulting collective behaviours and organising processes are a major challenge for the analysis of magnetised plasmas and represent the main interest of this thesis.

1.3.1 Definition criteria

There are 4 main criteria that define a plasma state [13]. The first criterion is linked to the effect of electric screening. In an ionised gas charged particles (electrons and ions) interactions are dominated, in the absence of external forces, by the long range Coulomb force F written as:

$$F = \frac{1}{4\pi\varepsilon_0}\frac{q_i q_j}{r^2} \tag{1.8}$$

with ε_0 the vacuum permittivity, (q_i, q_j) the charges of both (i, j) particles, and r the distance between them. Each particle reacts to attractive - repulsive forces caused by all the other particles in the plasma. However, the strongest contribution to the force on a particle will be from its nearest neighbours due to the $1/r^2$ dependence. This gives rise to collective effects. The electric field produced by a charged particle is rapidly reduced (screened out) due to the presence of the surrounding particles to within a distance called the Debye length. If we define L as the plasma size the condition for a plasma must satisfy:

$$L >> \lambda_D = \sqrt{\frac{\varepsilon_0 k_B T}{n_e e^2}} \tag{1.9}$$

with λ_D the Debye length, k_B the Boltzmann constant, e the elementary charge, T the temperature in Kelvin and n_e the electron density in m^{-3} in the plasma. The second criterion is an extension of the first criterion.

From λ_D as a radius we can define a Debye sphere where charges inside interact between themselves while screening external electric fields. The corresponding condition is:

$$n_e {\lambda_D}^3 >> 1 \tag{1.10}$$

i.e. there are enough electrons inside the sphere for collectively shielding electrostatic potentials. In order to have shielding it requires the quasi-neutrality of the plasma. Defining n_i as the ion density, with i denoting the species in the plasma, the third criterion is:

$$n_e = \sum_i n_i \tag{1.11}$$

The fourth criterion is related to the stability of the charge neutrality. In response to an external perturbation the plasma reacts with a natural oscillation of the more mobile electrons in order rearrange the charges and return to an equilibrium. However, collisions between electrons and neutrals can dampen these oscillation. If we define ν_{pe} and ν_{en} as the electron plasma frequency and the electron-neutral collision frequency respectively, then the required condition is:

$$\frac{1}{2\pi}\sqrt{\frac{n_e e^2}{m_e \varepsilon_0}} = \frac{\omega_{pe}}{2\pi} \equiv \nu_{pe} > \nu_{en} \tag{1.12}$$

The angular electron plasma frequency is noted ω_{pe} and represents the characteristic time for restoring neutrality after an external perturbation. An ideal plasma is considered collisionless when the electrostatic interactions dominate over the collisions of the neutral gas. There are different theoretical frameworks that describe the plasma depending on the scale of observation or regarding the Debye length: particle theory, kinetic theory ($L > \lambda_D$) and fluid theory ($L >> \lambda_D$).

1.3.2 Particle theory: gyromotion and drifts

This model describes the individual particle motion under the influence of external electromagnetic fields. The introduction of particle theory is necessary as it leads to more complex models (*i.e.* the kinetic model) when collective processes are considered. The dynamics of an individual particle with mass m, charge q and velocity v are described by the Newton's equation of motion:

$$m\frac{d\boldsymbol{v}}{dt} = q(\boldsymbol{E} + \boldsymbol{v} \times \boldsymbol{B}) \tag{1.13}$$

with the right hand side representing the Lorentz force due to $\boldsymbol{E}$ and $\boldsymbol{B}$, the electric and magnetic fields respectively (bold notations refer to vectors in a (x, y, z) coordinates space). In an uniform magnetic field $\boldsymbol{B} = B\hat{\boldsymbol{z}}$ aligned to the z axis with $\hat{\boldsymbol{z}}$ its unit vector, and no electric field $\boldsymbol{E} = 0$, the solution to the equation describes a circular orbit around the field line with perpendicular velocities:

$$v_{x,y} = v_{\perp} e^{\pm i\omega_c t} \qquad\qquad \omega_c = \frac{|q|\, B}{m} \tag{1.14}$$

Here ω_c is the cyclotron frequency describing the particle's gyration around the field line, counterclockwise for ions and clockwise for electrons. Integrating Eq. 1.13 with the solution 1.14 gives the particle's orbital trajectory:

$$x = x_0 \pm i\rho_L e^{i\omega_c t} \qquad\qquad y = y_0 \pm \rho_L e^{i\omega_c t} \tag{1.15}$$

with (x_0, y_0, z_o) the guiding center coordinates and ρ_L the Larmor radius of the orbit:

$$\rho_L = \frac{v_{\perp}}{\omega_c} = \frac{m v_{\perp}}{|q|\, B} \tag{1.16}$$

Considering the particle has a velocity $v_{\parallel}$ along the field line (*i.e.* in the $\hat{\boldsymbol{z}}$ direction) the resulting motion is an helicoidal trajectory around the field line. However, the addition of force fields (*e.g.* gravitational, electric) and gradients modify the particle's trajectory with superimposed drift velocities. Applying any perpendicular force field to the parallel direction set by the magnetic field produces a drift velocity of the form [15]:

$$\boldsymbol{v_F} = \frac{\boldsymbol{F} \times \boldsymbol{B}}{qB^2} \tag{1.17}$$

In the case of an uniform electric field E the derivation of the perpendicular component in Eq. 1.13 results in a drift velocity given by:

$$\boldsymbol{v_E} = \frac{\boldsymbol{E} \times \boldsymbol{B}}{B^2} \tag{1.18}$$

The combined motion of the gyration and the $E \times B$ drift is illustrated in Fig. 1.5. This drift is independent of the charge and the mass of the particle so both ions and electrons will drift in the same direction and at the same speed. During the part of the orbit where the particle is accelerated by the $\boldsymbol{E}_{\perp}$ field the Larmor radius is increased. During the other part, the particle is decelerated by the $E_{\perp}$ field and results in a smaller Larmor radius. The equation below is a special case of a stationary E field. A more complex motion occurs

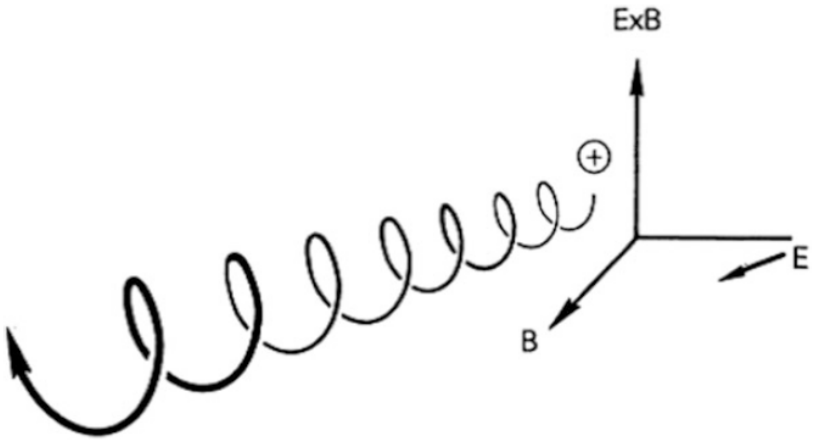

Figure 1.5: Schematics of a charged particle gyration under the $E \times B$ drift [15]

if the electric field is rapidly varying. In case of a non-uniform sinusoidal $E_\perp(k) \sim e^{ikx}$ field depending on the spatial angular frequency *i.e.* wavevector $k = 2\pi/\lambda$, a corrective term adds to the electric drift [15]:

$$\boldsymbol{v_E} = \frac{\boldsymbol{E} \times \boldsymbol{B}}{B^2} - \frac{1}{4}\rho_L^2 k^2 \frac{\boldsymbol{E} \times \boldsymbol{B}}{B^2} = \left(1 - \frac{1}{4}\rho_L^2 k^2\right) \frac{\boldsymbol{E} \times \boldsymbol{B}}{B^2} \sim \left(1 + \frac{1}{4}\rho_L^2 \boldsymbol{\nabla}^2\right) \frac{\boldsymbol{E} \times \boldsymbol{B}}{B^2} \tag{1.19}$$

This is known as the finite Larmor radius effect: the inhomogeneity causes a charge separation, affecting more ions due to its dependence on ρ_L^2. The derivative term $ik \sim \boldsymbol{\nabla}$ represents the resulting secondary electric field due to this separation, amplifying the inhomogeneity up to a drift instability. Differently, in case of a time-varying sinusoidal electric field $E_\perp(t) \sim e^{i\omega t}$, the time derivation from the equation of motion 1.13 brings an additional velocity term of the form:

$$\boldsymbol{v_{pol}} = \frac{m}{qB^2} \frac{d\boldsymbol{E}_\perp(t)}{dt} = \pm \frac{1}{\omega_c B} \frac{d\boldsymbol{E}_\perp(t)}{dt} \sim \pm \frac{i}{B} \left(\frac{\omega}{\omega_c}\right) \boldsymbol{E}_\perp(t) \tag{1.20}$$

This is known as the *polarisation* drift: the slow variation of the electric field causes inertial shifts of the guiding center the first half-cycle of each gyration, mostly affecting the ions due to the mass difference. Besides, the presence of an inhomogeneous magnetic field has an important impact on the particle's dynamics and is relevant for confining the plasma. The decomposition of the field geometry in the coordinates space (x, y, z) comes down to identifying inhomogeneous terms of the $\boldsymbol{\nabla B}$ matrix. Considering that the divergence of the field is $\boldsymbol{\nabla} \cdot \boldsymbol{B} = 0$, these terms correspond to the non-diagonal components: the perpendicular gradient (the perpendicular variation of the main component along the field line in the z direction *i.e.* $\partial B_z/\partial x$ and $\partial B_z/\partial y$), the curvature (the parallel variation of minor components *i.e.* $\partial B_x/\partial z$ and $\partial B_y/\partial z$), and the shear

(the perpendicular variation of minor components *i.e.* $\partial B_x/\partial y$ and $\partial B_y/\partial x$). The curvature is described by field lines' arcs in the (x, z) or (y, z) planes involving rotational trajectories. The shear is described by parallel field lines of opposite orientations in the z direction with rotating variations in the (x, y) plane, often caused by a prior curvature and observed in helical configurations. It is possible to define the gradient components by using the coordinates space ($\perp$, $\parallel$) with respect to the field lines: $\boldsymbol{\nabla}_\perp B$ and $\boldsymbol{\nabla}_\parallel B$, *i.e.* the perpendicular and parallel gradients to the field lines respectively. In order to study the particles' motion, it is assumed that these introduced inhomogeneities experienced by the particle (*e.g.* drifts mechanisms) do not significantly vary over the gyroscales in space and in time respectively:

$$\rho_L|\boldsymbol{\nabla} B| << \boldsymbol{B} \qquad\qquad \frac{\partial \boldsymbol{B}}{\partial t} << |\omega_c|\,\boldsymbol{B} \tag{1.21}$$

The particle's coordinates with position $\boldsymbol{r}$ from the center of the axes origin and velocity $\boldsymbol{v}$ can be decomposed in its different contributions:

$$\boldsymbol{r} = \boldsymbol{R} + \boldsymbol{\rho_L} = \boldsymbol{R} + \rho_L\left[\cos(\omega_c t)\hat{\boldsymbol{x}} + \sin(\omega_c t)\hat{\boldsymbol{y}}\right] \tag{1.22}$$

$$\boldsymbol{v} = \boldsymbol{v}_\parallel + \boldsymbol{v}_\perp = \boldsymbol{v}_\parallel + \boldsymbol{v_c} + \boldsymbol{v_d} = v_\parallel\hat{\boldsymbol{b}} + \omega_c(\boldsymbol{\rho_L}\times\hat{\boldsymbol{b}}) + \boldsymbol{v_d} \tag{1.23}$$

$\boldsymbol{R}$ is the guiding-center radius, $\boldsymbol{v_c}$ the cyclotronic velocity due to the gyromotion, $\boldsymbol{v_d}$ the sum of all velocity drifts caused by the magnetic inhomogeneities, and $\hat{\boldsymbol{b}} = \boldsymbol{B}/B$ the magnetic unit vector. By defining the mean field $\langle\boldsymbol{B}\rangle$ plus its associated perturbation $\tilde{\boldsymbol{B}}$ at the vicinity of the guiding center (x_0, y_0):

$$\boldsymbol{B} = \langle\boldsymbol{B}\rangle + (\boldsymbol{\rho_L}\cdot\boldsymbol{\nabla})\tilde{\boldsymbol{B}} \tag{1.24}$$

The Taylor expansion applied to Eq. 1.13 allows to identify the perpendicular and parallel components of the Lorentz force averaged over a gyration:

$$\langle\boldsymbol{F}\rangle = \langle q\omega_c(\boldsymbol{\rho_L}\times\hat{\boldsymbol{b}})\times(\boldsymbol{\rho_L}\cdot\boldsymbol{\nabla})\tilde{\boldsymbol{B}}\rangle = \left\langle q\omega_c\rho_L^2\frac{\partial\tilde{B}_z}{\partial r}\hat{\boldsymbol{r}} - q\omega_c\rho_L^2\frac{\partial\tilde{B}_r}{\partial r}\hat{\boldsymbol{z}}\right\rangle \tag{1.25}$$

The $\hat{\boldsymbol{r}}$ term corresponds to the perpendicular component to $\boldsymbol{B}$ noted $\langle\boldsymbol{F}_\perp\rangle$. This force is related to the gradient $\boldsymbol{\nabla}_\perp B$ causing a drift velocity given by:

$$\boldsymbol{v}_{\boldsymbol{\nabla B}} = \frac{\langle\boldsymbol{F}_\perp\rangle\times\boldsymbol{B}}{qB^2} = \frac{1}{2}\frac{v_\perp^2}{\omega_c}\frac{\boldsymbol{B}\times\boldsymbol{\nabla}B}{B^2} \qquad\qquad \langle\boldsymbol{F}_\perp\rangle = -\mu\boldsymbol{\nabla}_\perp B \tag{1.26}$$

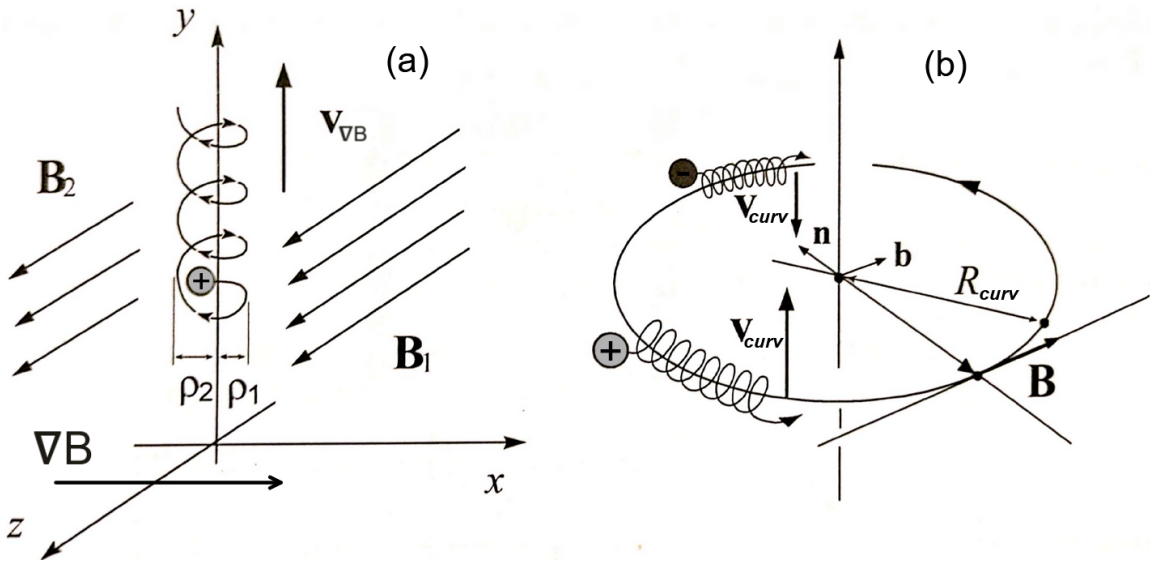

Figure 1.6: Schematics of the ∇B drift (a) and the curvature drift (b) [16]

This is called the ∇B drift, it is charge-dependant so ions and electrons move in opposite directions. The *magnetic moment* μ represents the ratio between the particle's gyrokinetic energy and the magnetic field:

$$\mu = \frac{mv_\perp^2}{2B} \tag{1.27}$$

Furthermore when the field lines present a curvature a centrifugal force $\boldsymbol{F_{cf}}$ acts on the particles along the field lines. Introducing the curvature radius R_{curv}, the cross product of the normal term $d\boldsymbol{v}_\parallel/dt \sim (v_\parallel^2/R_{curv})\hat{\boldsymbol{n}}$ in Eq. 1.13 with $\hat{\boldsymbol{b}}$ allows to identify an additional drift velocity:

$$\boldsymbol{v_{curv}} = \frac{\boldsymbol{F_{cf}} \times \boldsymbol{B}}{qB^2} = \frac{v_\parallel^2}{\omega_c}\frac{[(\boldsymbol{B}\cdot\boldsymbol{\nabla})\boldsymbol{B}]\times\boldsymbol{B}}{B^3} \qquad \boldsymbol{F_{cf}} = \frac{mv_\parallel^2}{R_{curv}}\hat{\boldsymbol{n}} \tag{1.28}$$

This is called the *curvature* drift, and also depends on the species. In Fig. 1.6 both drifts are illustrated. The ∇B drift is interpreted as the accumulation of unbalanced gyrations, *i.e.* the variation of the Larmor radius such as $\rho_1 < \rho_2$ due to the different magnetic regions determined by $B_1 > B_2$. The curvature drift is the result of the magnetic field bending and the subsequent centrifugal effect. The following sections explain how the combination of these two last drifts cause a major problem for plasma confinement. The condition for confining a particle depends on the shape of the field, in particular the component $\boldsymbol{\nabla}_\parallel B$ parallel to $\boldsymbol{B}$. The non-uniformity of the magnetic field can include zones where field lines converge or diverge. When the particles approach a region where the field lines converge a force arises which causes particles to decelerate

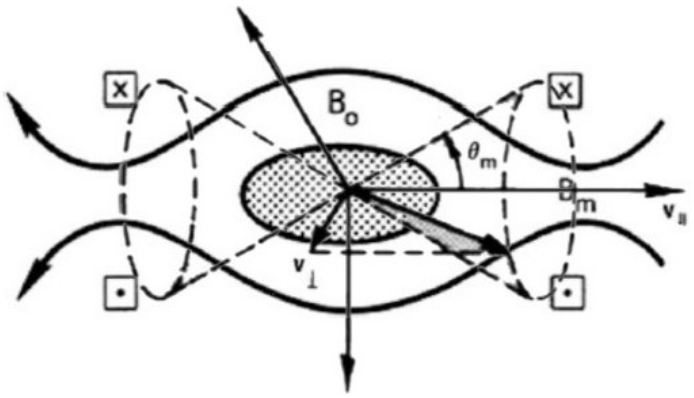

Figure 1.7: Schematics of a loss cone of a plasma trapped in a magnetic bottle [15]

and reverse their motion back along the field lines. This force corresponds to the $\hat{\boldsymbol{z}}$ term in Eq. 1.25 (assuming that $\partial\tilde{B}_r/\partial r \sim (-1/2)\partial\tilde{B}_z/\partial z$) which corresponds to the parallel component to $\boldsymbol{B}$ noted $\langle \boldsymbol{F}_{\parallel} \rangle$:

$$\langle \boldsymbol{F}_{\parallel} \rangle = -\mu \boldsymbol{\nabla}_{\parallel} B \qquad\qquad \frac{d\mu}{dt} = 0 \tag{1.29}$$

$\boldsymbol{F}_{\parallel}$ is known as the *mirror* force. The Larmor radius can change but the magnetic moment is an adiabatic invariant *i.e.* μ is approximately a constant of the motion as long as the hypotheses formulated in Eqs. 1.21 remain valid. That implies that $v_{\perp}^2$, *i.e.* the particle's energy: $mv^2 = m(v_{\parallel}^2 + v_{\perp}^2)$, is controlled by $\boldsymbol{B}$. It is therefore possible to build magnetic traps in order to confine plasmas by adjusting the field. The condition that defines when particles are trapped in a magnetic mirror bottle is given by [15]:

$$sin^2(\theta_m) = \frac{B_o}{B_m} < \frac{v_{\perp}^2}{v_{\parallel}^2} \tag{1.30}$$

where B_o is the magnetic field at the midplane, B_m the magnetic field at the mirror point (*i.e.* point of closure), and θ_m is the pitch angle. This angle defines a boundary region in the velocity space called the loss cone represented in Fig. 1.7: all particles which velocities are inside the cone will be able to escape the trap. As a consequence, confined plasmas in magnetic traps are not isotropic.

1.3.3 Kinetic theory: statistical approach

Instead of considering the motion for each individual particle in a plasma, the kinetic theory is a more practical approach based on distribution functions $f(\mathbf{x}, \boldsymbol{v}, t)$ that represent the probability of a particle to

exist at a position $\mathbf{x}$ with velocity $\boldsymbol{v}$ at time t [4]. With this statistical tool it is possible to define a phase space of Eulerian coordinates $(\mathbf{x}, \boldsymbol{v})$ containing sets of Lagrangian coordinates $\mathbf{X_i}(t)$ positions and $\boldsymbol{V_i}(t)$ velocities of the $\boldsymbol{i}$ orbit in the six-dimensional space. $\mathbf{X_i}(t)$ represents a set of occupied positions by a particle in the $\mathbf{x}$ space at successive t times. The function N_s for a species s with N_0 particles represents the number of particles contained in the phase space:

$$N_s(\mathbf{x}, \boldsymbol{v}, t) = \sum_{i}^{N_0} \delta[\mathbf{x} - \mathbf{X_i}(t)]\delta[\boldsymbol{v} - \boldsymbol{V_i}(t)] \tag{1.31}$$

with δ the Dirac delta function where:

$$\delta[\mathbf{x} - \mathbf{X_i}(t)] = \delta(x - X_i(t))\delta(y - Y_i(t))\delta(z - Z_i(t)) \tag{1.32}$$

$$\delta[\boldsymbol{v} - \boldsymbol{V_i}(t)] = \delta(v_x - V_{xi}(t))\delta(v_y - V_{yi}(t))\delta(v_z - V_{zi}(t)) \tag{1.33}$$

N_s describes a number of particles but it is referred as a density function in the literature. The integration of N_s over a volume $d^3\mathbf{x}d^3\boldsymbol{v}$ contains a number of particles within ($\mathbf{x}$, $\mathbf{x}$ + $d\mathbf{x}$) and ($\boldsymbol{v}$, $\boldsymbol{v}$ + $d\boldsymbol{v}$). The total number of particles in the plasma with electrons and ions is:

$$N(\mathbf{x}, \boldsymbol{v}, t) = \sum_{e,i} N_s(\mathbf{x}, \boldsymbol{v}, t) \tag{1.34}$$

The equation of motion for one particle subject to the Lorentz force is given by this approach to be:

$$\dot{\boldsymbol{V}}_{\boldsymbol{i}}(t) = \frac{q_s}{m_s}(\boldsymbol{E}^m[\mathbf{X_i}(t), t] + \boldsymbol{V_i}(t) \times \boldsymbol{B}^m[\mathbf{X_i}(t), t]) \qquad \dot{\mathbf{X}}_{\boldsymbol{i}}(t) = \boldsymbol{V_i}(t) \tag{1.35}$$

The superscript m refers to the microscopic $\boldsymbol{E}^m$, $\boldsymbol{B}^m$ fields produced by the interactions of the particles themselves, together with external applied fields [17]. These obey the Maxwell equations:

$$\begin{aligned} \boldsymbol{\nabla} \cdot \boldsymbol{E}^m(\mathbf{x}, t) &= \frac{\rho^m(\mathbf{x}, t)}{\varepsilon_0} & \boldsymbol{\nabla} \cdot \boldsymbol{B}^m(\mathbf{x}, t) &= 0 \\ \boldsymbol{\nabla} \times \boldsymbol{E}^m(\mathbf{x}, t) &= -\frac{\partial \boldsymbol{B}^m(\mathbf{x}, t)}{\partial t} & \boldsymbol{\nabla} \times \boldsymbol{B}^m(\mathbf{x}, t) &= \mu_0 \boldsymbol{j}^m(\mathbf{x}, t) + \frac{1}{c^2}\frac{\partial \boldsymbol{E}^m(\mathbf{x}, t)}{\partial t} \end{aligned} \tag{1.36}$$

with ρ^m and $\boldsymbol{j}^m$ the microscopic charge density and current density respectively:

$$\rho^m(\mathbf{x}, t) = \sum_{e,i} q_s \int_v N_s(\mathbf{x}, \boldsymbol{v}, t) d^3\boldsymbol{v} \qquad \boldsymbol{j}^m(\mathbf{x}, t) = \sum_{e,i} q_s \int_v N_s(\mathbf{x}, \boldsymbol{v}, t)\boldsymbol{v} d^3\boldsymbol{v} \tag{1.37}$$

Combining the derivation of the density phase space (eq. 1.31) and the equation of motion (eq. 1.35) leads to the conservation law of the density:

$$\frac{\partial N_s(\mathbf{x}, \boldsymbol{v}, t)}{\partial t} + \boldsymbol{v} \cdot \boldsymbol{\nabla}_{\boldsymbol{x}} N_s + \frac{q_s}{m_s}\left(\boldsymbol{E}^m(\mathbf{x}, t) + \boldsymbol{v} \times \boldsymbol{B}^m(\mathbf{x}, t)\right) \cdot \boldsymbol{\nabla}_{\boldsymbol{v}} N_s = 0 \tag{1.38}$$

This is known as the Klimontovich equation, with gradients notations $\boldsymbol{\nabla}_{\boldsymbol{x}} \equiv \partial/\partial \mathbf{x}$ and $\boldsymbol{\nabla}_{\boldsymbol{v}} \equiv \partial/\partial \boldsymbol{v}$. Starting from the Liouville equation or the Bogolyubov hierarchy leads to the same equation 1.38 but instead of describing individual particles it describes systems of particles [17]. However, this equation is too detailed containing all particles' orbits for one species, the goal being to know the average evolution of the plasma. For that purpose a mean field approximation is undertaken. The ensemble averaging defines $\langle N_s(\mathbf{x}, \boldsymbol{v}, t)\rangle$ as the distribution function f_s *i.e.* the probability of a particle inside a volume $\Delta\mathbf{x}\Delta\boldsymbol{v}$ sufficiently homogeneous in density. Within this volume the number of particles can fluctuate due to perturbations defined by the density fluctuation $\tilde{N}_s$. Each distribution can be then presented as the sum of its mean function plus its fluctuation as follows:

$$N_s(\mathbf{x}, \boldsymbol{v}, t) = f_s(\mathbf{x}, \boldsymbol{v}, t) + \tilde{N}_s(\mathbf{x}, \boldsymbol{v}, t) \tag{1.39}$$

$$\boldsymbol{E}^m(\mathbf{x}, t) = \boldsymbol{E}(\mathbf{x}, t) + \tilde{\boldsymbol{E}}(\mathbf{x}, t) \tag{1.40}$$

$$\boldsymbol{B}^m(\mathbf{x}, t) = \boldsymbol{B}(\mathbf{x}, t) + \tilde{\boldsymbol{B}}(\mathbf{x}, t) \tag{1.41}$$

By applying the ensemble averaging with $\langle \boldsymbol{E}^m\rangle = \boldsymbol{E}$, $\langle \boldsymbol{B}^m\rangle = \boldsymbol{B}$ and $\langle \tilde{N}_s\rangle = \langle \tilde{\boldsymbol{E}}\rangle = \langle \tilde{\boldsymbol{B}}\rangle = 0$, the equation (1.38) becomes:

$$\frac{\partial f_s(\mathbf{x}, \boldsymbol{v}, t)}{\partial t} + \boldsymbol{v} \cdot \boldsymbol{\nabla}_{\boldsymbol{x}} f_s + \frac{q_s}{m_s} (\boldsymbol{E} + \boldsymbol{v} \times \boldsymbol{B}) \cdot \boldsymbol{\nabla}_{\boldsymbol{v}} f_s = -\frac{q_s}{m_s} \langle (\tilde{\boldsymbol{E}} + \boldsymbol{v} \times \tilde{\boldsymbol{B}}) \cdot \boldsymbol{\nabla}_{\boldsymbol{v}} \tilde{N}_s\rangle = C[f_{s_1}, f_{s_2}] \tag{1.42}$$

This is known as the plasma kinetic equation or Boltzmann equation. The left hand side represents the collective effects. The right hand side represents the force arising from fluctuations, noted as $C[f_{s_1}, f_{s_2}]$ the Krook collision operator between two species s_1, s_2 accounting for binary Coulomb collisions in the $\Delta\boldsymbol{v}$ space. If the volume is considered to contain an infinite amount of particles the statistical approach reveals relative fluctuations can be neglected. The fluctuations terms are approximated to constants such as $\tilde{N}_s \sim N_0^{1/2}$ and fields $\tilde{\boldsymbol{E}} \sim e\tilde{N}_s \sim N_0^{-1/2}$ then the right hand size vanishes and the equation is reduced to:

$$\frac{\partial f_s(\mathbf{x}, \boldsymbol{v}, t)}{\partial t} + \boldsymbol{v} \cdot \boldsymbol{\nabla}_{\boldsymbol{x}} f_s + \frac{q_s}{m_s} (\boldsymbol{E} + \boldsymbol{v} \times \boldsymbol{B}) \cdot \boldsymbol{\nabla}_{\boldsymbol{v}} f_s = 0 \tag{1.43}$$

This is known as the Vlasov equation or collisionless Boltzmann equation. However, this equation represents a non-linear problem in a 7 dimensional space. The gyrokinetic approach tries to reduce up to 5 dimensions by changing the dependences of the distribution function $f_G(\mathbf{x_G}, v_{G\|}, \mu, t)$ taking the guiding center G as

reference with coordinates $\mathbf{x_G} = (x_G, y_G, z_G)$, the parallel velocity $v_{G\|}$, the magnetic moment μ (*i.e.* an invariant) and the time t. Gyrokinetic simulations are computational tools that help to study turbulence but these are overly time consuming and remain a research challenge for improving their performance.

1.3.4 Fluid theory: moments and drifts

The Boltzmann equation describes the evolution of the distribution function for different species in time and space and the interaction with the electromagnetic fields. However, in the macroscopic scale it is sufficient to evaluate the dynamics of the plasma by means of average quantities such as the density and temperature. In that case a fluid model is more convenient as it reduces the complexity of the equation by integrating over the velocity phase space $\boldsymbol{v}$ thereby reducing to a 4 dimensional problem. These macroscopic variables of the fluid are defined by the *moments* of the distribution function f_s usually assumed to be Maxwellian [18]:

$$n_s(\boldsymbol{x},t) = \int_v f_s(\boldsymbol{x},\boldsymbol{v},t)d^3\boldsymbol{v} \tag{1.44}$$

$$\boldsymbol{u}_s(\boldsymbol{x},t) = \frac{1}{n_s(\boldsymbol{x},t)}\int_v \boldsymbol{v} f_s(\boldsymbol{x},\boldsymbol{v},t)d^3\boldsymbol{v} \tag{1.45}$$

$$p_s(\boldsymbol{x},t) = n_s(\boldsymbol{x},t)T_s(\boldsymbol{x},t) = \int_v \frac{m_s}{3}(\boldsymbol{v}-\boldsymbol{u}_s(\boldsymbol{x},t))^2 f_s(\boldsymbol{x},\boldsymbol{v},t)d^3\boldsymbol{v} \tag{1.46}$$

with n_s the density (0th-order moment), $\boldsymbol{u}_s$ the mean velocity (1st-order moment), and p_s (or T_s) the pressure (or temperature) (2nd-order moment) of the species s in the plasma. Integrating the Boltzmann equation (Eq. 1.42) over the velocity space for each order leads to the Braginskii's transport equations [18]:

$$\frac{\partial n_s}{\partial t} + \boldsymbol{\nabla}\cdot(n_s\boldsymbol{u}_s) = 0 \tag{1.47}$$

$$n_s m_s\left(\frac{\partial \boldsymbol{u_s}}{\partial t} + (\boldsymbol{u}_s\cdot\boldsymbol{\nabla})\boldsymbol{u}_s\right) = n_s q_s(\boldsymbol{E}+\boldsymbol{u}_s\times\boldsymbol{B}) - \boldsymbol{\nabla}p_s - \boldsymbol{\nabla}\cdot\overline{\boldsymbol{\Pi}}_s + \boldsymbol{R}_s \tag{1.48}$$

$$\frac{3}{2}\left(\frac{\partial p_s}{\partial t} + \boldsymbol{u}_s\cdot\boldsymbol{\nabla}p_s\right) + \frac{5}{2}p_s\boldsymbol{\nabla}\cdot\boldsymbol{u}_s + \boldsymbol{\nabla}\cdot\boldsymbol{Q}_s = -\mathrm{Tr}[(\overline{\boldsymbol{\Pi}}_s^T\cdot\boldsymbol{\nabla})\boldsymbol{u}_s] - W_s \tag{1.49}$$

These equations are in order the continuity equation, the momentum transport equation, and the energy transport equation. The viscous stress $\overline{\boldsymbol{\Pi}}_s$ and pressure $\overline{\boldsymbol{P}}_s$ tensors are associated with anisotropy and related by the unit tensor $\overline{\boldsymbol{I}}$. Tr is the trace notation. The matrix $p_s\overline{\boldsymbol{I}}$ contains the isotropic entries:

$$\overline{\boldsymbol{\Pi}}_s = \overline{\boldsymbol{P}}_s - p_s\overline{\boldsymbol{I}} \qquad\qquad \overline{\boldsymbol{P}}_{s_1} = \int_v m_{s_1}\boldsymbol{v}_{s_1}\boldsymbol{v}_{s_2}f_{s_1}d^3\boldsymbol{v} \tag{1.50}$$

Figure 1.8: Schematics of the diamagnetic drift pointing downwards [15]

The terms associated with the Krook operator are the friction force $\boldsymbol{R}_s$ and friction heat W_s defined by:

$$\boldsymbol{R}_{s_1} = -\int_v m_{s_1}(\boldsymbol{v} - \boldsymbol{u}_{s_1})C[f_{s_1}, f_{s_2}]d^3\boldsymbol{v} \qquad W_{s_1} = \int_v m_{s_1} v^2 C[f_{s_1}, f_{s_2}]d^3\boldsymbol{v} \tag{1.51}$$

The heat flux $\boldsymbol{Q}_s$ is introduced as a notation for the heat generated by collisions between species:

$$\boldsymbol{Q}_s = \int_v \frac{m_s}{2}|\boldsymbol{v} - \boldsymbol{u}_s|^2 (\boldsymbol{v} - \boldsymbol{u}_s) f_s d^3\boldsymbol{v} \tag{1.52}$$

With the assumptions of a stationary (*i.e.* $\partial \boldsymbol{u_s}/\partial t \simeq 0$) incompressible (*i.e.* $\boldsymbol{\nabla} \cdot \boldsymbol{u_s} \simeq 0$) fluid, the cross product of the Laplace force in the simplified momentum equation with the $\boldsymbol{B}$ field gives the $E \times B$ drift:

$$\boldsymbol{u_E} = \frac{\boldsymbol{E} \times \boldsymbol{B}}{B^2} \tag{1.53}$$

In comparison with the particle theory, the fluid theory includes collective effects due to the presence of gradients of macrovariables. Including the $\boldsymbol{\nabla} p_s$ term the same derivation and cross product leads to the expression of the *diamagnetic* drift [15]:

$$\boldsymbol{u_{d,s}} = -\frac{\boldsymbol{\nabla} p_s \times \boldsymbol{B}}{q_s n_s B^2} \tag{1.54}$$

The drift depends on the charge so ions and electrons will drift in opposite directions. This is not caused by any applied force but rather a response by the fluid to pressure gradients. Phenomenologically this is illustrated in Fig. 1.8: the appearance of a density (or temperature) gradient indicates there are regions with more (or energetic) particles than others. When $\boldsymbol{B}$ is aligned in one direction, neighbouring regions with more orbits (or rapid gyration) create in between an effective fluid flow transverse to $\boldsymbol{B}$ and the gradient. In

the case of including the transverse components from the divergence of the stress tensor $\overline{\boldsymbol{\Pi}}_s$ the derivation of the momentum equation, using the perturbation theory neglecting the previous drifts orders, and the cross product with $\boldsymbol{B}$ results in the expression of the fluid *polarisation* drift [18]:

$$\boldsymbol{u_{pol,s}} = \frac{m_s}{q_s B^2}\boldsymbol{B} \times \frac{d\boldsymbol{u_s}}{dt} = \frac{m_s}{q_s B^2}\left(\frac{\partial \boldsymbol{E}_\perp(t)}{\partial t} + (\boldsymbol{u_s}\cdot\boldsymbol{\nabla})\boldsymbol{E}_\perp(t)\right) \sim \frac{m_s}{q_s B^2}\frac{\partial \boldsymbol{E}_\perp(t)}{\partial t} \tag{1.55}$$

Assuming that $\boldsymbol{u_s} = \boldsymbol{u}_{\parallel,\boldsymbol{s}} + \boldsymbol{u}_{\perp,\boldsymbol{s}} = \boldsymbol{u}_{\parallel,\boldsymbol{s}} + \boldsymbol{u_E} + \boldsymbol{u_{d,s}}$ the main contribution comes from the $E \times B$ drift and the higher order term is neglected. All these drifts combined give the total fluid drift:

$$\boldsymbol{u}_{\perp,\boldsymbol{s}} = \frac{\boldsymbol{E}\times\boldsymbol{B}}{B^2} - \frac{\boldsymbol{\nabla}p_s \times \boldsymbol{B}}{q_s n_s B^2} + \frac{m_s}{q_s B^2}\frac{\partial \boldsymbol{E}_\perp}{\partial t} \tag{1.56}$$

This expression is analogous to the drifts from the particle theory if $\boldsymbol{\nabla}p$ is considered as an effective gravitational force similar to $\boldsymbol{\nabla}B$ effects. For example the inclusion of non-diagonal terms from the stress tensor adds contributions to the diamagnetic drift such as magnetisation ($\boldsymbol{\nabla}\times\mu\boldsymbol{B}$) and curvature ($(\boldsymbol{B}\cdot\boldsymbol{\nabla})\boldsymbol{B}$).

1.3.5 Magnetohydrodynamics (MHD)

The Braginskii equations for a multi-species fluid are analogous to the Navier-Stokes equations in hydrodynamics. The *hydrodynamic* approximation of the plasma as a fluid under the influence of a magnetic field is called *magnetohydrodynamics*. The first use of this term is attributed to Alfvén in the context of solar physics [19]. The MHD theory is based on a number of assumptions [20]:

- The *Alfvén wave* is the restoring oscillation in response of a tension force (*e.g.* bending) of a magnetic field line, defined by the Alfvén velocity:

$$\boldsymbol{v_A} = \frac{\boldsymbol{B}}{\sqrt{\mu_0 n_i m_i}} \tag{1.57}$$

  Its frequency can be defined by $\omega_A = k_\parallel v_A$ with $k_\parallel$ the wavevector along the field line.

- The thermal velocities are non-relativistic $u_i << u_e << c$; waves have phase velocities much slower than the speed of light $\omega/k << c$, with frequencies lower than the electron plasma frequency $\omega << \omega_{pe}$; these conditions imply that high frequency oscillations are not taken into account which simplifies the

system by neglecting the net charge and displacement currents:

$$\varepsilon_0 \boldsymbol{\nabla} \cdot \boldsymbol{E}/en << 1 \qquad\qquad \varepsilon_0 \mu_0 \frac{\partial \boldsymbol{E}}{\partial t} << 1 \tag{1.58}$$

The net charge condition implies the charge-neutral approximation:

$$n \simeq n_i \simeq n_e \tag{1.59}$$

- The two-fluid plasma is treated as a single-fluid *i.e.* a new set of variables in the transport equations do not depend of the species, in that sense the mass ρ and current $\boldsymbol{j}$ densities are defined as:

$$\rho = m_e n_e + m_i n_i \qquad\qquad \boldsymbol{j} = ne(\boldsymbol{u_i} - \boldsymbol{u_e}) \tag{1.60}$$

The mean fluid velocity $\boldsymbol{u}$ is then:

$$\boldsymbol{u} = \frac{1}{\rho}(\rho_e \boldsymbol{u_e} + \rho_i \boldsymbol{u_i}) \tag{1.61}$$

- Collisions cause the system to tend towards equilibrium which is characterized by Maxwellian distributions *i.e.* $T_e \simeq T_i \simeq T$; the plasma is then considered isotropic simplifying the pressure tensor and the friction force with the collision frequency ν_{ei} and the conductivity σ:

$$\boldsymbol{\nabla}\overline{\boldsymbol{P}} \sim \boldsymbol{\nabla} p \qquad\qquad \boldsymbol{R_e} = -\boldsymbol{R_i} = -\nu_{ei} n_e m_e (\boldsymbol{u_e} - \boldsymbol{u_i}) = \frac{n_e e}{\sigma}\boldsymbol{j} \tag{1.62}$$

Here the pressure p is defined by:

$$p = p_e + p_i + \frac{1}{3}(\rho_e |\boldsymbol{u_e} - \boldsymbol{u}|^2 + \rho_i |\boldsymbol{u_i} - \boldsymbol{u}|^2) \tag{1.63}$$

In this context $\boldsymbol{u}$ and $\boldsymbol{B}$ are meant to be the primary variables, whereas $\boldsymbol{j}$ and $\boldsymbol{E}$ are secondary variables that can be expressed in terms of primary variables. The derivation of the momentum equation (Eq. 1.48) for electrons under the previous assumptions leads to an expression of $\boldsymbol{E}$ dependent of the other variables:

$$\boldsymbol{E} + \boldsymbol{u} \times \boldsymbol{B} = \frac{\boldsymbol{j}}{\sigma} + \frac{\boldsymbol{j} \times \boldsymbol{B}}{n_e e} - \frac{\boldsymbol{\nabla} p_e}{n_e e} + \frac{m_e}{n_e e^2}\left(\frac{\partial \boldsymbol{j}}{\partial t} + \boldsymbol{\nabla}\left(\boldsymbol{u}\cdot\boldsymbol{j} + \boldsymbol{j}\cdot\boldsymbol{u} - \frac{\boldsymbol{j}\cdot\boldsymbol{j}}{n_e e}\right)\right) \tag{1.64}$$

This is the generalised Ohm's law with its different contributions. The term $\boldsymbol{u} \times \boldsymbol{B}$ is responsible for the convection; the term $\boldsymbol{j}/\sigma$ is the classical Ohm's law responsible for the dissipation of magnetic energy due to resistive losses; the term $\boldsymbol{j} \times \boldsymbol{B}/n_e e^2$ is the Hall effect responsible for the matter diffusion due to the Lorentz

force; the term $\boldsymbol{\nabla} p_e / n_e e^2$ is the pressure gradient responsible for thermal electron diffusion related to the diamagnetic drift; and the last term corresponds to the electrons inertia. The set of transport equations also requires a closure condition being the equation of state equivalent to the energy conservation equation in the ideal adiabatic case with γ the adiabatic index where d represents the degrees of freedom of the system:

$$\frac{d}{dt}\left(\frac{p}{\rho^\gamma}\right) = 0 \qquad\qquad \gamma = \frac{2+d}{d} \tag{1.65}$$

Finally the set of MHD equations including resistivity terms is:

$$\frac{\partial \rho}{\partial t} + \boldsymbol{\nabla} \cdot (\rho \boldsymbol{u}) = 0 \tag{1.66}$$

$$\rho\left(\frac{\partial \boldsymbol{u}}{\partial t} + (\boldsymbol{u}\cdot\boldsymbol{\nabla})\boldsymbol{u}\right) = -\boldsymbol{\nabla} p + \frac{1}{\mu_0}(\boldsymbol{\nabla}\times\boldsymbol{B})\times\boldsymbol{B} \tag{1.67}$$

$$\frac{\partial p}{\partial t} + \boldsymbol{u}\cdot\boldsymbol{\nabla} p = -\gamma p \boldsymbol{\nabla}\cdot\boldsymbol{u} + (\gamma-1)\frac{\eta}{\mu_0^2}|\boldsymbol{\nabla}\times\boldsymbol{B}|^2 \tag{1.68}$$

$$\frac{\partial \boldsymbol{B}}{\partial t} = \boldsymbol{\nabla}\times(\boldsymbol{u}\times\boldsymbol{B}) + \frac{\eta}{\mu_0}\boldsymbol{\nabla}^2\boldsymbol{B} - \frac{1}{\mu_0}(\boldsymbol{\nabla}\eta)\times(\boldsymbol{\nabla}\times\boldsymbol{B}) \tag{1.69}$$

These are in order the continuity equation, the momentum conservation equation, the adiabatic equation of state, and the induction equation with $\boldsymbol{\nabla}\times(\boldsymbol{u}\times\boldsymbol{B})$ representing convection and $\eta\boldsymbol{\nabla}^2\boldsymbol{B}/\mu_0$ representing diffusion. The additional term related to the gradient $\boldsymbol{\nabla}\eta$, with $\eta \equiv 1/\sigma$ the resistivity, is often neglected. The ideal MHD comes from neglecting all resistive terms *i.e.* imposing perfect ideal conductivity. Then the Ohm's law and Maxwell-Ampère's law are approximated to:

$$\boldsymbol{E} = -\boldsymbol{u}\times\boldsymbol{B} \qquad\qquad \boldsymbol{j} = \frac{\boldsymbol{\nabla}\times\boldsymbol{B}}{\mu_0} \tag{1.70}$$

In order to maintain the plasma in the steady state, the momentum conservation equation (Eq. 1.67) becomes the force balance equation:

$$\boldsymbol{\nabla} p = \boldsymbol{j}\times\boldsymbol{B} \tag{1.71}$$

This is an equilibrium condition which implies the currents caused by Lorentz forces and the pressure forces are in constant competition. This simplification provides a less precise description of the plasma compared to the kinetic theory but is nonetheless efficient. The MHD theory is applicable to many different domains, from astrophysical plasmas to experimental fusion plasmas. This approach allows to describe the stability conditions of plasmas under magnetic confinement specially in devices with complex geometries such as tokamaks.

1.4 Tokamaks

The term *tokamak* is a russian acronym standing for "Toroidalnaya Kamera i Magnitnaya Katushka" (Toroidal Chamber and Magnetic Coil) used for naming the experimental fusion device developed by Tamm and Sakharov during the 1950s [21]. The tokamak concept was presented at the 2nd Geneva Conference on Peaceful Uses of Atomic Energy in 1958. Following this conference the International Atomic Energy Agency (IAEA) was created to coordinate the cooperation in controlled thermonuclear fusion research. The first tokamak was named T-1 with major radius $R = 0.67$ m, minor radius $a = 0.17$ m, toroidal magnetic field B_T (at R) = 1.5 T and plasma current $I_p = 100$ kA, which was located at the Kurchatov Institute of Atomic Energy in the USSR. Similar configurations such as the reversed-field pinch and the stellarator were also tested based on the Z-pinch research during the 1950s at the UK and the USA. A continuation of a series of Russian tokamaks [22] motivated the international community and several countries started proposing prototypes of national tokamaks since the 1970s. During the 1980s several tokamaks were built and operational such as ASDEX at Garching (Germany), JET at Culham (UK), and DIII-D at San Diego (USA). In 1988 IAEA officially published the concept of ITER (International Thermonuclear Experimental Reactor, the acronym means *The Way* in Latin) [23]. This project was signed as a collaboration between the EU, Japan, the USA and Russia, later joined by China, South Korea, and India with the aim to demonstrate the feasibility of a magnetically confined fusion reactor. In 2005 disputes between the EU and Japan were solved reaching an agreement to build ITER at Cadarache in France. ITER is designed with a major radius $R = 6.2$ m, a minor radius $a = 2.0$ m, a toroidal magnetic field B_T (at R) = 5.3 T and a plasma current $I_p = 15$ MA [24]. This tokamak is still under construction with the first plasma discharge due in 2027 and full fusion power operations in 2035 [25]. In the long term the construction of the DEMO reactor would be tested as the first power plant for generating net electricity, for the moment under the design phase.

1.4.1 Tokamak equilibrium

The tokamak concept is based on a transformer combining a primary circuit, *i.e.* the central solenoid, and a secondary circuit, *i.e.* the plasma. The central solenoid consists in a set of inner poloidal coils in the

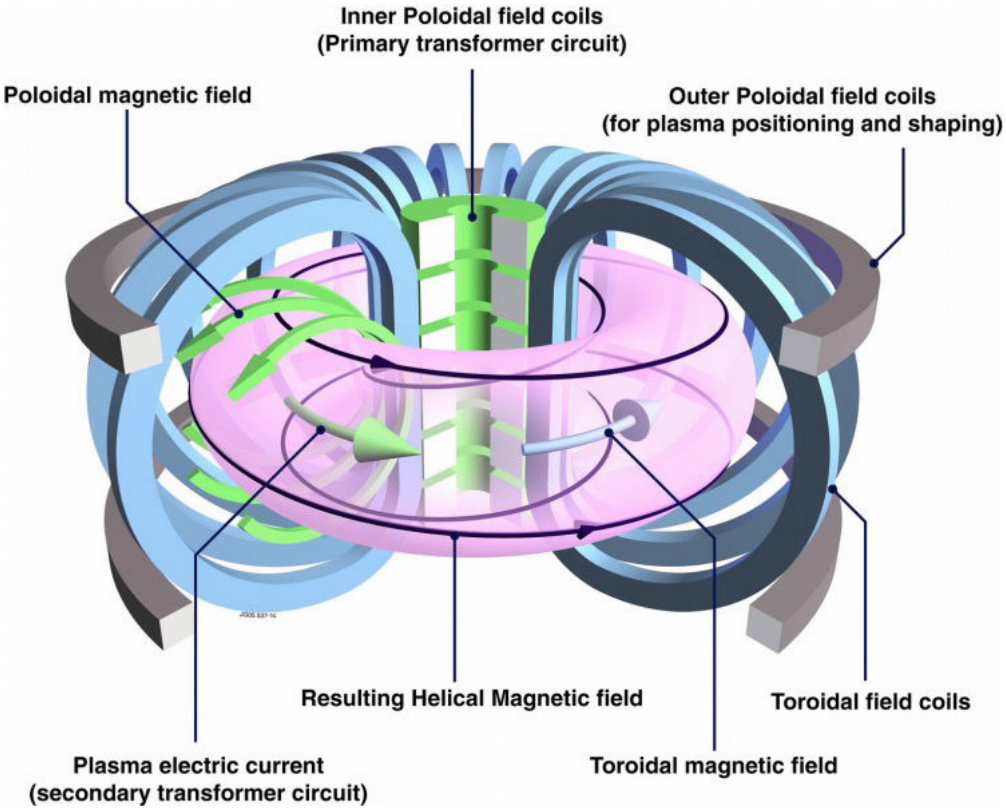

Figure 1.9: Schematics of a tokamak with toroidal and poloidal coils [26]

center of the torus. The varying ramping current in time through the inner poloidal coils at the central column induces a toroidal electric field driving a plasma current in the opposite direction to the solenoid current. This resulting toroidal current generates a poloidal field and the plasma resistance due to the collisions of accelerated particles acts as a self-heating process known as ohmic heating. This process is highlighted in green in Fig. 1.9. In order to enhance the stability of the plasma external toroidal coils induce a complementary toroidal magnetic field highlighted in blue. The combination of both fields produces a helical magnetic shape. However, multiple drifts inside the device let particles escape degrading the plasma stability, specially due to the magnetic drifts. The outer poloidal coils reshape the field for correcting the vertical drift by twisting the field lines all along the torus so even if the ∇B drift is still acting on the particles (*i.e.* drifting ions upward) it will bring them to their original position after one loop around the torus (*i.e.* driving ions downward). This applies respectively to electrons in the opposite direction. This configuration reduces the charges separation and improves the confinement. A consequence of this geometry is that it is

possible to define the magnetic topology by designing a nest of magnetic flux surfaces. The axisymmetry of the torus is defined by $(R,\ \theta,\ \phi)$ the radial, poloidal and toroidal coordinates. In this coordinate system it is possible to define Φ and Ψ the toroidal and poloidal fluxes respectively. For an arbitrary toroidal magnetic surface S the poloidal flux flowing across must satisfy the condition:

$$\boldsymbol{B} \cdot \boldsymbol{\nabla}\Psi = 0 \qquad\qquad \Psi = \int_S \boldsymbol{B_\theta} \cdot \boldsymbol{dS} \tag{1.72}$$

A similar remark is derived from the MHD equilibrium condition (Eq. 1.71) concerning the pressure:

$$\boldsymbol{B} \cdot \boldsymbol{\nabla} p = 0 \tag{1.73}$$

Both conditions indicate that magnetic field lines lie on surfaces of constant flux and pressure, the pressure $p(\Psi)$ is then a function of the flux. In this geometry the confined particles tend to follow characteristic trajectories. In the neoclassical theory the trapping condition is defined by the loss cone principle:

$$\frac{v_\parallel^2}{v_\perp^2} < \frac{B_{max}}{B_{min}} \sim \frac{1+\varepsilon}{1-\varepsilon} \sim 2\varepsilon \tag{1.74}$$

The inverse of the aspect ratio is defined as $\varepsilon \equiv a/R$. This leads to the existence of trapped particles bouncing between two positions depicting *banana* orbits on the poloidal cross section, while colliding with passing particles and producing the *bootstrap* current [27]:

$$j_{BS} \approx -\varepsilon^{1/2} \frac{1}{B_\theta} \frac{\partial p}{\partial R} \tag{1.75}$$

This expression of the current has been empirically tested and has shown to be beneficial for the plasma stability at the edge. However, the neoclassical theory is insufficient for describing turbulent regimes and instabilities. Turbulence remains a challenge that will be explored in later sections. Moreover, the ohmic heating presents two limitations. First, this method is based on the Faraday's law implying a continuous current ramping which is limited by the power supply and unable to achieve steady-state operations. Second, as the temperature increases the plasma resistance described by the Spitzer resistivity decreases such as [28]:

$$\eta_{Spitzer} = \frac{Ze^2 m_e^{1/2} \ln\Lambda}{(4\pi\varepsilon_0)^2 (k_B T_e)^{3/2}} \propto T_e^{-3/2} \qquad\qquad \Lambda = 4\pi n_e \lambda_D^3 \tag{1.76}$$

Here Λ is the plasma parameter and $\ln\Lambda$ is known as the Coulomb logarithm which measures the ratio of impact parameters in binary collisions. The resistivity reaches a stagnation point due to the deficit of

collisions unable to maintain no longer the self-heating process. Therefore the plasma requires auxiliary heating techniques such as generating electromagnetic waves into the plasma by damping energy to particles (*e.g.* electron-ion cyclotron resonance heating), or by injecting energetic neutral particles in the plasma transferring energy by collisions to the charged particles (*e.g.* neutral beam injection). Additional features such as the cooling system helps to evacuate the heat deposition for improving the magnets performance and the vessel preservation. The discovery of new superconducting materials still remains an essential research area for achieving the required strong fields for future reactors.

1.4.2 Ignition criteria

The main goal of thermonuclear reactors is to surpass the point where the required power for achieving fusion reactions is equal to the released energy from these reactions, known as *breakeven*. To some extent fusion machines will be commercially viable when producing surplus energy in continuous steady-state operation. The ability of a fusion reactor to produce net power output is estimated by the fusion gain factor:

$$Q = \frac{P_{fus}}{P_{aux}} \tag{1.77}$$

with P_{fus} the fusion power (from reactions) and P_{aux} the auxiliary heating power (from ohmic, resonance and injection heating). Breakeven occurs when $Q = 1$ and the ignition occurs when $Q \geq 1$ where the self-heating from fusion reactions is so dominant such that no more auxiliary heating is needed. The condition $Q = 5$ is considered to be the point where the self-heating process start being enough to sustain the plasma without external sources. For ITER a $Q = 10$ is estimated. It is possible to obtain a criterion for ignition by studying the contributions of the heating and losses:

$$P_{heat} = P_{\alpha} + P_{aux} \tag{1.78}$$

$$P_{loss} = P_{Bremsstrahlung} + P_{coll} + P_{turb} \tag{1.79}$$

The heating power is provided by the α particles as a result from the fusion reaction and the auxiliary heating techniques. The power losses can come from highly energetic radiation liberated due to the Bremsstrahlung effect, from collisions or turbulence. The α particles is related to the reaction rate assuming a D-T reaction

with a reactivity rate of $\langle\sigma v\rangle = 1.1\times10^{-24}\ T^2\ \mathrm{m^3\ s^{-1}}$ (T in keV) and $E_\alpha = 3.5$ MeV from Fig. 1.3 in section 1.2. The densities of deuterium and tritium are assumed to be equal in the plasma such as $n/2 = n_D = n_T$. The α heating power is defined by:

$$P_\alpha = \int n_D n_T \langle\sigma v\rangle E_\alpha dV = \int \frac{n^2}{4}\langle\sigma v\rangle E_\alpha dV \tag{1.80}$$

It is possible to define a characteristic confinement time τ_E of energy loss through heat transport with W the total energy of the plasma:

$$\tau_E = \frac{W}{P_{loss}} \qquad\qquad W = \int 3nTdV \tag{1.81}$$

At equilibrium *i.e.* $P_{heat} = P_{loss}$ the power balance allows to relate the auxiliary heating power with the previous parameters:

$$P_\alpha + P_{aux} = \frac{W}{\tau_E} \tag{1.82}$$

It is estimated that the fraction of α particle power P_α corresponds to the 20% of the fusion heating power *i.e.* $P_{fus} = 5P_\alpha$ [4]. Therefore the gain factor can be expressed in function of the plasma energy, α heating power, and the confinement time:

$$Q = \frac{5P_\alpha}{P_{aux}} = \frac{5}{\frac{(W/P_\alpha)}{\tau_E} - 1} \tag{1.83}$$

The term W/P_α is the Lawson time. The condition for ignition satisfying $Q \geq 1$ imposes to rearrange the gain factor (eq. 1.75) to result into the Lawson criterion [29]:

$$nT\tau_E \geq 5.10^{21}\ \mathrm{keV\ s\ m^{-3}} \tag{1.84}$$

This condition establishes a triple product relating density, temperature and confinement time. For instance, assuming a density of $n \sim 10^{20}\ \mathrm{m^{-3}}$ and a temperature of $T \sim 10-20$ keV corresponding to the D-T cross section maximum, this criterion establishes the confinement time to be greater than 2.5 s for a successful ignition. In order to maximise the confinement time the solution is to increase the density by building bigger reactors in size. This is an engineering challenge as the plasma current needed to drive the plasma relies on several heating methods as well as the technological upgrade on magnetic devices and wall materials. In that way the confinement time for ITER is predicted by elaborating empirical scaling laws depending on

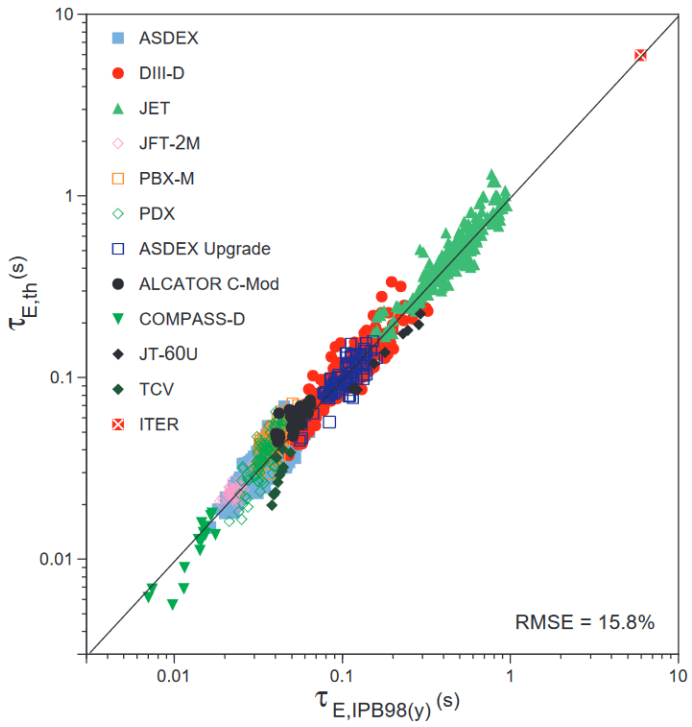

Figure 1.10: Log-linear fit between experimental energy confinement time from different tokamaks and the IPB98(y) scaling law [30]

several engineering parameters. For so long the reference law was the IPB98(y) scaling where each variable is related to a respective scaling exponent [30]:

$$\tau_E = 0.0365\ I^{0.97} B^{0.08} P^{-0.63} n^{0.41} M^{0.20} R^{1.93} \varepsilon^{0.23} \kappa^{0.67} \tag{1.85}$$

Here M is the average ion mass, and $\kappa \equiv S_0/\pi a^2$ is the elongation with S_0 being the plasma poloidal cross-section area. Several measurements from different tokamaks have reported values of the confinement times then compared to the IPB98(y) law. These experiments have been validating the scaling prediction when increasing the tokamak size and the strength of magnetic fields. From the 1960s to the 2000s the rate of progress of fusion performance based on the Lawson criterion has risen rapidly, however it has slowed down during the last two decades specially due to ITER delays. This general trend extrapolates the ITER performance with the resulting log-linear fit with measured triple product function of predicted values from the IPB98(y) law, presented in Fig. 1.10. It has been observed that the heating power degrades the confinement, amplifying gradients and instabilities, and indicated by the negative exponent -0.63. Nonetheless

experimental deviations from the power scaling have been recently reported [31]. The degradation was much weaker than the expected by the modified IPB98(y,2) law. Empirical laws are neglecting effects such as the choice of first walls materials plus electromagnetic and fast ion effects. Additionally forms of self-organised transport, that are not fully understood yet, could suppress the turbulence by affecting non-linearly other variables and hence improve the confinement.

1.4.3 Plasma-wall interaction: limiter and divertor configurations

Due to the ubiquitous nature of the magnetic field, each field line draw a certain path for a particle from a starting point connecting to an end. Thus particles are inevitably interacting with the walls causing sputtering on the surface. This path is known as the *connection length*. The magnetic topology can be modelled to reduce the contact of the plasma with the vessel components. The first tokamaks had a *limiter* where the field lines tend to connect as the target so the main plasma was directly in contact with the chamber wall. The Last Closed Flux Surface (LCFS), also known as the *separatrix*, separates between the confined plasma including the core (*i.e.* closed magnetic surfaces) and the boundary plasma at the edge (*i.e.* open magnetic surfaces) known as the Scrape-Off Layer (SOL). This is inefficient as the plasma gets contaminated by eroding the limiter material. As a solution the *divertor* was first conceived for ASDEX (Axially Symmetric Divertor EXperiment) [32] and was beneficial for the discharge performance. The divertor is a system often located at the bottom of the vessel that works as an exhaust device helping to evacuate the excess of heat, impurities and Helium in the plasma. In the divertor inner magnetic coils force the magnetic geometry to redirect the field lines towards the divertor plates acting as the new targets. The resulting shape traces an *X-point* referring to the disconnection point separating the confined and the divertor plasmas. The X-point is achieved by using the divertor coils to generate a current parallel to the plasma current until reaching a point where the poloidal magnetic field is null. It is possible to have one (*i.e.* single-null), two (*i.e.* double-null at upper and lower positions with respect to the core), or multiple X-points. An example showing both configurations is portrayed in Fig. 1.11. New configurations have been proposed for recent machines, known as *snowflake* [33], *X-* [34], and *Super-X* [35] divertors, which reshape the divertor magnetic geometry in order

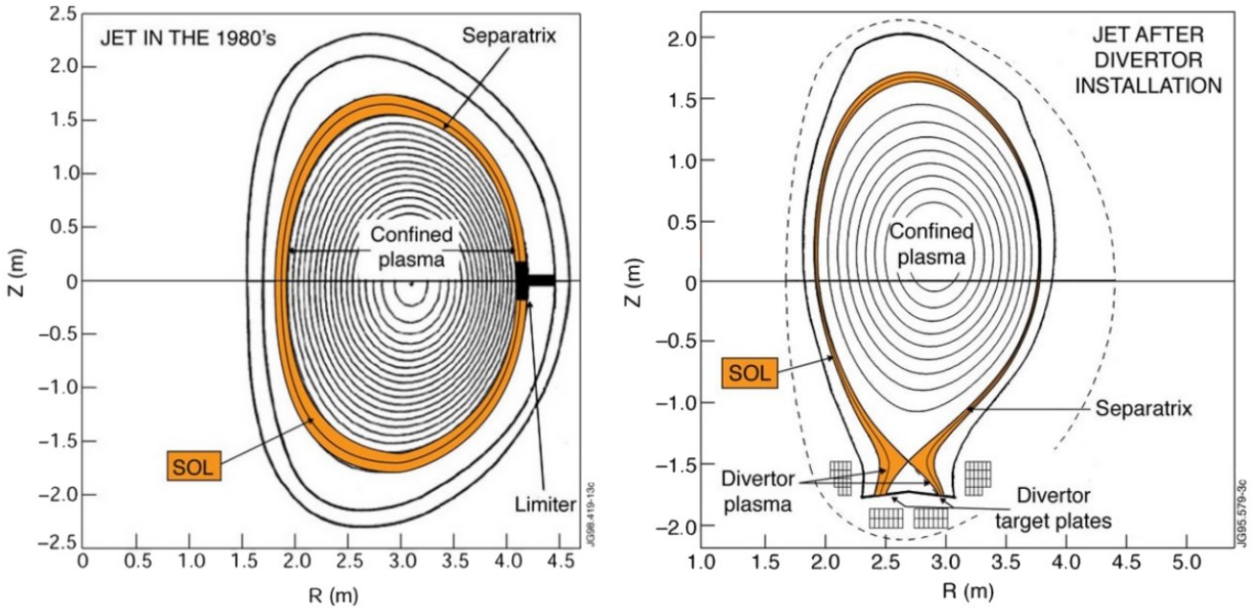

Figure 1.11: Schematics of toroidal cross section with magnetic surfaces at JET for limiter (left) and divertor (right) configurations [36]

to improve the heat exhaust. The divertor serves for multiple purposes that enhance the performance of the plasma. First, the recycling of neutral exhaust is re-introduced back into the plasma to re-ionise and sustain the reaction. Second, the practice of gas *seeding* by the injection of Nitrogen allows to create different plasma clouds that help dissipating the incoming exhaust by interacting with the neutrals which minimise the impact on the divertor tiles. This is known as *detachment* where the upstream divertor plasma "detaches" from the target. The confined plasma is no longer in contact directly with the target, unfortunately the SOL still interacts via open field lines with the walls. The choice of Plasma Facing Components (PFCs) is crucial for insuring the plasma-wall interactions to be negligible. Carbon was conventionally used as a low-Z material, which reduces the amount of impurities radiation compared to Beryllium, but is susceptible to be damaged by erosion and to retain Tritium between the structural cracks. Recent upgrades of several tokamaks have focused on replacing Carbon with Tungsten because it is the material with the highest melting point around 3000 K. The application of Beryllium and Tungsten is meant for ITER-like walls [37], tested already on different machines such as JET, in order to resist high temperatures, reduce melting and avoid releasing impurities in the plasma. For the moment a practical solution for reducing the presence of impurities on

vessel components is the boronisation process, applied prior experiments, which substantially improves the tokamak performance.

1.4.4 The Scrape-Off Layer

The Scrape-Off Layer (SOL) refers to the remaining plasma that escapes the confinement and interacts with the vacuum and the walls. The notion was introduced in the early tokamak concepts where it was said that the plasma was "scraped off" by the limiter. Initially the heat and particles are transported across the magnetic surfaces due to collisions, then at the edge particles start experiencing the cross-field transport *i.e.* the $E \times B$ drift pointing radially outwards. At the SOL the transport is redirected across the layer following the parallel direction until arriving to the divertor. The target surface acts a sink where a sheath is formed, ions travel at the acoustic speed and recombine enabling the recycling. Nonetheless the perpendicular contribution from the convective cross-field transport remains predominant during the process. Analytical models have the aim of predicting the SOL behaviour translated by a simplified system of the flux transport using the particle balance equation and Fick's law [38]:

$$\frac{d\Gamma_\perp}{dr} = -\frac{n}{\tau_\parallel} + S_{iz} \qquad\qquad \Gamma_\perp = -D_\perp \frac{dn}{dr} + nv_\perp \tag{1.86}$$

where is the radial coordinate defined by the outboard of the LCFS as $r > 0$, $n(r)$ the plasma density, $\tau_\parallel = 2L_\parallel/c_s$ the parallel loss time, $L_\parallel$ the connection length, c_s the acoustic speed, $S_{iz} = nn_n\langle\sigma v\rangle$ the ionization source with n_n the neutral density, and $D_\perp$ the anomalous diffusion coefficient. For simplification the purely transport case is assumed where there are no losses *i.e.* $v_\perp = 0$, neutrals recycling from the walls are all ionized at the LCFS hence $S_{iz} = 0$ and $n/\tau_\parallel = 0$, with $D_\perp$ being spatially constant. By studying the conservation of the total flux:

$$\boldsymbol{\nabla} \cdot (\boldsymbol{\Gamma}_\perp + \boldsymbol{\Gamma}_\parallel) = \boldsymbol{\nabla} \cdot (-D_\perp \boldsymbol{\nabla} n + n\boldsymbol{v}) = 0 \tag{1.87}$$

The different contributions of the diffusion-convection model are illustrated in Fig. 1.12. The coupling of the both equations gives the diffusion-convection balance:

$$D_\perp \frac{d^2 n}{dr^2} = -\nabla_\parallel n v_\parallel \sim -\frac{nc_s}{L_\parallel} \tag{1.88}$$

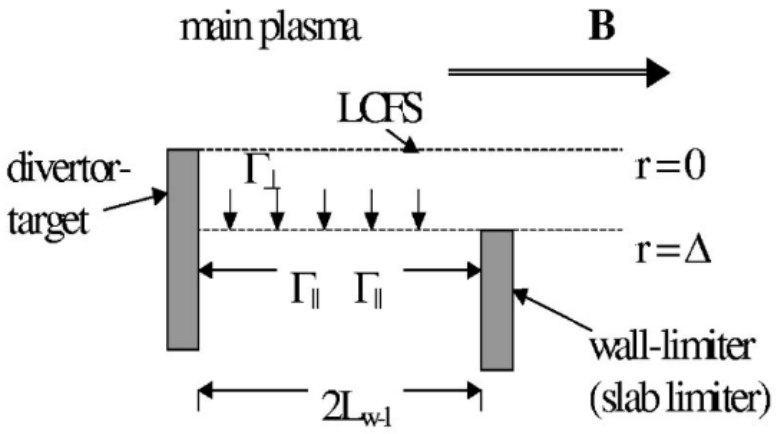

Figure 1.12: Schematics of the diffusion-convection model of the SOL [38]

The parallel gradient to the magnetic field and the velocity are approximated to the connection length and the acoustic speed respectively. The solution to this equation is of the exponential form for the density:

$$n(r) = n_\circ \exp\left(-\frac{r}{\lambda}\right) \qquad \lambda = \sqrt{\frac{2L_\parallel D_\perp}{c_s}} \tag{1.89}$$

with $n_\circ$ the density at the separatrix, and λ the SOL width. The typical values of the width is of the order of a few centimeters. This corresponds to a very thin area where high fluxes impact the target. For that reason the understanding of the SOL transport is relevant for new reactors. More details on the anomalous transport will be given in chapter 2.

1.4.5 Operational stability limits

There are a set of empirical parameters that help to determine the quality of the confinement.

Safety factor: The *safety factor* q is derived from the rotational transform [39]:

$$\frac{\iota}{2\pi} = \frac{d\Psi}{d\Phi} \tag{1.90}$$

The rotational transform is a measure of the pitch angle of field lines for one loop around the torus. If the ratio $\iota = n/m$ is a rational number, the field lines close on themselves after n toroidal and m poloidal circuits of the torus. The safety factor $q = 2\pi/\iota$ estimates the plasma stability and quantifies the helicity. $q(\Psi)$ is

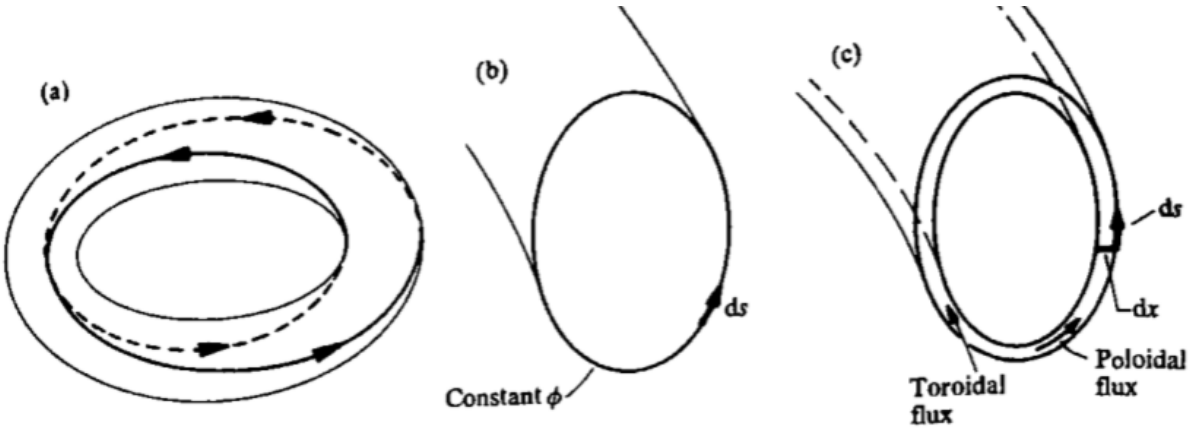

Figure 1.13: Schematics of a field line on $q = 2$ (a), poloidal integration path according to Eq. 1.91 (b), flux annulus containing toroidal $d\Phi$ and poloidal $d\Psi$ fluxes (c) [4]

conserved all over a single magnetic flux surface Ψ. The safety factor describes the number of loops done by the field line to returns to its original position. It is then equivalent to the number of toroidal circuits for one poloidal cross-section. For a closed poloidal circuit in Fig. 1.13 around a flux surface where ds is a distance in the poloidal direction while moving through a toroidal angle $d\phi$, q can be estimated by [4]:

$$q = \frac{1}{2\pi} \oint \frac{1}{R} \frac{B_\phi}{B_\theta} ds \qquad\qquad \frac{R d\phi}{ds} = \frac{B_\phi}{B_\theta} \tag{1.91}$$

with B_ϕ and B_θ the toroidal and poloidal magnetic fields respectively. For a large aspect-ratio tokamak, with r the minor radius of the flux surface and R the major radius:

$$q \simeq \frac{r}{R} \frac{B_\phi}{B_\theta} \tag{1.92}$$

Magnetic shear: The *magnetic shear* s represents the rate of the field lines twisting. It is defined as the radial gradient of the safety factor [4]:

$$s = -\frac{r}{q} \frac{dq}{dr} \tag{1.93}$$

For a negative shear disturbances at the edge are twisted vertically which causes an stabilising effect on tokamak instabilities [40].

Plasma Beta: The *plasma beta* β is a measure of the efficiency of the confinement [4]:

$$\beta = \frac{2\mu_0}{B^2} \int p dV \tag{1.94}$$

This parameter is the ratio of the plasma pressure $p = nk_BT$ to the magnetic pressure $p_{mag} = B^2/(2\mu_0)$ with V the plasma volume and $B^2 = B_\phi^2 + B_\theta^2$. β must be as high as possible, hence maximasing the density and temperature, and minimising the field. Alternatively toroidal β_T and poloidal β_P betas are also used for experimental scalings. β can be normalised in the form of the Troyon factor [41]:

$$\beta_N = \frac{aB_\phi}{I_p}\beta \tag{1.95}$$

This factor is often presented in %, where I_p is the plasma current in MA, a as the minor radius in m, and B_ϕ the toroidal magnetic field in T.

Greenwald density: The *Greenwald density* n_{GW} for D-T reactions is empirically defined by [42]:

$$n_{GW} = \frac{I_p}{\pi a^2} \tag{1.96}$$

The units for n_{GW} are in 10^{20} m^{-3}, I_p in MA and a in m. This represents the limit of particles that can be accepted by the limiters to be evacuated, otherwise leading to plasma disruption. It is speculated that radiation losses from impurities inside magnetic islands cause the density limit [43].

1.4.6 MHD instabilities in tokamaks

At the edge boundary critical gradients tend to trigger MHD instabilities. These fundamental gradients are the density gradient $\boldsymbol{\nabla} n$ (*i.e.* and/or current gradient $\boldsymbol{\nabla} j$), the pressure gradient $\boldsymbol{\nabla} p$ and the magnetic gradient $\boldsymbol{\nabla} B$. The coupling of multiple instabilities can lead to the deterioration of the confinement. The instabilities mentioned below are the most common in tokamaks.

Interchange instability: The description of the interchange instability can be approached from the Rayleigh-Taylor instability [44]: a light fluid is supporting a heavy fluid (*e.g.* vacuum and plasma), a

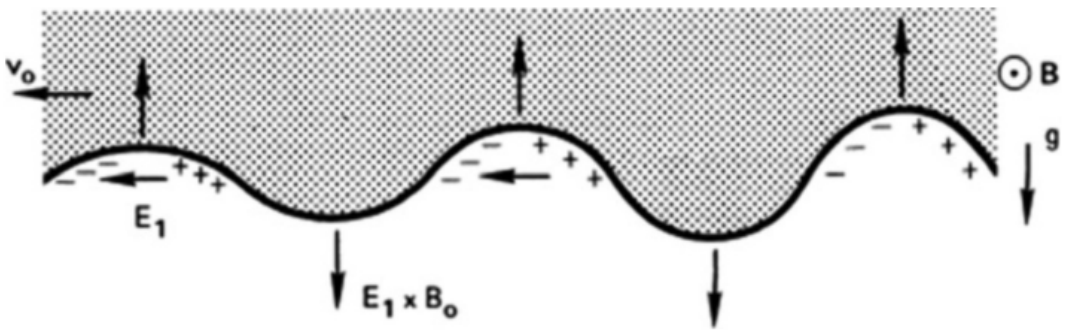

Figure 1.14: Schematics of the Rayleigh-Taylor instability [15]

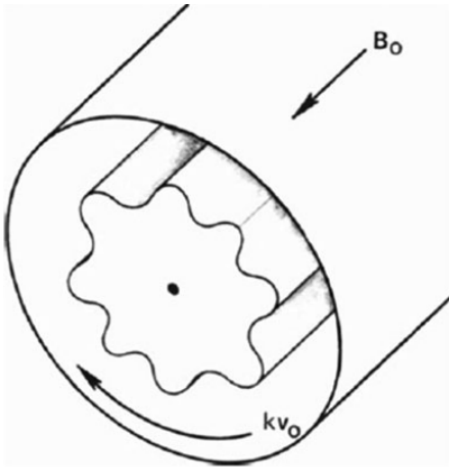

Figure 1.15: Flute-like shape of the interchange instability [15]

"fictitious gravity" as a pressure gradient acts then as a force, hence the interface tends to deform as shown in Fig. 1.14. The resulting ripple amplifies itself due to a secondary effect: heavy ions tend to be more affected by the drift, the ion depletion produces a response of electrons which ends in consecutive charge separations (*i.e.* $\boldsymbol{E_1}$ fields), then electrostatic fields form resulting in $\boldsymbol{E_1} \times \boldsymbol{B_0}$ drifts oriented in the same direction as the initial deformation. In the tokamak context, this gravitational force is assimilated to the centrifugal force that produces a drift of the form in Eq. 1.28 in section 1.3.2. In a cylindrical approximation, the resulting form of the ripple consists in a flute-like shape illustrated in Fig. 1.15. The effective gravity $\boldsymbol{g}$ is a representation of the centrifugal force caused by the magnetic curvature $\boldsymbol{\kappa}$ such as:

$$\boldsymbol{g} = \frac{\hat{\boldsymbol{b}} \times \boldsymbol{\kappa}}{B} \qquad\qquad \boldsymbol{\kappa} = (\hat{\boldsymbol{b}} \cdot \boldsymbol{\nabla})\hat{\boldsymbol{b}} \sim \frac{\boldsymbol{\nabla}_\perp B}{B} \tag{1.97}$$

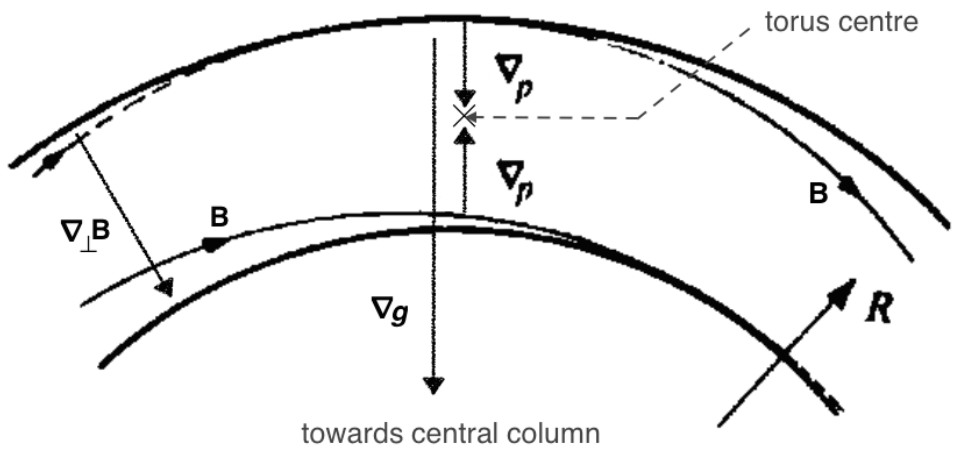

Figure 1.16: Schematics of a top down view of a tokamak [4]

The magnetic curvature is considered stabilizing known as favourable curvature (*i.e.* the High Field Side (HFS)) if the curvature and the pressure gradient are in opposite directions. On the contrary, the unfavourable curvature (*i.e.* the Low Field Side (LFS)) amplifies the deformation of the plasma when both gradients are aligned. Both cases with the orientation of gradients are exposed in Fig. 1.16.

Drift wave instability: Additionally the $\boldsymbol{E_1} \times \boldsymbol{B_0}$ drift caused by the interchange instability creates fluctuations that affect the density gradient along the ripple. The drift wave contributes by emphasizing the helical twist of the plasma, illustrated in Fig. 1.17. The motion of electrons projected on the applied magnetic field leads to dominant terms plus some fluctuating terms that subject electrons to drift in the parallel direction of the magnetic field. If a electrostatic perturbation takes place the response of electrons traveling along the field lines obeys the Boltzmann adiabatic relation trying to reach the thermodynamic equilibrium:

$$\frac{\delta n}{n} \sim \frac{e\delta\phi}{k_B T} \tag{1.98}$$

Initially, if the fluctuations of density δn and electrostatic potential $\delta\phi$ are in phase, there is an energy transport called *drift wave* with a velocity equal to the electron diamagnetic drift velocity [15]:

$$v_{De} = \frac{\omega}{k} = -\frac{k_B T}{eB_0}\frac{\delta n}{n} \tag{1.99}$$

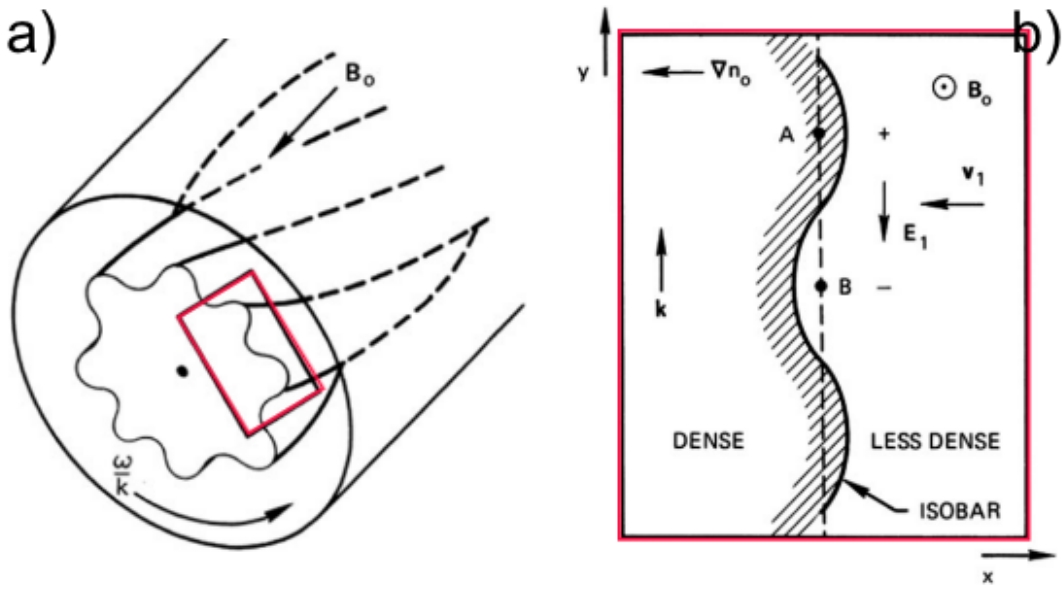

Figure 1.17: Schematics of a drift wave instability: a) representation in the cylindrical approximation; b) zoomed-in region [15]

However a slight phase shift between fluctuations of density and potential could mitigate or amplify inducing the drift wave instability. Depending on the shift, this effect creates unbalanced regions where the $\boldsymbol{E_1} \times \boldsymbol{B_0}$ drift becomes stronger, *i.e.* pointing outward where the plasma was already shifted outward, and vice versa. The parameter that triggers the phase shift is the resistivity as electron-ion collisions add delays in the transport.

Ballooning instability: The ballooning instability refers figuratively to the local inflation of the plasma analogous to the balloon shape. This instability is a consequence of the deformation of the plasma when the magnetic curvature alternates between favorable and unfavorable regions as shown in Fig 1.16. This instability occurs when the potential energy brought by the pressure gradient exceeds the magnetic energy that maintains the plasma confined, then the plasma is able to "bend" the field lines. The threshold condition is formulated by [4]:

$$-\frac{dp}{dr} \sim \frac{B_\phi^2/\mu_0}{q^2 R_c} \tag{1.100}$$

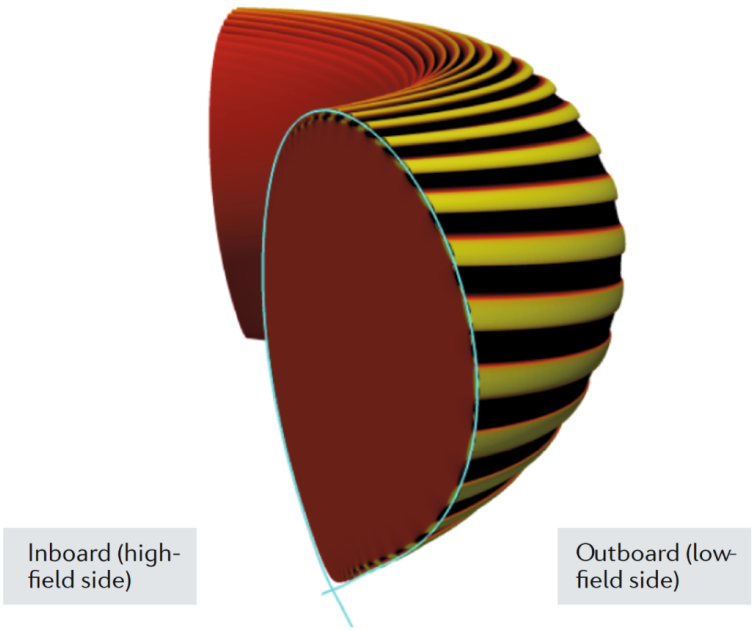

Figure 1.18: Illustration of the ballooning mode in the outboard side of a tokamak [45]

R_c is the radius of curvature of the toroidal magnetic field. In order to analyse this instability, the pressure gradient is normalised as follows:

$$\alpha = -\frac{2\mu_0 R q^2}{B^2}\frac{dp}{dr} \tag{1.101}$$

The study of (s, α) diagrams will be introduced in chapter 2, section 2.3.3. The resulting shape of the plasma at the edge takes the form of ridges in the poloidal direction, often referred as fingers. The characteristic structure of the ballooning mode is portrayed in the outboard (LFS) side in Fig. 1.18. Unfortunately this instability is one of the most problematic as it is responsible for explosive events. Sporadically plasma bursts occur causing deleterious effects such as disruptions and damages in the tokamak vessel.

Kink instability: The kink instability is a perturbation due to a current-driven mode characterised by irrational surfaces ($m = 1$, $n = 1$) that is developed if the Kruskal-Shafranov limit is surpassed *i.e.* $q > 1$ [46]. Phenomenologically it can be visualised in Fig. 1.19 as the plasma surfaces "kinking" into an helix around the toroidal axis. The plasma in local kinks is being driven in the direction of weaker magnetic fields. In the deformed kink the magnetic pressure increases which re-amplifies the deformation.

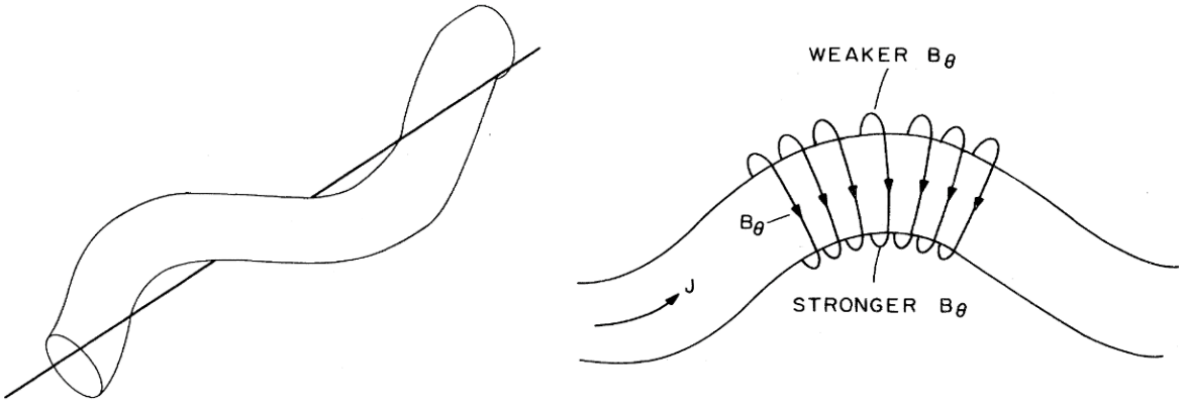

Figure 1.19: Schematics of a kink instability, from [20]

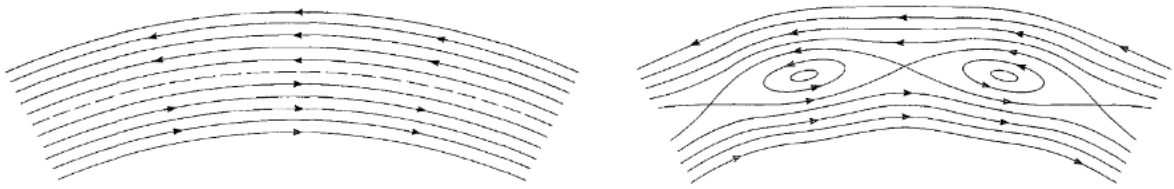

Figure 1.20: Schematics of magnetic reconnection and tearing instability forming islands [4]

Tearing instability: The tearing instability is a perturbation that forms chains of successive magnetic islands represented in Fig. 1.20. The cause of the island formation is the magnetic reconnection where field lines tend to break and reconnect in the plasma. The reconnection occurs due to a transfer of magnetic field energy to plasma kinetic and thermal energy. The overlapping of islands due to resonance effects modifies the magnetic field topology which can lead to plasma disruptions [47].

1.5 Thesis outline

Magnetised plasmas tend to exhibit a chaotic behaviour due to its turbulent ubiquitous nature. Nevertheless intermittent events appear as quasi-regular fluctuations above the random background. Despite the fact that these fluctuations are associated with forms of anomalous transport, in some propitious circumstances these induce self-regulating processes in the plasma *i.e.* forming self-organised structures. Self-organisation

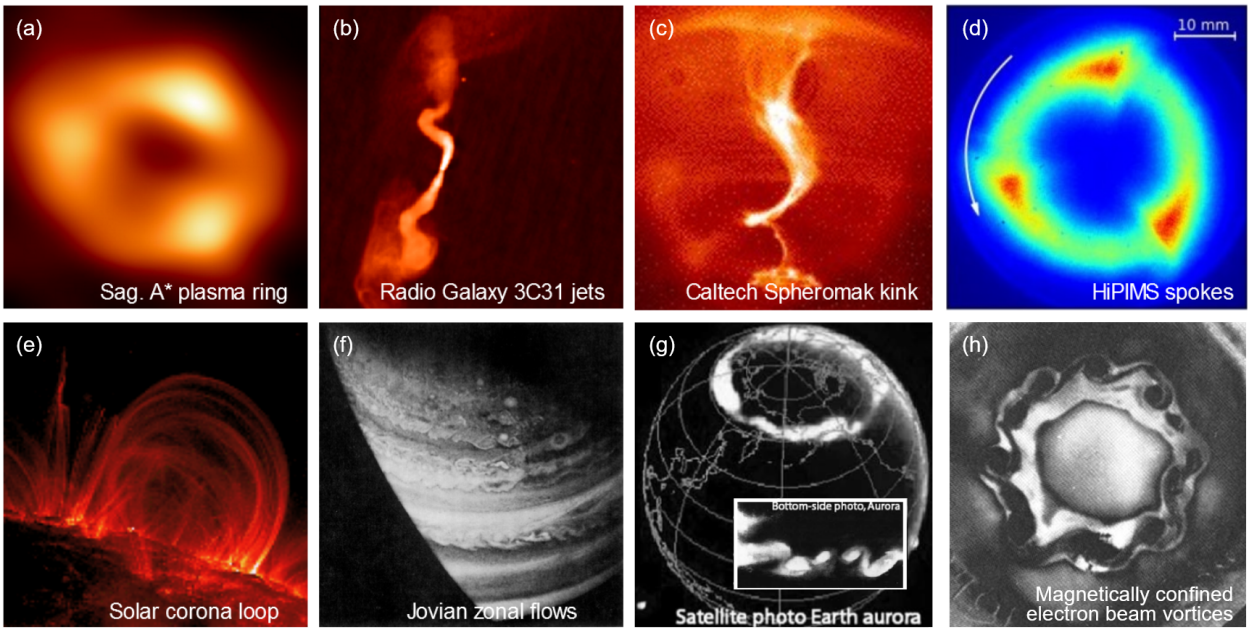

Figure 1.21: Self-organisation in magnetised plasmas: (a) plasma ring surrounding the black hole Sagittarius A* [48]; (b) Radio Galaxy 3C31 with two conical inner plasma jets developing into distorted plumes [49]; (c) magnetised plasma kinks in the Caltech spheromak [50]; (d) rotating spokes in a high power impulse magnetron sputtering discharge [51]; (e) coronal loops over the eastern limb of the Sun [52]; (f) zonal flows forming cloud patterns in Jupiter [53]; (g) Earth aurora around the Arctic [54]; (h) vortices within a magnetically confined electron beam [55]

is not an universally defined concept in plasma physics and its notion varies *ad hoc* depending on the area or publication. The formation of coherent structures in magnetised plasmas remains a challenge in the plasma research area. It is relevant to comprehend how these transient structures form by the identification of patterns in stochastic processes. Such behaviour is manifested in diverse plasmas, from astrophysical to laboratory ones, in the form of vortices or higher dense zones as seen in Fig. 1.21. The evolution of transient vortices can lead to the growth of filamentary elongated structures. However, the universal mechanism between the generation of small-scale vortices and the appearance of large-scale filaments remains a problem to solve. True is a certain organisation can be visualised in the arrangement of filamentary structures at the edge of tokamak plasmas as shown in Fig. 1.22. The motivation of studying these processes is to predict these patterns. Ultimately the understanding of self-organisation of fusion plasmas will allow to discover

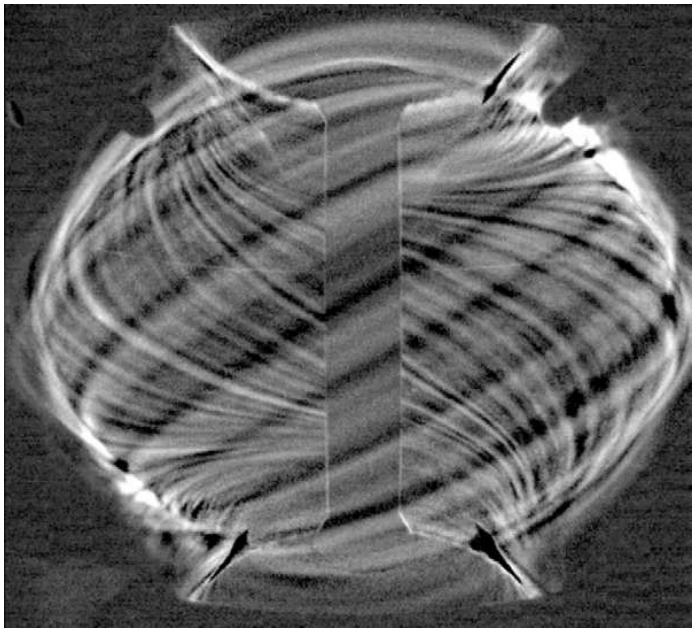

Figure 1.22: Visible light image of filaments in a L-mode discharge on MAST. The image was digitally enhanced due to the fast moving structures [56]

self-regulating regimes where the turbulence itself leads to the improvement of the plasma performance. The initial purpose of this thesis was the study of rotating spokes in RF magnetron plasmas. However, the subject matter changed to the characterisation of edge plasma phenomena in tokamaks. During the thesis period, the participation in the analysis of different experiments led to investigate multiple topics such as SOL filaments, shoulder formation, zonal flows, and ELM-precursors. Such topics have been explored in COMPASS and MAST experimental data. This thesis treats these subjects in the following order. Chapter 2 is divided in 3 sections: first a summary of self-organised phenomena in magnetised plasmas; second a review of SOL filamentary structures; and third a review of Edge-Localised Modes (ELMs). Chapter 3 introduces the diagnostics and methods employed for the analysis of the next chapters. Chapter 4 presents the analysis of probe measurements for studying the edge plasma conditions in the COMPASS tokamak and the conditions triggering shoulder formation. Chapter 5 presents the imaging analysis for the visualisation of ELM-filaments in the MAST tokamak. Chapter 6 presents the spectral analysis for the characterisation of ELM-precursors in the MAST tokamak. Chapter 7 is the conclusion to this thesis.

Chapter 2

Literature review

2.1 State-of-the-art: self-organisation in magnetised plasmas

This introduction aims to guide the reader through different approaches to self-organisation phenomena in magnetised plasmas which is still an open and complex debate. We will follow the chronological order of discoveries in each section. All these sections derive from a vast literature, therefore additional material is cited if the reader is interested in a specific topic. In the following order these sections include: reversed-field pinch plasmas, spokes, and zonal flows. Astrophysical phenomena such as dynamos and accretion-ejection structures are excluded. Note that RFP dynamos and astrophysical dynamos do not refer to the same effect. The goal is to give an heuristic overview that seeks a brief description of self-organisation in experimental devices. The conclusions from the subsection dedicated to zonal flows will serve as a prelude to the following reviews on scrape-off layer filaments (section 2.2) and edge-localised modes (section 2.3) in tokamak plasmas.

2.1.1 A phenomenological introduction to turbulence

Turbulence is a hydrodynamic regime that is associated with a chaotic seemingly random behaviour such as the observed patterns in smoke plumes, crashing waves or storm clouds. One might intuitively think that

turbulence must be the opposite concept to any order of organisation. Fluid dynamics, including turbulence, are described by the Navier-Stokes equations for incompressible flows formulated between 1822 and 1845:

$$\frac{\partial \boldsymbol{u}}{\partial t} + (\boldsymbol{u} \cdot \boldsymbol{\nabla})\boldsymbol{u} = -\boldsymbol{\nabla} p + \rho \boldsymbol{g} + \nu \boldsymbol{\nabla}^2 \boldsymbol{u} \tag{2.1}$$

$$\boldsymbol{\nabla} \cdot \boldsymbol{u} = 0 \tag{2.2}$$

It is possible to categorise different flows' regimes with the fluid Reynolds number:

$$R_e = \frac{uL}{\nu} \tag{2.3}$$

i.e. the ratio between the inertial and the stress forces, with u the flow velocity, L the system's dimension, and ν the viscosity, establishing: the laminar regime for low $R_e << 1$ numbers, and the turbulent regime for a large range of high $R_e >> 1$ numbers. Turbulence is characterised by the formation of structures often called *eddies* or Karman vortex stress after Karman's work in aerodynamics [57]. In 1941 Kolmogorov published a model describing three-dimensional turbulent flows in hydrodynamics known as K41 theory (the original article is in Russian [58], a complete review was compiled by Frisch [59]). This theory was based on Richardson's idea of cascades when describing weather balloons' motions in a turbulent atmosphere [60]. The concept of cascade refers to the fragmentation of an organised hierarchy of eddies in space *i.e.* how eddies behave with an injection of energy ε, evolve from the large to the small scales in the inertial range, and finally dissipate. This can be visualised in Fig. 2.1 with ℓ the eddy's characteristic scale following the law $r^n \ell$ with r the axis distance and n the cascade rate. Of course this conception is idealised and based on multiple assumptions: the isotropy and homogeneity of turbulence, the self-similarity (*i.e.* all eddies' scales are affected by the same conditions during the inertial range) and the locality (*i.e.* large eddies do not interact with small eddies). In the review of Diamond, S.I. Itoh and K. Itoh, further assumptions are discussed [61]: during the energy injection the creation of eddies is attributed to fluid stirring which triggers an unbalanced state that breaks the system's symmetry. The cascade would be understood as a restoration phenomena back to the equilibrium while the eddies would keep in memory that symmetry during the inertial range. The K41 theory analyses the transfer of turbulent energy in different scales using the statistical approach *i.e.* it reconstructs the energy spectrum $\mathcal{E}(k)$ in the Fourier space in function of the wavenumber $k \sim \ell^{-1}$.

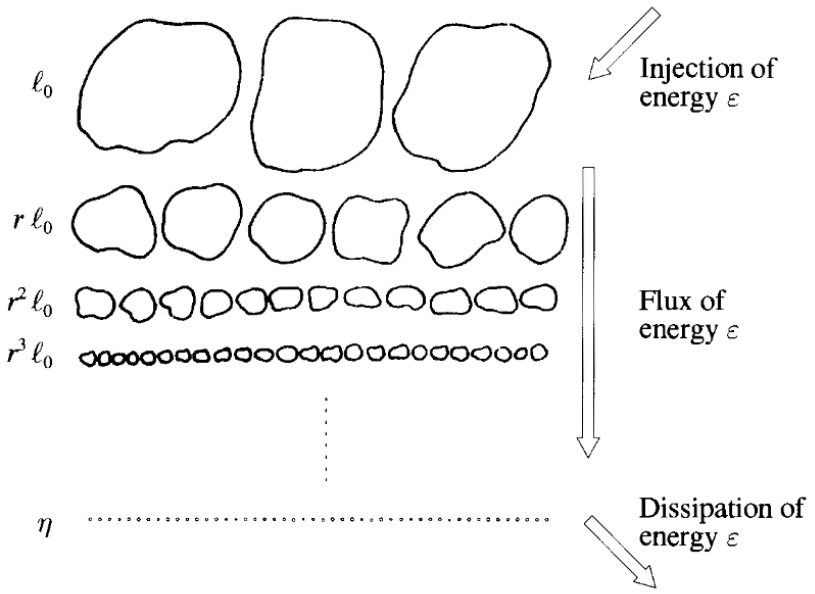

Figure 2.1: Richardson-Kolmogorov idealised concept of cascade from [59].

The kinetic energy of a fluctuation in the flow is related to the energy spectrum:

$$\frac{1}{2}\langle \boldsymbol{u_k}^2 \rangle = \int_0^\infty \mathcal{E}(k)dk \tag{2.4}$$

with u_k the characteristic speed of the eddy. By integrating the advection equation (2.1) in the Fourier space with the eddies' velocity being $u_k \sim \sqrt{k\mathcal{E}(k)}$, Kolmogorov predicted the following scaling law:

$$\mathcal{E}(k) = C_K \varepsilon^{2/3} k^{-5/3} \tag{2.5}$$

where $C_K \sim 1.6$ is a dimensionless constant. The exponent $-5/3$ or decrement indicates the cascade scales rate in the inertial range. The same reasoning was applied for a two-dimensional incompressible MHD turbulence in the 1960s by Iroshnikov [62] and Kraichnan [63, 64], named IK theory. The coupling between the field and the matter introduces two agents of turbulence: the magnetic eddy, a zero-frequency cell, and the shear Alfvén wave. The first feature is analogous to the hydrodynamic concept with a stochastic behaviour. This last new feature can be understood as an oscillatory packet or beat that involves a collective behaviour. The IK theory predicts then a different cascade of the form:

$$\mathcal{E}(k) = C_{IK} (\varepsilon v_A)^{1/2} k^{-3/2} \tag{2.6}$$

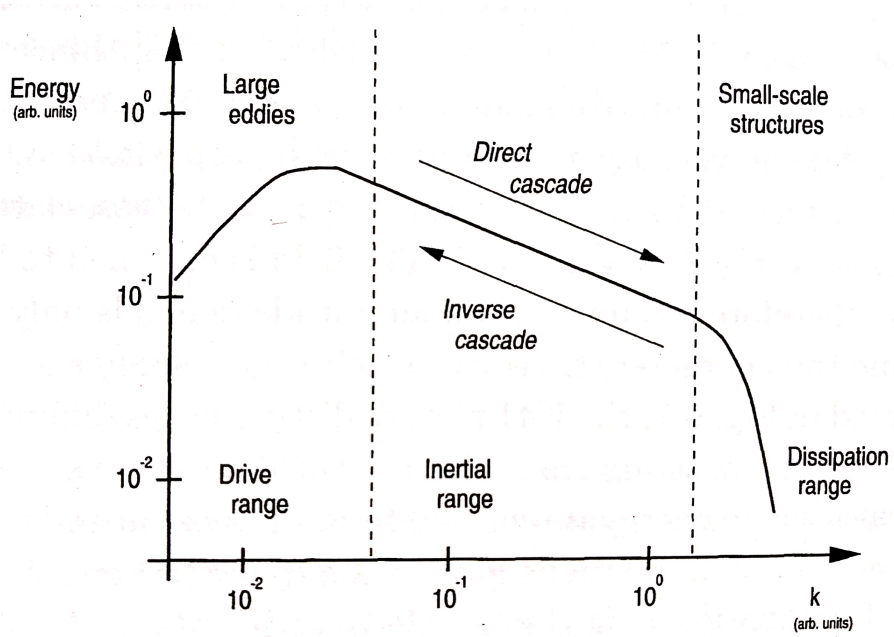

Figure 2.2: Schematics of turbulence energy spectrum from [65].

with $C_{IK} \sim 6.7$ a dimensionless constant and a -3/2 exponent scales rate. However this is not the unique process in the IK spectrum: an inverse cascade is also predicted following a -5/3 Kolmogorov-like law from Eq. (2.5) *i.e.* an energy transfer from the small to the large scales. In Fig. 2.2 an energy spectrum displays different ranges at their corresponding scales, distinguishing between direct and inverse cascades *i.e.* the energy can be transferred in both directions. In order to explain both processes, the direct cascade law can be rewritten according to Kraichnan, first of the form [64]:

$$\mathcal{E}(k) = C'_{IK}\eta^{2/3}k^{-3} \tag{2.7}$$

later corrected in the logarithmic form [66]:

$$\mathcal{E}(k) = C''_{IK}\eta^{2/3}k^{-3}[\ln(k/k_1)]^{-1/3} \quad (k >> k_1) \tag{2.8}$$

with $C'_{IK}, C''_{IK} \sim 2.6$ other constants, k_1 the bottom limit of the inertial range, and η the squared-vorticity rate or enstrophy:

$$\eta \equiv \int_S |\boldsymbol{\omega}|^2 \, dS \qquad\qquad \boldsymbol{\omega} = \boldsymbol{\nabla} \times \boldsymbol{u} \tag{2.9}$$

The enstrophy is a quantity that evaluates the degree of vorticity caused by the flow. The vorticity is the angular velocity of the flow visualised as the eddy's spin. In the 3D K41 model the flow deformation or

strain $\boldsymbol{\nabla} u$ creates a volumetric deformation of the eddy which has its own vorticity $\boldsymbol{\omega}$. The vorticity rate varies according to the Euler's vorticity equation:

$$\frac{d\boldsymbol{\omega}}{dt} = (\boldsymbol{\omega} \cdot \boldsymbol{\nabla})\boldsymbol{u} \tag{2.10}$$

The combination of the strain and the vorticity results into a stretching of the 3D eddy along the rotation axis. The enstrophy represents the energy dissipation generated by the stretching of a large scale vortex forming an elongated small scale tube. In the IK model the scalar product in the 2D space gives $(\boldsymbol{\omega} \cdot \boldsymbol{\nabla})\boldsymbol{u} = 0$ implying the conservation of the enstrophy. In the absence of volume the enstrophy is transferred by the collision of Alfvén packets: without any perturbation an Alfvén wave propagates *ad infinitum* along the magnetic field, even when several packets travel in the same direction these do not interact, however when two packets counter-propagate the resulting interaction or shearing generates a cascade to lower energies and smaller scales via a scattering process (nonetheless the steepening of uni-directional packets as compressible shocks has been studied [67]). In the inverse cascade the transfer of energy to larger scales is brought by the shape of the field *i.e.* the deformation of magnetic field lines can amplify the field itself creating larger magnetic eddies. In 2D the distorsion of magnetic potential $\boldsymbol{A}$ contours (defined as $\boldsymbol{B} = \boldsymbol{\nabla} \times \boldsymbol{A}$) is responsible for coagulating small structures to form larger ones. In 3D the twist of field lines associated to an helical shape amplifies the field itself, known as dynamo effect, which is measured by the magnetic helicity:

$$H_M = \int \boldsymbol{A} \cdot \boldsymbol{B} \; dV \tag{2.11}$$

It is worth to point out that the IK theory still represents an idealised case under particular assumptions (*e.g.* isotropic turbulence and 2D space). The GS theory by Goldreich and Sridhar [68] is a generalisation of the IK theory taking into account the anisotropy that amplifies during the direct cascade and distinguishing between weak ($\mathcal{E}(k) \sim k^{-2}$) and strong turbulence ($\mathcal{E}(k) \sim k^{-5/3}$). To conclude, the two cascades respond to different roles in vortex formation. The inverse energy cascade requires a simultaneous direct enstrophy cascade: the enstrophy minimisation contributes to the formation of large eddies. This process is not a simple restoration to the equilibrium and does not have to be inconsistent with the second law of thermodynamics. This law is intuitively associated with direct energy cascades based on the entropy maximisation. However, the "self-organised" process responds to energy transfers due to the viscosity and the magnetic field.

2.1.2 Reversed-Field Pinch (RFP) plasmas

Several experiments have attempted to reproduce the dynamics of astrophysical plasmas with a special interest in thermonuclear fusion. In parallel with the tokamak research during the 1950s, the development of the reversed-field pinch configuration had the aim of achieving fusion reactions by compressing toroidal currents with strong magnetic fields. In 1958 the Zero Energy Thermonuclear Assembly (ZETA) experiment [69] claimed reaching temperatures around 10^6 K and producing neutrons from deuterium reactions. However it was later shown that its performance was not as promising as predicted. Nonetheless a spontaneous magnetic field reversal at the plasma edge (*i.e.* outer radial region) was discovered which seemed to be a key element for improving the plasma stability. In 1974 the relaxation theory proposed by Taylor [70] stated that this self-reversed phenomenon was caused by a quiescent state. This state was characterised by a minimized magnetic energy where the magnetic helicity H is an invariant of the motion. Under the assumption of a perfectly conductive fluid, this is formulated by the force-free magnetic field theory proposed by Woltjer [71] with the equation:

$$\mu_0 \boldsymbol{j} = \boldsymbol{\nabla} \times \boldsymbol{B} = \alpha \boldsymbol{B} \tag{2.12}$$

with α a constant, which implies that the current and the field must be parallel. Although working for a few decades, the Taylor description has been proven to be inaccurate: it portrays an ending relaxed state without explaining the self-organisation of the magnetic field while being subjected to turbulent effects. Furthermore the discovery in the 1990s of different fluctuating regimes such as Single (SH), Quasi-Single (QSH) and Multiple (MH) Helicity states, and the intermittent switching between these states due to dissipative effects presented a more complicated picture. In order to find a simplified model, a different explanation was proposed in 1978 with the experimental observation of a helical kink instability during the self-reversal in the fast pinch device High-Beta Toroidal Experiment (HBTX-1) [72]. An intuitive interpretation is given by Escande *et al.* [73] visualised with a wire model, illustrated in Fig. 2.3. The kink creates a helical distorsion which amplifies the field and the flux internally. At the same time it creates an unbalance with the outer fluxes that needs to be restored. The saturation of the instability occurs during the reversal of the outer field in order to reach an equilibrium, with an eventual magnetic shearing in between. A secondary process,

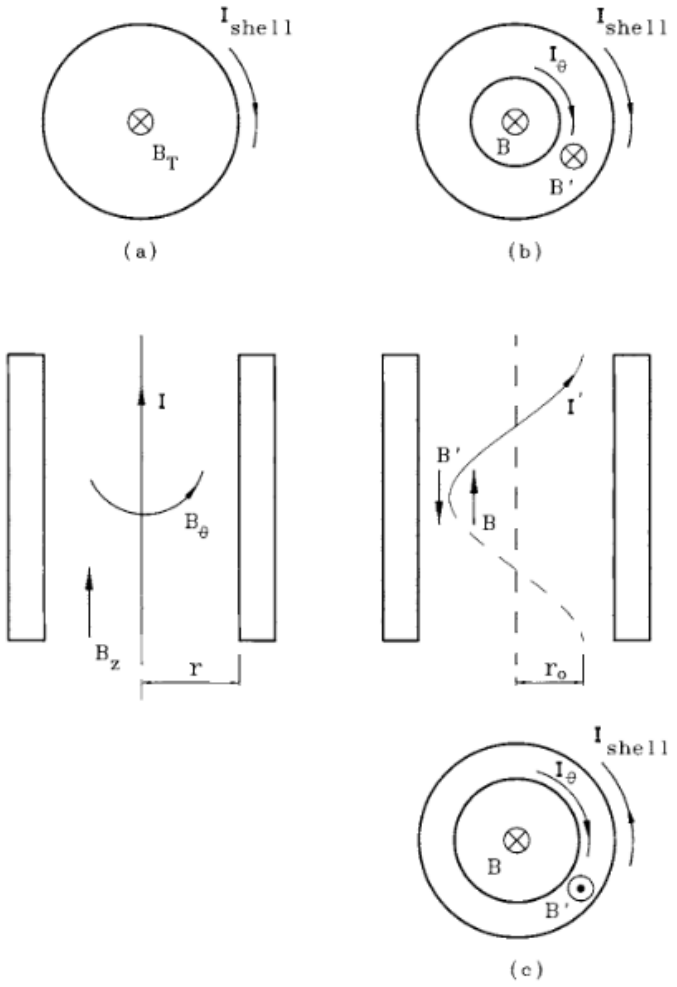

Figure 2.3: Wire model from [73]; (left) the initial axisymmetric state, (top right) the helical distorted state with increased B field, (bottom right) the self-reversal of the outer B' field or 'shell' region

revealed by resistive MHD simulations during the 2000s by Bonfiglio *et al.* [74], corresponds to a dynamo due to the formation of the helical distorsion, where the electromotive force in the Ohm's law is written as:

$$\boldsymbol{u} \times \boldsymbol{B} = \eta \boldsymbol{j} + \boldsymbol{\nabla} \Phi \tag{2.13}$$

where Φ is the electrostatic potential. When the RFP configuration is setting up, the plasma loses the initial axisymmetry and current density modulations start taking place along the magnetic field lines. Thus the deformation rearranges into regions of charge imbalance where electrostatic fields tend to develop. There is then a combination of two contributing fields: first the uniform applied electric field noted $\boldsymbol{E_{loop}}$, second

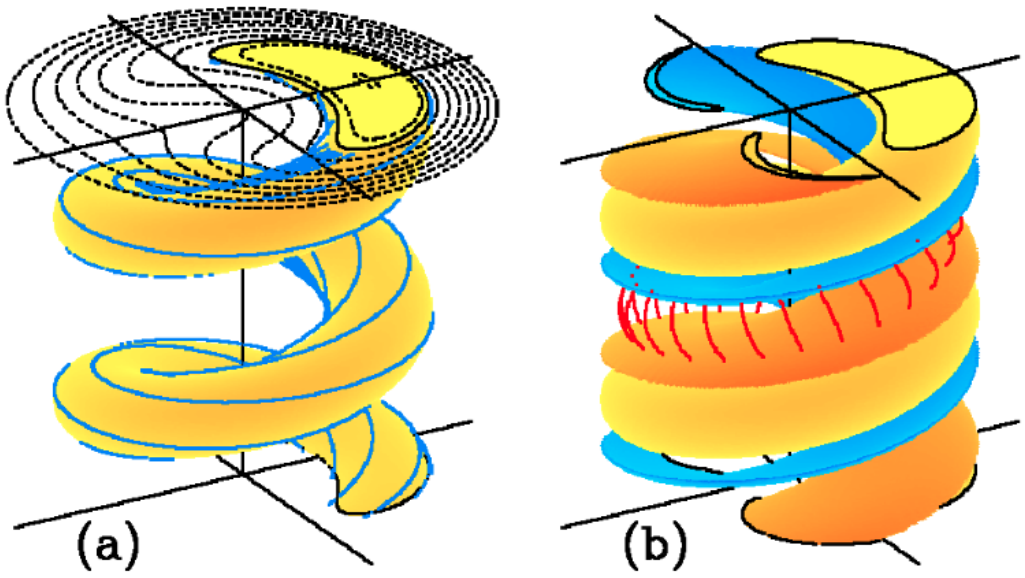

Figure 2.4: Simulated periodical cylinder associated to the RFP dynamo from [74]; (a) the helical magnetic surfaces, (b) charge separation in the helix with red lines representing the electrostatic field

the existence of a fluctuating electrostatic field noted $\boldsymbol{E_\rho} = -\boldsymbol{\nabla}\Phi$ caused by two dipolar pairs of helical distributions which are illustrated in Fig. 2.4 (b). This combination results into a $\boldsymbol{E} \times \boldsymbol{B}$ drift in the perpendicular direction:

$$\boldsymbol{u}_\perp = \frac{(\boldsymbol{E} - \eta \boldsymbol{j}) \times \boldsymbol{B}}{B^2} \simeq \frac{(\boldsymbol{E_{loop}} + \boldsymbol{E_\rho}) \times \boldsymbol{B}}{B^2} \tag{2.14}$$

which contributes to the dynamo effect. With all these mechanisms being enumerated, the RFP has been adapting its operational purpose, not as a fusion reactor, but as an experimental device for unveiling self-organised phenomena. In 2009 experiments in the RFX-mod device [75] changed the paradigm of self-organisation in RFPs with the discovery of the single helical axis (SHAx) state: by increasing the toroidal current up to 1 MA for the first time, a spontaneous helical equilibrium formed accompanied with a reduction of magnetic fluctuations and the formation of an internal transport barrier with core temperatures reaching 1 keV. The formation of the barrier is indicated by the shaded regions of temperature profiles in Fig. 2.5. This mechanism is comparable to the effect of zonal flows in tokamaks improving the confinement (this notion is explained in detail in section 2.1.4). Similarly other self-organised states have been found in other devices such as the SSX spheromak [76], they have been compared with externally-shaped helical states

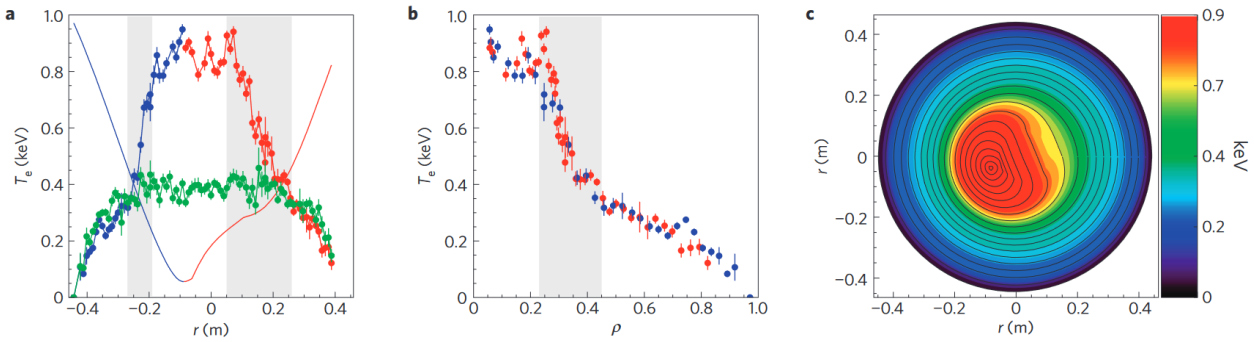

Figure 2.5: Mapping of the temperature profile of the SHAx state: (a) typical electron temperature profile, red and blue refer to the two opposite sides with respect to the helical magnetic axis, green refers to a typical profile of the MH state; (b) temperature profile plotted as a function of effective radius; (c) reconstruction of the full 2D map of the temperature on the poloidal plane [75]

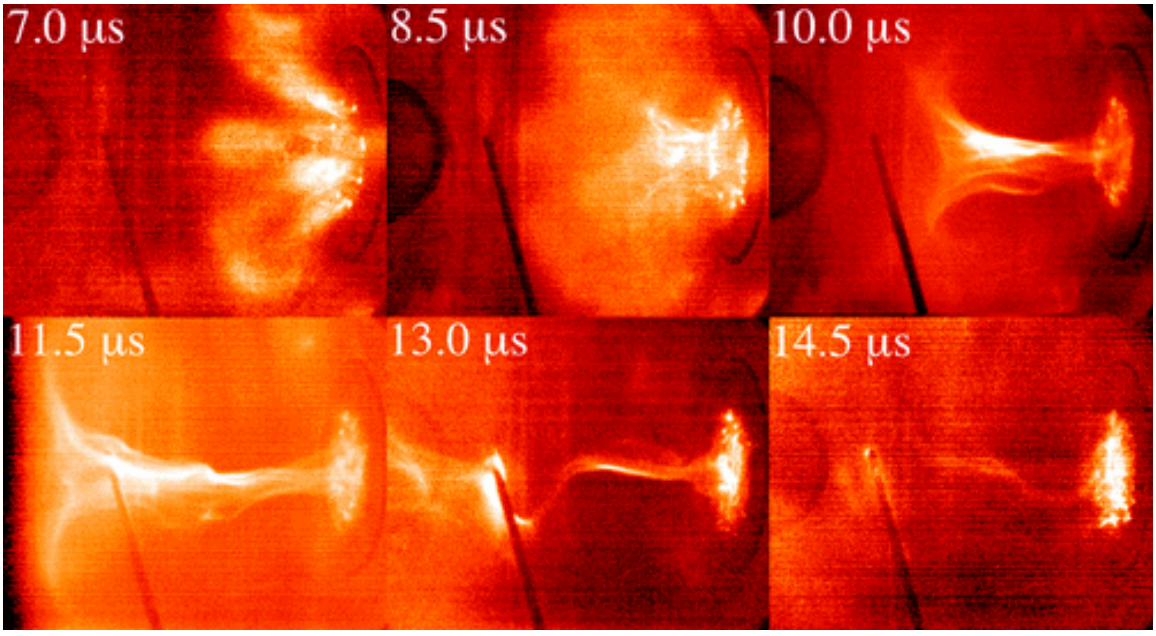

Figure 2.6: Caltech coaxial gun spheromak; the circular gap between outer and inner electrodes is visible toward right side of each frame; a B probe is visible; a kink is fully formed at the 13.0 μs frame [80]

in the HSX stellarator [77], and simulated in a tokamak geometry due to the dynamo $\boldsymbol{u} \times \boldsymbol{B}$ mechanism [78]. A recent review of all analytical RFP models that involve self-organised phenomena was compiled by Escande [79]. Trying to respond to the challenges from the astrophysical domain, the experimental research at Caltech by Hsu and Bellan [80] has been proposing some answers for jets dynamics by reproducing plasmas in a spheromak. During the evolution of the plasma column the formation of rotating kinks were observed (Fig. 2.6). It was concluded that a helical perturbation identified as a kink instability acts as a dynamo converting toroidal to poloidal flux. From RFP experiments, Bellan [81] undervalued ideal MHD assumptions as oversimplified and proposed a resistive MHD model where the continuous transfer of toroidal magnetic flux and axial bunching due to the poloidal field creates a pinch force allowing the jet self-collimation.

2.1.3 Spokes

Several rotating low-temperature plasma devices have observed the formation of transient rotating structures named *spokes*. In the 1950-60s experiments based on discharges with arc, Penning, hollow-cathode configurations and homopolar devices studied this particular behaviour without using a common terminology. Simon [82] (in a slab geometry) and Hoh [83] (in a Penning-type geometry) predicted theoretically the same instability in weakly ionised plasmas. The triggering conditions of the instability were in agreement with the experimental results reported by Chen and Cooper [84], Bonnal *et al.* [85], and Briffod *et al.* [86]. Phenomenologically, an initial E_r field appears due to a radial density perturbation between ions and electrons. In these devices the ions are unmagnetised (*i.e.* $\rho_{L,i} \sim L$), only the magnetised electrons rotate at a velocity $v_\theta \sim E_r/B_z$. A charge separation is induced which generates an azimuthal electric field E_θ. The resulting $\boldsymbol{E_\theta} \times \boldsymbol{B_z}$ drift pushes the density outwards plus combined with the density gradient it ends by amplifying the instability. This mechanism is illustrated in Fig. 2.7. The Simon-Hoh mechanism was also remarked at that time by Morse [87] similar to flute-like or vane rotating density perturbations, and it is still consider nowadays a candidate to trigger the structures' formation. Nonetheless Janes and Lowder's work [88] is considered to be the starting point of using the term *spoke* for referring to an anomalous diffusion due to density non-uniformities and not due to collisions. Since the 1970s several experimental setups with

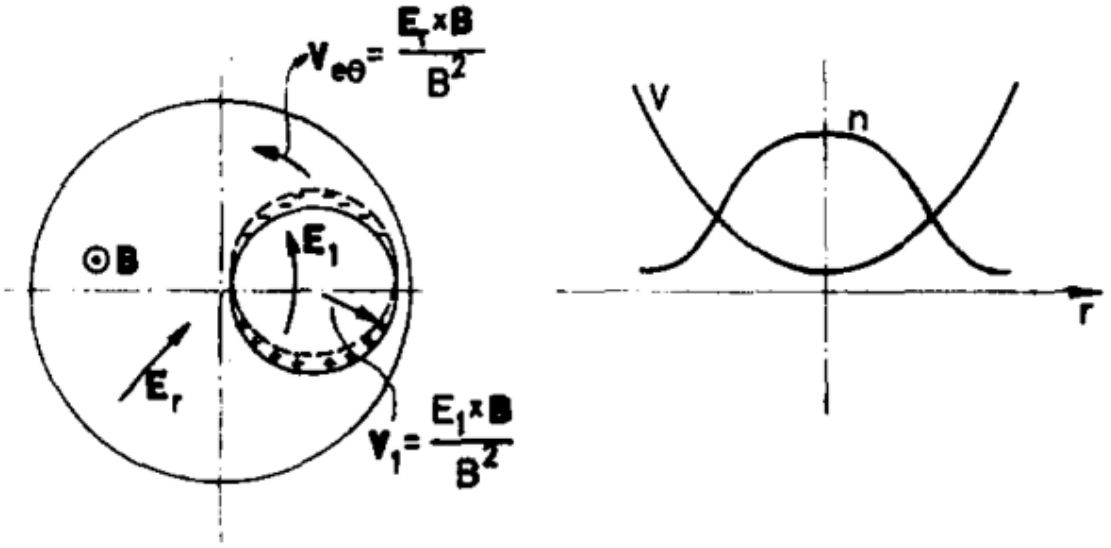

Figure 2.7: The Simon-Hoh instability on a Penning-type discharge (left), the steady-state distributions of density and potential in the radial direction (right) [83]

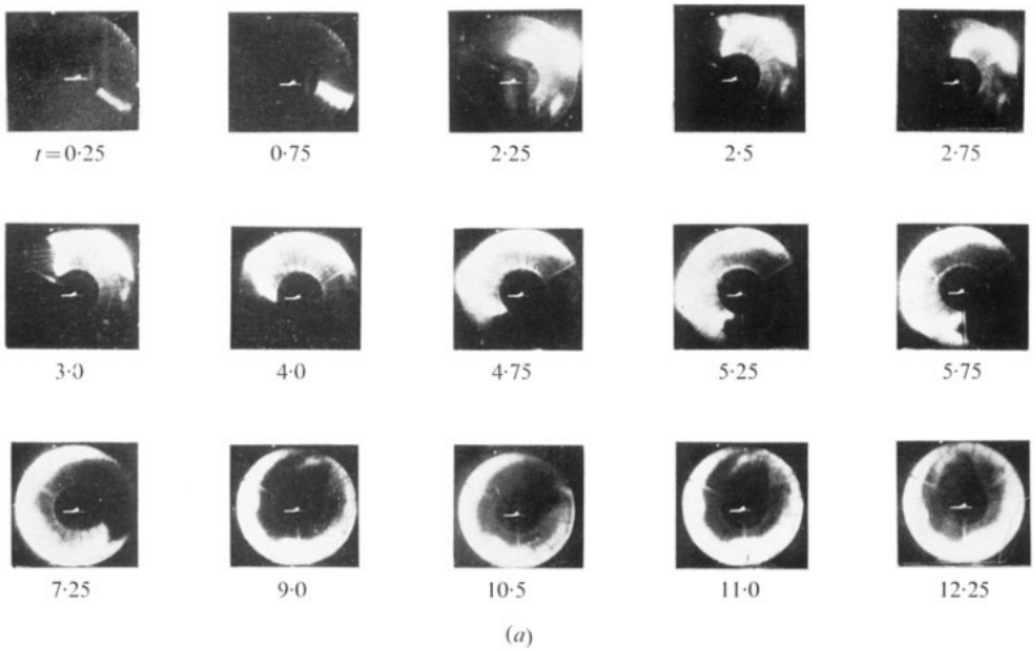

Figure 2.8: Photographs showing the evolution in time of spokes in an homopolar device under a field of 1.15 T and a pressure of 500 N.m^{-2} [89]

a cross-field $E \times B$ configuration have been detecting these structures and proposing new models. Barber *et al.* [89] inferred different regimes of the plasma behaviour: an uniform disk for low pressure and high magnetic field, or the formation of rotating spokes at high pressure as shown in Fig. 2.8. A shockwave model was used for describing the spokes regime based on Rankine-Hugoniot equations while taking into account the driving magnetic force. The plasma velocity seemed to match with the predicted shock velocity. It was speculated that the transition between disc and spoke must be linked to a pre-breakdown ionisation phenomenon *i.e.* a balance between pressure, magnetic field imposing limitations on the voltage discharge and the plasma rotation velocity as the ionisation does not occur homogeneously and with an uniform rate. By means of Langmuir and magnetic probes Himmel, Mobius and Piel [90] described the spoke structure as unchanged during the discharge and presenting two distinctive zones: zone 1 with a steep increase of electron density, zone 2 with a slow decaying density dragging the zone 1 by the $E \times B$ drift. This distinction between zones seemed to indicate that the non-homogeneous ionization was caused by the effect of rotation. The association of the spoke to diffusion due to collective plasma processes is similar to the solar ionisation mechanism described by Alfvén [91] introduced as the critical ionisation velocity (CIV) theory. The critical velocity corresponds to the point where the ionisation is carried by the kinetic energy of the ions. The spokes velocity matched the CIV noted u_{cr} imposing a criteria for the minimal discharge voltage U_D:

$$u_{cr} \sim \sqrt{\frac{2W_i}{m_i}} \qquad\qquad U_D = (r_0 - r_i)u_{cr}B \tag{2.15}$$

with m_i and W_i the ion mass and ionisation potential of the gas respectively, r_0, r_i the radius of outer and inner electrodes respectively. It was speculated that the rapid non-homogeneous ionisation was caused by an additional turbulent electron heating. The process where the azimuthal drift transfers energy to the electrons can be due to the two-stream instability, analogous to the Kelvin-Helmholtz instability. In that way, Piel *et al.* [92] introduced modifications in the CIV model under the case of an inhomogeneous plasma by formulating the modified dispersion relation of the two stream instability by adding the contribution of the density gradient. However, due to the complexity of finding solutions to the modified dispersion relation, Piel only exposed the turn-on conditions for the existence of a two-stream instability within this framework. Vast part of the literature kept referring to spokes with different expressions such as ionisation zones, anomalous transport, plasma oscillations or fluctuations but the most common are plasma non-

homogeneities. Biel *et al.* [93] observed self-excited periodical oscillations with frequencies between $\sim$ (10, 60) kHz in a cylindrical hollow cathode discharge. By means of Thomson scattering measurements it was possible to detect higher electron dense regions rotating in the azimuthal direction with a phase shift giving a mode number $m \sim 1$. The shape along the axis described an helix of wavelengths around $\sim$ (0.5, 2) m. However when increasing some parameters such as the magnetic field strength or the chamber pressure these oscillations start becoming irregular or chaotic. In order to explain these observations Biel and Kempkens proposed a theoretical description starting from the Braginskii equations: the assumptions included a two-species fluid, with a strong magnetic pressure with $\beta << 1$ so neglecting magnetic fluctuations and ion inertia terms, plus taking into account the ion viscosity over neglected electron viscosity [94]. From the experimental data it was verified that the arc rotation frequency matched the analytically predicted $E \times B$ drift frequency. It was observed that the axial pressure gradient reaches its maximum with the azimuthally rotating electron density. The axial pressure gradient is related to the strong gradients of density and temperature which are responsible for bending potential surfaces. It was theorised that the observed fluctuations on density and potential with transitions between coherent to chaotic behaviours are related to the existence of anomalous transport associated to an electron diffusive mechanism enhancing the ionisation. The convective transport due to the $E \times B$ drift dominates over other transport forms by collisions, temperature and density gradients. Helical waves were also associated to detected oscillations in a hollow-cathode discharge by Oks *et al.* [95]. The use of probes allowed to detect low-amplitude peaks in the ion current with a frequency of $f \sim 50$ kHz in absence of magnetic field. When the plasma was magnetised the frequency became variable depending on the type of gas, the pressure and the discharge current. For instance the heavier the gas the lower is the frequency *e.g.* (6, 15, 22) kHz for krypton, argon, and nitrogen respectively. Likewise when increasing the current the frequency drops, and increasing the pressure requires to increase the magnetic field up to a threshold point where oscillations appear. The correlation between different probes' signals indicated a phase shift corresponding to a $m \sim 1$ azimuthal mode driven by a rotational instability. The observed oscillations were associated to the so-called helical or current-convective instability studied by Nedospasov [96] and Vladimirov [97]. Spokes started to gain special attention during the development of Hall-thrusters and magnetrons since the 2000s. Magnetron devices are traditionally used for coating applications while Hall-

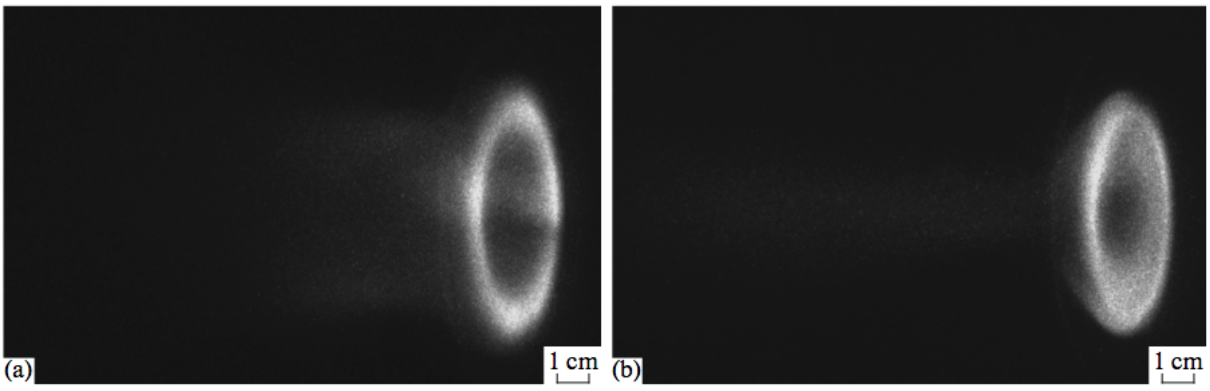

Figure 2.9: Photographs of a magnetron in: (a) balanced mode with multiple spokes forming jets in the axial direction, (b) unbalanced mode with an homogeneous glow [102]

thrusters are expected to work as propulsion devices for spacecrafts' orbital corrections. Both are in essence magnetic traps for electrons near the anode with an annular geometry while the electric field accelerates ionised atoms from cathode to anode. We can enumerate some contributions in the domain of Hall-thrusters: Choueiri [98] mapped the magnetic field with a Hall probe and reconstructed contours of plasma parameters reporting spokes propagating azimuthally in the frequency band of $\sim$ (5, 25) kHz, different to gradient-driven instabilities in the $\sim$ (20, 60) kHz band, and vanishing when increasing the discharge voltage; Chesta *et al.* [99] used Langmuir probes to identify azimuthal $m \sim 1$ modes with phase velocities $v \sim$ (1, 4) km/s in the band of $\sim$ (5, 10) kHz also dependent of the applied low voltage, distinguishing them from $\sim$ (20, 100) kHz oscillations or breathing modes; Parker *et al.* [100] used a fast camera capturing increased light emission from spokes propagating in the $E \times B$ direction with speeds (1, 3) km/s in the (15, 35) kHz band. In the domain of magnetrons the term spoke was not used at the beginning, we can cite: Martines *et al.* [101] detected coherent modes using probes in a DC planar magnetron plasma with azimuthal numbers $m \sim$ (3, 7) at frequencies $f \sim 100$ kHz for pressures $p \sim$ (0.5, 4) Pa associating the cross-field transport to drift waves; Kozyrev *et al.* [102] confirmed the existence of bunches, by means of a high-speed camera in a High Power Impulse Magnetron Sputtering (HiPIMS) device, which increment with the applied current taking the form of jets along the axis between the cathode and the anode shown in Fig. 2.9; Anders *et al.* [103] performed a similar experiment and linked the observed ionisation zones rotating in the $E \times B$ direction to spokes from

Hall-thrusters; Yang *et al.* [104] reported the possibility of a $-E \times B$ reversal motion when lowering the applied current. Since the 2010s publications started employing self-organisation terminology as a reaction to the visualised formed patterns. Ni *et al.* [105] used fast cameras to visualise self-organized ionization zones and associated plasma flares in a HiPIMS device. Ehiasarian *et al.* [106] reported striations or faint bands with alternating low and high intensity that add up with pressure, with azimuthal numbers $m \sim (1, 4)$ and frequencies between $f \sim (100, 200)$ kHz, and hypothetically caused by a two stream instability. Anders [107] pointed out a feedback mechanism allowing the patterns' formation by taking into account ions being in contact with the target surface, releasing secondary electrons plus the ions returning as neutrals to the racetrack, both elements sustaining the next arriving spokes at the location therefore repeating the process cyclically and suggesting each spoke is interlinked with its neighbors' status. de los Arcos [108] used the self-organised term to portray the evenly distributed patterns at the racetrack and reported 4 different regimes (normal glow, abnormal glow or chaotic spokes, stable spokes, and runaway threshold) by trying different target materials and currents between $1 - 40$ A. Brenning *et al.* [109] proposed an unified spoke model by combining the modified CIV model by Piel *et al.* and the HIPIMS description by Anders *et al.*, *i.e.* the two-stream instability as driven mechanism and the secondary electrons as additional feature (fig (c) in Fig. 2.10), fig (d) in Fig. 2.10 displays how the instability generates electric field oscillations in between magnetic equipotential lines that drives electrons vertically causing anomalous ion–electron collisions according to Lundin *et al.* [110]. Recent reviews by Panjan *et al.* [111], Hecimovic and von Keudell [112] recapitulate the spokes' properties and speculate about the origin of the self-organised behaviour. A spoke model proposed by Held *et al.* [113] is illustraded in Fig. 2.11 which accounts for the effect of the magnetic pre-sheath. Such feature could attract the sputtering ions back to the surface causing a retrograde $E \times B$ rotation of spokes. Furthermore, the hypothesis of the Simon-Hoh Iinstability has been recently reinforced as the main mechanism for the generation of spokes in HIPIMS plasmas [113]. Recent simulations by Boeuf and Takahashi [114] pointed out that the Simon-Hoh mechanism arises due to the combination of the density gradient ∇n and the ∇B drift as an additional heating source for electrons and the stabilisation for spokes. The simulations performed by Smolyakov *et al.* [115] have proposed that small-scale turbulence caused by anti-drift waves (or Hall drift waves) can grow into the Simon-Hoh instability and lead to the formation of

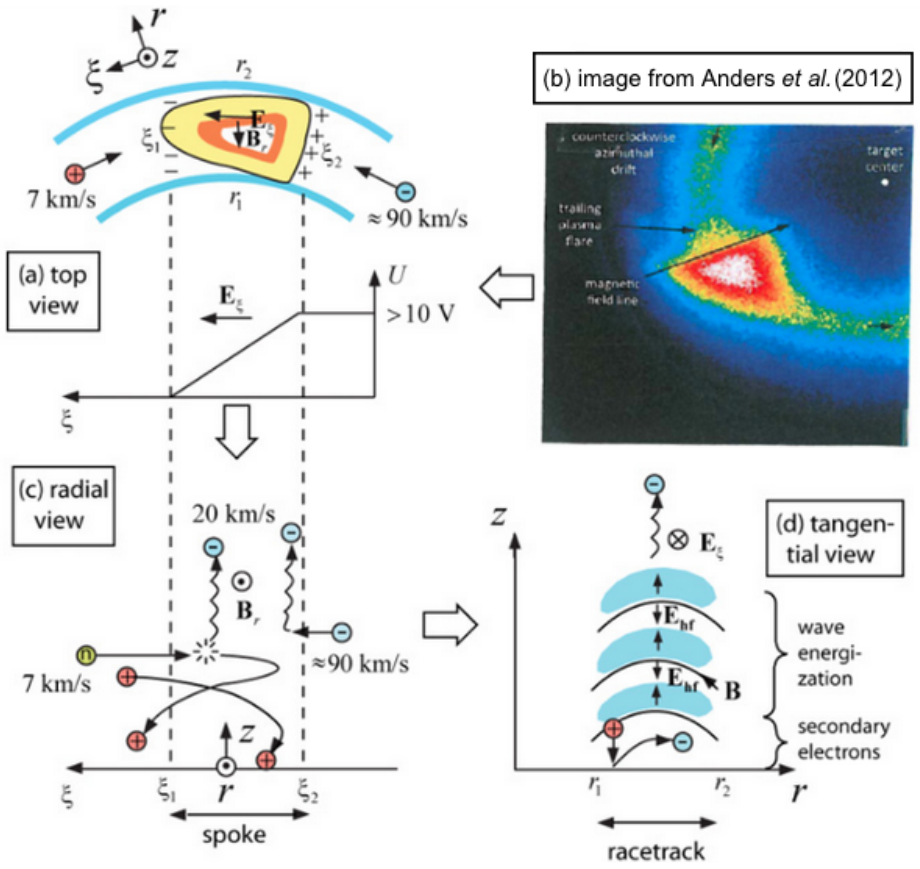

Figure 2.10: Unified spoke model from Brenning *et al.* [109], (b) image from Anders *et al.* [103]

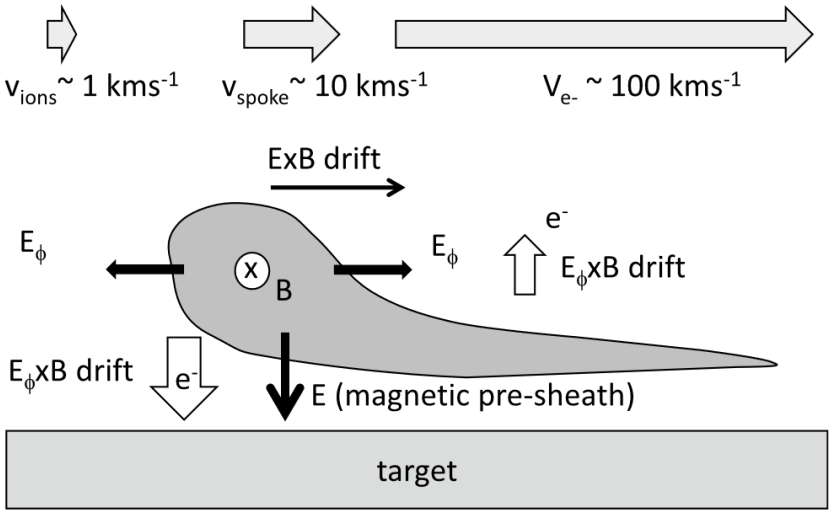

Figure 2.11: Schematics of the side view of a spoke with azimuthal E_ϕ and pre-sheath E electric fields plus the induced $E \times B$ drifts; typical velocities are indicated on top [113]

larger structures (*i.e.* spokes) via an inverse energy cascade. Anti-drift waves are related to the ∇n gradient combined with the ion inertia in partially ionised plasmas. This mechanism is analogous to drift waves instabilities and zonal flows in fully magnetized plasmas.

2.1.4 Zonal Flows (ZFs)

The expression *zonal flow* was originally used in the domain of geophysical fluid dynamics. It describes localised vorticity patterns observed in oceanic waves formed in gulfs as well as in Jovian (*i.e.* Jupiter's-like) atmospheric cloud belts in rotating planetary systems (this goes beyond the topic of this thesis, an extensive study was published by Williams [53]). In the context of magnetised plasmas, in 1978 Hasegawa and Mima [116] developed a drift-wave turbulent model in a 2-dimensional compressible plasma fluid (with cold ions) that predicts the conservation of enstrophy plus the inverse cascade process of energy transfer to smaller scales (see section 2.1.1). Following that work Hasegawa, Maclennan and Kodama [117] compared turbulence spectra from Rossby waves (driven by Coriolis force's gradients) and drift waves (caused by unphased fluctuations of potential and density in plasmas), predicting that the formation of a zonal flow pattern in a cylindrical magnetised plasma could be due to the inverse cascade process such as $\mathcal{E}(k) \sim k^{-8/3}$. The zonal flow is organised in the azimuthal direction with a radial periodicity of $2\pi/k_c$ with k_c the critical scale of the cascade, with different bands azimuthally moving in opposite directions, hence inhibiting transport in the radial direction and improving the confinement. On the experimental side, in 1982 Wagner *et al.* [118] discovered a high confinement regime *i.e.* H-mode in the ASDEX tokamak only affected by short bursts. This regime was characterised by high $\beta_N \sim 2.65$ values and the confinement time and the stored plasma energy both increased by a factor 2 compared to the low confinement regime *i.e.* L-mode. This improvement was achieved by the input of additional heating *e.g.* neutral beam injection, and the X-point divertor configuration reducing the contact with walls while evacuating heat and impurities. The L-H transition was triggered by the arrival of a thermal wave (described as a large sawtooth) at the edge causing a reduction of the anomalous transport parameters and radial diffusivity: this is referred as transport barrier [119]. This barrier manifested in the radial profiles with a pedestal shape at the edge shown in Fig.

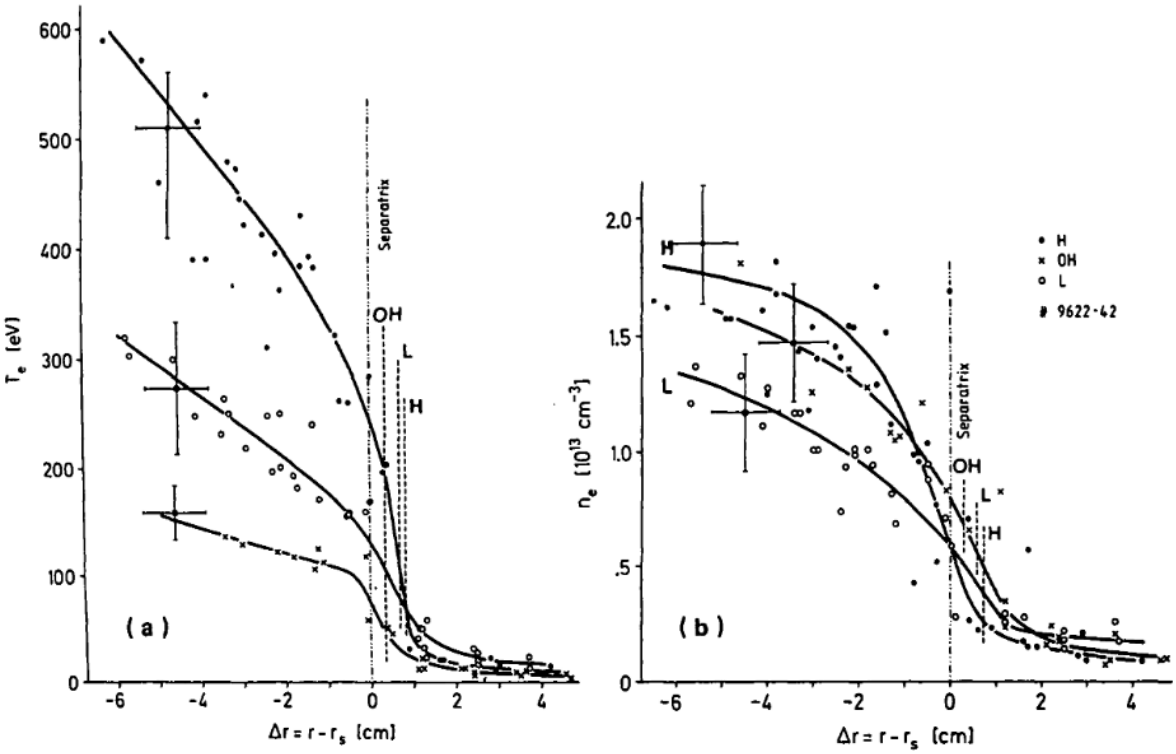

Figure 2.12: ASDEX radial profiles in the midplane of electron temperature (left) and density (right) for different regimes: H (H-mode), OH (Ohmic Heating), L (L-mode); the vertical bars are estimations of the separatrix location [120]

2.12 [120]. The pedestal extends a few centimeters radially inside the separatrix and can extend into the SOL where the density tends to drop significantly, implying the edge density and pressure gradients become more pronounced in the H-mode. Meanwhile during the 1980s the work done by Hasegawa and Wakatani had been very prolific in the understanding of turbulence for tokamak plasmas. From the assumptions of the Hasegawa-Mima model the velocity of the fluid is dominated by the $E \times B$ drift and the ion vorticity equation becomes:

$$\boldsymbol{\nabla} \times \boldsymbol{u} \simeq \boldsymbol{\nabla} \times \boldsymbol{u_E} = \boldsymbol{\nabla} \times \frac{-\boldsymbol{\nabla}\phi \times B_0 \hat{\boldsymbol{z}}}{B_0^2} = \frac{\boldsymbol{\nabla}^2 \phi}{B_0} \hat{\boldsymbol{z}} \tag{2.16}$$

where $\hat{\boldsymbol{z}}$ is the unit vector in the direction of the magnetic field, and coupled with the continuity and momentum equations considering a density perturbation (index 1) over background (index 0) such as:

$$n = n_0(x) + n_1(x, y, t) \qquad\qquad n_1/n_0 << 1 \tag{2.17}$$

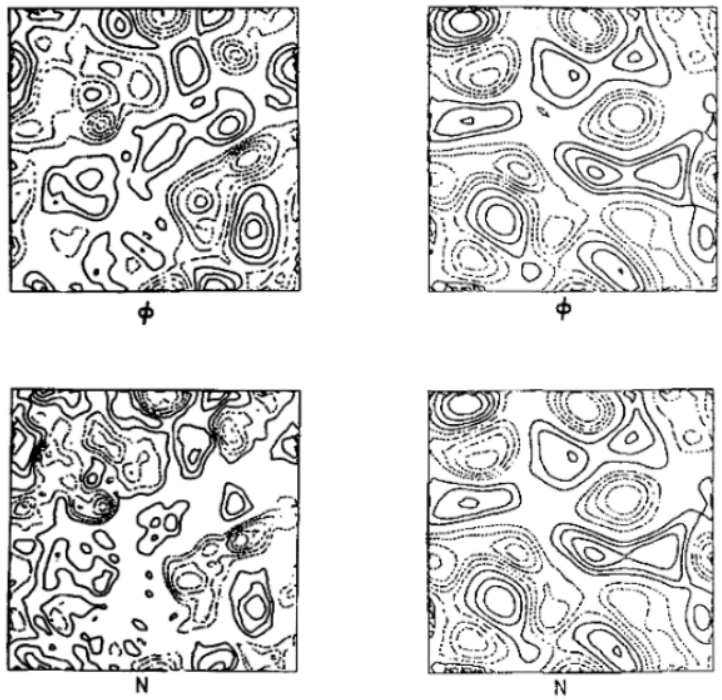

Figure 2.13: Hasegawa-Wakatani (ϕ, n) contours in a (x, y) plane, N refers to the normalised density n; (left) simulations when $c_1 \to 0$; (right) simulations when c_1 is large [122]

and introducing the following normalisations:

$$\phi \equiv \frac{e\phi}{T_e} \qquad n \equiv \frac{n_1}{n_0} \qquad t \equiv t\omega_{ci} \qquad (x, y) \equiv \frac{(x, y)}{\rho_s} \tag{2.18}$$

with $\rho_s = \sqrt{m_i T_e}/eB$ the hybrid Larmor radius, the derived coupled equations finally lead to the Hasegawa-Wakatani equations [121]:

$$\left(\frac{\partial}{\partial t} - (\boldsymbol{\nabla}\phi \times \hat{\boldsymbol{z}}) \cdot \boldsymbol{\nabla}\right) \boldsymbol{\nabla}^2\phi = c_1(\phi - n) + c_2\boldsymbol{\nabla}^4\phi \tag{2.19}$$

$$\left(\frac{\partial}{\partial t} - (\boldsymbol{\nabla}\phi \times \hat{\boldsymbol{z}}) \cdot \boldsymbol{\nabla}\right) (n + \ln n_0) = c_1(\phi - n) \tag{2.20}$$

with c_1 the adiabaticity operator and c_2 the diffusion coefficient:

$$c_1 = -\frac{T_e}{e^2 n_0 \eta \omega_{ci}} \frac{\partial^2}{\partial z^2} \qquad c_2 = \frac{\mu}{\rho_s^2 \omega_{ci}} \tag{2.21}$$

where η is the resistivity, and $\mu = 3T_i\nu_{ii}/(10m_i\omega_{ci}^2)$ is the kinematic ion-viscosity coefficient. This set of equations is analogous to the Helmholtz vorticity equation. In this case it describes the evolution of turbulence caused by the resistive drift wave instabilities and was useful in order to interpret experimental

results from tokamak devices. On the left hand side, the first term related to the temporal derivative comes from the conservation laws of density and momentum, while the second non-linear term related to the spatial derivatives represents the advection due to the $E \times B$ drift; on the right hand side resistive terms take the role of energy damping and turbulence regulation. A result from numerical simulations of the Hasegawa-Wakatani model is shown in Fig. 2.13 with the formation of isolated potential contours in the 2D plane. It was noticed that when increasing the adiabaticity operator the contours followed a Boltzmann distribution *i.e.* $n_e \sim e\phi/T_e$ [122]. Therefore if c_1 keeps increasing ad-infinitum, resistive effects are neglected and ϕ, n fluctuations start being in phase hence no drift-wave instability is developed; on the opposite case strong turbulence grows generating uncorrelated vortexes. In that way Hasegawa [123] arranged an extensive review on self-organisation phenomena, a concept he defined as subjective but still participates in the formation of coherent structures, while still looking for a theoretical framework that could explain this process. Fortunately in 1987 the paper published by Hasegawa and Wakatani [124] offered the first theoretical proof of turbulence generating self-organised potential contours in a cylindrical magnetised plasma. Simulations reproducing these contours are shown in Fig. 2.14 (b). The model reformulated the Hasegawa-Wakatani equations in a three-dimensional space by including a combination of the drift-wave and the interchange resistive instabilities which introduce two key effects: curvature and magnetic shear. The equations are re-written in function of the potential vorticity ζ:

$$\zeta = \frac{\rho_s^2}{a^2}\boldsymbol{\nabla_\perp^2}\phi - \ln n \tag{2.22}$$

$$\frac{d\zeta}{dt} = \frac{\mu}{\omega_{ci}a^2}\boldsymbol{\nabla_\perp^2}\phi \tag{2.23}$$

$$\frac{\partial}{\partial t}\frac{\zeta^2}{2} + \boldsymbol{\nabla}\cdot\left(\boldsymbol{u_E}\frac{\zeta^2}{2}\right) = \frac{\mu}{\omega_{ci}a^2}\zeta\boldsymbol{\nabla_\perp^4}\phi \tag{2.24}$$

where a is the cylinder radius (the time being normalised in this case by $(\omega_{ci}\rho_s^2/a^2)^{-1}$), the last equation representing the conservation of enstrophy which is a requirement for the condensation of turbulence energy to the large scales. Regarding the self-organised structure, it is noticeable the formation of an axisymmetric potential surface ($m = n = 0$) being closed defined as a $\phi(r) = 0$ surface estimated for a normalised radius of $r \simeq 0.7$ which inferred the existence of counter-rotating azimuthal zonal flows *i.e.* a shear flow. The resulting status of the plasma leads to a steep increase of the density gradient, a reduction of the radial diffusion,

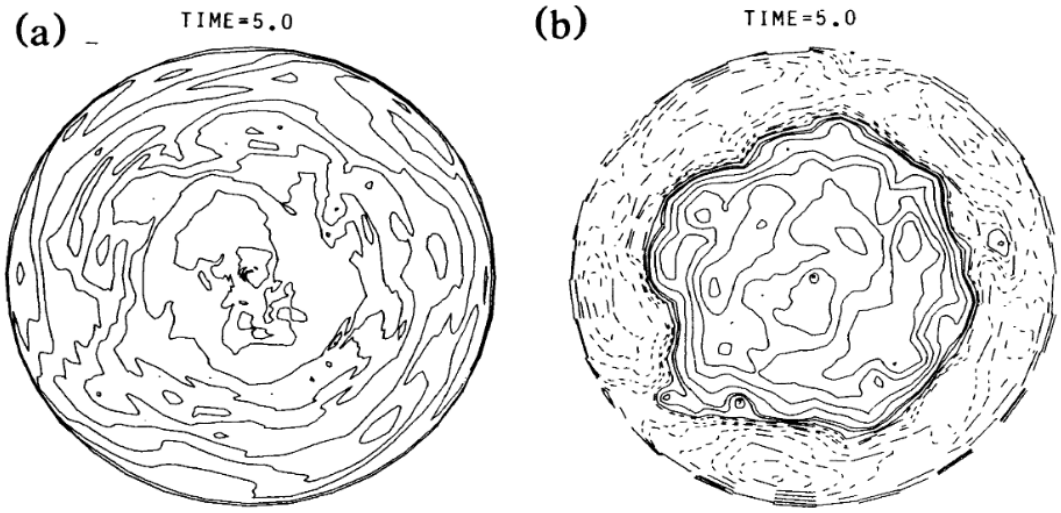

Figure 2.14: Hasegawa-Wakatani contours of (a) density, (b) electrostatic potential: solid (dashed) lines designate positive (negative) contours, the closed potential contour in (b) corresponds to the shear flow [124]

and thus an improved confinement. During the 1990s the question of the confinement status in tokamak plasmas was specially focused on the threshold for the formation of transport barriers. Observations from the DIII-D tokamak by Groebner *et al.* [125] reported that a reversal of the E_r component to negative values (*i.e.* pointing towards the center) and the increase of v_θ gradients seemed to be linked to a reduction of the turbulence fluctuations at the edge. The triggering conditions for the L-H transition were theoretically analysed by Shaing and Crume [126], and Biglari, Diamond and Terry [127], often called BDT model, which predicted a correlation between the radial electric field and the poloidal flow. The BDT model indicates that the poloidal shearing caused by the $E \times B$ drift velocity is dominant compared to curvature effects, and this shearing is in competition with the decorrelation rate of the turbulence. In other terms, it is intuitively predicted that the shearing rate must be superior to the instabilities' growth rate in order to suppress edge fluctuations. The theory of poloidal flow generation was investigated by Diamond *et al.* [128, 129], starting from the momentum equation:

$$\frac{\partial \langle u_\theta \rangle}{\partial t} = -\frac{\partial}{\partial r}\left(\langle \tilde{u}_r \tilde{u}_\theta \rangle - \frac{1}{m_i n_i \mu_0} \langle \tilde{B}_r \tilde{B}_\theta \rangle \right) - \mu_\theta \langle u_\theta \rangle \tag{2.25}$$

where μ_θ is the poloidal flow-damping rate. The non-linear fluctuating $\langle \tilde{u}_r \tilde{u}_\theta \rangle$ term represents the Reynolds stress and the second fluctuating $\langle \tilde{B}_r \tilde{B}_\theta \rangle$ term represents the damping by magnetic pumping: the turbulence

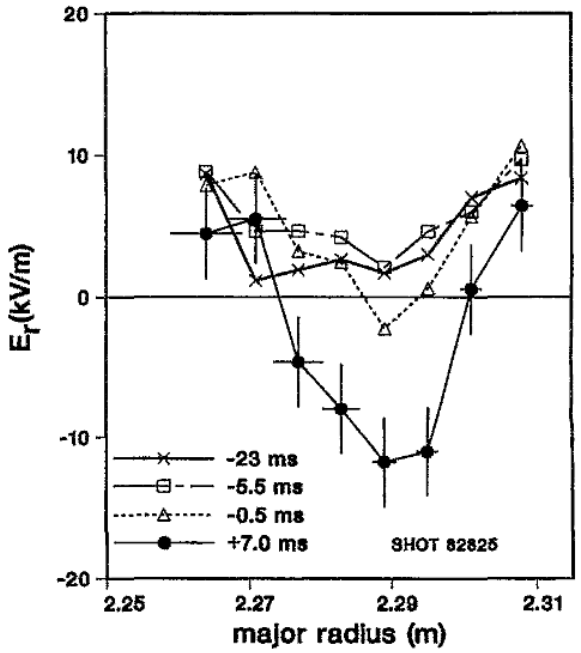

Figure 2.15: Evolution of the radial electric field at the pedestal during the L-H transition in DIII-D, different scatter plots indicate the time related to the L-H transition onset [131]

itself would generate a mean poloidal flow by means of the Reynolds stress. Other analysis performed by Hahm and Burrell [130] concluded that only the $E \times B$ flow shear is the only mechanism responsible for the suppression of turbulence. Moyer *et al.* [131] measured the evolution of the radial electric field during the L-H transition in DIII-D which is presented in Fig. 2.15 and shows the correlation of the strong E_r gradient with the barrier at the pedestal. This process was often referenced in the literature as a paradigm shift and is still not fully understood yet. Nonetheless it can be inferred by formulating the radial force balance and identifying its different contributions:

$$E_r = \frac{\nabla p_i}{Z_i e n_i} - u_{\theta i} B_\phi - u_{\phi i} B_\theta \tag{2.26}$$

Concerning the first term, the ion pressure gradient and the radial electric field are linked by positive feedback between the steepening of the gradient that maintains the radial electric field and the E_r shear that reduces the turbulent transport and enables the gradient to keep increasing. The second term represents the ion poloidal flow caused by the inertia of the zonal flow mechanism and it is dominant compared to the third

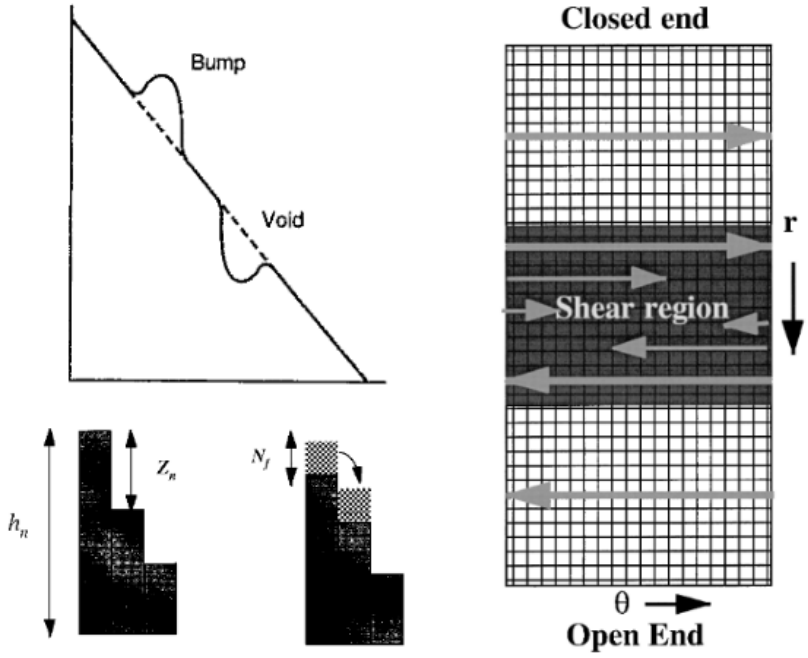

Figure 2.16: Schematics of the gradient idealised shape with "bumps" and "voids" (up left), a representation of the sand-pile model (bottom left), and pile flowing directions in the shear region (right) [132, 133]

term *i.e.* the ion toroidal flow that comes from momentum inputs such as the neutral beam injection. Both of these terms also theoretically bring viscosity and friction to the system and transfer momentum to the walls. It is supposed that zonal flows trigger the L-H transition and then the pressure gradient acts retroactively with the radial electric field in order to sustain the H-mode. Under the assumption of the existence of critical values of gradients, Newman, Carreras, Diamond and Hahm [132, 133] developed the self-organised criticality (SOC) model. According to this model, there are thresholds defining regimes of marginal stability. Passing a threshold comes to trigger a different type of transport that plays a role of smoothing the gradients and then to relax profiles and find meta-stable regimes. This mechanism refers to an avalanche-like transport that is represented by a sand-pile process in Fig. 2.16. Small-scale fluctuation cells perceive local strong gradients then are redistributed at the boundaries in order to restore the stability below the gradient's critical value. When localised in a shear region the flowing piles collide and the avalanche structure becomes decorrelated implying that the shear is dominant contributing to the suppression of turbulence and thus enabling the formation of steep gradients. In other terms, both mechanisms interplay in the L-H cycle between the barrier

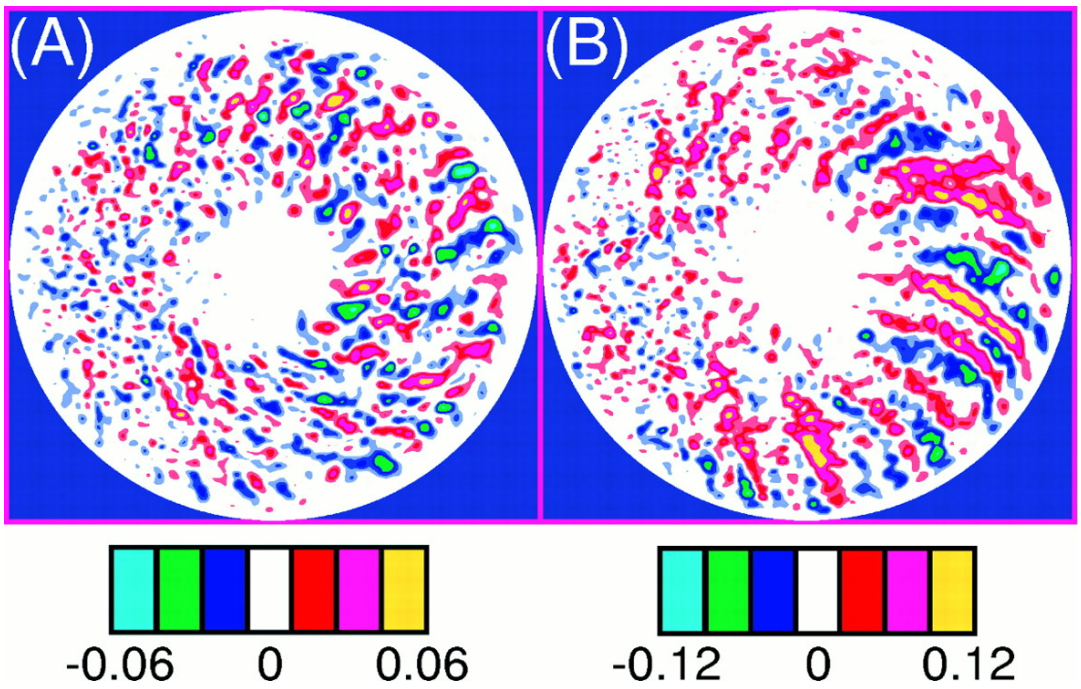

Figure 2.17: Poloidal contours in: turbulent regime (A), suppressed turbulence (B) [134]

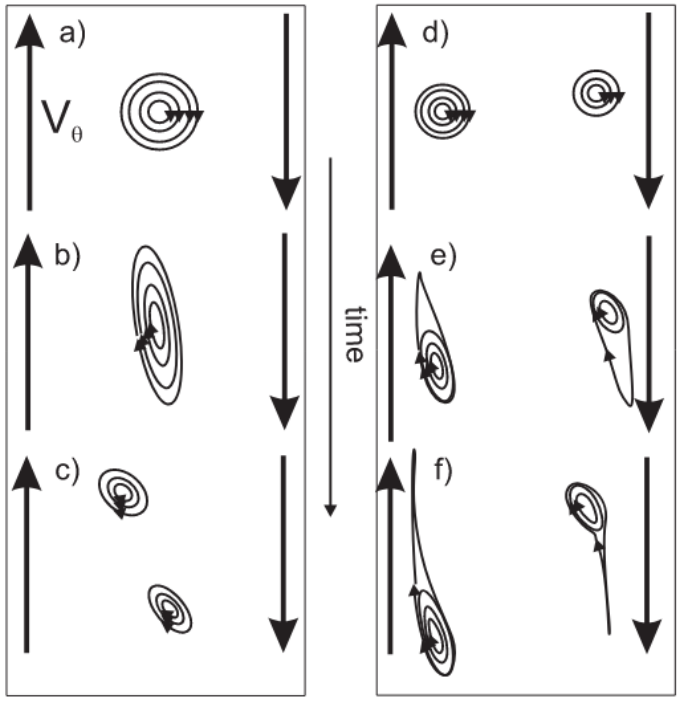

Figure 2.18: Schematics of two models of turbulence suppression due to zonal flows: decorrelation (left), vortex thinning (right) [138]

formation and the profile relaxation similarly to a predator prey model. At the beginning of the 2000s several machines were able to achieve H-mode recognizing it as a global mechanism for the improvement of confinement [135]. Fortunately the first evidences of zonal flows being the self-organised process triggering transport barriers were published: numerically by gyrokinetic simulations by Lin *et al.* [134, 136] (Fig. 2.17) and experimentally in the CHS stellarator by Fujisawa *et al.* [137]. These studies confirmed that zonal flows are a natural rotation mechanism generated by the Reynolds stress of turbulent fluctuations that, by means of poloidal shearing, suppress the turbulence itself. However it is still unknown how the energy from the turbulent eddies is transferred to the poloidal flow. Two hypotheses are illustrated in Fig. 2.18: the decorrelation mechanism proposed by the BDT model, and the vortex thinning proposed by Manz *et al.* [138]. Many other challenges remain active research topics. Two types of zonal flows, low frequency and high-frequency ZFs, have also been predicted such as the Geodesic Acoustic Modes (GAMs) [139] and also reported experimentally [140, 141]. Furthermore the H-mode is also characterised by quasi-periodic disruptive ejections of plasma degrading the barrier caused by Edge-Localised Modes (ELMs), which are still not understood. Detailed reviews on ZFs were published by Terry [142] and Diamond *et al.* [143].

2.1.5 Summary and challenges

There is a vast number of self-organised magnetised plasmas in nature that can be recreated in laboratory under several configurations. However the triggering conditions of self-organisation are constrained by unknown turbulent processes. The study of turbulence requires to understand the behaviour of vorticity which has remained a challenge since Helmholtz's work in the 1850s. The Kelvin-Helmholtz instability is a common process to all kinds of plasmas (and other fluids, oceanic flows, clouds formation, ...) when sheared flows are involved between two medium (*e.g.* plasma-vacuum) [144]. It differentiates from the Rayleigh-Taylor instability when the gravitational force can be neglected compared to a strong parallel velocity at the interface acquired by the shearing process, for that reason it's often referred as the parallel velocity gradient instability. It was often referred as diocotron instability in the context of magnetron plasmas [145]. It is a relevant mechanism of generating vortexes at the small scale in the Sun's atmosphere [146], as seen in

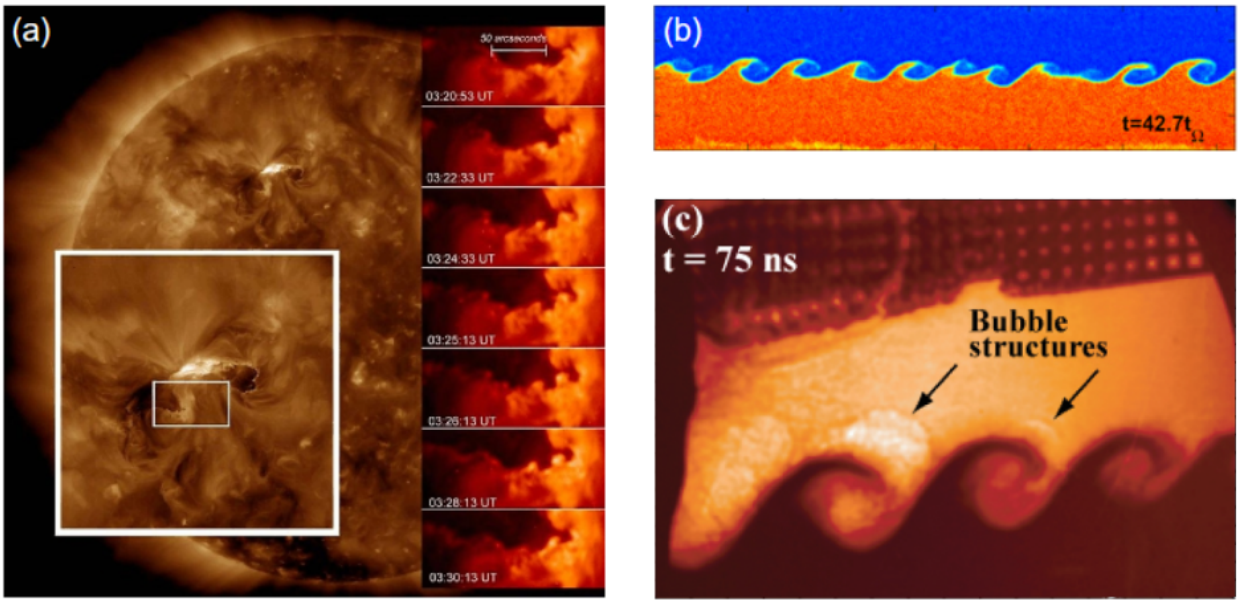

Figure 2.19: (a) Surfer waves in the Sun's atmosphere by the Kelvin-Helmholtz instability, from [146]; (b) Simulations of filaments formation due to interchange and Kelvin-Helmholtz instabilities reduced by shear flow in the boundary of the tokamak SOL [147]; (c) X-ray radiography of Kelvin-Helmholtz vortexes by the Omega Laser in a high-energy-density plasma [150]

Fig. 2.19, also in the formation of quasi-periodic oscillations in accretion disks which produce jets [148], or causing poloidal asymmetries of edge fluctuations in tokamak plasmas [149]. Similar phenomena occur with laser shock-waves in plasmas for applications in inertial fusion [150]. This instability can be amplified in sheared toroidal rotating plasmas which becomes a major problem for confinement [151]. Additional effects such as the dynamo effect [152] and the magnetic reconnection [153] also play a role in the transfer of energy from the field to the plasma. All these processes lead to self-organised states. In order to understand these processes, the vorticity equation had been adapted for magnetised plasmas by Taylor and McNamara [154] and Hasegawa, Mima and Wakatani [116, 121] as a function of the electrostatic potential ϕ:

$$\frac{\partial}{\partial t}\left(\boldsymbol{\nabla}^2\phi - \phi\right) - [(\boldsymbol{\nabla}\phi \times \hat{\boldsymbol{z}}) \cdot \boldsymbol{\nabla}]\boldsymbol{\nabla}^2\phi = \text{RHS} \tag{2.27}$$

RHS is an acronym for 'Right-Hand Side', predicting inverse cascades for large wavenumbers such as $\mathcal{E}(k) \sim k^{-3}$ [121, 122]. The observable self-organised phenomena suggest that universal mechanisms in the right-hand side of the vorticity equation regulate the turbulence. This challenge goes beyond this thesis.

2.2 Scrape-off layer filaments

This section is a review of intermittent phenomena in tokamaks. The following sections focus specially on fusion plasmas, *i.e.* the dynamics of plasma filaments at the SOL. In these sections concepts such as the shoulder formation in SOL profiles are introduced as these are active fields of research and part of this thesis.

2.2.1 A phenomenological introduction to intermittency

Turbulence is difficult to study due to the interaction of small and large scales. In the Navier-Stokes equation this is manifested by the advection term $\boldsymbol{u} \cdot \boldsymbol{\nabla u}$ which contains non-linear terms affecting multiple scales. In comparison with the idealised conception of turbulence in theoretical models, the existence of irregular events, observed in experiments, underlines the limitations of those models and the complexity of the problem. This irregular behaviour of turbulence is labelled *intermittency* which causes high amplitude events such as bursty phenomena. These events are characterised by an intermixing of coherence and randomness in terms of Das, Kaw and Jha [155]. The statistical approach based on the Kolmogorov ansatz serves as a tool for parametrising cascades. However these intermittent events create deviations from the predicted scaling laws. The issue is that the K41 theory is sustained by several assumptions such as the conservation of the energy dissipation ϵ and the spatial self-similarity of the eddies during the inertial range. However in a more realistic perspective of the problem, that interplay between multiple scales that lead to intermittent events is the key factor that violates these idealised conditions. A solution aiming to track these deviations consisted in the evaluation of the differential increments in velocity expressed by the structure function:

$$S_p(l) = \langle |\delta u|^p \rangle \sim l^{\zeta_p} \tag{2.28}$$

with l the scale length of the eddy, ζ_p the scaling index and p the scaling order, the dependence between ζ_p and p quantifies the deviation from linearity characterised by gaussian isotropic distributions. The models which adopt this methodology show that the intermittent structures follow a fractal pattern with less and less space filling between the eddies. Each model then predicts different scaling indexes of the eddies' geometry under turbulent intermittency. Some examples are the β-model by Novikov and Stewart [156] then improved

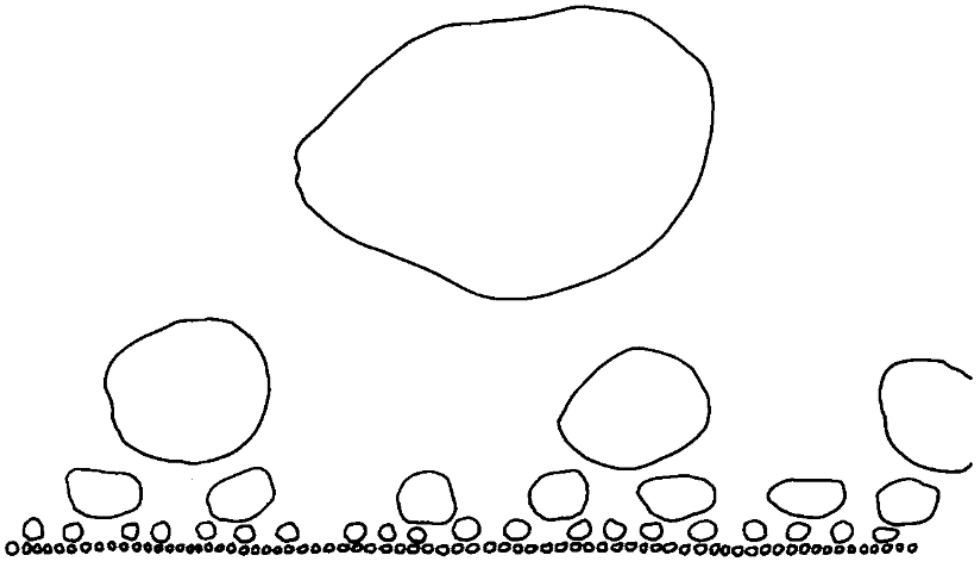

Figure 2.20: Novikov-Stewart-Frisch idealised concept of intermittent inverse cascade from [157].

by Frisch *et al.* [157] (an example is illustrated in Fig. 2.20) and the log-Poisson model by She and Lévêque [158]. A different statistical approach by Kraichnan [159] studied the evolution of turbulent structures by employing probabilistic distribution functions (PDFs) of the velocity gradient of s, the transverse component of u. The PDF represents the probability of a variable s which quantifies the evolution of fluctuations within $(x,\, x+dx)$. The PDF P is defined initially as a Gaussian distribution in s_0 characteristic of a pure random nature of the background:

$$P(s) = (2\pi\langle s_0^2\rangle)^{-1/2}\exp\left(-\frac{1}{2}\frac{s_0^2}{\langle s_0^2\rangle}\right)\frac{\partial s_0}{\partial s} \tag{2.29}$$

Then non-Gaussian deviations from the PDF are caused by intermittent events and can be visualised by its shape. This approach shows that the skewness S and kurtosis K defined by:

$$S = \frac{\langle s^3\rangle}{\langle s^2\rangle^{3/2}} \qquad\qquad K = \frac{\langle s^4\rangle}{\langle s^2\rangle^2} \tag{2.30}$$

i.e. the degree of asymmetry and the degree of flatness or peakness, third and fourth orders of the PDFs respectively, tend to be finite at high Reynolds numbers. In the case of magnetised plasmas the statistical approach has been widely adopted instead of the multifractal approach. The convective turbulence present at the plasma edge is manifested by the appearance of intermittent bursts *i.e.* high current spikes presented in Fig. 2.21 collected by probes at the edge. The analysis of scrape-off layer intermittent fluctuations in

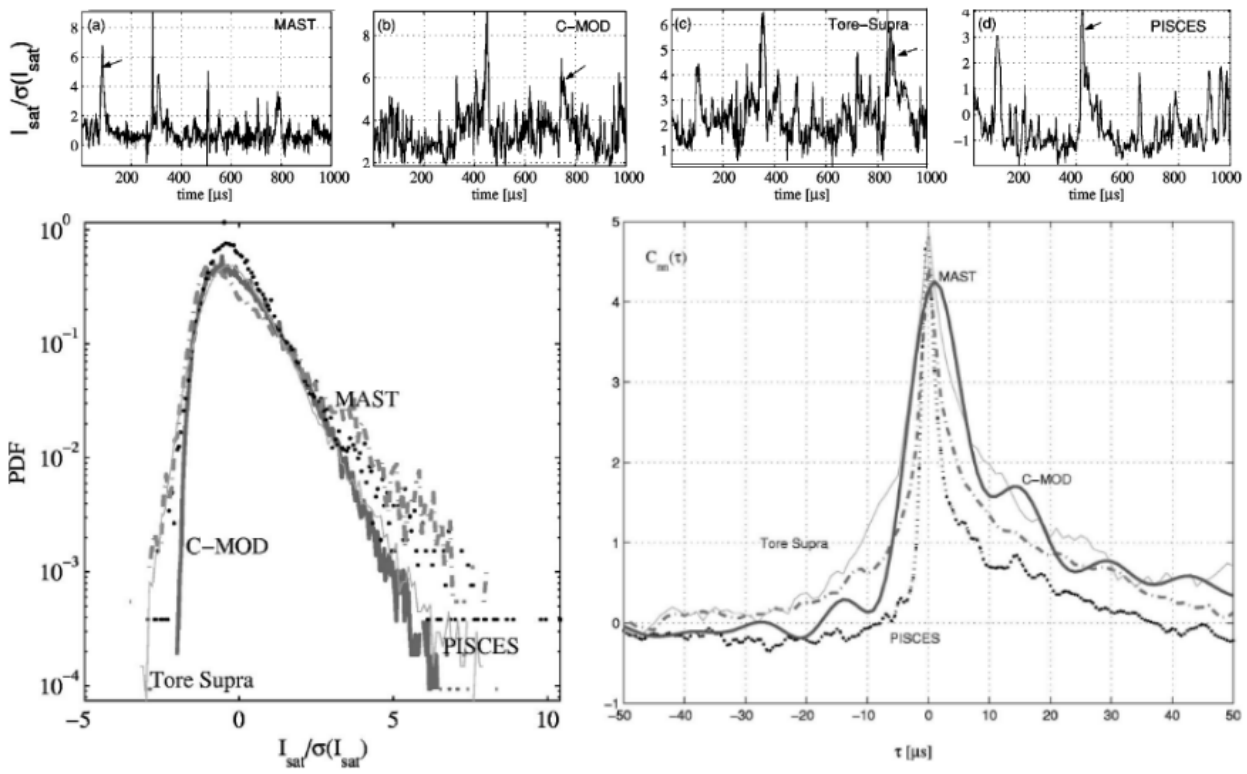

Figure 2.21: (top) Ion saturation current collected with probes in MAST (a), Alcator C-Mod (b), Tore Supra (c), PISCES (d) with arrows indicating blobs; (bottom left) normalised PDFs of ion saturation currents from the 4 devices; (bottom right) conditional averaging of blobs from the 4 devices; from Antar *et al.* [161]

tokamak plasmas is characterised in non-Gaussian PDFs by their skewness. A positive skewness reports the detection of intermittent positive bursts, known as blobs, whereas a negative skewness reports the detection of intermittent negative bursts, known as holes, respectively. For Gaussian distributions these parameters are equal to zero ($S = 0$, $K = 0$) whereas in the far SOL intermittent bursts are typically characterised with positive skewness ($S > 1$ and $K > 1$) as it is illustrated in Fig 2.21 (bottom left) with a positive large tail. The work done by Antar *et al.* [160, 161] shown that PDFs of the ion saturation current collected with probes in different devices tend to converge which implies this intermittent behaviour is universal to all kinds of magnetically confined plasmas. An additional statistical tool used for the study of intermittent objects is the conditional averaging of intermittent peaks above a threshold. This method allows to extract the typical features of blobs such as lifetimes and velocities.

2.2.2 Definition of Intermittent Plasma Objects (IPOs)

In the literature of magnetically confined plasmas, the terminology addressing these intermittent events is broad. These events are often referred by their manifestation as filaments, avaloids, streamers or blobs depending on the diagnostic used for their observation and the idealised form conceived in theoretical models. Nevertheless they all belong to the family of *intermittent plasma objects*. These objects tend to form at the separatrix transporting heat and particles, and then propagate radially outwards driven by cross-field convection. It is an active domain of research and is still a matter of debate if IPOs could be considered coherent structures being the product of sheared flows at the plasma edge. The term *transient* is often more appropriate due to their short-lived appearance instead of the term *coherent* which implies a long-term regular behaviour. According to the definition given in the review by D'Ippolito, Myra and Zweben [162] a filamentary structure must satisfy the following three criteria:

- (1) it has a monopole (single-peaked) density distribution with a peak value much higher (typically $\geq$ 2–3 times) than the surrounding root-mean-square fluctuations of the background plasma;
- (2) it is aligned parallel to the magnetic field and its variation along the field is much weaker than in the transverse direction;
- (3) it has a dominant convective $E \times B$ velocity component in the direction of a charge-polarizing force, and an associated potential and vorticity with a dipole structure in the direction transverse to its propagation.

The first criterion comes from the necessity of choosing an arbitrary threshold used for conditional averaging in order to select particular windows where intermittent events arise. The second criterion refers to the distinction between the parallel and the perpendicular non-uniformities, the parallel ones being spread at the ion sound speed. The third criterion allows the perpendicular non-uniformities to develop as blob structures in the far SOL due to the contributions of the $E \times B$ and $\boldsymbol{\nabla} B$ curvature drifts. It is common that both concepts *filaments* and *blobs* are usually treated as synonyms in the literature. In order to avoid misunderstandings in this thesis we will tend to differentiate between *filaments* as the elongated plasma tubes

aligned with the field lines and *blobs* as the non-uniformities connected in the birth region to the plasma and propagating outwards in the approximated radial direction.

2.2.3 Experimental observations of filaments

The ambiguity in the filament-blob definition can be understood by the examination of multiple structures under different experimental conditions. In the first observations of blobs, these were described as mesoscale structures (*i.e.* in between the gyroradius scale and the machine size) that were "irregularly organised". These measurements are principally effectuated in the vicinity of the SOL where it is possible to observe the formation of these structures escaping the plasma from the separatrix. Since the 1980s, different techniques such as probes and optical diagnostics have been improved in order to analyse the activity of filaments.

Probe measurements: The first measurements were taken in the Caltech tokamak by Zweben [163]. The intermittent nature of plasma structures is represented by their fluctuating signature in the ion saturation current collected by probes. This was remarked in section 2.2.1 with the work of Antar *et al.* [160, 161] in Fig. 2.21. Each peak corresponds to the interaction of a filamentary structure with a probe. The disposition of several probes at different positions allows to track the excursions of passing blobs and extract their characteristics *e.g.* sizes and velocities. From ion saturation current it is possible to infer the local values of density and temperature. For instance, the use of 200 probes in the Versatile Toroidal Facility (VTF) [164] allowed to depict for the first time the mushroom shape of a blob as shown in Fig. 2.23. Statistical methods (*e.g.* PDFs, conditional averaging) have demonstrated that blobs show regular tendencies. The principle of probes and statistical techniques will be explained in detail in chapter 4 on COMPASS.

Camera imaging: The first observations of blobs were reported by Goodall through camera imaging in ASDEX [165]. Since then, the technological improvements have upgraded the capabilities of fast cameras with sufficient time resolution to visualise the evolution of the SOL filaments. The view of these cameras is wide enough to cover the whole chamber and collect passive light from the plasma. For example, a picture

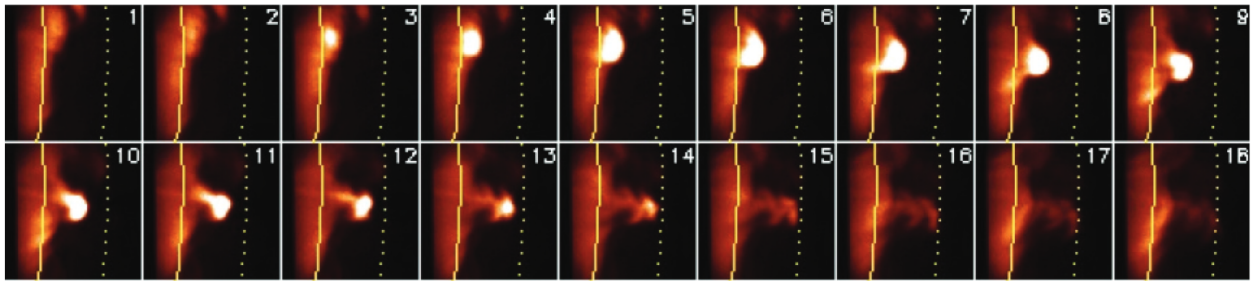

Figure 2.22: Blob creation and propagation during H-mode with the GPI diagnostic in NSTX. The inter frame time is 7.0 μs and the field of view is 25 $\times$ 25 cm. The blob moves radially from the outer midplane separatrix (solid line) towards the limiter shadow (dashed line) [176]

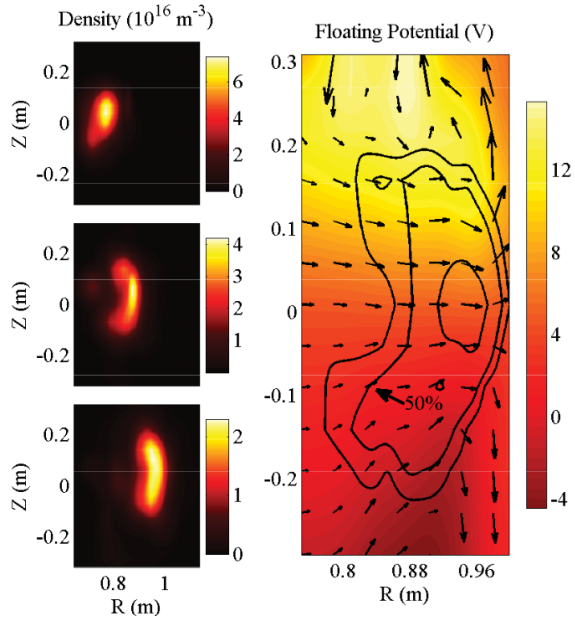

Figure 2.23: Probe measurements on VFR: (left) poloidal cross sections of a typical blob at 3 different times ($\Delta t \sim 100$ μs); (right) floating potential consistent with the blob propagation [164]

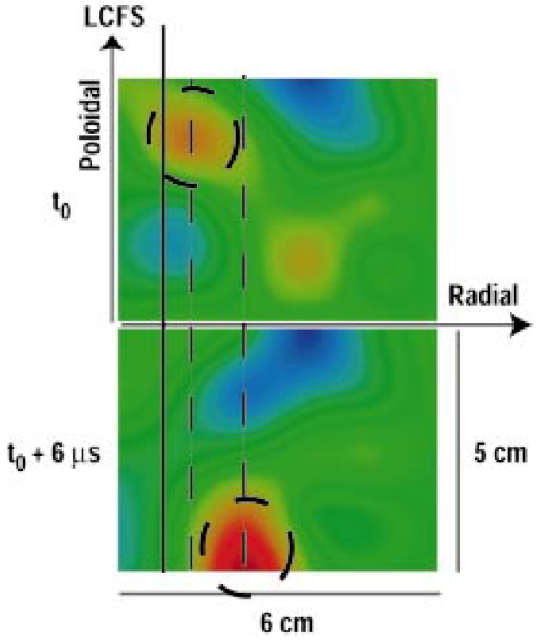

Figure 2.24: Two BES frames showing 2D density plots on DIII-D ($\Delta t \sim 6$ μs between frames). Red indicates high density and blue low density; structures are marked with dashed circles [177]

Tokamak	Lifetime (μs)	Size (cm)	Radial velocity (km/s)	References
MAST	50	1 - 8	0.5 - 2	[168]
NSTX	60 - 70	2 - 4	0.5	[169]
DIII-D	15 - 20	0.5 - 3.9	0.3 - 2.7	[170]
AUG	-	0.5 - 9.5	0.2 - 3.5	[171]
JET	25	1 - 2	1	[172]
C-Mod	10 - 30	0.0 - 1.5	-	[173]

Table 2.1: Typical parameters of L-mode filaments in tokamaks

of visible L-mode filaments was shown in Fig. 1.22 on MAST [56]. In order to obtain the characteristic dimensions of filaments with more accuracy, tomographic inversion techniques can be applied to camera frames. Progress in this domain has been recently demonstrated in TCV [166] and COMPASS [167]. This method will be presented in chapter 5 for MAST.

Gas puff imaging: This technique consists in injecting gas (*e.g.* D, He, N) at a localised section of the vessel. The gas atoms interact with the blob, are ionised, and hence the resulting excitation release radiation in the blob area. This emission allows to visualise the motion of filamentary structures. The GPI diagnostic has been tested in different machines such as Alcator C-Mod [173], RFX-mod [174], and NSTX [175, 176]. In Fig. 2.22 the formation process of a blob enhanced by the GPI at NSTX is shown. The use of this technique was not explored in this thesis.

Beam emission spectroscopy: The BES consists in a 2D imaging technique that uses a neutral beam to enhance the emission of a particular area of the plasma. This diagnostic has been mostly employed in DIII-D [177], in NSTX [178] and TEXTOR [179] for the description of structures at the plasma edge. The detection of structures at the separatrix in DIII-D is shown in Fig. 2.24. The principle of the beam emission spectroscopy will be introduced in chapter 4 and exploited in chapters 5 and 6 in MAST.

The results from several machines have demonstrated that filament-blob structures behave similarly in different configurations. The characteristic of typical blob features are presented in Table 2.1. Typical blobs present similar values around the same magnitude *e.g.* lifetimes of ~ 10 μs, radial sizes of ~ 1 cm, and radial velocities of ~ 1 km/s. These different techniques have pointed out that the blobs radial velocity is comparable to the $E \times B$ velocity drift, considered as the main driven mechanism generating these structures.

2.2.4 Analytical models of filament transport

The first models of edge turbulence failed to describe accurately the SOL behaviour that was observed in early experiments. Nonetheless the common agreement between different models is that blobs are born due to the appearance of strong gradients at the edge. Nedospasov pointed out the flute-interchange instability as the main responsible mechanism for driving plasma out in the low field side [180]. One major difficulty is the unfavourable curvature at the edge when field lines end up in contact with walls and causing resistive ballooning instabilities to grow according to Garbet *et al.* [181]. In order to simplify the problem, D'Ippolito, Myra and Krasheninnikov [182, 183] restrained the model of filament dynamics principally due to convective cross-field transport. This model, often referred as Krasheninnikov model, only describes non-interacting single filaments and its assumptions include the quasi-neutrality across the filament and a constant temperature (*i.e.* $\boldsymbol{\nabla} p = T\ \boldsymbol{\nabla} n$) in the SOL. The filament motion is predicted by tracking all different contributions of currents forming a loop equivalent to the circuit shown in Fig. 2.25. The curvature due to the $\boldsymbol{\nabla} B$ gradient generates the effective centrifugal force $\boldsymbol{F_g}$. The interchange mechanism is triggered *i.e.* the $\boldsymbol{F_g} \times \boldsymbol{B}$ drift contributes to polarise the filament and amplify the $\boldsymbol{E} \times \boldsymbol{B}$ drift which propels the filament into the SOL. The resulting blob becomes a dipole structure generating a diamagnetic current $\boldsymbol{j_{dia}}$ which acts as the source of the circuit. From there the current $\boldsymbol{j}_{\|}$ flows along the field line. The resistivity $\eta_{\|}$ plays a crucial role in the filament transport because it determines the magnitude of the charge polarization potential ϕ in the poloidal direction. If the resistivity is low, the current dissipates through to the sheath, where the field line is in contact with a limiter, which acts as a closure of the circuit. If the resistivity is high, the parallel current is unable to circulate and the perpendicular polarization current $\boldsymbol{j}_{\perp,\boldsymbol{pol}}$ by the ions inertia

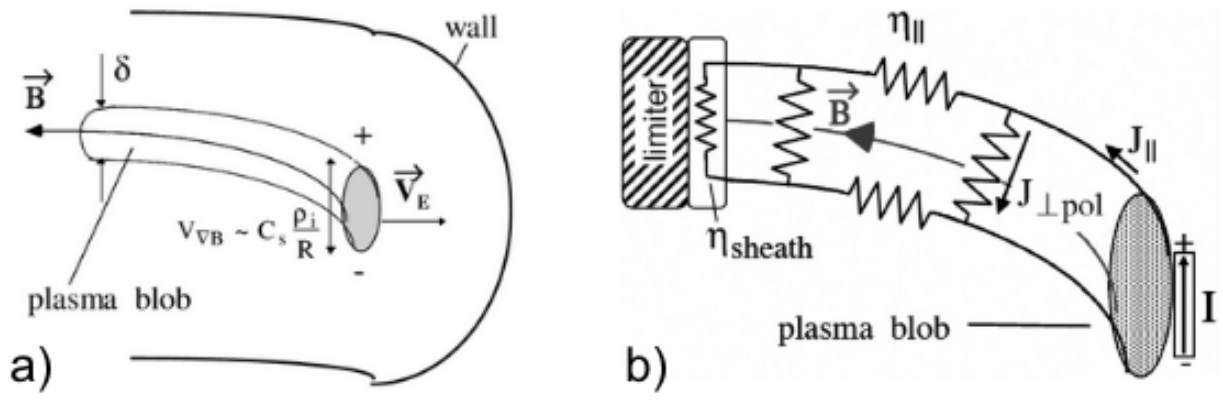

Figure 2.25: Schematics of the simplified model for the plasma filament motion; a) result of the $\boldsymbol{\nabla} B$ interchange effect amplifying the $\boldsymbol{E} \times \boldsymbol{B}$ drift; b) equivalent circuit with current source I, sheath at limiter, and polarisation current; from Krasheninnikov *et al.* [182, 183]

emerges as the easiest way for evacuating the current, driving the plasma to the divertor. The path of least resistance for closing the circuit is determined by these different currents and is transcribed by the following set of equations. First, the current conservation equation is given by:

$$\boldsymbol{\nabla} \cdot \boldsymbol{j} = \boldsymbol{\nabla} \cdot \boldsymbol{j}_{\perp} + \boldsymbol{\nabla} \cdot \boldsymbol{j}_{\parallel} = 0 \tag{2.31}$$

Second, assuming the main drift is caused by the $E \times B$ advection, the continuity equation is:

$$\frac{dn}{dt} = \frac{\partial n}{\partial t} + \boldsymbol{u_E} \cdot \boldsymbol{\nabla} n \sim 0 \tag{2.32}$$

The perpendicular current can be decomposed in its different contributions:

$$\boldsymbol{j}_{\perp} = \boldsymbol{j_{dia}} + \boldsymbol{j}_{\perp,\boldsymbol{pol}} \tag{2.33}$$

The divergence of the diamagnetic current can be expressed by the effect of the curvature $\boldsymbol{\kappa}$:

$$\begin{aligned} \boldsymbol{\nabla} \cdot \boldsymbol{j_{dia}} &= \boldsymbol{\nabla} \cdot \left(\frac{\boldsymbol{\nabla} p \times \boldsymbol{B}}{B^2} \right) \\ &= \frac{\boldsymbol{B}}{B^2} \cdot \boldsymbol{\nabla} \times \boldsymbol{\nabla} p - \boldsymbol{\nabla} p \cdot \left(\boldsymbol{\nabla} \times \frac{\boldsymbol{B}}{B^2} \right) \\ &= -\boldsymbol{\nabla} p \cdot \left(\frac{2}{B^2} \boldsymbol{B} \times \boldsymbol{\kappa} + \frac{2}{B^2} \boldsymbol{B} \times \boldsymbol{\nabla} B \right) \\ &= -2 \boldsymbol{\nabla} p \cdot \left(\frac{\boldsymbol{B} \times \boldsymbol{\kappa}}{B^2} \right) \sim -2 \boldsymbol{\nabla} p \cdot \boldsymbol{g} \end{aligned} \tag{2.34}$$

Assuming that the magnetic field is mainly toroidal, the cross product $\boldsymbol{B} \times \boldsymbol{\nabla} B$ is pointing in the vertical direction, then the term $\boldsymbol{\nabla} p \cdot (\boldsymbol{B} \times \boldsymbol{\nabla} B)$ is zero. The curvature term is equivalent to a gravity term $\boldsymbol{g}$. The divergence of the polarisation current is defined by the electrostatic potential ϕ due to force $\boldsymbol{F_g}$:

$$\boldsymbol{\nabla} \cdot \boldsymbol{j}_{\perp,\boldsymbol{pol}} = \boldsymbol{\nabla} \cdot \left(nq \frac{m_i}{qB^2} \frac{d\boldsymbol{E}_\perp(t)}{dt} \right) = -\boldsymbol{\nabla} \cdot \frac{d}{dt} \left(\frac{nm_i}{B^2} \boldsymbol{\nabla}_\perp \phi \right) \tag{2.35}$$

Replacing all the terms, the charge conservation equation leads to the vorticity equation:

$$\boldsymbol{\nabla} \cdot \frac{d}{dt} \left(\frac{nm_i}{B^2} \boldsymbol{\nabla}_\perp \phi \right) = \boldsymbol{\nabla}_\parallel j_\parallel + 2 \left(\frac{\boldsymbol{\nabla} \times \boldsymbol{B}}{B^2} \right) \cdot \boldsymbol{\nabla} p \tag{2.36}$$

The left-hand side represents the inertial force of polarisation currents, whereas the right-hand side represents the dissipative and driving forces and compression of parallel and diamagnetic currents due to curvature-interchange effects that collaterally generate new instabilities. Different closures of the system correspond to different physical effects characterising different blob schemes recapitulated in the review by Krasheninnikov *et al.* [184]. Each scheme leads to an analytical solution of the blob velocity and hence describes a particular regime of the SOL transport by establishing scaling laws. In this case this translates into substituting the $\boldsymbol{\nabla}_\parallel j_\parallel$ operator for a term dependent on the electrostatic potential ϕ. The simplified Krasheninnikov model chooses as boundary condition the sheath-connected current with n_t the density at the target [182, 183]:

$$j_{\parallel,sh} = n_t e c_s \left[1 - \exp\left(\frac{e\phi}{T} \right) \right] \sim \frac{n_t e^2 c_s \phi}{T} \tag{2.37}$$

The integration of the vorticity equation along the connection length noted $L_\parallel$, *i.e.* the parallel length of a field line from one to another target, for a blob density n_b leads to the following expression, introducing (x, y) the outwards force (*i.e.* radial) and binormal (*i.e.* poloidal) directions respectively:

$$\frac{e\phi}{T} \sim \frac{\omega_{ci}}{2n_t B} \int_0^{L_\parallel} dl \frac{B}{R} \hat{\boldsymbol{x}} \cdot (\boldsymbol{B} \times \boldsymbol{\nabla} n) \sim \frac{L_\parallel \omega_{ci}}{2Rn_t} \frac{\partial n_b}{\partial y} \tag{2.38}$$

This equivalence links the electrostatic potential and the density gradient of the blob in the binormal direction, then it can be reinjected in the continuity equation 2.32 in order to derive the blob velocity. Considering a cylindrical plasma filament with a Gaussian density profile:

$$n_b(x, y) = n_b(x) \exp\left(-\frac{y^2}{2\delta^2} \right) \tag{2.39}$$

with δ_b the blob size, the solution for the blob velocity in this regime is:

$$v_b = c_s \frac{L_\parallel}{R} \left(\frac{\omega_{ci}}{\delta_b} \right)^2 \frac{n_b}{n_t} \tag{2.40}$$

Therefore in the sheath-connected regime the velocity follows the scaling: $v_b \sim \delta_b^{-2}$. On the contrary, in the high resistive case the inertial term of the vorticity equation becomes predominant and the parallel term is null *i.e.* the closure of the circuit is effectuated by the charge polarisation current. In the inertial regime the velocity follows a different scaling: $v_b \sim \delta_b^{1/2}$. Introducing $\Delta\theta$ the deviation of the thermodynamic variable from Θ the uniform background, the corresponding scaling is given by [185]:

$$v_b = c_s \left(2 \frac{\delta_b}{R} \frac{\Delta\theta}{\Theta} \right)^{1/2} \tag{2.41}$$

From that model several generalisations have been developed that account for different parameters such as the magnetic geometry, the collisionality or electromagnetic effects. In the presence of an X-point the closure tends to be determined by the magnetic shear. In this case the Wentzel-Kramers-Brillouin (WKB) limit has been used as a theory which comes to solve the dispersion relation describing growth rates scalings depending on the instability regime [186]. Different boundary conditions are proposed by the WKB heuristic model that dependent on the conductivity σ, where at the vicinity of the X-point [187]:

$$\boldsymbol{\nabla}_\parallel j_\parallel \sim \frac{(\sigma_\parallel \sigma_\perp)^{1/2}}{L_\parallel \delta_b} \phi \tag{2.42}$$

A more general framework that encloses the description of filaments between the midplane and the X-point is the so called *two-region* model [188, 189]. This model is based on the mapping of magnetic field lines between these two regions and studies the variation of the field in the perpendicular radial-poloidal plane. Phenomenologically this can visualised in Fig. 2.26: the X-point configuration works as a magnetic fan due to the disconnection of the magnetic geometry; the circular shape of the blob at the midplane tends to stretch into an elliptical shape; the flux tube is sheared and then takes the form of a divertor-leg blob. At that point there is a transition to the sheath-connected model when the blob is back in contact with the divertor plates as a surface. The magnetic geometry is not the only factor that has a major impact on this regime but also the collisionality. Turbulent regimes were found when surpassing limits of density due to an increase of collisionality [190]. In order to report these different regimes different methods were proposed

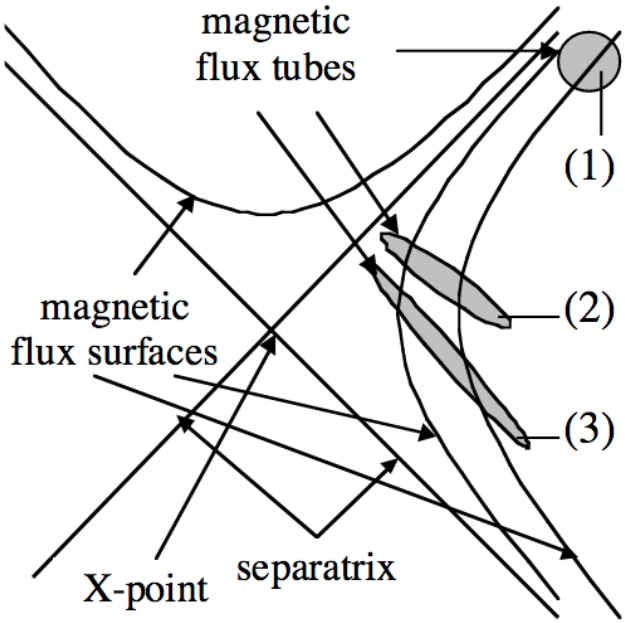

Figure 2.26: Schematics of the two region model, evolution of the cross-section of a magnetic flux tube in the vicinity of separatrix [191]

for the prediction of scalings which are not only restricted to the blob size. One approach for resistive ballooning models such as the WKB limit is the *blob correspondence principle* that consists in linearising the dispersion relation in order to obtain heuristic closures [186]. A different approach is the arrangement of regime diagrams by a set of non-dimensional parameters. In the WKB limit the characteristic parameters used for describing regimes are the normalised frequency X, correlated with the collisionality and the size, and growth rate Y, correlated with the magnetic curvature strength, of the modes responsible for driving blobs, defined as:

$$\mathrm{X} = \frac{\omega_\eta}{\omega_a} \qquad\qquad \mathrm{Y} = \frac{\gamma_{mhd}^2}{\omega_a^2} \tag{2.43}$$

$\omega_\eta = \nu_e ke2$ is the magnetic diffusion frequency, ω_a is the Alfvén frequency, and γ_{mhd} is the growth rate of the instability mode. In the two-region model the scalings are determined by four major parameters:

$$\Lambda = \frac{\nu_{ei} L_\parallel}{\omega_{ce}\rho_s} \qquad \Theta = \hat{\delta}^{5/2} \qquad \epsilon_x = \frac{k_{\perp,1}}{k_{\perp,2}} \qquad \hat{v} = \frac{v}{v_*} \tag{2.44}$$

These parameters are the collisionality Λ, the scaled blob size Θ, the magnetic field line fanning ϵ_x, and the blob velocity $\hat{v}$. The subscripts (1, 2) of the wavevector $\boldsymbol{k}_\perp$ refer to regions 1, the outboard midplane region,

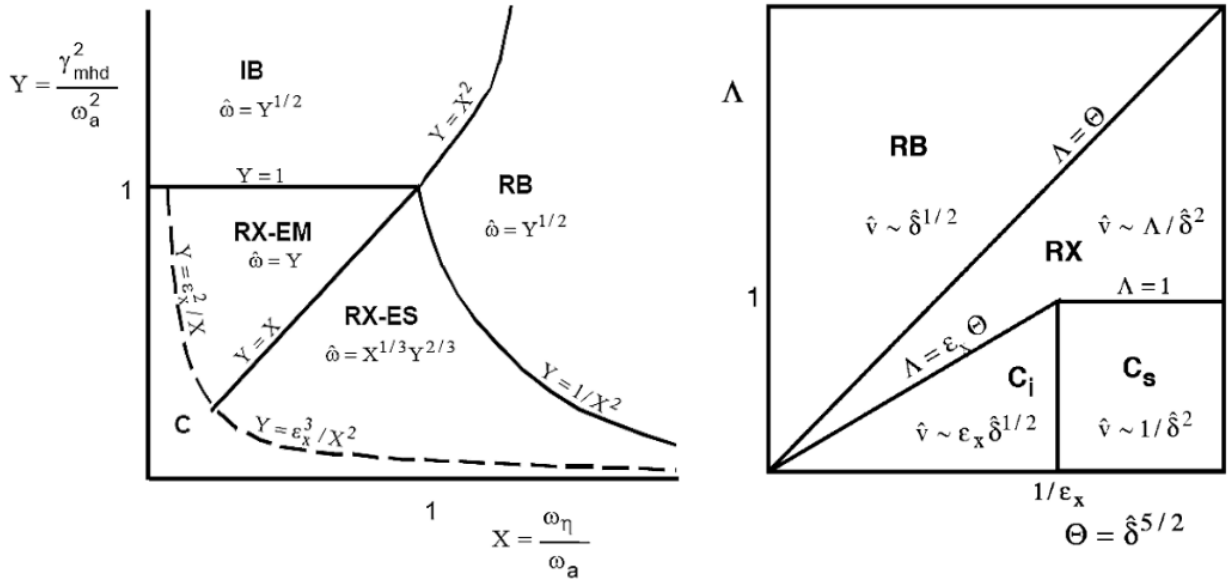

Figure 2.27: Blob transport diagrams: (left) for the WKB limit [186]; (right) for the two-region model [188]

and 2, the divertor X-point region. These variables allow to predict different scalings of filament propagation and velocities. Each area on these diagrams allows to identify a particular instability that drives the blob transport, these are noted by the following acronyms [184]:

- the Ideal Ballooning (IB) regime: the curvature drive is balanced by the inertia caused by the polarization current *i.e.* $\omega_a \sim \gamma_{MHD}$ corresponds to the Alfven wave.
- the Resistive Ballooning (RB) regime: the resistivity dominates line bending so that midplane and divertor regions are disconnected; this corresponds to the inertial regime where the parallel current is neglected.
- the Resistive X-point (RX) regime: the midplane curvature drive is balanced by the parallel current term in the X-point region; RX-ES and RX-EM indicate electrostatic and electromagnetic X-point modes respectively.
- the sheath-Connected (C) regime: in the sheath C_s regime the filament is connected to the limiter; in the ideal C_i regime midplane and divertor are connected but dependent on the fanning parameter related to the magnetic shear.

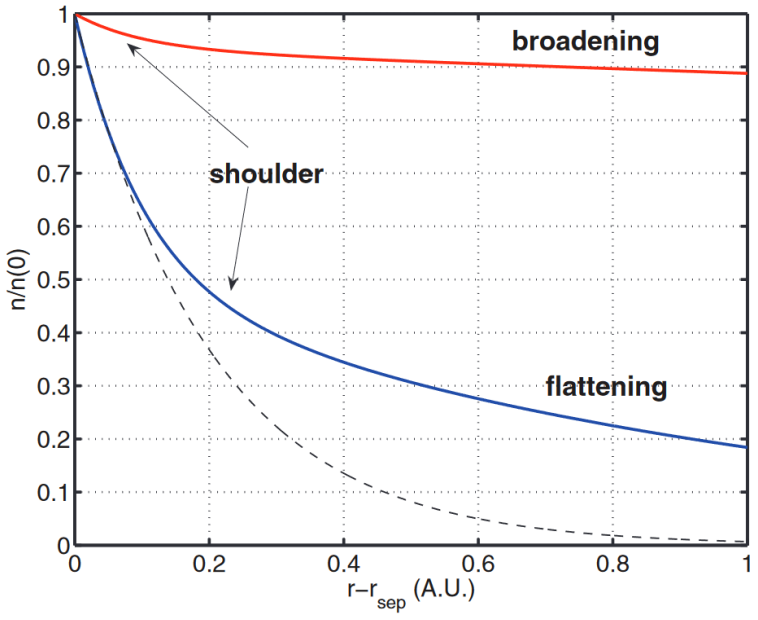

Figure 2.28: Schematic representation of typical SOL profiles at two fuelling rates: low (blue curve), *i.e.* flattening regime, and high (red curve), *i.e.* broadening regime. The dashed line represents a pure exponential decay in contrast with the. The far SOL extends outwards from the shoulder position [192]

2.2.5 Challenges: anomalous transport and shoulder formation

Models are still unable to fully explain the turbulent behaviour of SOL filaments. Phenomena associated with forms of so-called anomalous transport are experimentally observed against the predictions of the neoclassical approach. Transitions of the SOL density profiles have been reported across different tokamaks. By increasing the fuelling rate, the SOL start exhibit separated regions with distinct density profiles: a near SOL, close to the separatrix where the gradients are steep, and the far SOL towards the walls. In between, the boundary between these two regions is so-called *shoulder* [192]. Two regimes are distinguished by describing the density transition: from a flattening regime at low fuelling, up to a broadening effect at high fuelling. Both cases are represented in Fig. 2.28 being described by non-exponential profiles. The decay lengths indicates the progression of the broadening effect on the density profile. This effect is manifested by the change of filamentary structures. Blobs become more elongated, with higher velocities, hence increasing the risk of surface interactions with the first wall. Shoulder formation has been observed experimentally in different tokamaks such as Alcator C-mod [193], DIII-D [194], TCV [195], AUG [196], and MAST [197].

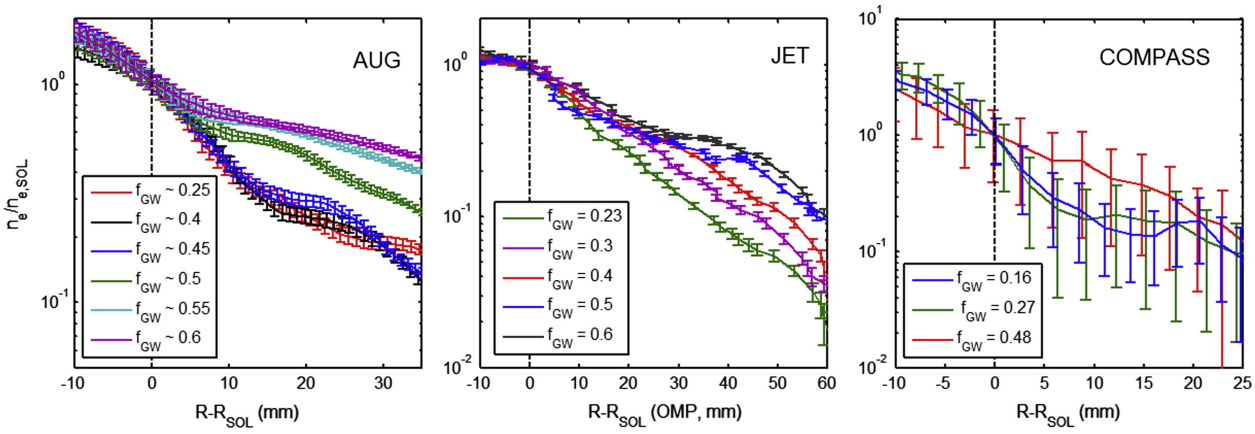

Figure 2.29: Density in the SOL vs. radial distance to the separatrix for the various levels of $f_{GW} = n_e/n_{GW}$. Profiles are normalized to their value at the separatrix, indicated as a dashed black line. AUG and JET profiles are measured by Li-beams, COMPASS profiles are measured by BPPs [199]

This region represents the boundary between the *near* and the *far* SOL with the shoulder causing a density broadening effect and outer divertor detachment. The near SOL is shifted close to the separatrix whereas the far SOL exhibits a density flattening effect. The distinction between both regions can be determined by the decay or e-folding length: short and long for the near and far SOL respectively [198]. The shoulder formation seems to be triggered by a non-linear threshold combining the Greenwald criterion [193] and the divertor collisionallity regime [196] which is not fully understood yet. In order to facilitate the comparison between multiple machines, SOL broadening transitions tend to be standardized by the Greenwald factor:

$$f_{GW} = \frac{\langle n_e \rangle}{n_{GW}} \tag{2.45}$$

Here $\langle n_e \rangle$ is the averaged electron density (core and edge) and n_{GW} corresponds to the Greenwald density limit. Density profiles analysis shown in Fig. 2.29 reported a correlation between shoulder formation, blob enlargement up to 5 cm on average, and values of $f_{GW} \simeq (0.5,\ 0.6)$ for AUG and JET [199]. Experiments in DIII-D [194] and JT-60U [200] reported the observation of shoulders for similar values with $f_{GW} \simeq (0.5,\ 0.55)$ respectively. However, COMPASS was only able to reach values of $f_{GW} \leqslant 0.48$ and a shoulder was not formed [199]. Nonetheless, recent probe measurements on COMPASS were undertaken during high density discharges in the order of $n_e \sim 10^{20}$ m^{-3} which suggested to be close to shoulder formation. Moreover, these studies appointed that the condition $\Lambda_{div} > 1$ [199, 201] is necessary for triggering shoulder formation.

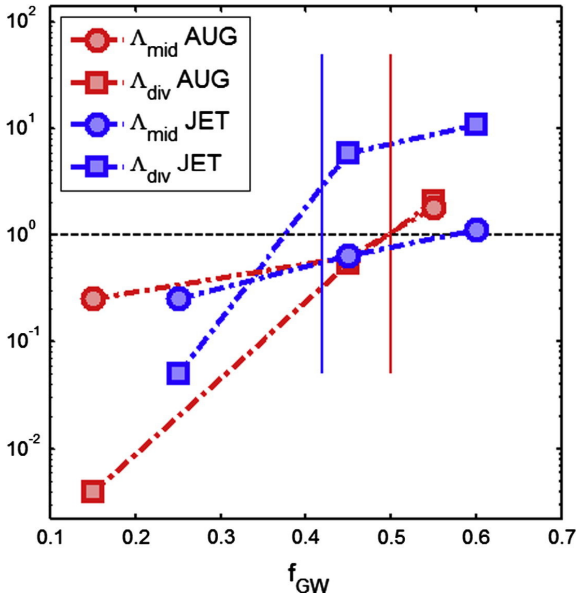

Figure 2.30: Effective collisionality parameter Λ for different f_{GW} values at AUG (red) and JET (blue). Circles/squares indicate Λ values at the midplane/divertor [199]

A diagram in Fig. 2.30 reveals the correlation between both (f_{GW}, Λ_{div}) parameters in AUG and JET. However, these trends have not yet been confirmed in COMPASS. This phenomena will be studied in detail in chapter 4 by statistically analysing blobs during shoulder formation in COMPASS discharges.

2.3 Edge-Localised Modes

This section is a review of edge-localised modes in tokamaks. The following sections focus specially on the phenomenon of plasma ejections that is extremely problematic for future reactors. The motivation of this review is to unveil the nature of ELM-precursors and the mechanism responsible for triggering these events.

2.3.1 Introduction to ELMs

An ELM is a quasi-periodic relaxation oscillation appearing in H-mode plasmas [202]. As discussed in section 2.1.4 on zonal flows, the formation of a transport barrier allows to improve the plasma confinement.

Zonal flows are responsible for the regulation of the turbulence at the edge due to shearing. However, the steepening of gradients at the pedestal tend to trigger instabilities. When surpassing a certain saturation limit, the stability is no longer sustained and catastrophic events occur. These events are manifested as violent ejections of filaments all over the chamber that rapidly arise in a few microseconds. These eruptions allow to relax the unstable regime at the expense of degrading the confinement, hence the transport barrier collapses. Nevertheless, the quasi-periodicity of these ejections suggests that the barrier relaxation and the ELM trigger correspond to the same mechanism. Note that ELMs are often mentioned in the literature to refer to the catastrophic event itself, also known as ELM crash. In fact these are edge fluctuations localised at the pedestal where the transport barrier is formed. These modes are closely related to MHD instabilities that end up by triggering these events. Because of their disruptive impact, ELMs were extensively studied in DIII-D [203] in order to understand its link to the L-H transition and the regulating effect of barriers. However these mechanisms are still not fully understood yet. The main advantage of ELMs is the release of impurities during the ejections. However, the main drawback is more critical as plasma bursts impact the walls and can severely damage the facing components. Giant ELMs (*i.e.* type-I ELMs) can not be tolerated in ITER [204]. Therefore research on this topic is one of the major challenges nowadays in fusion machines.

2.3.2 Observation of ELM filaments

ELM-filaments can be visualised by means of fast camera imaging. These frames are background subtracted in order to distinguish between the filaments and the vessel components. Three different phases for MAST plasmas, during L-mode, at the ELM crash, and during the inter-ELM period are compared in Fig. 2.31. Filaments tend to be attached to the geometry imposed by the magnetic field. Filaments motion is characterised by its continuous toroidal rotation always located in the vicinity of the separatrix. The intensity traces in function of the toroidal angle are also indicated. The magnitudes of light intensity from SOL filaments vary considerably depending on the regime. In contrast with the L-mode filaments that show certain intensity peaks, the inter-ELM regime shows a less active plasma with the lowest light intensity. The light emission of L-mode filaments is approximately twice that of the inter-ELM. At the ELM crash, filaments violently

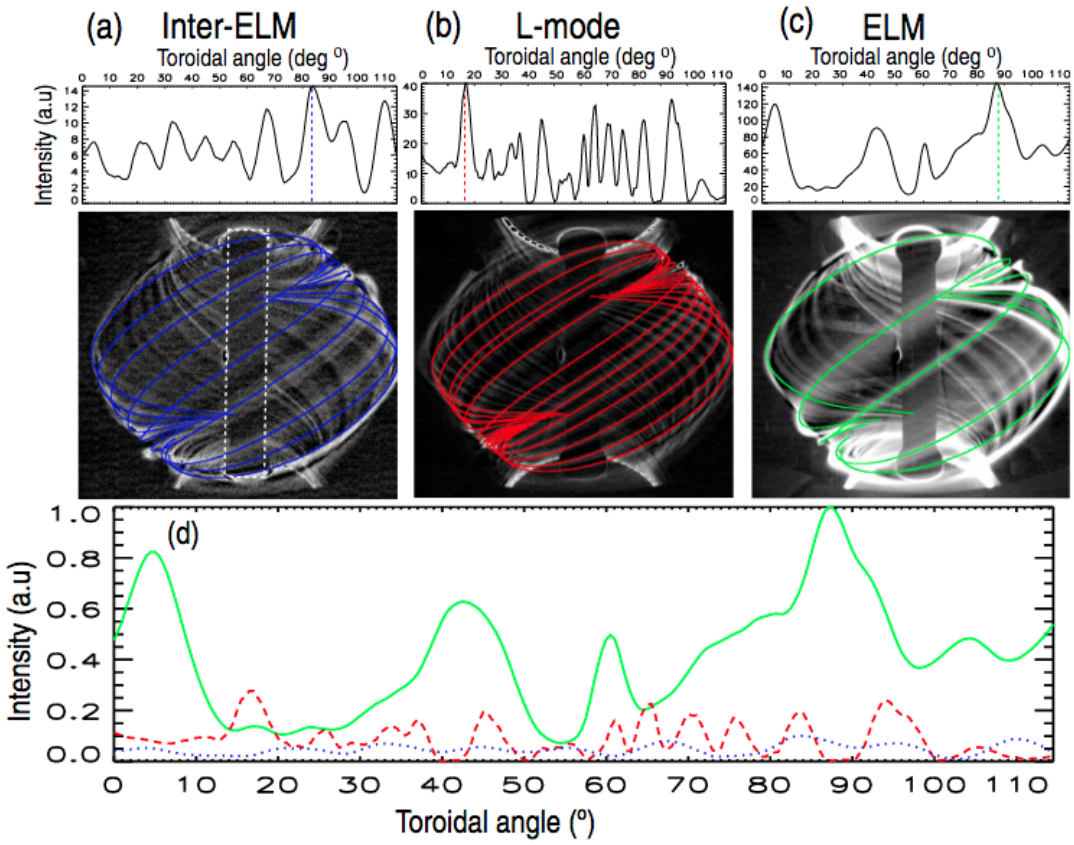

Figure 2.31: Intensity traces of mapped field lines as a function of the toroidal angle spanning the centre column for (a) inter-ELM, (b) L-mode and (c) ELM periods within the same discharge; detected filaments are subsequently projected on the corresponding full view camera images. In (d) the intensity traces are superposed normalized to the peak ELM intensity showing the contrast in measured intensities across the three phases [205]

appear with significant emission peaks spread irregularly among the toroidal locations. The ELM-filament intensity highly surpass the emission level from both L-mode and inter-ELM regimes. The structure and the collective motion of ELM filaments is more complex. During the explosive event, all individual filaments are largely uncorrelated from each other. In comparison with the inter-ELM phase and the L-mode filaments, the ELM filaments are not regularly spaced and their spacings are constantly changing. This irregularity is mainly due to the variation of the toroidal velocities during the ELM crash. From the average spacing between filaments, the toroidal mode numbers are inferred around $5 < n < 15$ [205].

2.3.3 Theory of ELMs: peeling-ballooning modes

Several models have theorised about the origin and mechanism of ELMs. Unfortunately, there is no definitive model being able to fully explain the ELM process. Theoretical approaches attempt to describe the MHD proprieties of the plasma edge region. However this task becomes difficult due to the computational limitations. The common approach is the study the stability of the edge pedestal profile parametrised by the perturbed energy equation [206]. This equation evaluates the plasma energy content in the presence of perturbations. The linearization of the Braginskii equations (chapter 1, section 1.3.4) around an equilibrium state, while assuming that resistivity is negligible (ideal MHD), allows for expressing all the variables (density, temperature, magnetic flux, velocity) as a function of the plasma displacement $\boldsymbol{\xi}$. We can then express the potential energy δW as a function of $\boldsymbol{\xi}$. The "energy principle" states that the plasma is stable if δW is positive for any displacement $\boldsymbol{\xi}$. δW is calculated as an integral over a plasma volume where destabilizing effects are present. δW is thus expressed as [206]:

$$\delta W = \frac{1}{2}\int \left(\frac{|\boldsymbol{B_{1,\perp}}|^2}{\mu_0} + \frac{|\boldsymbol{B_0}|^2}{\mu_0} \left|\boldsymbol{\nabla}\cdot\boldsymbol{\xi}_\perp + 2\boldsymbol{\xi}_\perp\cdot\boldsymbol{\kappa}\right|^2 + \gamma p_0 \left|\boldsymbol{\nabla}\cdot\boldsymbol{\xi}\right|^2 \right) dV$$
$$- \int \left(2(\boldsymbol{\xi}_\perp\cdot\boldsymbol{\nabla}p_0)(\boldsymbol{\kappa}\cdot\boldsymbol{\xi}_\perp) + j_{0,\parallel}\left(\boldsymbol{\xi}_\perp\times\frac{\boldsymbol{B_0}}{B_0}\right)\cdot\boldsymbol{B_{1,\perp}} \right) dV \quad (2.46)$$

Here, the subscript 0 refers to equilibrium quantities whereas the subscript 1 refers to perturbation quantities, $\boldsymbol{\kappa}$ is the curvature of the equilibrium magnetic field, $\gamma = 5/3$ is the adiabatic index, and $\boldsymbol{j}_\parallel$ is the parallel current density. The $\parallel$ and $\perp$ subscripts respectively designate the parallel and perpendicular components with respect to the equilibrium magnetic field B_0. In Eq. 2.46 the first integral corresponds to the stabilizing terms. The first term represents the energy associated with the bending of the magnetic field lines and it is the dominant term for the shear Alfvén wave. The second term represents the energy associated with the compression of the magnetic field and is dominant for the compressional Alfvén wave. The third term represents the energy associated with the compression of the plasma, it is the main source of energy for the sound wave. The second integral corresponds to the destabilizing terms of indefinite sign. The first term is proportional to $\boldsymbol{j}_\parallel$ and is associated with current-driven modes. The second term is proportional to the pressure gradient and is associated with pressure-driven modes. The interplay between both parameters (*i.e.* current and pressure gradient) allows to describe the ELM cycle represented in Fig. 2.32 into separated

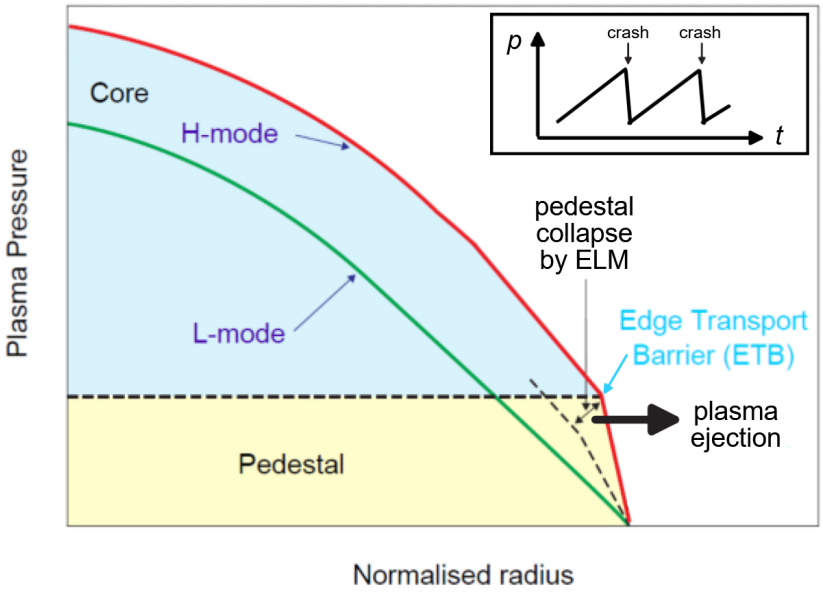

Figure 2.32: Schematics of pressure profile relaxation due to an ELM [207]

stages. First, a linear instability, where the edge pressure gradient ∇p (or p'_{ped}), increases until it surpasses a stability threshold. Second, after the threshold is reached a non-linear instability takes the lead and the mode grows explosively releasing heat and particles. This threshold corresponds to a MHD saturation limit. Limits can be identified in diagrams distinguishing stable and unstable areas depending on the edge currents and pressure gradients as in Fig. 2.33. Nonetheless the increasing edge pressure is not deleterious during the initial stage because it enables to sustain the H-mode, only until the limit is exceeded. Then the relaxation is triggered when releasing plasma allowing ∇p to decrease until stability is reached and starting a new ELM cycle. The poloidal shear flows keep maintaining the H-mode if it's strong enough through heating power consisting in a self-regulating process [202]. The MHD stability criterion is the critical ∇p for maintaining the transport barrier [208]. The first studies by Connor *et al.* [209] associated ELM bursts to "detonations" that could be explained by MHD ballooning instabilities, *i.e.* associated modes driven by pressure gradients. These detonations are similar to solar flares and magnetic substorms [210]. MHD models have been used to describe explosive events in astrophysical plasmas first associated with the Rayleigh-Taylor-Parker instability [211], then applied by Wilson and Cowley to tokamak plasmas associating bursts to ballooning instabilities [212]. DIII-D experiments shown a strong deviation from transport barrier width scalings with pressure in high triangularity [213]. Ideal ballooning models do not predict that the stability limit can be exceeded by

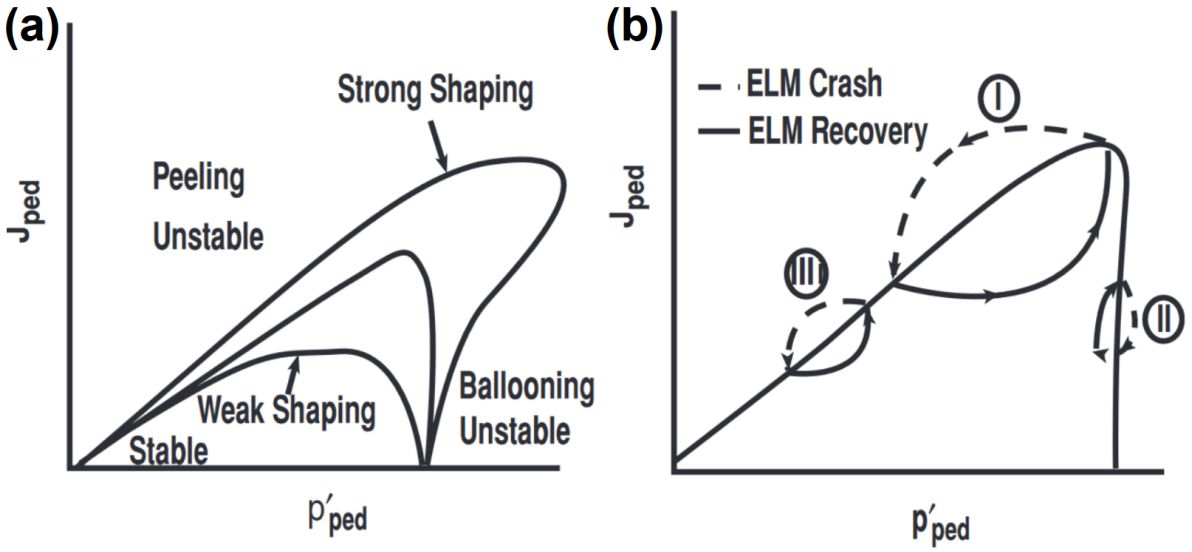

Figure 2.33: Schematic stability diagrams: (a) variation of pedestal stability boundaries with discharge shaping; (b) model of three types of ELM cycle [216].

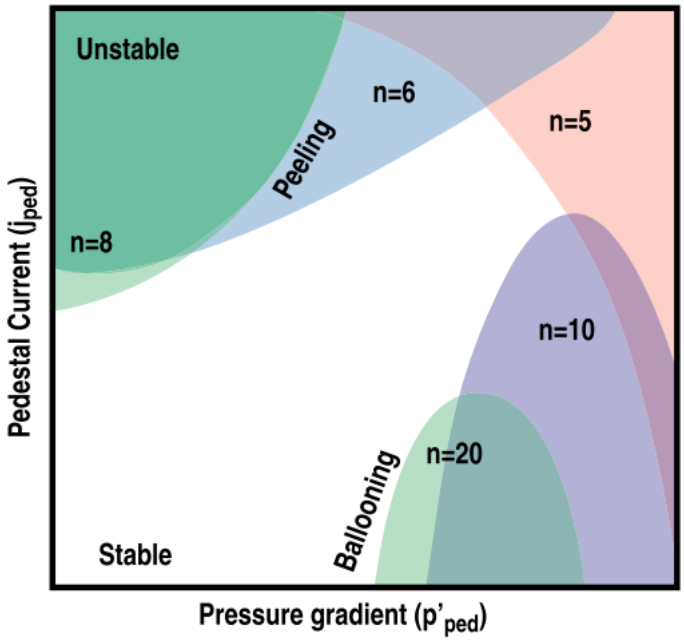

Figure 2.34: Stability diagram of H-mode pedestal with peeling and ballooning instabilities indicating the associated toroidal mode numbers n [202].

a substantial increase of edge pedestal current $\boldsymbol{j_{ped}}$ by a factor 2-3 [213, 214]. Neglected features by the ideal ballooning theory are the bootstrap current and the diamagnetic drift. The bootstrap current arises at the edge from sharp pressure gradient enhanced by the toroidal field causing an poloidal drift of electrons with velocity $\boldsymbol{v_\theta} = (\boldsymbol{\nabla} p \times \boldsymbol{B})/qB^2$. The model proposed by Snyder *et al.* [215] shown that the bootstrap current plays two relevant roles: reducing the edge magnetic shear stabilizing high n ballooning modes; and amplifying the drive to low-intermediate n external kink or peeling modes. This framework was tested with ELITE simulations which were in agreement with growth rates measured from DIII-D discharges [216]. Then the instability responsible for ELMs might consist in a coupling of peeling-ballooning modes with a vast range of mode numbers around $3 < n < 30$. A summarised stability diagram is illustrated in Fig. 2.34 for peeling-ballooning unstable areas with respective n numbers. Further investigation is required to demonstrate that the peeling-ballooning mechanism is universal. The non-linear saturation process generating ELMs is yet unclear and remains an active area of research.

2.3.4 Classification of ELMs

ELMs are phenomenologically classified in three main categories [217]. This classification was first established in DIII-D [218]. Type-I ELMs or "giant" ELMs usually correspond to ideal ballooning modes, their repetition frequency increases with the heating power. They are associated with isolated sharp peaks of D_α line emissions. These are a signature of photons emission from the ionisation of deuterium (D^0) neutrals. This high peak is due to deposited layers of deuterium on walls that significantly emit during an ELM burst. Type-II ELMs are often mentioned as "grassy" ELMs being characterised by a low amplitude as part of the L-H transition triggered by a strong edge pressure gradient and appear in the diagram in a second stability region [219]. Type-III ELMs are resistive ballooning modes coupled with peeling modes, their repetition frequency decreases with the heating power. The difference is that type-I ELMs seem to occur as highly turbulent phenomena whereas type-III ELMs are less explosive but repetitive. In other terms, type-I ELMs would not be tolerated in operational reactors whereas type-III can be managed. The difference between type-I and type-III ELMs is shown in Fig. 2.35 during the same discharge. Type-I ELMs were firstly detected

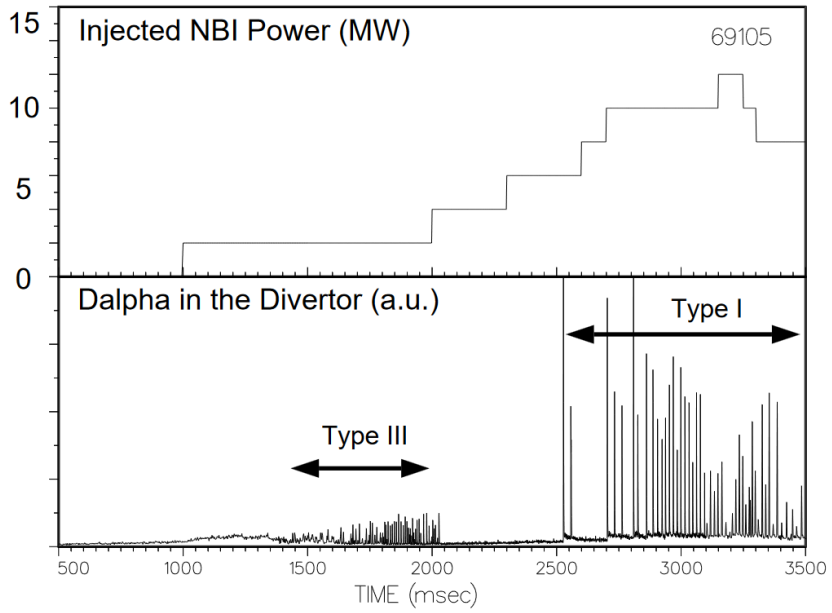

Figure 2.35: Typical sequence of ELMs during a power rise in DIII-D, with type-III ELMs (at low heating power) and type-I ELMs (at high heating power) [217]

in large size machines such as DIII-D [218] and ASDEX-Upgrade [217] then JET [220]. Type-III ELMs were seen in both big [217, 218] and small tokamaks such as COMPASS [221], TCV [222] and Alcator-Cmod [223]. However for these cases type-I ELMs were not observed in ASDEX before the upgrade. These differences were first explained due to a lack of diagnostics and to machines conditions when studies were undertaken: tokamaks have different size and heating power which determine how strong the temperature gradient ∇T would affect the stability at the edge [224]. This was taken as evidence showing that an ideal ballooning instability model was not enough to explain ELM transport. A different category corresponds to dythering cycles which do not relate to MHD instabilities, these phenomena are described as fast L-H-L sequences. "Dythering" refers to the sporadic character of the transition threshold between L- and H-mode.

2.3.5 ELM mitigation techniques

ELM mitigation techniques have the aim in contributing with additional transport through the pedestal in order to maintain the barrier and avoid the saturation limit. The mitigation, specially the supression, is

essential for ITER in order to avoid the most problematic ELMs. The ELM suppression can be achieved by using Resonant Magnetic Perturbations (RMPs) delivered by coils that were first demonstrated in DIII-D [225]. Unfortunately this technique is limited in the case of high collisionality *i.e.* at high density operations. A different method consists in voluntary triggering ELMs in advance by the injection of cryogenic deuterium pellets [226]. The use of pellets increases the frequency of ELMs but reduces its amplitude while keeping the transport barrier. Additionally, changes on the divertor configuration also seem to have an impact on ELM bursts appearances: the corresponding divertor upgrade on JET [227, 228] passed from the production of stable type-III ELMs to ELM-free periods limited by type-I ELMs. The position of the X-point regarding the target could explain how heat diffusion is correlated to the responsible MHD instabilities. As seen in TCV [217, 222] the orientation of the $\boldsymbol{\nabla} B$ gradient towards the X-point enables the reduction of the $\boldsymbol{B} \times \boldsymbol{\nabla} B$ drift therefore explaining the ELM-free regime. Recent simulation in AUG predict that low triangularity plasmas can avoid type-I ELMs by shrinking the SOL and obtaining only small ELMs [229].

2.3.6 Challenges: inter-ELM fluctuations and ELM-precursors

Fluctuations have been detected prior the onset time of an ELM crash. These oscillations are known as inter-ELM fluctuations. The contribution of the bootstrap current to the poloidal transport would be responsible for the evolution of inter-ELM fluctuations. The bootstrap current arises at the edge from sharp pressure gradients enhanced by the toroidal field causing an poloidal drift of electrons with a characteristic velocity $\boldsymbol{v_\theta} = (\boldsymbol{\nabla} p \times \boldsymbol{B})/qB^2$. This current also show multiple dependencies with plasma collisionallity ν^*, aspect ratio ε, and proportional to $\boldsymbol{\nabla} T$ and $\boldsymbol{\nabla} n$ specially when ions and electrons transports tend to evolve in separated timescales [230]. A more extended review of several machines has been recently published by Laggner *et al.* [231]. Three different categories of inter-ELM pedestal fluctuations were proposed and can be interpreted by the radial force balance (Eq. 2.26). Each category is enclosed inside a frequency range. The first category appears between 30 kHz to 150 kHz known as "washboard" modes, localized close to the separatrix, with $n \sim 3-8$. The second category appears at higher frequencies than ≥ 200 kHz, localized close to the $v_{E\times B}$ minimum, with $n \sim 8-12$. The third category appears at low frequencies ≤ 30 kHz, localized

Tokamak	Diagnostic	Frequency (kHz)	Toroidal mode number	References
JET	Magnetics	5 - 25	1 - 13	[220]
AUG	2D ECE	20 - 50	28 ± 7	[232]
NSTX	GPI & Magnetics	20	5 - 10	[233]
MAST	BES	20	30 - 40	[234]
KSTAR	2D ECE	20 - 50	6	[235]
JT-60U	ECE	5	6 - 17	[236]
TCV	Magnetics	-	1	[237]

Table 2.2: Table of characteristic parameters of ELM-precursors

at the pedestal top close to the $v_{E\times B}$ zero crossing, with $n \sim 13 - 14$. This last category is identified as the ELM-precursor and plays a role in the ejection of plasmas. A precursor activity refers to fast transient fluctuations prior to an ELM release and located in the pedestal region. These fluctuations start generally appear around ~ 200 μs before the ELM crash. Experiments in different tokamaks have localized this mode at the top of the pedestal, with a characteristic frequency of ~ 20 kHz but with discrepancies concerning the toroidal mode number. The Table 2.2 summarises the main findings on ELM-precursors. The origin of these fluctuations is still not understood and represents a challenge in the research area on ELMs. On MAST ELM-precursors were inferred by Scannell *et al.* [238] using fast camera and interferometry diagnostics in relatively shorter periods of $100 - 200$ μs before an ELM as shown in Fig. 2.36. These were described as periodic excursions manifested as peaks or large fluctuations of $\simeq 20-30$ μs each in density profiles before the D_α peak as a reference of the ELM protrusion. On camera frames the formation of filaments were visualised ~ 50 μs before the ELM burst. Further research on MAST by Kirk *et al.* [234] analysed precursors using the Beam Emission Spectroscopy (BES) diagnostic as shown in Fig. 2.37. ELM-precursors were characterised with a frequency of ~ 20 kHz, appearing 100 μs before the ELM, with a poloidal wavelength of ~ 10 cm, and a radial size of ~ 2 cm. However, further investigations by Dunai *et al.* on MAST were not published. Regarding other tokamaks, the disparity between ELM-precursors' parameters among different machines leaves open questions. Note that the experiments in MAST gave measurements of high toroidal numbers

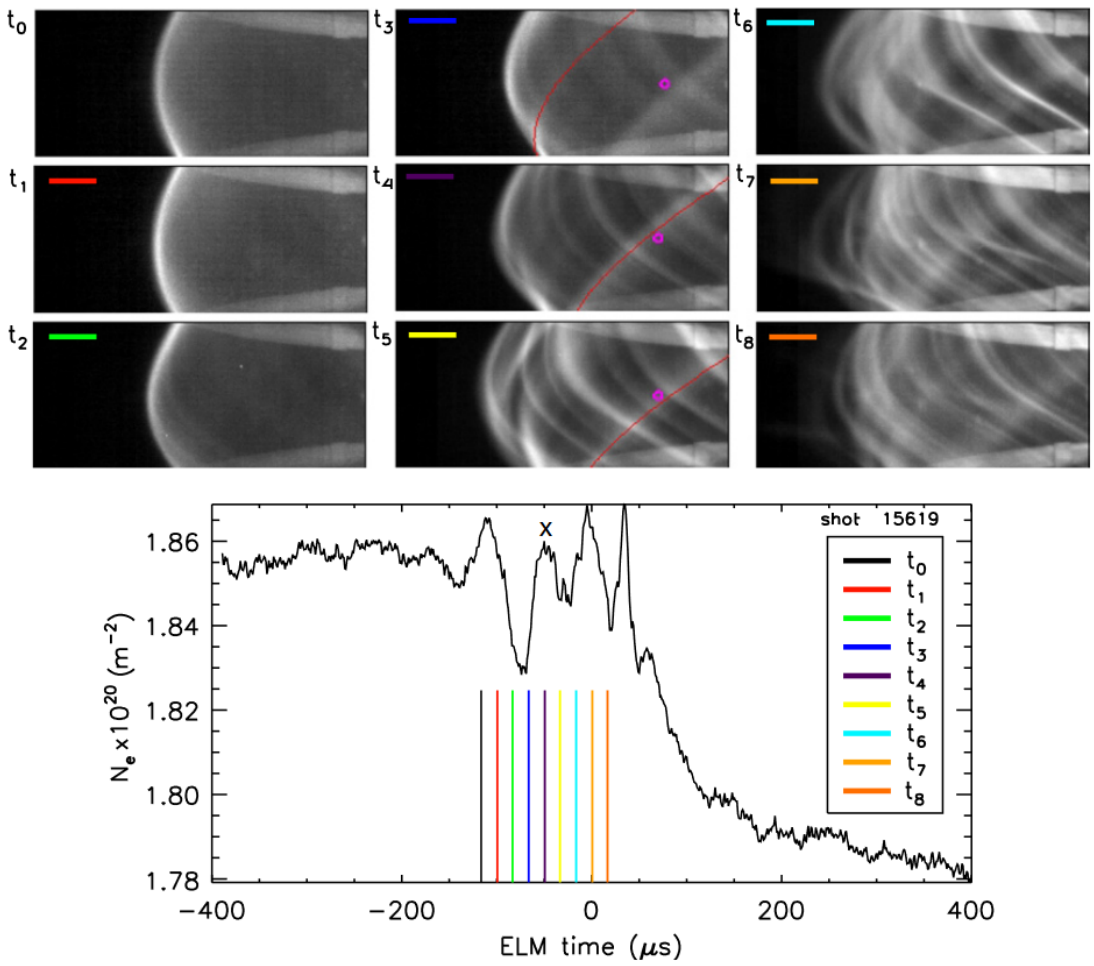

Figure 2.36: MAST shot #15619. ELM-filaments observed by a Photron camera with a frame time of 16 μs and 10 μs integration time. The line integral density is measured by the interferometer. The intersection of the line of sight with the foreground LCFS is indicated as a circle on frames at t_3, t_4 and t_5 [238]

$n \sim 30 - 40$ [234] in contrast with the results in NSTX such as $n \sim 5 - 10$ [233]. Chapter 5 is dedicated to interpreting the BES images and tomographic inverted frames in order to confirm the precursors dynamics. Several studies have undertaken Morlet wavelet analysis in order to extract the spectral properties of ELM-precursors in different tokamaks. At JET [239] magnetic fluctuations were observed by Mirnov coils before an ELM. The computed wavelet spectrum in Fig. 2.38 (c) highlighted significant spectral energy bands associated with coherent modes a few ms before the ELM crash at frequencies $f \sim 20$ kHz corresponding to toroidal mode numbers $n \sim 8$. It was noticed that the frequency of the precursor could decrease from 20 to 18 kHz before the ELM. A different spectral line at frequencies $f \sim 15$ kHz during the inter-ELM

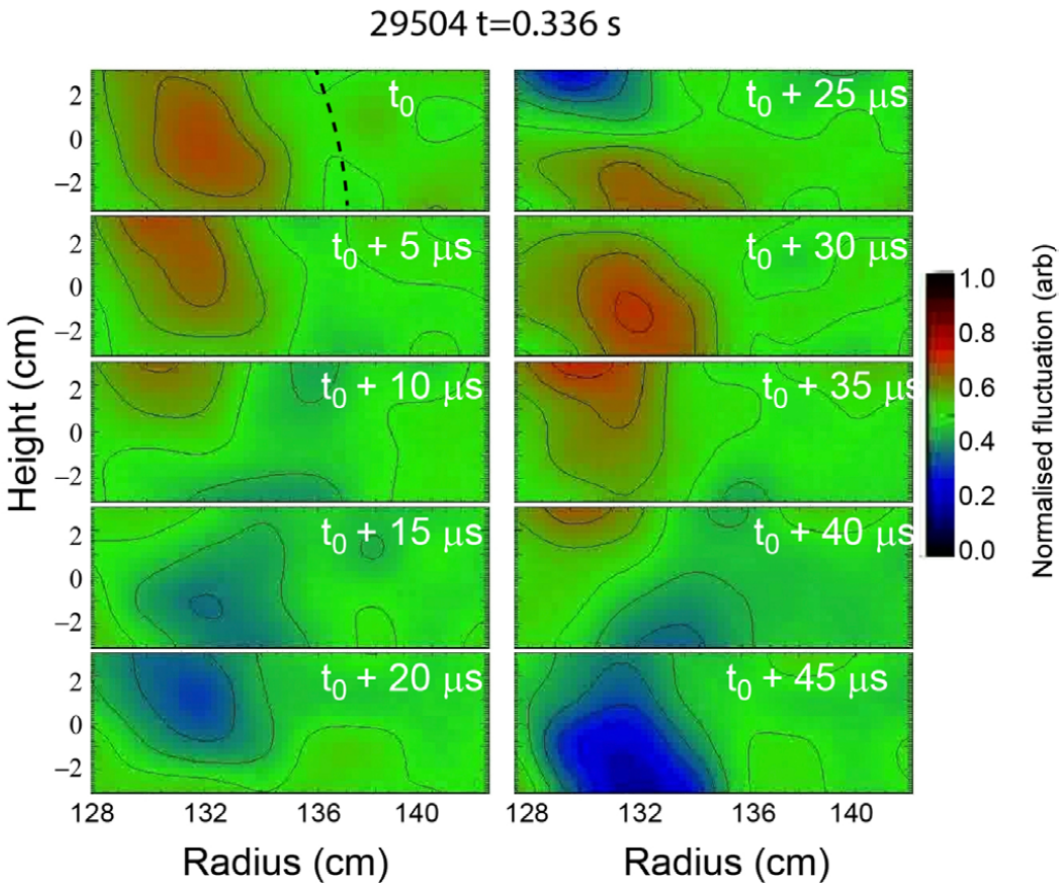

Figure 2.37: Turbulence imaging of the plasma edge using a BES system on MAST discharge #29504. The images show the normalized density fluctuations for frames separated in time by 5 μs relative to a notional time $t_0 \sim 100$ μs before the ELM crash. The dotted curve in the first frame shows the LFCS location [234]

period was identified as a sawtooth precursor. In comparison with the precursors, the dark areas during the ELMs crash (associated with higher emission) cover the lower frequencies $f \leq 15$ kHz with toroidal numbers around $n \sim 1-2$. Additionally, a bispectral analysis was employed in order to quantify the coupling of non-linear interactions between different frequency modes during the ELM trigger. The bispectrum identifies the spectral components at frequencies ω, ω_1 and ω_2 of non-linear modes satisfying the three-wave coupling condition $\omega = \omega_1 + \omega_2$. As shown in Fig. 2.39 (a) the area of highest amplitude in the bispectrum (during the precursor's lifetime) corresponds to the interactions at $\omega_1/2\pi \sim 20$ kHz and $\omega_2/2\pi < 5$ kHz. A less significant spectral area correspond to the interaction between $(\omega_1/2\pi, \omega_2/2\pi) \sim (20, 20)$ kHz. Closer to the ELM crash, these spectral features disappear leading to interactions in the low frequencies at $(\omega_1/2\pi, \omega_2/2\pi) \leq (5, 5)$

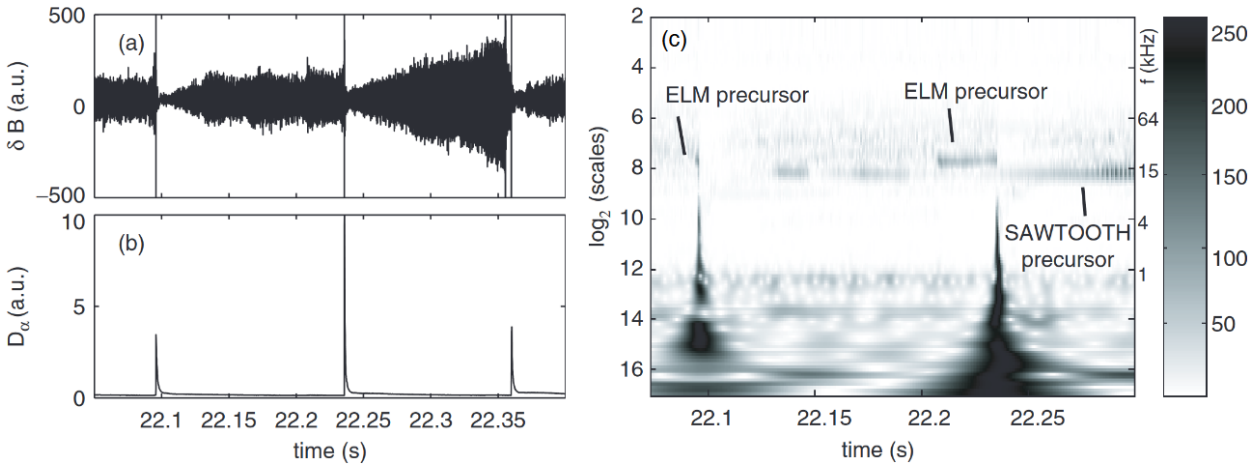

Figure 2.38: JET pulse #53062: (a) magnetic fluctuations measured by an outer edge Mirnov coil; (b) D_α emission measured in the outer divertor; (c) wavelet spectrum of the Mirnov coil signal indicating ELM-precursor activity ($f \sim 20$ kHz) before 2 ELMs at $t \sim 22.10$ s and $t \sim 22.23$ s [239]

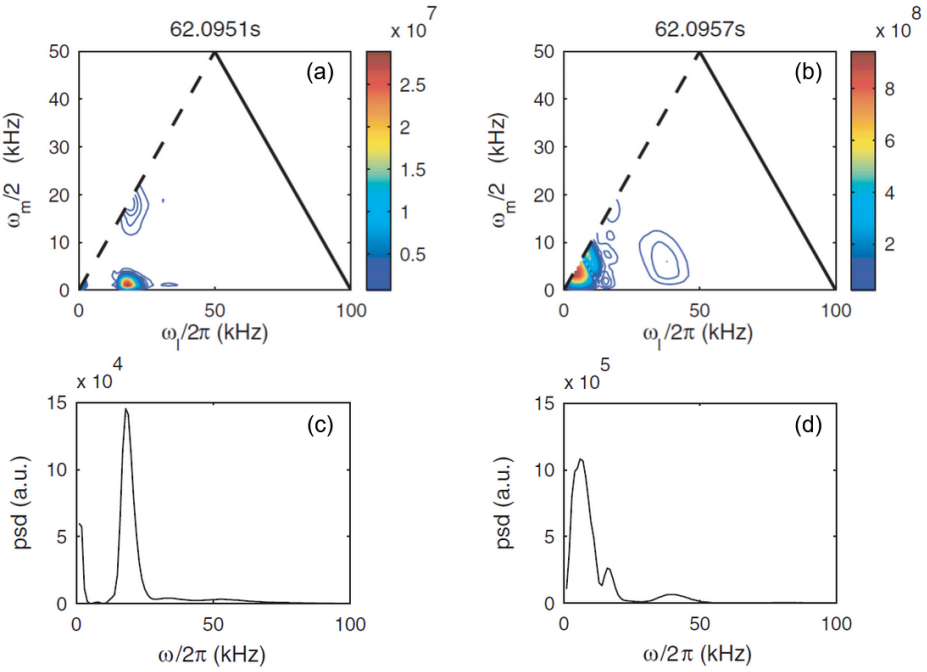

Figure 2.39: JET shot #53062: bispectra and power spectral density of magnetic perturbations at 800 μs before the ELM with a non-linear coupling at $(\omega_1/2\pi, \omega_2/2\pi) \sim (20, 2)$ kHz (a & c), and 200 μs before the ELM with a non-linear coupling at $(\omega_1/2\pi, \omega_2/2\pi) \leq (5, 5)$ kHz (b & d) [239]

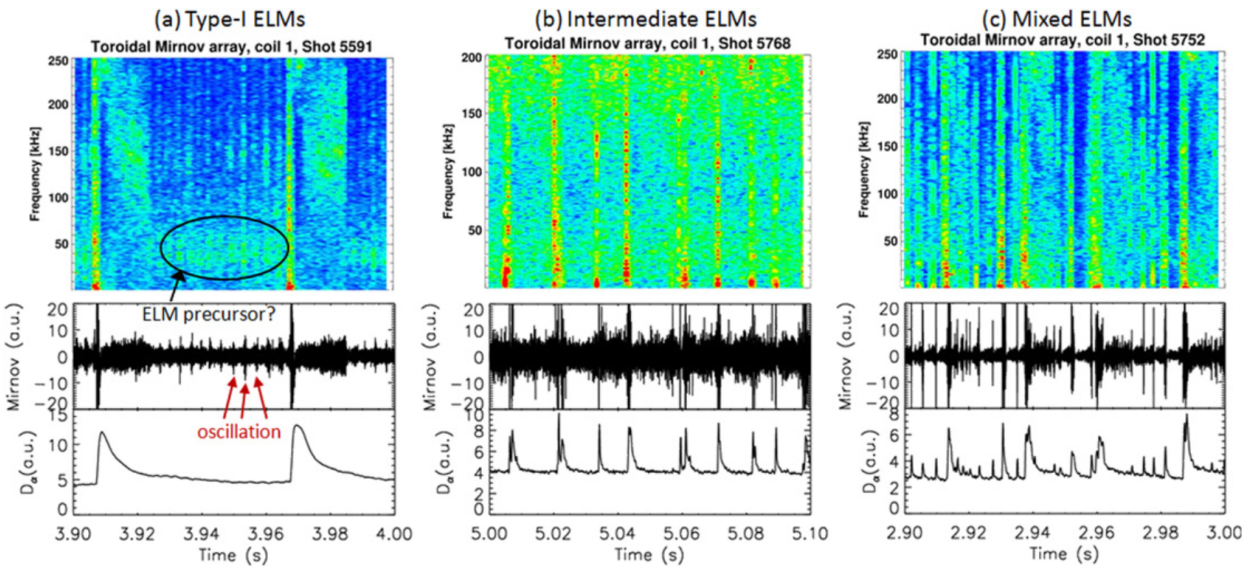

Figure 2.40: KSTAR: Wavelet analysis of toroidal Mirnov signals plus line integrated D_α emission signals for: (a) type-I ELMs indicating an encircled area at $f \sim 25 - 50$ kHz for a potential ELM-precursor (shot #5591); (b) intermediate ELMs (shot #5768); (c) mixed ELMs (shot #5752) [240]

kHz and a secondary component at $(\omega_1/2\pi, \omega_2/2\pi) \sim (40, 5)$ kHz as shown in Fig. 2.39 (b). It was deduced that the dominant interaction with the highest spectral density corresponds to the ELM-precursor with lower frequency modes. Lower spectral density areas are associated with the higher harmonics of that interaction. At KSTAR [240] Mirnov coil signals detected intermittent fluctuations related to different ELM regimes. The wavelet spectra for type-I ELMs in Fig. 2.40 (a) revealed an increased spectral energy signature in the band $f \sim 25 - 50$ kHz for a period of $40 - 50$ ms before the ELM. These modes coexist with low frequency oscillations at $f \sim 300 - 400$ Hz during the inter-ELM period. Several oscillations in the magnetic signal correspond to rapid peaks appearing at the range $f \sim 100 - 150$ kHz on the spectrum. The intermediate ELMs (possible type-III ELMs) and mixed ELMs (type-I and small ELM peaks) spectra portray a less clear picture without precursor activity but covering all frequencies. At NSTX [233] Gas-Puffing Imaging (GPI) measurements (see Fig. 2.41 (a)) made during RF-heated H-mode plasmas reported strong edge intensity fluctuations before ELM events. High spectral power was observed at $f \sim 20$ kHz coexisting with modes at $f \sim 5$ kHz as shown in Fig. 2.41 (b). The corresponding wavenumbers were found between $k_\perp \sim 0.05 - 0.21$ cm^{-1} (*i.e.* $\lambda \sim 30 - 126$ cm) and phase velocities of $v \sim 13$ km / s. These intensity fluctuations (Fig. 2.41

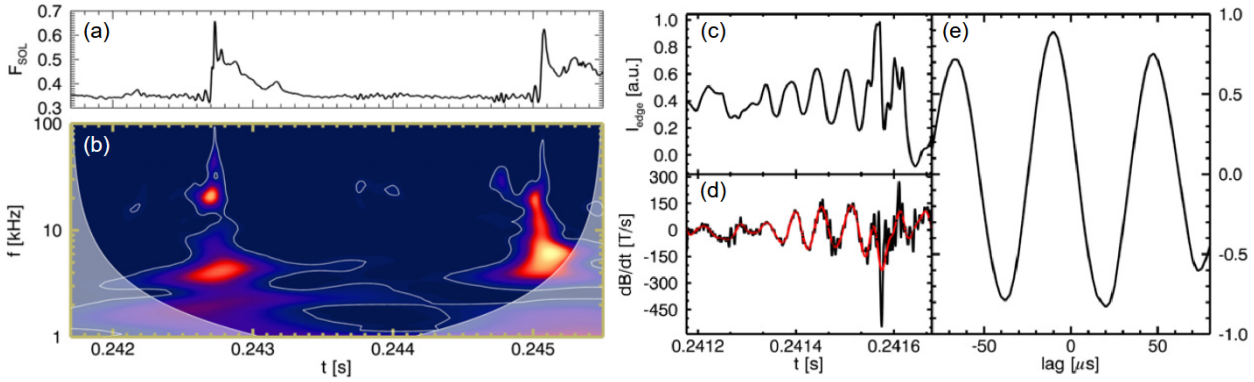

Figure 2.41: NSTX shot #141919: (a) time trace of the SOL fraction intensity F_{SOL} from the GPI system; (b) wavelet spectrum of integrated edge intensity I_{edge} with highlighted spots at $f \sim 5$ kHz and $f \sim 20$ kHz (the grey area corresponds to edge boundary effects, the contour cone line is the 95% significance level). NSTX shot #141917: time traces of (c) I_{edge} and (d) low-pass filtered magnetic signals at 200 kHz (the red trace is bandpass filtered at 20 kHz); (e) correlation coefficient between I_{edge} and magnetic signals [233].

(c)) were also strongly correlated with magnetic coil data (Fig. 2.41 (d)) as seen in Fig. 2.41 (e). From the magnetic fluctuations the calculated toroidal mode numbers correspond to low values around $n \sim 5-10$. At AUG [232] a velocimetry technique was employed on electron temperature fluctuations measured by a 2D Electron Cyclotron Emission Imaging (ECEI) system. Two types of fluctuations were distinguished during the inter-ELM period of type-I ELMs: first, ELM-precursors appearing 2 ms before the ELM crash (defined as shown in Fig 2.42 (a)); second, ELM-triggers appearing 200 μs before the ELM crash. Off-midplane electron temperature fluctuations appear in the wavelet spectra in the frequency range of $f \sim 20-40$ kHz as shown in Fig. 2.42 (b). Cross-correlation wavelet spectra reported poloidal mode numbers of $m = 112 \pm 12$ and toroidal mode numbers of $n = 28 \pm 7$. These values correspond to a structure characterised by poloidal wavelengths of $\lambda_\theta = 10$ cm and phase velocities of $v = 2$ km / s. The main change between the off-midplane fluctuations and the ELM trigger is the increase of bicoherence. The bicoherence is a normalised bispectrum which measures the phase coupling of non-linear modes. Higher integrated bicoherence was reported (Fig. 2.42 (c)) which indicates intensified nonlinear activity. In bicoherence plots (Figs. 2.42 (d) and (e)), the following spots are respectively associated with particular coupling: (A) indicates the coupling of off-midplane fluctuation at $f_2 = -25$ kHz with its second harmonic $f_1 \sim 50$ kHz; (B) indicates the

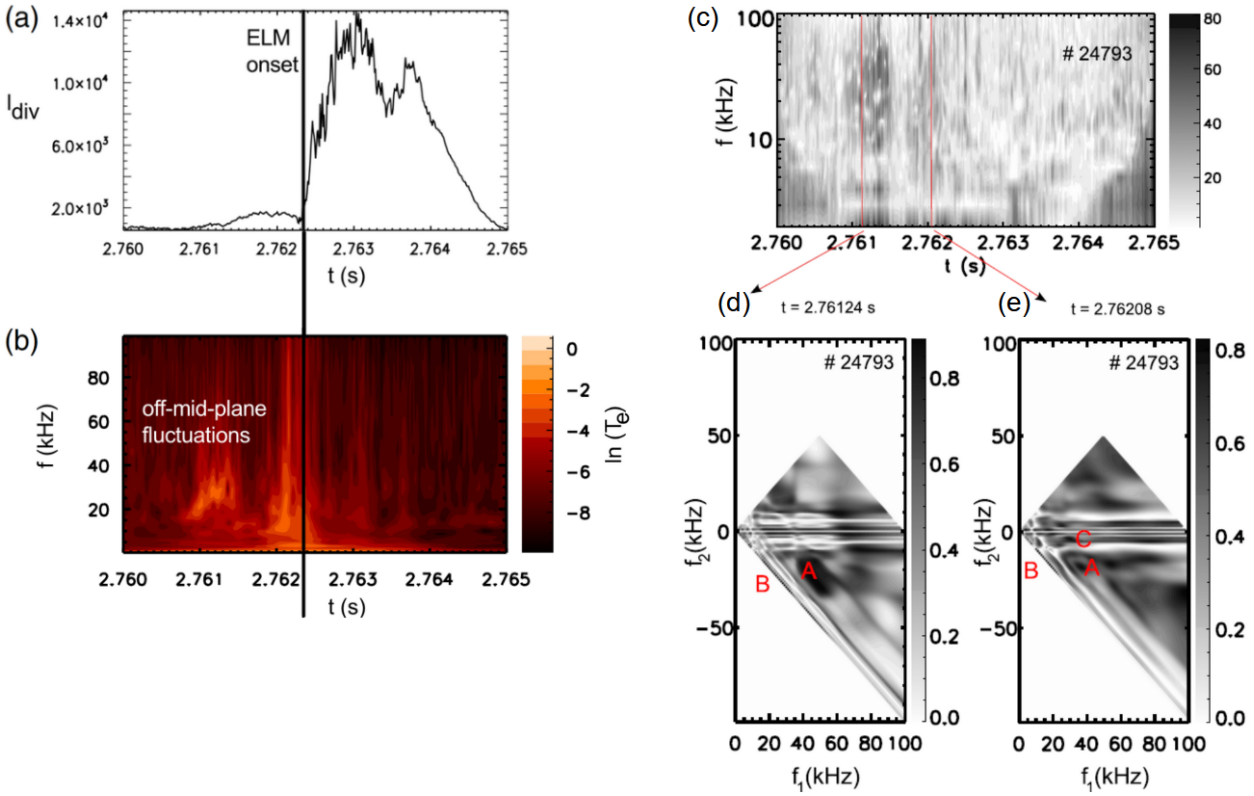

Figure 2.42: AUG shot #24793: Divertor current with peak foot definying the ELM onset time; (b) wavelet spectrum of electron temperature fluctuations (arbitrary logarithmic intensity scale), indicating off-midplane fluctuations at $f \sim 20 - 40$ kHz plus the ELM trigger covering all frequencies; (c) integrated bicoherence of electron temperature fluctuations; (d) bicoherence during the off-midplane fluctuations and (e) bicoherence at the ELM onset with C indicating a strong coupling between $f_1 \sim 20$ kHz and $f_2 \sim 5$ kHz modes [232]

coupling of all frequencies with a sheared (zonal) flow at $f_2 = \pm 1$ kHz. Additionally at the ELM trigger in Fig. 2.42 (e), it is noticed the strong coupling of the $f_1 \sim 20$ kHz mode with the $f_2 \sim 5$ kHz mode indicated by the spot (C). It was speculated that a transfer of energy from a 20 kHz (tearing-like) mode to a 5 kHz (ballooning-like) can lead to the trigger instability causing the ELM burst with fluctuations appearing on all scales. Note that both AUG and JET bicoherence analysis results in the same coupling frequencies of 20 kHz and 5 kHz prior to the ELM crash (*e.g.* Fig. 2.39). Other similarities between these tokamaks include a range of toroidal mode numbers around $n \sim 1 - 30$, wavelengths of $\lambda \sim 10 - 100$ cm and velocities of $v \sim 1 - 10$ km / s. The application of wavelet transforms to MAST data will be tested in chapter 6.

Chapter 3

Diagnostics and methods review

3.1 Introduction

A preliminary section presents the technical specifications of COMPASS and MAST. A review of probe theory serves as an introduction for the measurements of the edge plasma in COMPASS. The Beam Emission Spectroscopy (BES) and the fast camera in MAST are described as the experimental setup used in the imaging analysis. The OMAHA coil is presented for complementing the spectral analysis with the BES. Additionally, the principles of the analysis methods are explained in detailed. These techniques are the blob detection algorithm, the Elzar code and the wavelet transform.

3.2 Tokamaks

3.2.1 COMPASS

COMPASS (Compact Assembly) was a tokamak located at the Institute of Plasma Physics of the Czech Academy of Sciences (*a.k.a.* IPP Prague) that operated from 2009 to 2021. It was originally conceived

during the 1980s at the UKAEA Culham Centre for Fusion Energy. It started its operations in 1989 with only C-shaped plasmas. It was upgraded in 1992 under the name of COMPASS-D referring to the D-shaped plasma in the divertor configuration. Its purpose was the study of MHD physics and shape control with error field corrections. However, the rising interest for spherical tokamaks pushed towards the development of the MAST tokamak. Due to the lack of human and hardware resources for both projects, the UKAEA decided to suspend the COMPASS-D program in 2001. In 2004 the UKAEA offered COMPASS-D to the IPP Prague in agreement with Euroatom. In 2006 the IPP Prague decommissioned the CASTOR tokamak and COMPASS-D was transported to the Czech Republic for its installation. The commissioning of the new COMPASS was focused on enhancing the technical specifications and equipping diagnostics to assist the machine in preparation for predicting scaling laws of ITER physics [241]. The COMPASS design was conceived to be a small-size tight aspect ratio tokamak with an ITER-like geometry at a scale of 1 / 10th of its size which had the aim of achieving H-mode with observable type-I ELMs. The main COMPASS parameters are shown in Table 3.1. The name of COMPASS is simplified dropping the D because of its ability to adopt different plasma shapes. The scientific program was mainly focused on the study of edge stability, SOL and ELM physics, plasma-wall interactions, runaway electrons, and disruptions. After the re-installation phase the first plasma took place in December 2008 [242]. A period of operation testing of 3 years was dedicated to the final commissioning of diagnostic systems. The set of installed instruments are presented in Fig. 3.1. The Thomson Scattering (TS) system and the Beam Emission Spectroscopy (BES) system (using a Lithium beam) measured the electron temperature and density profiles. The Atomic Beam Probe (APB) operated as an extension of the BES system by collecting lithium ions that give an information on the edge current profile. The radiometer, based on Electron Cyclotron Emission (ECE) or Electron Bernstein Waves (EBW), the interferometer and the reflectometer gave additional measurements of the temperature and density. The bolometer, Soft X-Ray (SXR), and Visible light (VIS) detectors were used for the tomographic reconstruction of emissivity profiles. Two cameras are located at the midplane and at the divertor for monitoring the overall plasma emission in the chamber, plus two fast Photron cameras for tracking SOL filaments. More than 440 magnetic coils in total were installed, such as Mirnov and Rogoswki coils shown in Fig. 3.2, as well as saddle coils for resonant magnetic perturbations in order to migitate

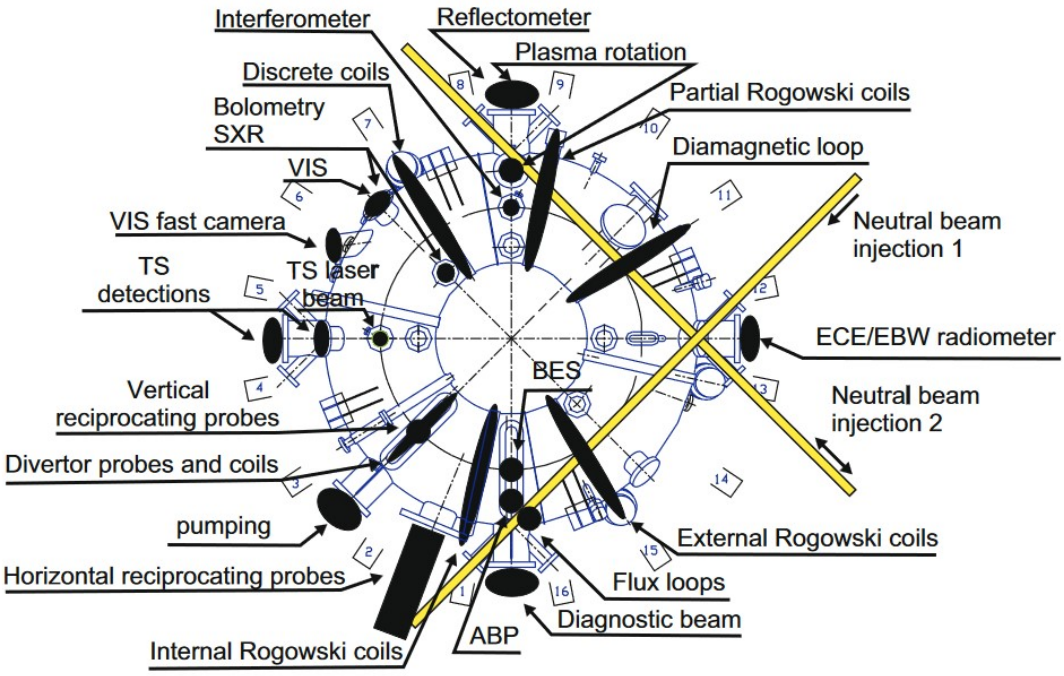

Figure 3.1: Top down view schematics of COMPASS diagnostics [242]

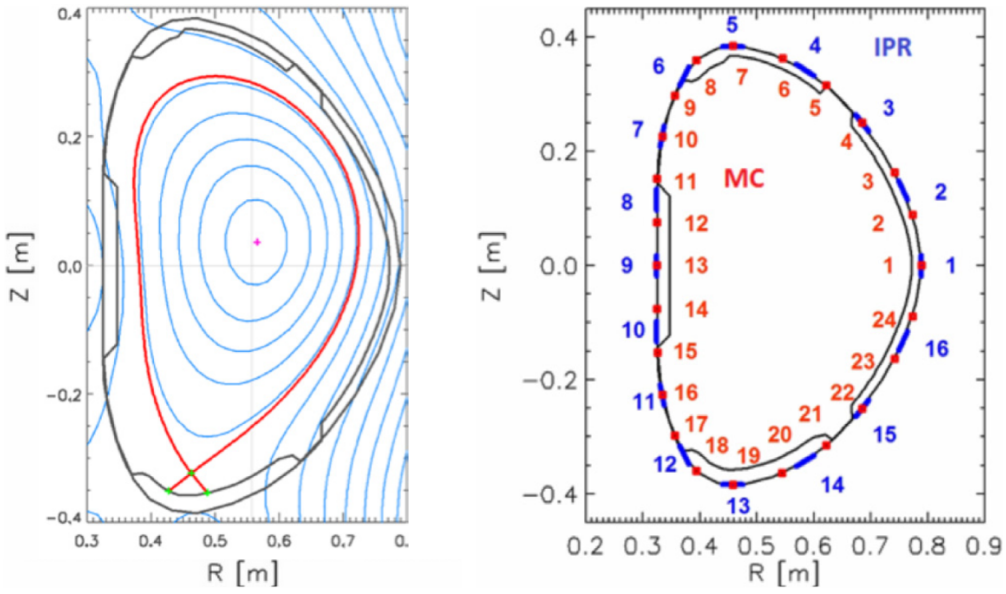

Figure 3.2: Cross-sections of the COMPASS chamber; (left) plasma cross-section by EFIT reconstruction; (right) poloidal positions of magnetic diagnostics sensors: red-Mirnov coils (MC), blue-internal partial Rogowski (IPR) coils [243]

Parameters	Values
Major radius R	0.56 m
Minor radius a	0.23 m
Plasma current I_p (max)	400 kA
Magnetic field B_T (max)	$0.9 - 2.1$ T
Vacuum pressure	1×10^{-6} Pa
Elongation	1.8
Plasma shapes	C, D, Single-Null Diverted (SND), Elongated
Pulse length	~ 1 s
Beam heating power P_{NBI} (40 keV)	2 x 0.4 MW

Table 3.1: Table of characteristic parameters of COMPASS [244]

ELMs. Two reciprocating manipulators, one horizontal at the midplane and one vertical from the top, can use diverse types of probes on the head to measure plasma edge potential fluctuations. A set of divertor probes are also embedded in the divertor tiles to analyse the temperature and density in that region. Some of these different types of probes will be introduced in later sections. Two injectors of Hydrogen were installed being part of the Neutral Beam Injection (NBI) heating system. In 2012 H-mode plasmas in COMPASS, including type-I ELMs in single null X-point configuration, were successfully achieved with the support of the NBI system, in contrast with the H-mode plasmas in COMPASS-D only assisted by Ohmic Heating (OH) [243]. The comparison between both scenarios (*i.e.* OH and NBI) is shown in the D_α emission signal (*i.e.* type-III and type-I ELMs respectively) in Fig. 3.3. COMPASS continued its campaigns being part of a few operating tokamaks in Europe during that time along with JET and AUG. In August 2021 it was shut down for its disassembly in view of the preparations for the new COMPASS-U (Upgrade) tokamak. COMPASS-U will be a medium-size tokamak, with $R = 0.894$ m and $a = 0.27$ m, with the aim of supporting the operations of ITER as well as of addressing the design challenges of DEMO. New milestones are expected from exploring new confinement regimes incorporating more enhancements. These constitute coils producing a high magnetic field of 5 T, a central solenoid producing a plasma current of 2 MA, and a large chamber

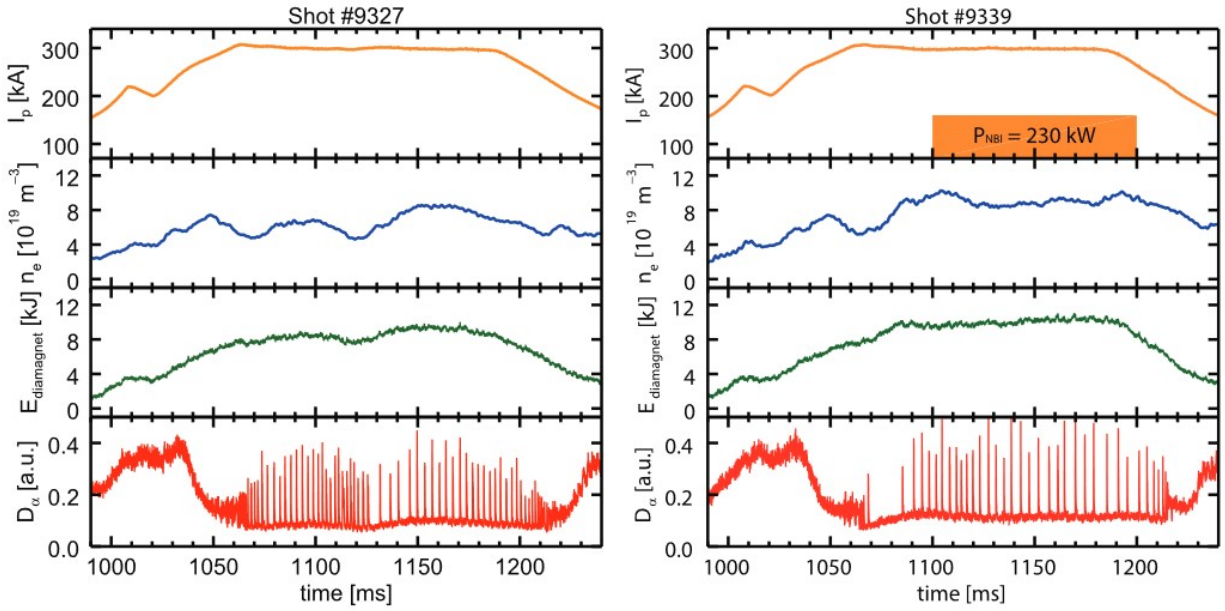

Figure 3.3: COMPASS discharge characteristics with plasma current I_p, line averaged density n_e, total stored plasma energy $E_{diamagnet}$ measured by the diamagnetic coils, and line integrated D_α emission as a function of time; (left) shot #9327, ohmic H-mode with type-III ELMs; (right) shot #9339, NBI assisted H-mode with type-I ELMs [243]

size containing densities close to $n \sim 10^{20}$ m^{-3}. Further optimisations include: a closed divertor with several plasma shapes (SND, DND, snowflake); enhanced power supplies with NBI power of $\sim 3-4$ MW plus two diagnostic beams at 0.5 MW, and ECRH providing 1 MW of heating power; and PFCs coated with inconel and tungsten [245]. COMPASS-U will start its operations in 2023.

3.2.2 MAST

MAST (Mega Amp Spherical Tokamak) was a tokamak located at the Culham Centre for Fusion Energy (CCFE), managed by the United Kingdom Atomic Energy Authority (UKAEA), and operated from 1999 to 2013. It was conceived to become the successor of START (Small Tight Aspect Ratio Tokamak) [246] that operated during the 1990s being pioneer on the design of the spherical conception. The Spherical Tokamak (ST) was proposed in 1986 by Peng and Strickler [247] in order to build a low-budget but high-performing

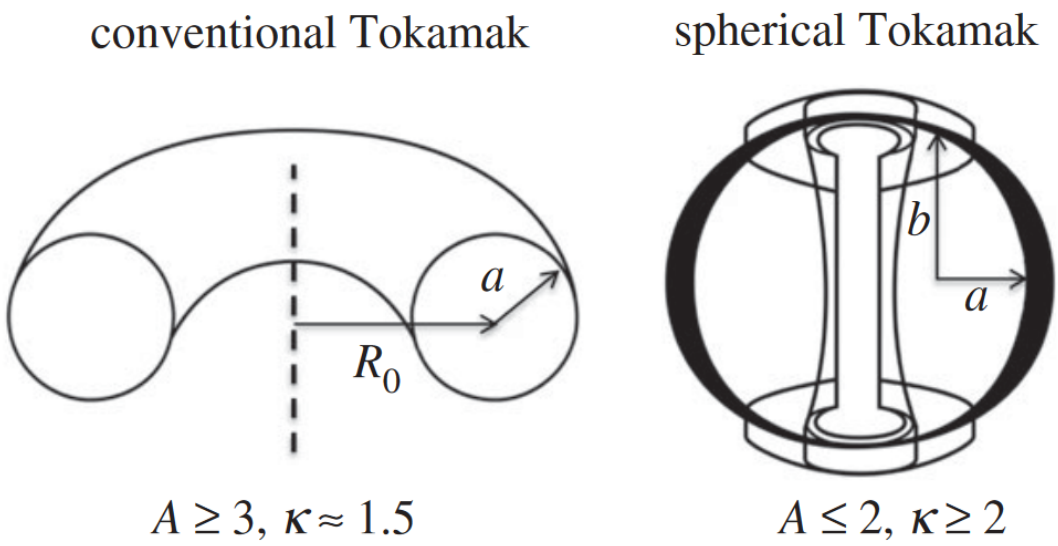

Figure 3.4: Schematics of conventional and spherical tokamaks. The aspect ratio $A = R_0/a$ with $R_0 = R$ the major radius, and the elongation $\kappa = b/a$ [249]

fusion experiment. In 1987 HSE (Heidelberg Spheromak Experiment) was the first device to be converted into a ST [248]. This machine combined the principle of the spheromak and the stability of the tokamak. The difference between a conventional and a spherical tokamak is illustrated in Fig. 3.4. The characteristic shape is determined by the low aspect ratio such that $A = R/a \sim 1$. The space between the torus and the central solenoid is reduced and the conventional cylinder shape of tokamaks becomes vertically elongated. The resulting compact design can be visualised as a cored-apple shape: the plasma core is close to the central rod so being subjected to a higher toroidal field. This arrangement simplifies the requirements of supplementary coils so without the necessity of fast positioning control. The plasma exhibits a natural elongation (*e.g.* $\kappa \sim 2$) which improves the plasma stability due to the enhancement of the bootstrap current. The good performance of STs was demonstrated by the experiments on START surpassing the expectations with a β-record of $\beta_T \sim 30\%$, more than twice the value of DIII-D with $\beta_T \sim 13\%$ at that time, and even beyond the Troyon limit with $\beta_N \geq 4$ [250]. START was able to access H-mode, exceeding the predicted triple product scalings for ITER [251]. These results sparked the interest of STs which led to the construction of MAST at CCFE and NSTX at PPPL. Then the research plan was focused on proving the viability of STs to become fusion power plants while assisting to optimise scenarios for ITER. MAST was designed to be

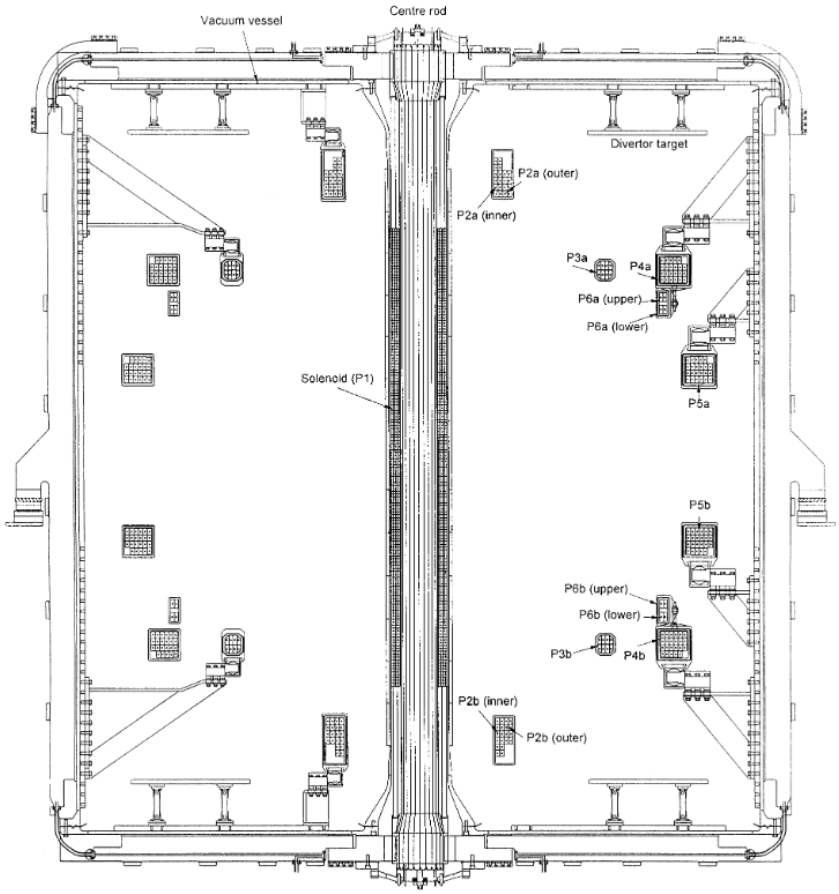

Figure 3.5: Vertical cross section of the MAST vacuum vessel, with the central solenoid (P1) and poloidal field (PF) coils [252]

a medium-size spherical tokamak, twice the size of START, with D-shaped plasma cross sections and the possibility of a double-null configuration similar to contemporary tokamaks such as AUG and DIII-D. The vertical cross section of MAST is illustrated in Fig. 3.5. The central rod contains the solenoid (P1) that is responsible for inducing the plasma current. A set of five poloidal field (PF) coils are mounted internally in the vessel. This configuration took advantage of a new technique known as merging-compression: the current ramp-up is not fully sustained by the central solenoid (P1) flux but is supported by the P3 coils. The breakdown creates two upper & lower plasma rings that merge into the main plasma when encountered at the center by magnetic reconnection. This process is illustrated in Fig. 3.6 with visible frames during the MAST plasma start-up. Then the P1 coil can be used to maintain the resulting plasma during the flat-top phase. The P2 coils are dedicated to form the X-point. The P4 and P5 coils serve for shaping

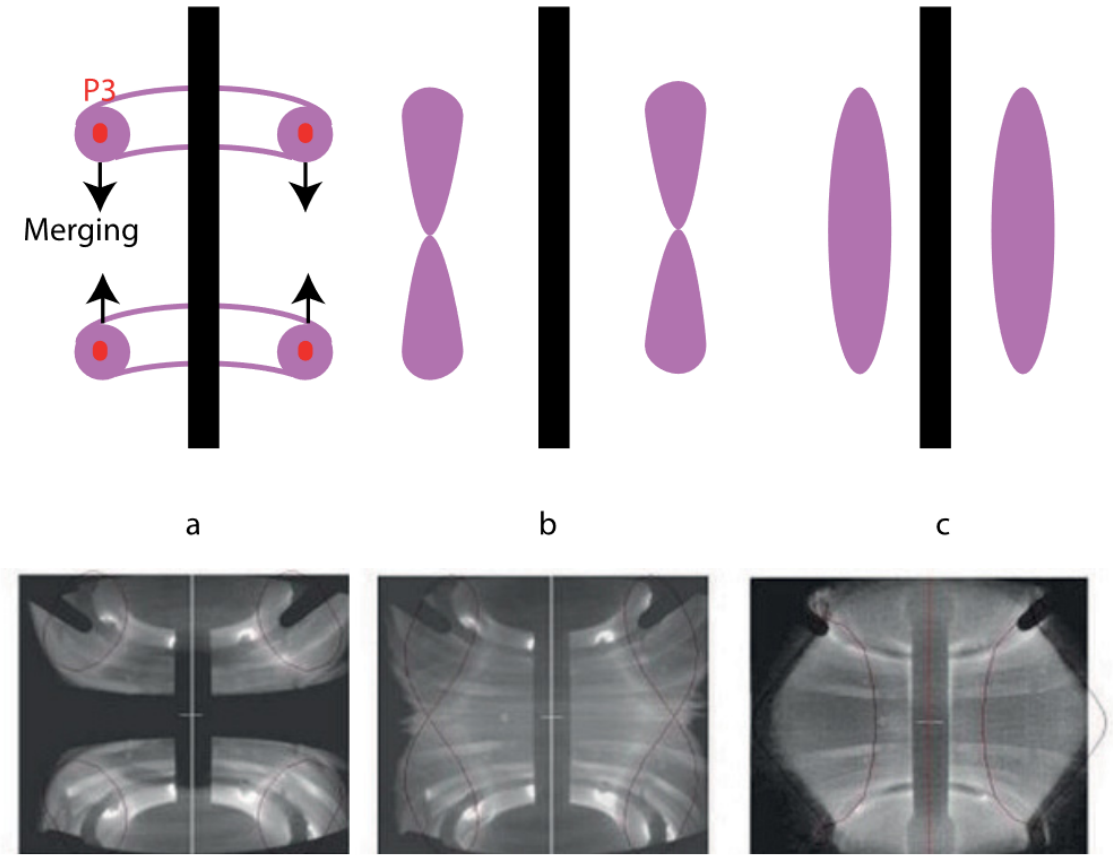

Figure 3.6: Schematic (top) and visible images (bottom) of the merging-compression on MAST at 2 ms (a), 3 ms (b) and 6.6 ms (c) from the start-up [253]

and compression of the plasma while P6 coils provide additional vertical position control. This compact setup allowed to reduce costs as well as providing more space for installing diagnostics. MAST is organised in 12 sectors in the toroidal plane with the toroidal angle increasing anticlockwise *e.g.* $\phi = 0°$ between sector 3 and 4, $\phi = 90°$ between sector 12 and 1, and so on. Several diagnostics systems are mounted in different ports designated by the sector number. Some diagnostics are: the dual Thomson scattering systems, the charge-exchange recombination and Doppler spectroscopy systems, the bremsstrahlung diagnostic, the neutral particle analyser, 500 Langmuir probes and a reciprocating probe at midplane, infrared thermography and halo current detectors [254]. Existing parts from COMPASS were upgraded and reinstalled in MAST such as the power supply for the coils set as well as the electron cyclotron resonance heating system. The neutral beam injection system combined two 70 keV deuterium injectors with 5 MW of heating power,

Parameters	Values
Major radius R	0.85 m
Minor radius a	0.65 m
Aspect ratio R/a	1.3
Plasma volume V	10 m^3
Plasma current I_p (max)	1.3 MA
Magnetic field B_T (max) (0.7 m)	0.63 T
Elongation κ	2.2
Pulse length	$\sim$ 1 s
Beam heating power P_{NBI} (70 keV)	5 MW

Table 3.2: Table of characteristic parameters of MAST [255]

loaned from the Oak Ridge National Laboratory. From December 1998 MAST started a period of tests, achieving H-mode plasmas in 2000, until presenting its first results in 2001 [255]. After corrections of the first design, the revised physical parameters of MAST are given in Table 3.2. MAST joined the MST1 campaign team coordinated by EUROfusion with AUG and TCV for the experimental collaboration of medium-sized tokamaks. These campaigns proved the successful performance of MAST surpassing the limitations of START. The functioning of the merging–compression method was demonstrated without the contribution of the solenoid flux. Moreover the L-H transition occurred at low NBI power of $\sim$ 530 kW, however the threshold was $\sim$ 30% superior to the predicted one. The H-mode regime was characterised with ELM-free periods of $\sim$ 60 ms interrupted by giant type-I ELMs. Additionally the Greenwald limit was exceeded. The next experimental steps were focused on the sustainment and exhaust issues: results shown the enhancement of the bootstrap current at high elongation with NBI heating, and divertor power loading was suitable in regimes with tolerable ELMs [256]. The operations continued while improving the diagnostics setup, specially focused on the characterisation of SOL filaments and the mitigation of ELMs. Unfortunately, the awareness of the MAST technical limitations from its conception led to the necessity of planning an upgrade [257]. The original structure of the vacuum vessel would be kept while many components and diagnostics would be

improved such as the Super-X divertor [258]. In October 2013 MAST was shut down entering a rebuilding period of engineering works which were successively extended [259]. In October 2020 MAST-U (MAST-Upgrade) started its operations. The aim of MAST-U is to demonstrate the feasibility of spherical tokamaks as fusion reactors. In that way MAST-U campaigns will provide results in preparation of STEP (Spherical Tokamak for Energy Production) committed to become the world's first fusion power plant in 2040.

3.3 Diagnostics

3.3.1 Langmuir Probe

The Langmuir Probe (LP) was invented and extensively studied by Langmuir and Mott-Smith [260] as a type of electrical diagnostic. The design consists in a metal tip, acting as an electrode or collector, that protrudes from a insulating material (*e.g.* ceramic or boron nitride tube) which is immersed in a plasma. Probes come in different geometries of which tips can be spherical, cylindrical or planar. An example of generic Langmuir probe is illustrated in in Fig. 3.7 a). The local plasma parameters where the probe is positioned can then be measured. The operating principle is based on biasing the probe, relative to the local plasma potential, by sweeping a voltage V applied to the probe tip and collecting a current I from the plasma. A low impedance series resistor connected to the tip is used to measure the resulting current through the probe circuit. The measure must be carried avoiding a big voltage drop across it so that the applied voltage is equal to tip voltage. This produces a current - voltage ($I - V$) characteristic as shown in Fig. 3.7 b). Three collection regions on the characteristic can be identified:

- The ion collection region (C): the ion current is defined by convention to be negative, where the bias voltage is so negative with respect to the floating voltage ($V < V_f$) that the ions are accelerated towards the probe and all electrons are repelled. The ion current is so small because the ion's thermal speed (in the plasma bulk) is so small (due to its high mass) that the current is small even after accelerating through the sheath.

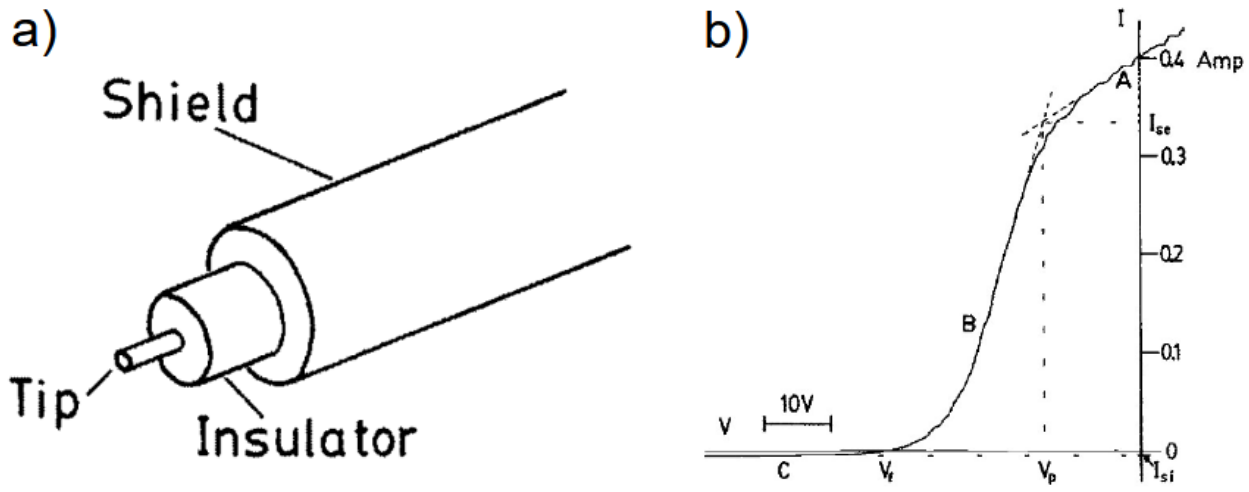

Figure 3.7: a) Schematics of a generic Langmuir probe; b) current - voltage $I - V$ characteristic of a Langmuir probe experiment [261]

- The transition region or electron retardation region (B): the ion current is negligibly compared to the electron current. In this region the electron current decreases because of electrons being repelled by the probe voltage. The trend is approximated to an exponential function of the voltage difference between the plasma potential and the bias voltage ($V_p - V$) for Maxwellian plasmas but can be true for non-Maxwellian plasmas (*e.g.* Langmuir's paradox).

- The electron collection region (A): the electron current is defined by convention to be positive where the bias voltage surpasses the floating voltage ($V > V_f$). The bias voltage being above the plasma potential ($V > V_p$) causes electrons to be attracted (*i.e.* accelerated) to the probe and repels ions. The slope is due to the sheath expansion (*i.e.* larger sheath boundary area). The mass only determines the magnitude of the ion/electron current *i.e.* ions are heavier so have a lower thermal velocity (even at the same temperature as electrons). Electrons have a smaller mass so have a higher thermal speed.

The voltage limits of the transition region define two characteristic potentials. Firstly, the floating potential V_f corresponds to the total probe current being zero. This is because of the cancelling of the negative (ion) current with the positive (electron current), *i.e.* the probe tip "floats" within the plasma adjusting its potential such that the net current is zero. Secondly, the plasma potential V_p corresponds to the intersection

of linear extrapolations from regions A and B as shown in Fig. 3.7 b). The intersection point is the knee indicating the electron saturation. The plasma potential corresponds to the electrostatic potential of the plasma relative to the ground potential. An idealised $I - V$ characteristic would have constant saturation currents (at $V < V_f$ and $V > V_p$), however, this is not the case in practice: the collection of ions (or electrons) depends on the sheath structure surrounding the tip, the probe bias relative to V_p and the geometry of the tip. The non-saturation in region C is a result of the non-uniformity of the sheath over the probe surface and the sheath expansion as the probe bias is increased. With increasing bias the sheath expands increasing its collection area and therefore the collected current. The transition region B contains information such as the energy distribution (and therefore the temperature and plasma density) of electrons reaching the probe. Under the assumption of thermal equilibrium of electrons obeying the Maxwellian distribution, the density is governed by the Boltzmann relation:

$$n_e = n_\infty \exp\left(\frac{eV}{T_e}\right) \tag{3.1}$$

n_∞ is defined as the density far from the origin of the potential. In the plasma far from the sheath where the hypothesis of quasi-neutrality is valid, the Poisson equation that relates the potential and the density is written as:

$$\nabla^2 V = -\frac{e}{\epsilon_0}(n_i - n_e) = \frac{e}{\epsilon_0} n_\infty \left(1 - \exp\left(\frac{eV}{T_e}\right)\right) \sim \frac{1}{\lambda_D^2} V \tag{3.2}$$

The Taylor expansion of the exponential is possible assuming $eV << T_e$, then the solution to Eq. 3.2 describes the spatial variation of the potential with λ_D the characteristic length:

$$V = V_0 \exp\left(-\frac{x}{\lambda_D}\right) \tag{3.3}$$

The sheath width is of the order of the Debye length (depending on plasma parameters and sheath properties). However the quasi-neutrality is not respected near to the sheath. The ion density can be derived from the balance between the ion kinetic energy and the potential energy near and far from the source of the potential:

$$\frac{1}{2} m_i v_i^2 + eV = \frac{1}{2} m_i v_\infty^2 + eV_\infty \tag{3.4}$$

For simplification it is assumed that the ions have zero energy at ∞, taking $V_\infty = 0$ as the origin of potential and ignoring collisions. It is possible to define the ion velocity v_i and the resulting ion current J_i as the ion

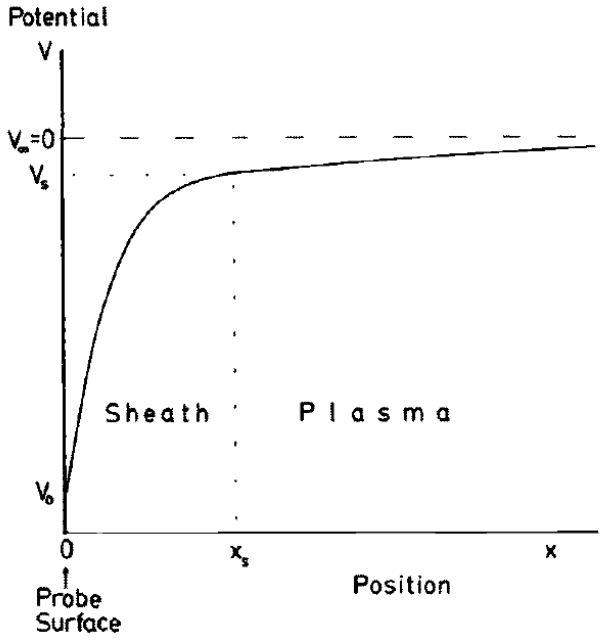

Figure 3.8: Schematics of the electric potential variation near the surface of a biased probe [261]

particle current density Γ_i passing through the probe surface area A_p that is constant in equilibrium:

$$v_i = \sqrt{-\frac{2eV}{m_i}} \qquad\qquad J_i = A_p\Gamma_i = A_p n_i v_i = constant \tag{3.5}$$

Then the ion density close to the probe is expressed as:

$$n_i = \frac{J_i}{A_p}\sqrt{\frac{m_i}{-2eV}} \tag{3.6}$$

In this case the Poisson equation is of the form:

$$\nabla^2 V = -\frac{e}{\epsilon_0}\left(\frac{J_i}{A_p}\sqrt{\frac{m_i}{-2eV}} - n_\infty \exp\left(\frac{eV}{T_e}\right)\right) \tag{3.7}$$

This equation has two solutions depending on the two distinct regions shown in Fig. 3.8: in the plasma where V is approximately constant and $\nabla^2 V$ is neglected; and in the sheath where the term $\nabla^2 V$ cannot be ignored. At the plasma-sheath interface it is possible to define a sheath potential V_s which satisfies:

$$n_i = n_s\sqrt{\frac{V_s}{V}} \qquad\qquad n_s = n_\infty \exp\left(\frac{eV_s}{T_e}\right) \tag{3.8}$$

Then Eq. 3.7 can be reformulated in terms of the sheath potential:

$$\nabla^2 V = -\frac{e}{\epsilon_0} n_s \left(\sqrt{\frac{V_s}{V}} - \exp\left(\frac{e(V-V_s)}{T_e}\right)\right) \sim -\frac{e}{\epsilon_0} n_s \left(-\frac{1}{2V_s} - \frac{e}{T_e}\right)(V - V_s) \tag{3.9}$$

The Taylor expansion simplifies the expression in order to extract the solution which indicates the condition of the potential where the sheath forms:

$$V_s = -\frac{T_e}{2e} \tag{3.10}$$

Re-injecting the solution to the ion velocity in Eq. 3.5 results into the expression of the ion velocity at the sheath interface:

$$v_i = c_s = \sqrt{\frac{T_e}{m_i}} \tag{3.11}$$

This is known as the Bohm criterion [262] stating that the ions entering the sheath must satisfy that the ion speed must reach the local plasma sound speed. In the planar approximation the sheath width is assumed to be constant over the probe surface. An ideal planar probe characteristic is usually shown as having a constant current independent of the bias (*i.e.* a saturation current) in regions A and C in Fig. 3.7 b). Assuming that the probe is sufficiently negative biased for a sheath to form, the ion current drawn by the probe is considered as equal to the ion current across the sheath surface A_s:

$$I_i = eJ_i = eA_s n_s v_i = eA_s n_\infty \exp\left(\frac{eV_s}{T_e}\right)\sqrt{-\frac{2eV_s}{m_i}} = eA_s n_\infty \exp\left(-\frac{1}{2}\right)\sqrt{\frac{T_e}{m_i}} \tag{3.12}$$

The electron current to the probe is given by the thermal equilibrium value since most electrons are repelled, *i.e.* a random current reduced by the Boltzmann factor:

$$I_e = -eJ_e = -\frac{1}{4}eA_p n_e v_{th,e} = -\frac{1}{4}eA_p n_\infty \exp\left(\frac{eV}{T_e}\right)\sqrt{\frac{T_e}{2\pi m_e}} \tag{3.13}$$

By defining the total current drawn from the probe as $I = I_e + I_i$:

$$I = eA_p n_\infty \sqrt{\frac{T_e}{m_i}}\left(-\frac{1}{4}\exp\left(\frac{eV}{T_e}\right)\sqrt{\frac{m_i}{2\pi m_e}} + \frac{A_s}{A_p}\exp\left(-\frac{1}{2}\right)\right) \tag{3.14}$$

This equation gives the $I - V$ characteristic but it is simplified for the case where $T_i < T_e$ then it does not contain information about the ion temperature. Nonetheless it can be used to determine the floating potential when the net current is zero *i.e.* when $I = 0$ the Eq. 3.14 results in:

$$V_f = \frac{T_e}{2e}\left(\ln\left(2\pi\frac{m_e}{m_i}\right) - 1\right) \tag{3.15}$$

However in order to estimate the electron temperature it requires to know previously the plasma potential as the reference point of voltage. The electron temperature can be obtained by deriving Eq. 3.14. In the

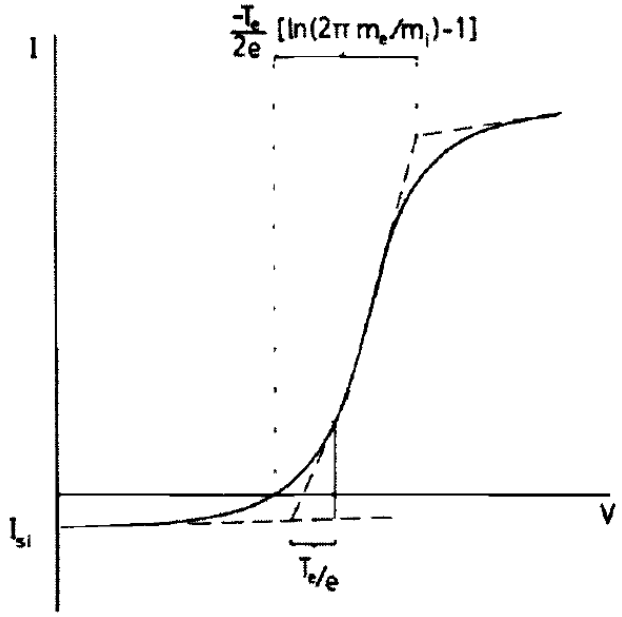

Figure 3.9: Schematics of the slope in the transition region of a $I - V$ characteristic [261]

ideal case where both areas are equal *i.e.* $A_p = A_s$, it is possible to define both ion and electron saturation currents respectively:

$$I_{i,sat} = eA_p n_\infty \sqrt{\frac{T_e}{m_i}} \qquad\qquad I_{e,sat} = -eA_p n_\infty \sqrt{\frac{T_e}{2\pi m_e}} \tag{3.16}$$

The electron temperature can be estimated by taking the slope of the $I - V$ characteristic:

$$T_e = e(I - I_{i,sat}) \left(\frac{dI}{dV}\right)^{-1} \tag{3.17}$$

An example is illustrated in Fig. 3.9 where the linear fit of $\ln(I - I_{i,sat})$ as a function of V corresponds to the slope coefficient T_e/e. The plasma potential corresponds to the voltage that reaches the electron saturation current, *i.e.* the intersection point of both linear fits performed at the retardation and electron saturation regions. The potential difference $V_f - V_p$ corresponds to the voltage in which the probe is floating within the plasma and is dependent on the ratio of both saturation currents:

$$V_f - V_p = -\frac{T_e}{e} \ln \left| \frac{I_{e,sat}}{I_{i,sat}} \right| = -\frac{T_e}{e} \ln |\mathcal{R}| \tag{3.18}$$

These equations are for collisionless sheaths *i.e.* low pressure plasmas. However, in the case of magnetised plasmas or collisional sheaths, these assumptions are no longer valid. In magnetised plasmas the collection

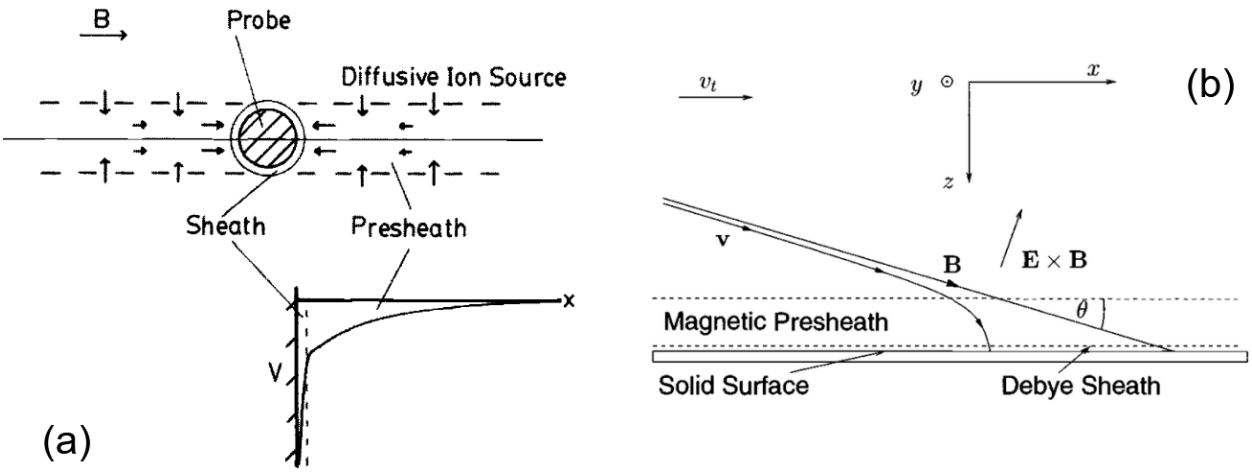

Figure 3.10: Schematics of the sheath and pre-sheath in a strong magnetic field (a); case where magnetic field is oblique to the probe surface with θ the collection angle (b) [261]

depends on the particle gyration around the field lines determined by the ratio ρ_L/a_p with a_p the typical probe dimension. This effect tends to affect more the electrons (*i.e.* $\rho_{L,e} < a_p$) which impedes the electron current being collected and causes non-isotropic electron energy distributions deviating from the Maxwellian [261]. Only the projection of the probe surface area in the direction of the magnetic field corresponds to the effective collection area as shown in Fig. 3.10 (a). Along this magnetic flux tube a quasi-neutral pre-sheath forms where the ions fall into by diffusion then these are accelerated until reaching the Bohm velocity. If collisions are assumed to take place in the pre-sheath, the eventual ionisation of neutrals can drastically alter the sheath structure which affects the collected current. Furthermore, if the surface is oblique to the magnetic field lines (Fig. 3.10 (b)), a perpendicular component of the plasma flow arises due to $E \times B$ drifts (the electric field being generated by the sheath potential gradient) or diamagnetic drifts (the pressure gradient being caused by the difference of particles amount along the pre-sheath). For complex magnetic field shapes, probes can be built with multiple angles θ of collection (*e.g.* rotatable or Gundestrup probes). In these types of plasmas obtaining the plasma parameters becomes more complicated. The measurement of the electron temperature and plasma density relies then on alternative methods such as the Thomson Scattering. Sheath models are usually tailored to a specific set of plasma conditions (*e.g.* fully collisional, collisionless, etc) and no generalised theory exists. For magnetised plasmas probe theory is still not well developed and is limited to a few special cases and simplifying approximations (*e.g.* the planar probe geometry).

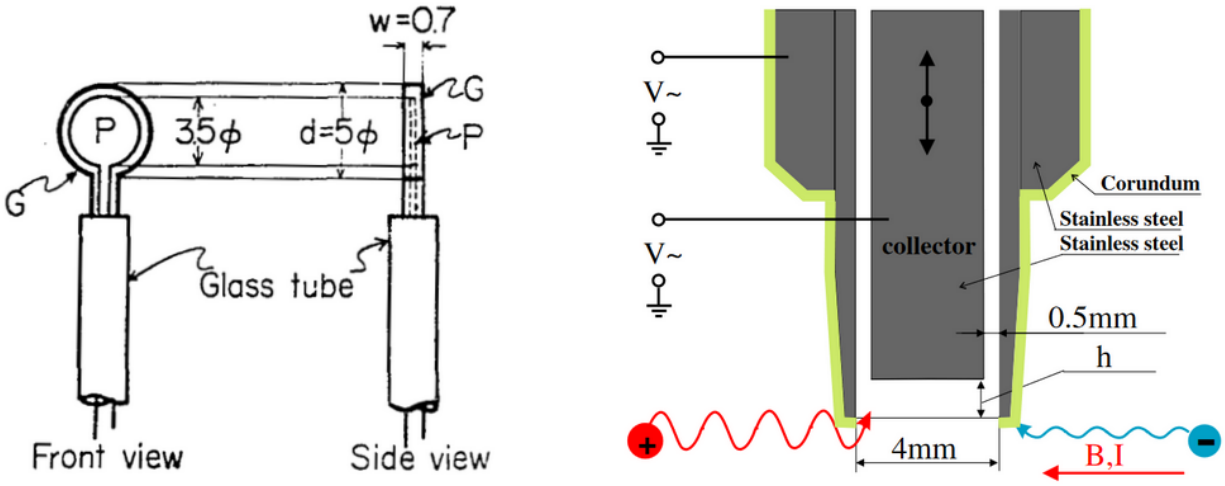

Figure 3.11: (Left) Original design of the ISP by Katsumata *et al.* [264]; (right) schematics of the ISP in CASTOR and its positioning with respect to the magnetic field by Komm *et al.* [265]

3.3.2 Ball-Pen Probe

The Ball-Pen Probe (BPP) was conceived by Adamek *et al.* [263] in order to provide a solution for a more accurate measurement of the plasma potential in strongly magnetised plasmas. This design was inspired by the Ion Sensitive Probe (ISP) proposed by Kastumata *et al.* [264]. The aim was to reduce the collection of electrons for balancing the electron and ion currents. The original ISP shown in Fig. 3.11 a) consisted of a planar probe P, in parallel with the magnetic flux lines, surrounded by a guard-ring electrode G with a width of the order of twice the electron Larmor radius $\rho_{L,e}$. The G electrode intercepts electrons while the biased planar probe P collects ions, the resulting $I - V$ is only profiled by the ion distribution and the ion temperature can be extracted. In the CASTOR tokamak the ISP design shown in Fig. 3.11 b) was modified as a cylindrical collector submerged into a shielding tube and oriented perpendicularly to the magnetic field [265]. The retraction depth is typically a few ion Larmor radii $\rho_{L,i}$ to capture ions while the tube obstructs electrons with small electron Larmor radii $\rho_{L,e}$ radii. In terms of the Eq. 3.18 the principle of the ISP consists in equalising both saturation currents until the ratio satisfies:

$$\mathcal{R} = \frac{I_{e,sat}}{I_{i,sat}} \sim 1 \tag{3.19}$$

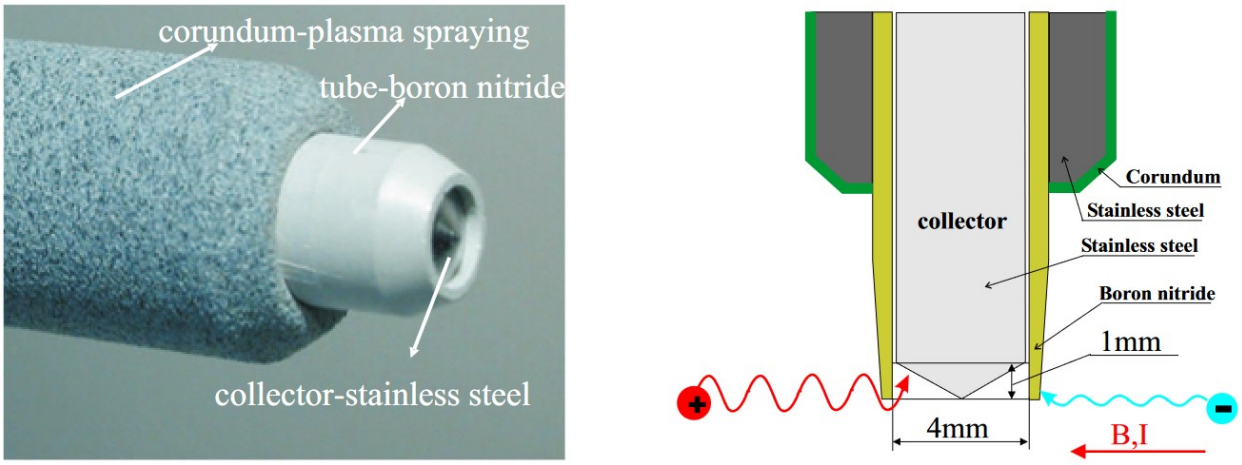

Figure 3.12: (Left) Photograph of a BPP in CASTOR; (right) schematics of the BPP and the positioning with respect to the magnetic field [263]

This causes the probe to float at the plasma potential *i.e.* $V_f \sim V_p$. Different approaches were previously used on tokamaks adopting the same principle such as the Emissive Probe (EP) [266] and the Heavy Ion Beam Probe (HIBP) [267]. The EP consists of a heated wire thermionically emitting electrons which, being accelerated into the plasma, enhance the collection of the ion current. The HIBP consists of a beam of highly energetic ions which collide with the plasma particles producing secondary ions that get into an electrostatic grid analyzer from which the plasma potential is obtained. However, these methods have several technical drawbacks, either for being too invasive and fragile (*e.g.* EP and ISP) or requiring a complicated setup (*e.g.* HIBP), and with difficulties in the interpretation of the $I-V$ characteristic. The interest of using the BPP is to avoid these limitations. In contrast with the ISP's stepped planar collector, the BPP collector is conically shaped. Similarly with the ISP design in CASTOR, the collector depth can be adjusted so varying the exposed area as shown in Fig. 3.12. When the collector is exposed outside the shielding tube the BPP acts as a LP. When the collector is retracted inside the tube there is an optimal depth where the logarithm $\ln(\mathcal{R})$ is minimised where the ratio $\mathcal{R}$ is close to unity and the collector's voltage is close to the plasma potential. The performance of the BPP was tested in CASTOR plasmas measuring the probe potential $\Phi^{BPP} \sim 23$ V for a depth of $h \sim -0.5$ mm as shown in Fig. 3.13. The BPP was used on the CASTOR tokamak between 2004 and 2006 performing better than the EP [268]. Its efficiency has been empirically confirmed

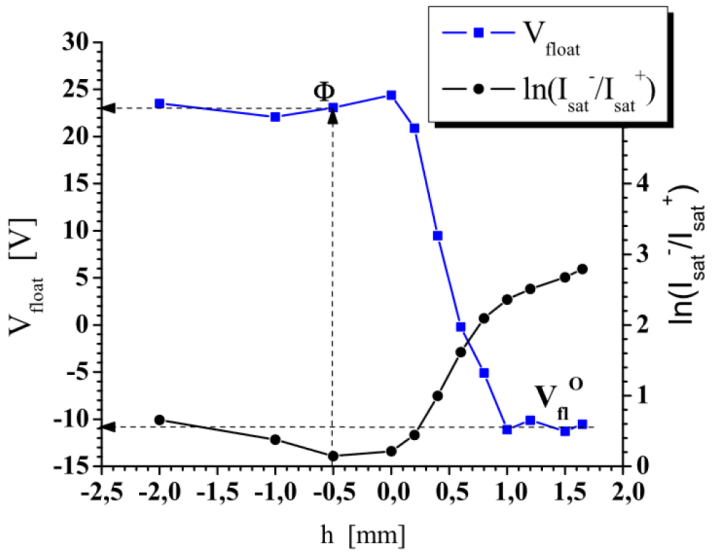

Figure 3.13: Measurement of the BPP on CASTOR with variation of the floating potential V_f (blue) and $\ln(I_{e,sat}/I_{i,sat})$ (black) with respect to the collector depth h [263]

in low-temperature plasmas [269, 270] and tokamak plasmas such as AUG (in L-mode [271] and ELMy H-mode [272]), MAST (with a flat collector similar to a ISP [273]) and ISSTOK [274] in good agreement with COMPASS experiments [275]. The BPP convention denotes the logarithmic ratio $\ln(\mathcal{R})$ as the factor α. By using a combination of LP and BPP probes, the Eq. 3.18 is re-written to provide an estimation of the electron temperature:

$$T_e \sim \frac{\Phi^{BPP} - V_f}{\alpha_{LP} - \alpha_{BPP}} \qquad \alpha \equiv \ln \mathcal{R} \tag{3.20}$$

For each probe (LP, BPP), factors (α_{LP}, α_{BPP}) are empirically measured across a number of experiments. However, since the experiments in CASTOR the BPP measurements overestimated the reduction effect of the collected electron current [268]. Similar observations in experiments with an ISP reported an asymmetry in the ion/electron collection [276]. Different models have pointed out the role of the $E \times B$ drift that transports electrons towards the collector and hence perturbs the measurement [265, 277]. The origin of the cross-field motion can be due to the sheath in the shielding tube or the space charge due to gyration of ions into the collector gap which is in agreement with recent 3D particle-in-cell simulations [278]. However, all these models only take into account the ISP geometry (*i.e.* with a flat collector). The theoretical principles of the BPP (*i.e.* with a conical collector) are not fully understood and require further investigation.

3.3.3 Beam Emission Spectroscopy (BES)

The Beam Emission Spectroscopy (BES) technique was developed in the late 1980s by different teams, *e.g.* Seraydarian *et al.* at DIII-D [279] and Boileau & Hellermann *et al.* at JET [280, 281], from the research based on Charge eXchange Recombination Spectroscopy (CXRS). The CXRS technique uses a beam injecting neutrals into the plasma and focuses on the collisions between neutrals (*i.e.* deuterium atoms) and ions (*i.e.* deuteron nucleus). The use of a neutral beam allows to locally induce and increment the number of reactions. The beam acts as a probe injecting fast neutral particles into the plasma and induce fluorescence emission in order to extract the plasma properties of a specific region *e.g.* the plasma edge. These neutrals are capable of traveling freely without being affected by the magnetic field. The charge exchange reaction consists in the ionisation (noted by the superscript $+$) of beam neutrals, transferring electrons to plasma ions which become neutral (noted by the superscript 0) in an excited state (noted by the superscript $*$):

$$\mathrm{D}^{0}_{beam} + \mathrm{D}^{+}_{plasma} \longrightarrow \mathrm{D}^{+}_{beam} + \mathrm{D}^{0*}_{plasma} \tag{3.21}$$

The excited-state deuterium D^{0*}_{plasma} eventually emits radiation (*i.e.* photons) by spontaneous decay which can be quantified by the Balmer-α spectral line noted D_α respectively. Then the spectroscopy system is responsible for collecting these photons emitted by the plasma deuterium, reconstruct the spectrum and infer the properties of ions in the plasma. In the case of the BES technique, the analysed emission comes from excited beam neutrals D^{0*}_{beam} instead of the deuterium from the plasma. Several collisional processes are involved in the excitation, either with ions (D^{+}), impurities (Z^{+}) or electrons (e^{-}):

$$\mathrm{D}^{0}_{beam} + \mathrm{D}^{+}_{plasma} \longrightarrow \mathrm{D}^{0*}_{beam} + \mathrm{D}^{+}_{plasma} \tag{3.22}$$

$$\mathrm{D}^{0}_{beam} + \mathrm{Z}^{+}_{plasma} \longrightarrow \mathrm{D}^{0*}_{beam} + \mathrm{Z}^{+}_{plasma} \tag{3.23}$$

$$\mathrm{D}^{0}_{beam} + \mathrm{e}^{-}_{plasma} \longrightarrow \mathrm{D}^{0*}_{beam} + \mathrm{e}^{-}_{plasma} \tag{3.24}$$

However, the frequency of the emitted radiation experiences deviations from its natural wavelength due to the motion of neutrals while observed in the line-of-sight of the spectroscopy system. The induced D_α emission depends on the velocity of the neutrals and on the angle between the beam and the magnetic field lines. The emission line appears shifted in the spectrum due to the Doppler effect by the beam velocity v_b. This

effect is advantageous as the beam emission line can be distinguished from the plasma background emission. Aligning the beam tangential to the flux surfaces allows the spectroscopy system to observe the Doppler-shifted emission at the plasma edge. Additionally the intersection with the field lines causes the neutrals to be subjected to the Lorentz force $v_b \times B$. The resulting electric field causes the Stark motion effect which makes the emission line to shift and split into several components in the spectrum. Different collisional-radiative models are used to predict the spectrum. These models consist in deriving the rate population equations that correlate the intensity of spectral lines with the local measurement. Nonetheless the difference between the CXRS and the BES is the type of measurement: the CXRS provides an estimation of the local ion velocity, temperature and density, whereas the BES observes the spatial and temporal evolution of the local density fluctuations independent of the plasma ions. For that reason the BES technique is convenient for characterizing the density turbulence at the edge of tokamak plasmas. The first applications of BES systems were tested in the early 1990s by Fonck *et al.* in PBX-M [282], Durst *et al.* in TFTR [283], and Mandl *et al.* in JET [284]. In MAST, a BES trial system was developed in 2008 by Field *et al.* [285], later upgraded in 2011 [286]. An overview of the BES opto-mechanical system with schematics of the collection ray path is shown in Fig. 3.14. The spectroscopy system shared the collection optics and spectrometer of the CXRS system [287]. The detectors were Avalanche Photo-Diode (APD) arrays that transcribe the collected emissions into electrical signals. The in-vessel periscope contains a first collection mirror M1 which redirects the incident light vertically, a collection lens L1 which produces a reduced image by de-magnification, and a second deflection mirror M2. The viewing location and focusing of lenses is calibrated between discharges by rotating the collection mirror and the filter using a stepping motor drives. In comparison with the trial system a grating was placed for diffracting the emission from impurities such as C^{5+} ions whereas the D_α emission remains unaffected. These components are supported with a tube mounted into a flange at the vacuum boundary. In between the boundary a field lens L2 concentrates the light passing through a small aperture window W1 at the flange and arriving at the ex-vessel optics. A pair of intermediate lenses L3 outside the window conducts the light along a tight cone up to the base plate optics. The filter cell contains the field lenses L4 adjusting the ray path in parallel in order to pass through the interference filter F1 in between. This filter restrains the collected light to pass through except for the wavelengths related to the

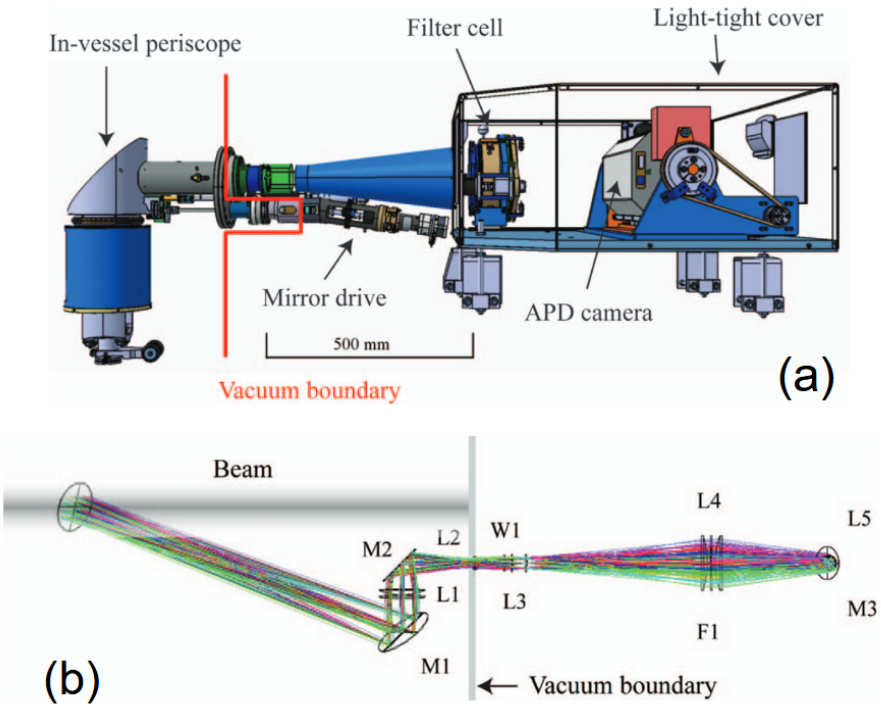

Figure 3.14: Overview (a) and optical layout with beam and collection ray path (b) of the BES imaging system [286]

Doppler shifted emissions. Lastly a deflection mirror M3 guides the light into the camera lens L5 which forms an image for the APD sensors. The BES trial system used a 8-channel 1D APD detector coordinated with the SW beam. The upgraded BES system was mounted to the port HM-07 and was assisted by the SS beam. The BES camera was based on multiple detectors in the radial and poloidal directions for obtaining two-dimensional measurements of localised density fluctuations. This technique is often referred as 2D BES imaging and was previously tested in DIII-D [288]. The APD camera consisted in a Hamamatsu S8550 array sensor designed and manufactured by ADIMTECH Ltd from the Hungarian Academy of Sciences [289]. The Hamamatsu sensor integrates 8 radial $\times$ 4 poloidal channels with a $\sim 2.3 - 2.6$ cm spatial and 0.5 MHz temporal resolutions. Each channel corresponds to a photosensitive area connected to a p-n junction that generates an electrical current when receiving photons. The dimensions of the APD camera are shown in Fig. 3.15. The incident photon flux is of the order of $\sim 10^{11}$ s^{-1}. The active area of each pixel of 1.6 $\times$ 1.6 mm^2 corresponds to a collection light *étendu* of $\Delta\xi = \Delta A \Delta\Omega \sim 1.1 \times 10^{-6}$ m^2 sr pixel^{-1} with ΔA is

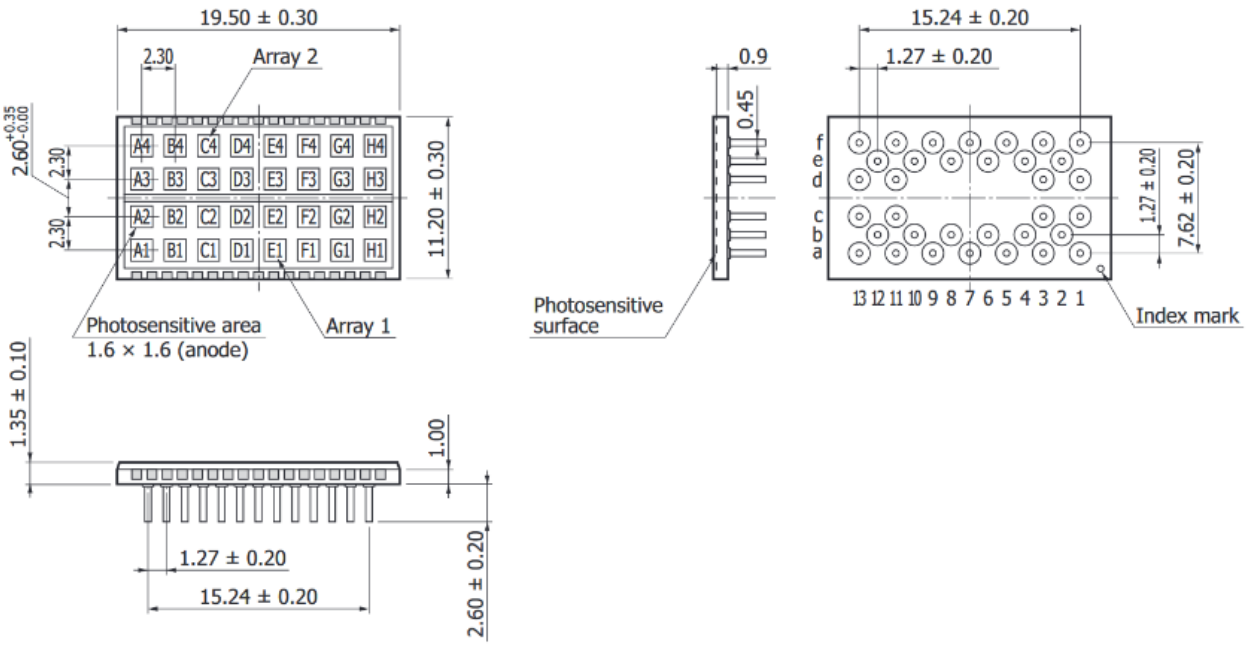

Figure 3.15: Schematics of the Hamamatsu S8550 APD array sensor with 32 channels, 8 by 4 photodiode arrays; dimensions are in cms [286, 289]

the light collection area and $\Delta\Omega$ the solid angle at some location along the light path. The pitch of the APD camera defines the viewing area covering 16×8 cm^2 at the plasma edge being large enough to contain the pedestal and the SOL. In order to correlate the D_α intensity with the density fluctuation, a model was developed and tested with numerical simulations for predicting the spectra of the 2D BES imaging system. The intensity is expressed in terms of the emissivity $\varepsilon_j(r,l)$ of the D_α emission that is dependent on the position r relative to the location l along the beam and the energy component j. The beam power with an initial injection energy E_0 is separated into different energy components (E_0, $E_0/2$, $E_0/3$) noted E_j with respective wavelengths appearing in the spectrum. The beam density is defined by the Gaussian profile:

$$n_{b,j}(r,l) = \frac{\Gamma_j(l)}{\pi v_{b,j} W_b} \exp\left(-\left(\frac{r}{W_b}\right)^2\right) \tag{3.25}$$

The beam flux $\Gamma_j(l) = P_b f_j / eE_j$ is expressed in terms of power fractions $f_j(\rho) = f_0(1-\rho^m)$ of the total beam power P_b for each energy component j, with $\rho = \Psi_N^{1/2}$ the normalized radius and m an arbitrary number. W_b is the half-width of the Gaussian that depends on the NBI source. Additionally the beam flux is modelled to take into account the attenuation of the beam along the step length Δl between a time step

$\Delta t = t_i - t_{i-1}$ with the beam stopping rate $\langle \sigma v \rangle_{bs,j}$:

$$\Gamma_j(t_i) = \Gamma_j(t_{i-1}) \left(1 - n_e \langle \sigma v \rangle_{bs,j} \frac{\Delta l}{v_{b,j}} \right) \tag{3.26}$$

It is predicted that the light intensity is approximately proportional to the product of the beam neutral density and the electron density. Then the emissivity is defined as the excitation rate produced by the interaction between the beam neutrals and the electrons with the excitation rate coefficient $\langle \sigma v \rangle_{ex,j}$:

$$\varepsilon_j(r,l) = n_{b,j}(r,l) n_e \langle \sigma v \rangle_{ex,j} \tag{3.27}$$

The line-integrated spectral intensity $I_{j,k}(\lambda)$ of the Doppler shifted beam emission for each energy component j and each line of sight k is calculated from:

$$I_{j,k}(\lambda) = \int I_N[\lambda_0, \Delta\lambda(v_{b,j}, \theta_k)] \varepsilon_j(r,l) dl' \tag{3.28}$$

where l' is the location along the line of sight and $I_N[\lambda, \Delta\lambda]$ is the normalized Gaussian line profile of the D_α line emission and shifted along the line of sight by the wavelength $\Delta\lambda = v_{b,j}/c \cos \theta_k$ where θ_k is the angle between the line of sight k and the beam direction. The total simulated spectrum $I_k(\lambda)$ takes into account additional contributions from the "passive" D_α emissions distinguished from the "active" D_α emissions caused by the beam:

$$I_k(\lambda) = \sum_j I_{j,k}(\lambda) + I_{D_\alpha}^{cold}(\lambda) + I_{D_\alpha}^{hot}(\lambda) + I_{CII}(\lambda) + I_{BG} \tag{3.29}$$

The unshifted D_α line is referred as "cold" intensity, whereas the charge-exchange emissions line is referred as "hot" intensity. Furthermore, background intensity is included coming from other impurity emissions, specially from the emission of ionised carbon (CII), and broadband emissions due to bremsstrahlung (BG). A predicted spectra shown in Fig. 3.16 was produced from simulations for beam energies of 75 keV and 60 keV, which were benchmarked with measurements from the BES trial system. The unshifted D_α line corresponds to the dominant peak at $\lambda \sim 656.1$ nm. The CII doublet lines appear at $\lambda \sim (657.8,\ 658.3)$ nm. These lines are matched in the measured spectra using the Motional-Stark-Effect diagnostic shown in Fig 3.17. The wavelength of the Doppler shifted D_α emission depends on the viewing radius and energy component. Several Doppler shifted D_α lines are displayed in predicted spectra for different radii and energy component. The transmission coefficient of the filter indicates the bandpass envelope as a function of the wavelength.

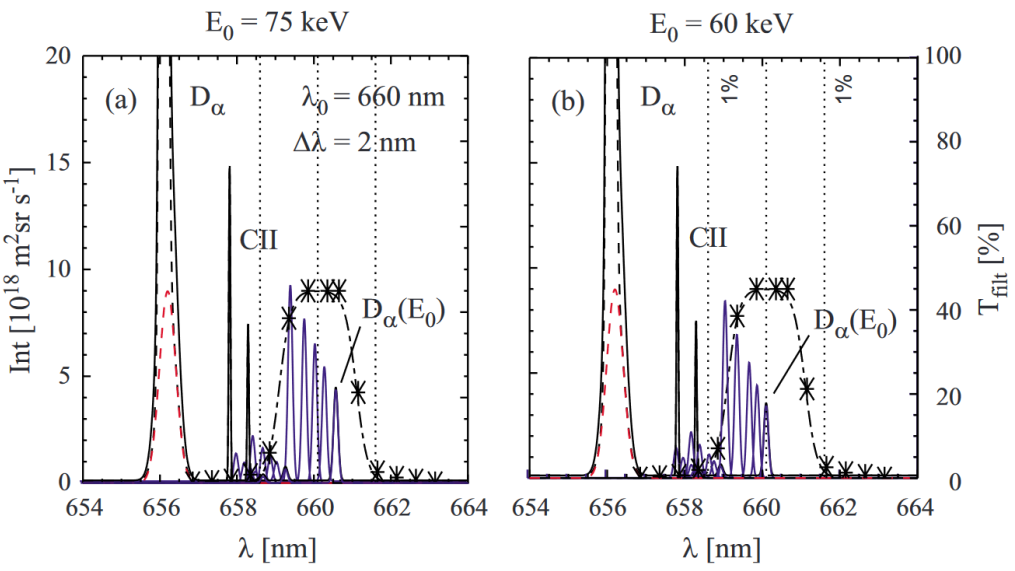

Figure 3.16: Predicted spectra from the BES trial model for NBI energies of 75 keV (a) and 60 keV (b). The total emission is shown in black for a viewing radius of 0.9 m, and the contribution to the beam emission from the three energy components for viewing radii of 0.9, 1.0, 1.1, 1.2, and 1.3 m is superimposed in blue. The transmission of the interference filter T_{filt} is shown in black dotted-dashed [285]

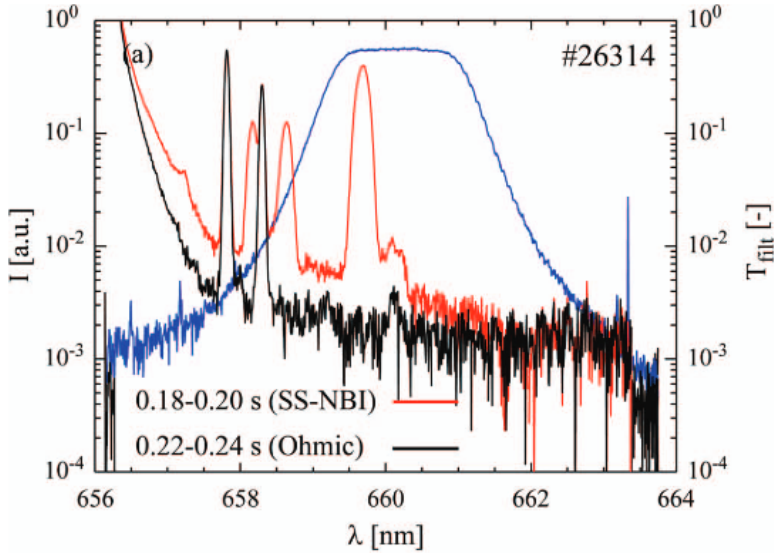

Figure 3.17: Measured spectra by the 2D BES system for discharge #26314 during SS-NBI beam heating of 62 keV (red) and during Ohmic heating (black) at viewing radius of 1.2 m. The transmission of the interference filter T_{filt} is shown in blue [286]

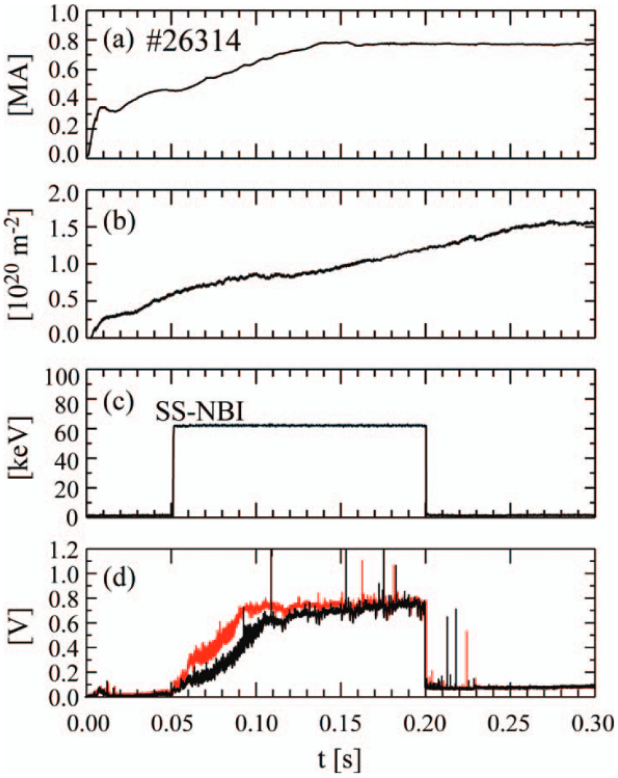

Figure 3.18: Evolution during discharge #26314 of (a) plasma current, (b) line-integrated electron density, (c) SS beam injection energy, and (d) BES signals from channels 13 (upper trace) and 16 (lower trace) in the frequency band from 0 to 50 kHz [286]

The interference filter acts as a bandpass of central wavelength $\lambda_0 \sim 660.2$ nm and full-width-half-maximum $\Delta\lambda \sim 2.0$ nm, masking the lines outside the envelope region. For instance, in the measured spectrum the active D_α line is observed at $\lambda \sim 659.7$ nm for a viewing radius of $R = 1.2$ m. Finally, the integration of the spectra under the filter bandpass function for a channel results into the spectrally integrated intensity which corresponds to a produced current per channel. Then the pre-amplifier takes the role of a current to voltage converter followed by an applied gain and noise level reduction [290]. The output voltage of the APD camera preamplifier is given by:

$$V_{out} = GeM_{APD}Q_{eff}i_\gamma R_L \tag{3.30}$$

$M_{APD} \sim 5$ is the internal gain of the APD, $G \sim 100$ is the gain of the second stage, $Q_{eff} \sim 85\%$ is the high quantum efficiency at the D_α shifted line, $R_L \sim 68$ kΩ is the load resistance of the transimpedance amplifier,

and $i_\gamma = eT_{opt}\Gamma_\gamma$ the incident photon current with T_{opt} the filter transmission and Γ_γ the photon rate passing through the filter. The APDs share a common anode which applies a bias voltage of 290 V resulting in an intrinsic gain of 5. The magnitude of the BES signals is of the order of ~ 0.6 V for an incident photon flux of $\sim 3.4 \times 10^{11}$ s^{-1}. Two examples of BES signals are presented in Fig. 3.18 (d). After starting the SS beam the BES signals increase slowly because the plasma radius at the outboard midplane was increasing during the early phase and is initially inside the observed radial location. The relatively constant intensity during the density ramp implies that the increasing density is compensated by an increase in the beam attenuation at the observed location. At the SS beam cut-off the BES signal significantly drops. Prior to each ELM release BES signals from channels viewing the pedestal region can record the density oscillations caused by the presence of ELM-precursors.

3.3.4 Fast camera

The use of fast framing cameras started in the 1980s with film recordings in different tokamaks with little published discussions. The first papers were published by Goodall in ASDEX and DITE [165], and Zweben and Medley in TFTR [291]. The camera imaging enabled to report visual events of the plasma behaviour at the edge, specially observations of SOL filaments. Progress has been made on the fast camera capabilities *e.g.* resolution, exposure time, frame rate, in order to track the motion of filaments with higher accuracy. This technique is non-invasive compared to the use of probes, and only collects passive D_α light compared to the BES system so without the assistance of the NBI system. In MAST, an ultra-high speed camera was used named Photron SA1.1 [292] (Fig. 3.19) which was a loan from the University of Swansea for the campaign between May and September 2013. The camera captured the passive light emission from unshifted D_α lines at 656 nm. The camera was unfiltered to maximise the light throughput of the optics. A focal length lens of 5.733 mm was chosen for adjusting the image to widely collect light from the main chamber. The imaging process was performed by a Complementary Metal-Oxide-Semiconductor (CMOS) active-pixel sensor. This sensor consists in a 2D array of 1024 $\times$ 1024 pixels. Each pixel of 20 μm size corresponds to a photosensitive diode collecting photons plus an amplifier for current-voltage conversion. The analog-digital converter was

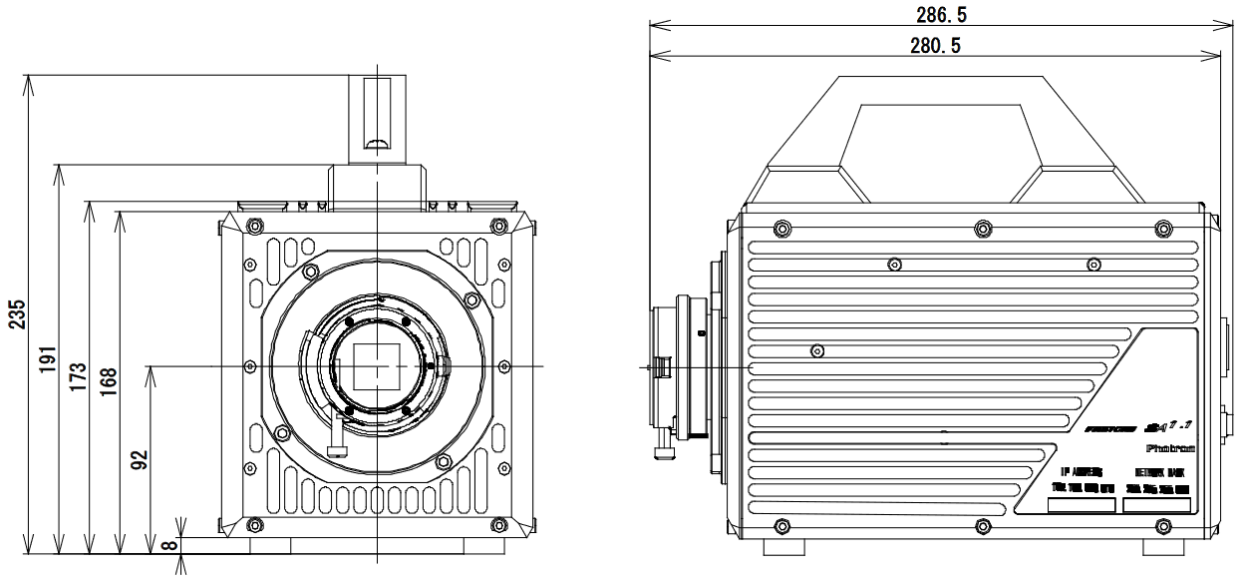

Figure 3.19: Schematics of the Photron SA1.1 camera; dimensions are in mms [292].

set in monochrome scale hence converting light intensities in 12 bits assigning digital values in the dynamic range between 0 and $2^{12} = 4096$. In order to maximise the performance of the camera for visualising SOL filaments, it was required to operate with a reduced sensor area for increasing the frame rate. For instance, the use of the full-size sensor corresponds to effectuate 5400 frames per second (fps). Then the windowing of the sensor limited the frame segment to 256 $\times$ 160 pixels allowing 100000 fps by only viewing half of the plasma at midplane. The spatial and temporal resolutions correspond to a size of 3.20 $\times$ 5.12 mm^2 and a frame rate of 100 kHz respectively. The camera operated with an exposure time of 3 μs which was estimated as optimal to avoid the blurring of filaments due to the toroidal rotation [293].

3.3.5 Outboard Mirnov Array for High-frequency Acquisition (OMAHA) coil

The Mirnov coil was invented by Mirnov for detecting the electromagnetic signature of energetic particle driven modes at the edge of cylindrical and toroidal plasmas [294]. At the beginning of MAST operations, the original Mirnov coils suffered from severe limitations for measuring high frequency magnetic field fluctuations. For instance, the inboard coil shielding attenuated signals at frequencies above 100 kHz, and the coil cabling was not terminated causing resonances at 300 kHz. Hence, these were unable to detect high frequency modes

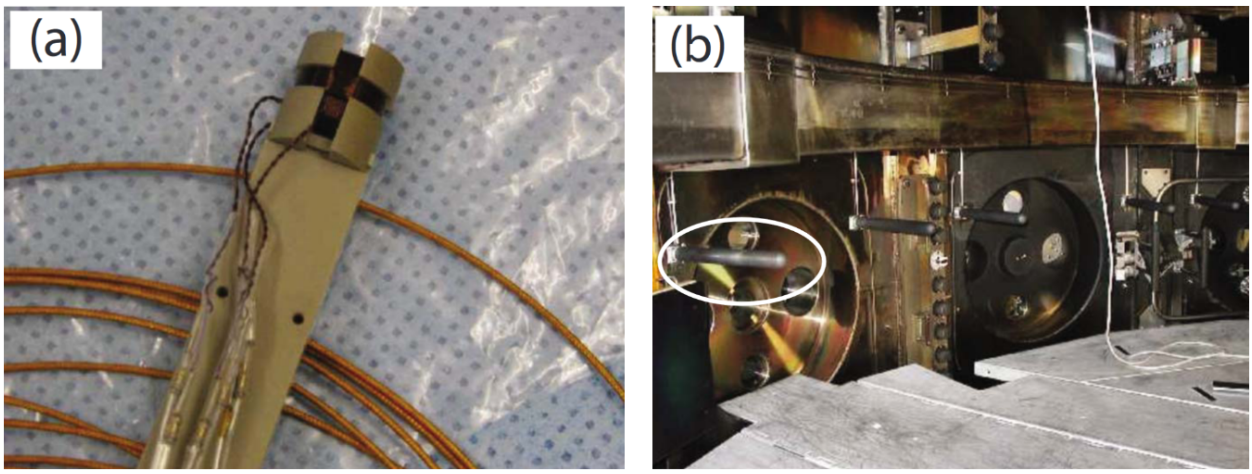

Figure 3.20: OMAHA coils: (a) picture of a three-axis probe head; (b) a probe test tube bolted to the vessel wall, the leftmost OMAHA probe is identified by the white ellipse [295]

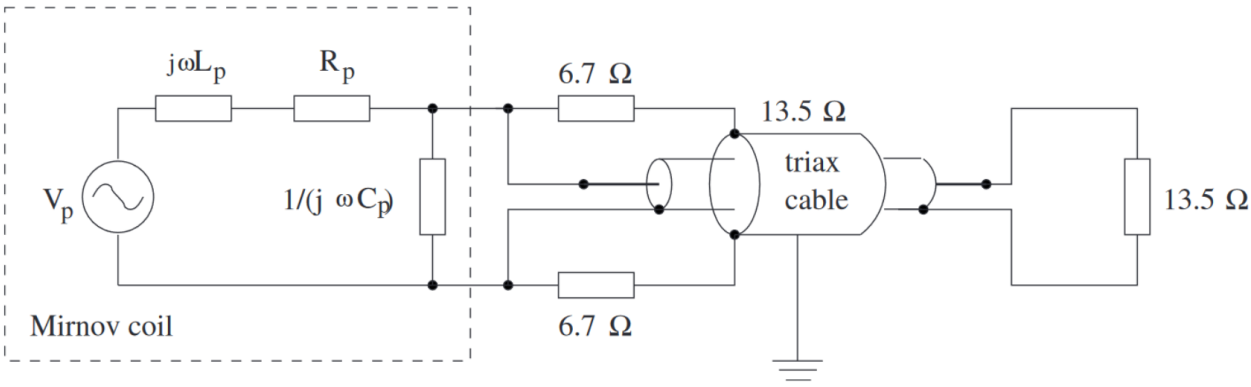

Figure 3.21: An equivalent circuit of the OMAHA probe design for each coil, showing ground connections and the circuit connection for the triaxial cable [295]

e.g. shear Alfvén eigenmodes in the range of $f \geq 100$ kHz that can degrade the confinement. The necessity of detecting high-frequency modes led to the implementation of the Outboard Mirnov Array for High-frequency Acquisition (OMAHA) coils [295]. The design of the OMAHA coil consists in a single probe head with three orthogonal coils aligned in the three orientations (R, Z, ϕ). A picture of a three-axis probe head and the locations of several probes in the vessel wall are shown in Fig. 3.20. This configuration allows to measure the orientation of passing modes relative to the equilibrium magnetic field with respective components denoted by δB_R, δB_Z and δB_ϕ. The equivalent circuit for an OMAHA probe is shown in Fig. 3.21. The Mirnov

coil is represented by a RLC circuit, with inductance L_p, wire resistance R_p, and inter-turn capacitance C_p, connected to a triaxial cable with the shield and ground connections. When detecting a sinusoidal magnetic fluctuation $B_c(\omega)$ with ω the angular frequency of the mode, the coil produces a voltage $V_p(\omega)$ of the form:

$$V_p(\omega) = j\omega AN B_c(\omega) \tag{3.31}$$

A is the probe cross-sectional area, N is the number of turns, and j is the complex number. The impedance of the coil circuit with a triaxial cable of impedance Z_0 is matched by two 6.7 Ω resistors. The termination of the triaxial cable is connected in parallel to a 13.5 Ω resistor where an A/D converter digitises the measured voltage drop. A matching network $X_m(\omega)$ (representing the resistors noted as "parallel impedance") is required to match the cables' characteristic impedance Z_0 to minimise energy losses, resonances and reflections (*i.e.* known as "transmission line"). This matching condition is represented by both equations for high signal and low signal frequencies respectively:

$$\begin{aligned} 1/(j\omega C_p)\big\|R_p + j\omega L_p\big\|\, X_m &= Z_0 \quad (\omega < \omega_r) \\ X_m &\approx Z_0 \quad (\omega \ll \omega_r) \end{aligned} \tag{3.32}$$

Here the $\|$ notation represents the parallel combination of impedance, and ω_r is the coil's self-resonant frequency. The relation between the magnetic fluctuation and the voltage signal is given by the transfer function $H_{V,\delta B} = V/\delta B$. The transfer function is given by:

$$H_{V,\delta B} = \frac{1/(j\omega C_p)\|X_m\|\, Z_0}{R_p + j\omega L_p + 1/(j\omega C_p)\|X_m\|\, Z_0} \times j\omega AN \tag{3.33}$$

The transfer function is plotted in Fig. 3.22 including magnitude and phase for shield and no-shield cases. It was assumed that OMAHA coils were shielded during the experiments. Note that the expected frequencies of 20 kHz would be near the top end of the linear regime with almost a 90° phase shift between the output voltage and the input magnetic field. An algorithm was implemented for adjusting the number of coil turns and finding optimal coil locations. The windings give a different NA number for each coil: $NA = 6.5 \times 10^{-3}$ m^{-2} for δB_ϕ, $NA = 7.5 \times 10^{-3}$ m^{-2} for δB_Z, $NA = 8.8 \times 10^{-3}$ m^{-2} for δB_R. The final configuration allows to sample signals with a temporal resolution of 2 MHz being able to register the wide range of magnetic fluctuations such as the ELM-precursor.

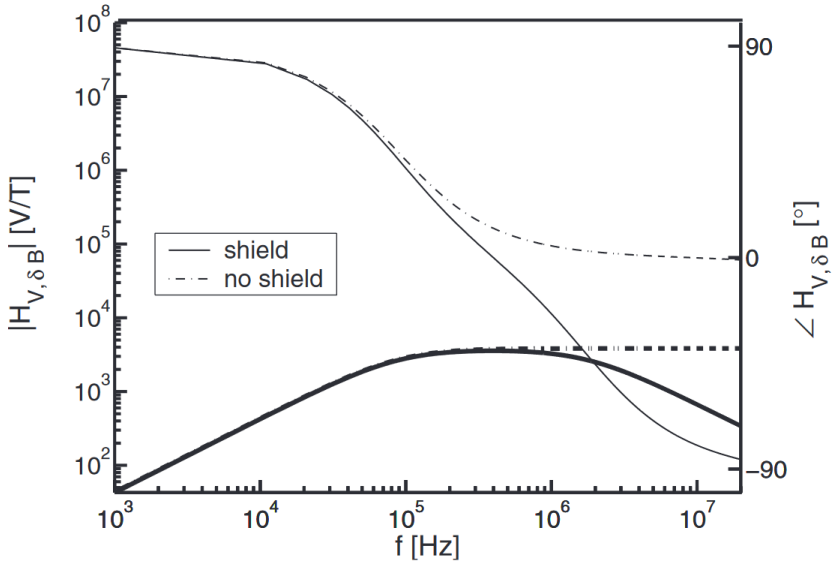

Figure 3.22: Magnitude (heavy lines) and phase (light lines) of the transfer function $H_{V,\delta B}$, with thin graphite conducting shielding (solid lines) and no shielding (dashed lines) cases [295]

3.4 Methods

3.4.1 Blob detection algorithm

The blob detection algorithm is inspired from the model proposed by Carralero *et al.* [196]. The signature of blob structures are detected in the raw signal of the ion saturation current I_{sat} as intermittent positive bursts propagating through the background plasma fluctuations. A representative example in Fig. 3.23 shows the application of this technique in ion saturation measurements at a probe pin in AUG. Two levels are defined: the baseline level I_{base} and the threshold I_{thres}. The baseline I_{base} is calculated from the mean value of all local minima. This is used to separate the background signal from the potential "blob event" peaks. The threshold I_{thres} determines the "exclusion zones" exceeding this level and enclosing a blob event. According to the convention from Boedo *et al.* [170] the threshold is defined as follows:

$$I_{thres} = \mu_{I_{sat}} + 2.5\ \sigma_{I_{sat}} \tag{3.34}$$

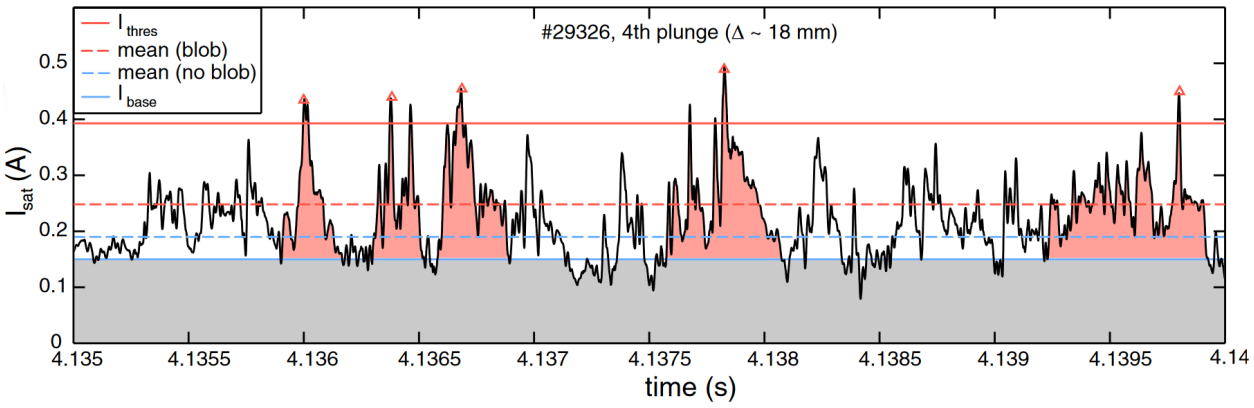

Figure 3.23: Blob detection algorithm: raw data from a I_{sat} signal during the fourth plunge of discharge #29326 in the SOL region beyond $\Delta \sim 18$ mm from separatrix [196]

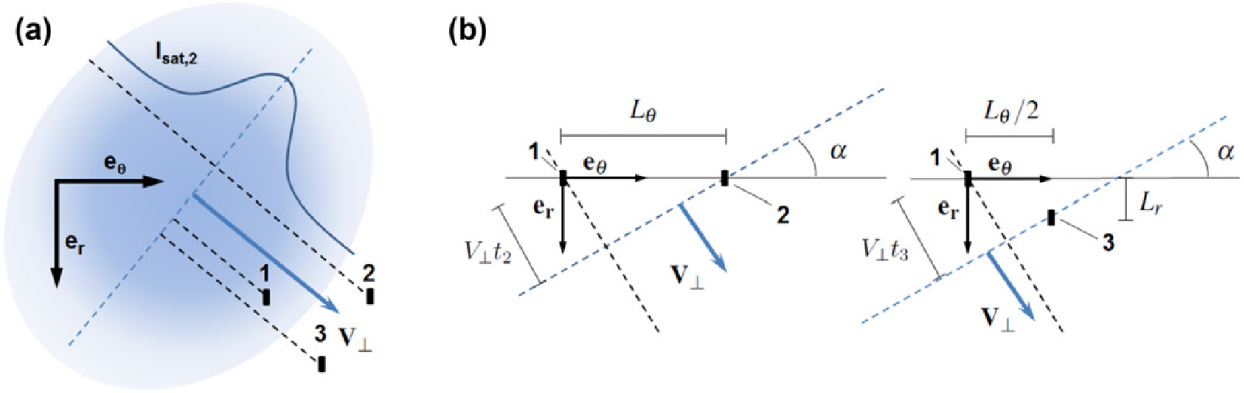

Figure 3.24: Blob propagation model: (a) generic blob propagating towards the three probe pins; (b) geometric description of the passage over the pins [196]

$\mu_{I_{sat}}$ is the mean value and $\sigma_{I_{sat}}$ is the standard deviation of the raw signal I_{sat}. The factor 2.5 is an arbitrary choice for adjusting the threshold [170]. The red solid line indicates the detection threshold. Detected events are indicated by red triangles. The exclusion zone around an event is indicated in red. The blue solid line represents the baseline, the dashed blue line represents the average signal without blobs and the dashed red line represents the average signal during blobs. The approach used here for the determination of the blob velocity is illustrated in Fig. 3.24. The signal $I_{sat,2}$ is represented over the trajectory. The blob can be modelled as a front propagating at a velocity $v_\perp$ in the perpendicular propagation with an angle α

with respect to the binormal direction. Both $v_\perp$ and α can be calculated from the cross-correlation times between pins 1 and 2, t_2, and 1 and 3, t_3. L_r and L_θ stand for the radial and binormal separation of the pins. These relations depend on the configuration of the probe head in the distribution of pins. Three approximations are required in the model, namely: the blob density distribution is approximated as an ellipse in the perpendicular plane, the blob perpendicular size is greater than the separation between pins, and the blob is symmetric with respect to an axis parallel to the direction of propagation.

3.4.2 Elzar code

Elzar is a code based on the *spice-weasel* background subtraction algorithm developed by B. Dudson [296]. It was then improved to become a tomographic inversion technique for identifying and tracking L-mode filaments from fast camera frames by T. Farley *et al.* [297, 298]. The tomographic inversion consists in reconstructing the information from camera frames by reprojecting the contained features in a new plane with simplified coordinates. Conventional inversion techniques rely on the Abel transform, however 3D objects such as filaments without a toroidal and poloidal symmetric structure require a more complex approach. Elzar exploits the helical geometry of the field similarly to the method of wavelet-vaguelette decomposition proposed by Nguyen *et al.* [299]. Elzar is based on two assumptions concerning the nature of filaments: firstly filaments are assumed to be aligned well to the background magnetic field which can be calculated via magnetic reconstruction; secondly the light emission from a filament is treated as being constant in the direction parallel to the magnetic field. Then a filament observed from fast camera frames is identified by superimposing the images to the field lines from the equilibrium magnetic field. Then the camera pixel intensities I are expressed as a weighted sum of basis images of uniformly emitting field lines, $I_{basis,j}$:

$$I = \sum_{j=0}^{N} \varepsilon_j I_{basis,j} \tag{3.35}$$

The emissivity vector ε_j describes the weighting of the jth field line basis image to the camera image. Then the aim is to reconstruct a 2D plane where field-line aligned filaments intersect and detected as enhanced emissivity areas. The Elzar algorithm is implemented in the following steps: pre-processing, inversion, and filament identification. Firstly, the pre-processing consists in subtracting the background light for

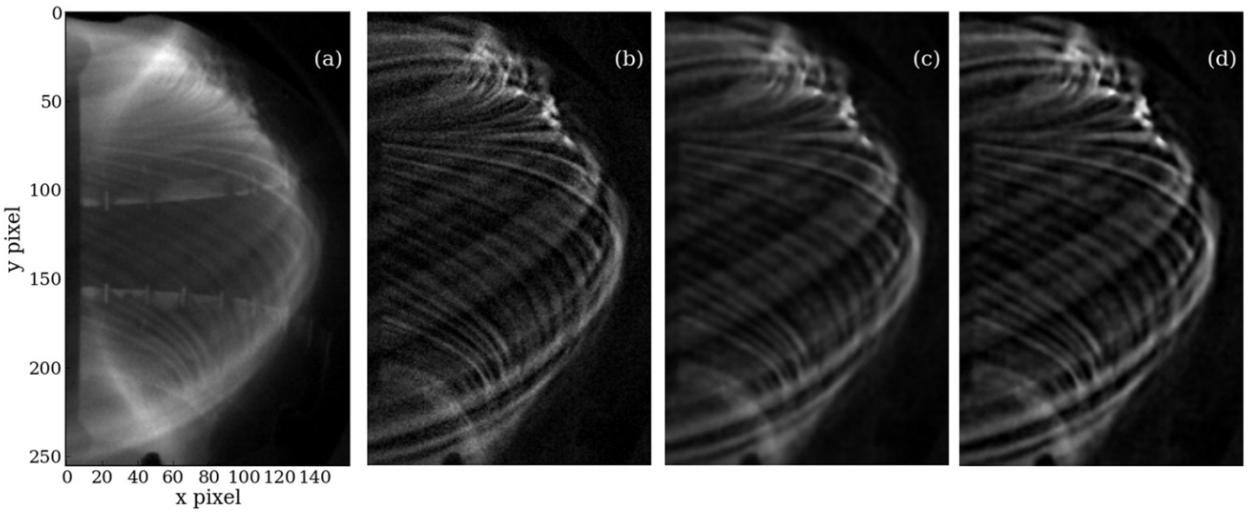

Figure 3.25: (a) Raw image from MAST shot 29841 at 0.22424 s. (b) Background subtracted image using 10 frames prior to the desired frame to construct a background. (c) Application of the bilateral median filter. (d) Application of a Gaussian de-blur [298].

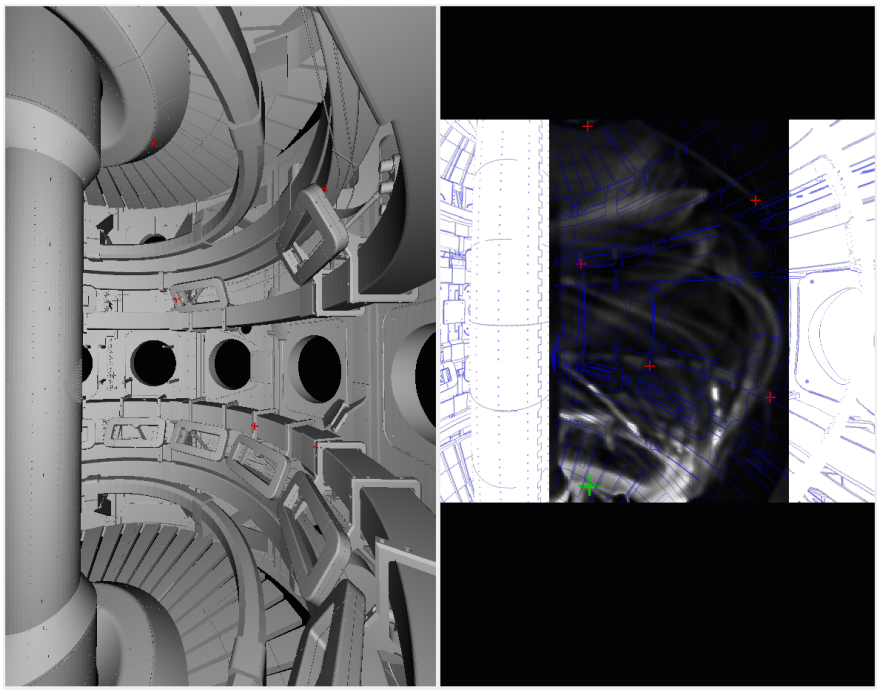

Figure 3.26: Calcam GUI calibration for MAST shot 29827. On the left a 3D MAST CAD model. On the right the fast camera frame taken at the ELM crash. Six pairs of red points representing features of the reactor interior were chosen. These pairs between the 3D CAD model and the 2D frame enable the mapping fit (blue schematics completing the 2D frame).

highlighting filaments. This step is crucial for distinguishing SOL filaments from vessel components in the background. The background subtraction is achieved by taking the pixelwise minimum in the light intensity over a set of frames that preceded the frame of interest [296]. Supplementary steps include applying a bi-lateral median filter for removing noise and applying a Gaussian de-blur to resharpen the image. The result of each pre-processing step is exposed in Fig. 3.25. Secondly, the inversion superimposes field lines on filaments of the pre-processed frame then projecting the traced emissivity from field lines in the inverted plane. This step requires a camera calibration using Calcam [300]. This software projects 3D coordinates of points along the field lines onto the 2D camera frame. In this way 3D magnetic information can be mapped onto the camera field of view. An example of Calcam calibration is shown in Fig. 3.26. The frame was chosen at the ELM crash with maximum light exposure when vessel components are more visible. The magnetic field structure is provided by the EFIT kinetic equilibrium reconstruction using a 4th order Runge-Kutta integrator [301, 302]. The time resolution for the EFIT reconstruction was chosen as high as possible around $1-2$ ms. The calibration provides a geometry matrix $\mathbb{G}$ that contains the ensemble of basis field line images $I_{basis,j}$ for each j field line. Then the equation (4.11) is reformulated in terms of the geometry matrix in the Einstein summation convention:

$$I_i = \mathbb{G}_{ij}\varepsilon_j \tag{3.36}$$

The index i here refers to the dimensions of the image vector $\boldsymbol{I}$ defined by the frame resolution $i = m \times n = 256 \times 160$. The dimensions $j = p \times q$ correspond to the resolution of the inversion grid describing the field aligned emission in the toroidal plane. The resolution of the inversion grid was empirically tested which requires a radial spacing < 4 mm and a toroidal spacing $< 0.2°$. The solution to the equation (4.12) passes through the ordinary least squares approach to obtain the inverted emissivity vector $\hat{\boldsymbol{\varepsilon}}$:

$$\hat{\boldsymbol{\varepsilon}} = \underset{\varepsilon}{\operatorname{argmin}} \parallel \mathbb{G}\boldsymbol{\varepsilon} - \boldsymbol{I} \parallel^2 \tag{3.37}$$

The notation "$\underset{\varepsilon}{\operatorname{argmin}}$" is the operator returning the value of $\boldsymbol{\varepsilon}$ that minimizes its argument. The ordinary least squares solution is given by [303]:

$$\hat{\boldsymbol{\varepsilon}} = (\mathbb{G}^T\mathbb{G}^{-1})\mathbb{G}^T\boldsymbol{I} = \mathbb{H}\mathbb{G}^T\boldsymbol{I} = \mathbb{H}\mathcal{E} \tag{3.38}$$

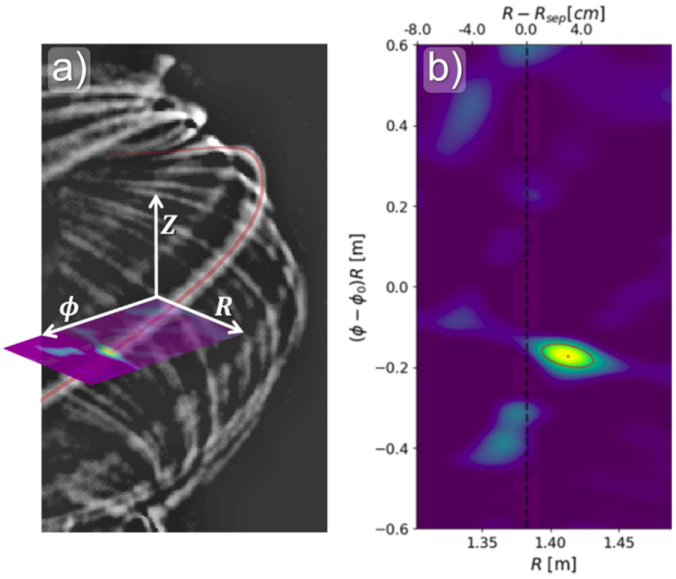

Figure 3.27: (a) An experimental camera frame from MAST shot 29852, with the pre-processing step applied. (b) Inversion calculated using the frame in (a). The inversion in (b) is also superimposed on the frame in (a) to illustrate the (R, ϕ) midplane coordinate system [298].

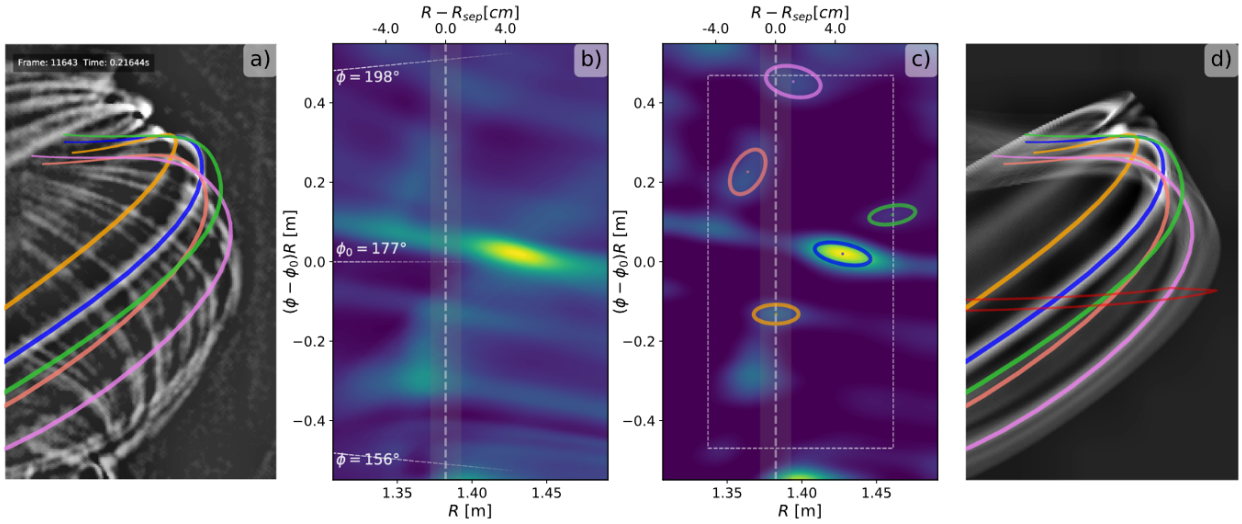

Figure 3.28: Elzar results for MAST shot 29852; a) Pre-processed frame with superimposed field lines; b) Reprojection of emissivity matrix the dashed vertical line represents the separatrix estimated by EFIT; c) Inversion plane with elliptical contours representing the intersection of projected filaments, the dashed white rectangle is the analysis region to avoid boundary effects; d) Reprojection of the emissivity data in (c), the red line indicates the inversion plane from which the emission is projected along field lines [298]

Here $\mathcal{E} = \mathbb{G}^T \boldsymbol{I}$ is the moment matrix and $\mathbb{H} = \mathbb{G}^T\mathbb{G}^{-1}$ the Gramian matrix with the notation T referring to the transpose. The problem has replaced the calculation of $\hat{\boldsymbol{\varepsilon}}$ by the inverse of the matrix $\mathbb{H}$ by means of a non-negative simultaneous algebraic reconstruction algorithm with Laplacian regularization [304]. The result of the inversion is shown in Fig. 3.27 b) where the intensities correspond to the $\mathcal{E}$ moment matrix. The inverted plane is parametrised in a new set of coordinates $(x,\, y)$ defined as $x = R$ and $y = (\phi - \phi_0)R$. The resulting inversion is a curved trapezoidal $(R, (\phi - \phi_0)R)$ plane where the length of y is kept constant. ϕ_0 is established as the plane center within the range (170°, 270°) *i.e.* from close-to-camera angle to far-from-camera angle. Thirdly, the filament identification is based on a wathershed algorithm by detecting intensity contours above a set threshold (Fig. 3.28 c)) then fitting 2D Gaussians for extracting positions, widths, amplitudes and orientations of the filaments. Lastly, due to geometrical distorsions and overlapping field lines, an additional benchmarking step can be applied by comparing detected filaments with synthetic filaments. Filaments can be matched as "true positives", otherwise these can be labeled as "false positives" or "missed" synthetic detections.

3.4.3 Wavelet transform theory

Signal processing is usually focused on identifying repetitive patterns associated with characteristic frequencies. A transform consists in a convolution of the signal with a function which shares similar characteristics to the original signal. The main goal is to decompose the signal into families of elementary waveforms. The transform theory presented in this section is an extension of Fourier's theorem to more general cases. The Fourier transform is a convolution method based on the decomposition of signals (*i.e.* time series) into a linear sum of independent sinusoidal periodic frequencies. The argument and modulus of the complex Fourier coefficients gives respectively the phase and the amplitude of detected harmonics. The waveform will be noted Ψ_γ with γ a multi-index parameter. This parameter acts as a 'filter' feature of the signal so spectral info can be extracted over a range of scales. For instance, in Fourier analysis this waveform is chosen to be sinusoidal in nature, *i.e.* $\Psi_\gamma(t) \sim \exp(i\omega t)$. The waveforms are noted $\hat{\Psi}_\gamma(\omega)$ in the frequency domain. The transform correlates a signal in the time-frequency space with its waveforms as probability

distributions defined by its localisation (defined as the positions in time and frequency), spread (defined as standard deviations in both domains) and energy (defined as the amplitude squared). The localisation corresponds to the waveform positions (u, ξ) in the time and frequency domains given by:

$$u = \int t|\Psi_\gamma(t)|^2 \mathrm{d}t \qquad \xi = (2\pi)^{-1} \int \omega|\hat{\Psi}_\gamma(\omega)|^2 \mathrm{d}\omega \tag{3.39}$$

The spread corresponds to the waveform variances (σ_t^2, σ_ω^2) in the time and frequency domains given by:

$$\sigma_t^2 = \int |t-u|^2|\Psi_\gamma(t)|^2 \mathrm{d}t \qquad \sigma_\omega^2 = (2\pi)^{-1} \int |\omega-\xi|^2|\hat{\Psi}_\gamma(\omega)|^2 \mathrm{d}\omega \tag{3.40}$$

The maximum energy corresponds to the square of transform coefficients S_f in both time and frequency domains given by the convolution of an arbitrary function f (*i.e.* representing the original signal) and a waveform Ψ_γ. The coefficients are computed via integration as a superposition of the signal and the waveform for each windowed section defined by positions (u, ξ) and spreads (σ_t^2, σ_ω^2):

$$|S_f(u,\xi)|^2 \;=\; \left| \int f(t)\Psi_\gamma^*(t)\mathrm{d}t \right|^2 \;=\; \left| (2\pi)^{-1} \int \hat{f}(\omega)\hat{\Psi}_\gamma^*(\omega)\mathrm{d}\omega \right|^2 \tag{3.41}$$

The notation $*$ corresponds to the complex conjugate. The accurate decomposition of the original signal in the frequency domain consists in optimizing the adjustment of the spread which relies on the chosen waveform function. The time and frequency resolutions (defined by the spreads in both domains) are restricted by the Heisenberg uncertainty principle:

$$\sigma_t \sigma_\omega \geq \frac{1}{2} \tag{3.42}$$

This decomposition can be interpreted by using the Heisenberg representation as shown in Fig. 3.29. As an example the chosen waveform is a Gaussian waveform of the form:

$$g(t) = \exp(i\omega t)\, \exp\left(-\frac{t^2}{2\sigma_t^2}\right) \tag{3.43}$$

As seen in the box represented in Fig. 3.29, the product $\sigma_t\sigma_\omega$ defines a resolution window that is constant for a waveform of this form *i.e.* the area covered by the box is always fixed no matter the position or energy. This limitation affects the identification of low and high frequency features in a signal. A function that avoids this drawback is the wavelet. The Morlet wavelet was proposed by Grossmann and Morlet in order to decompose Hardy functions [305]. The Morlet wavelet consists of a complex exponential modulated by a

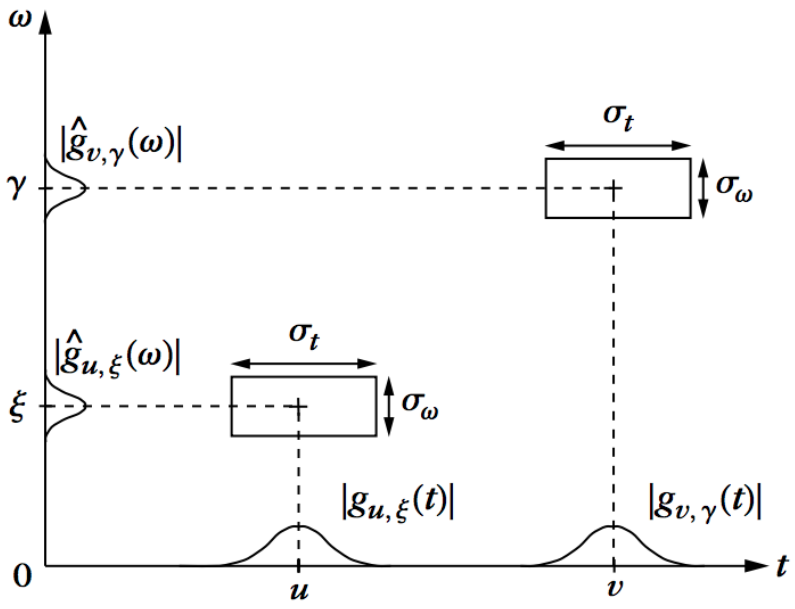

Figure 3.29: Heisenberg representation of Gaussian waveforms $\Psi_\gamma = g$ in a time-frequency $(t,\ \omega)$ space; $\sigma_t\sigma_\omega$ boxes represent the width of the function in both time and freq domains [306]

Gaussian as shown in Fig. 3.30:

$$\psi_s(t) = (\pi s^2)^{-1/4} \exp\left(\frac{i\omega_0 t}{s}\right) \exp\left(-\frac{t^2}{2s^2}\right) \tag{3.44}$$

This waveform introduces an additional parameter as the γ index: s the wavelet scale (in seconds). The parameter ω_0 is a nondimensional frequency defining a mother wavelet $\psi_{u,s}(t)$ [307]. The mother wavelet is an initial wavelet located at the time index u which is used to generate a family of multiple wavelets by translation, *i.e.* shifting along the time index v, and by dilation, *i.e.* adjusting the scale s which stretches or widens its width. The wavelet transform for a discrete series x_u with u the series index of N elements at a time-step δt is the convolution of the series x_u with a generated wavelet $\psi_{u,s}(t)$ acting as a window function. The discretization of Eq. 3.41 with a wavelet as the chosen waveform takes the following expression:

$$W_v(t,s) = \sum_{u=1}^{N-1} x_u \psi^*_{u,s}(t) = \sum_{u=1}^{N-1} x_u \frac{1}{\sqrt{s}} \psi^*_s\left(\frac{u-v}{s}\delta t\right) \tag{3.45}$$

Here * is the complex conjugate. This transform works in a similar way as a Fourier transform by translation of the x series elements, plus including the dilation of the wavelet but with a zoom feature (modifying the s scales). The translation is parametrised by the series index $u = 0, 1, ..., N-1$ with $x_u = u\delta t$. For reducing

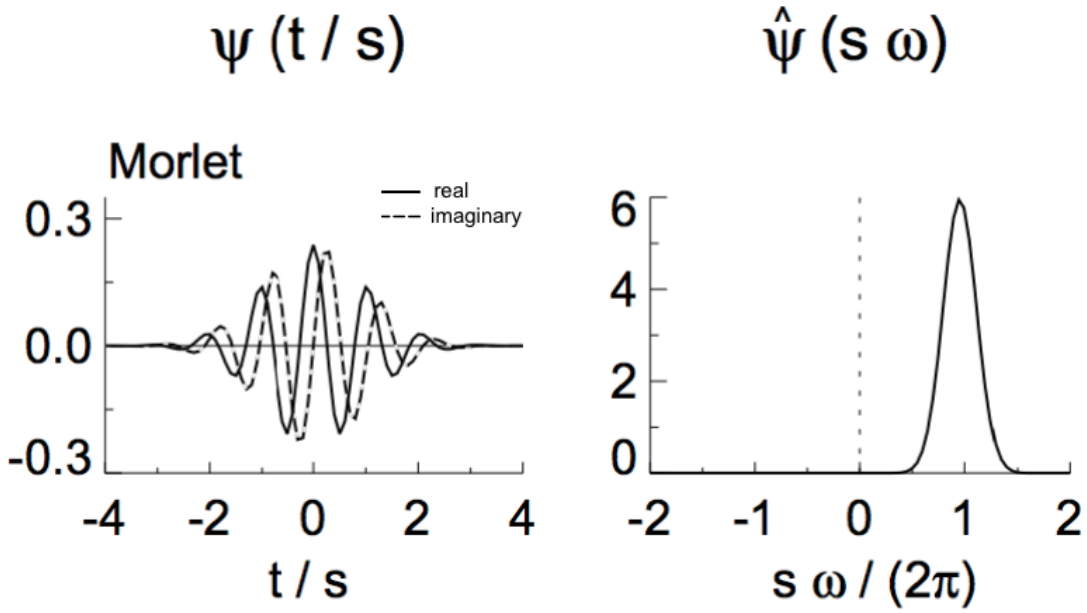

Figure 3.30: Morlet wavelet $\Psi_\gamma = \Psi$ in the time domain (left) and transform $\hat{\Psi}_\gamma = \hat{\Psi}$ in the frequency domain (right). Real part (solid) and imaginary part (dashed) for the wavelets in the time domain. The scale was chosen to be s = 10 δt for graphical representation [307]

the computational effort, the "dyadic" convention of the scaling parameter is defined by fractional powers of two such as $s = s_0 2^{j\delta j}$. The smallest resolvable scale is chosen as $s_0 \sim 2\delta t$. The dilation is parametrised by the octave index varying as $j = 0, 1, ..., J$ with $J = (\delta j)^{-1} \log_2(N\delta t/s_0)$ and the factor for scale averaging is empirically chosen as $\delta j \sim 1/12$ which depends on the spectral width of the wavelet [307]. However, the computed values at the boundaries of the spectrum are not reliable. The portion of the wavelet beyond the edges of the signal time produces erroneous coefficients. The error becomes more important when decreasing the octave index j, *i.e.* for larger wavelets. These boundary effects are indicated by the so-called cone of influence. Note that this waveform has the following form in the frequency space:

$$\hat{\psi}_{u,s}(\omega) = \sqrt{s}\hat{\psi}\left(s\left(\omega - \frac{\eta}{s}\right)\right) \tag{3.46}$$

Here η/s is the position in the frequency domain. In the Heisenberg representation, the transform coefficients $W_v(t, s)$ contained in a box spread differently due to the dilation as seen in Fig. 3.31. The width of the spreading box is adjusted by the wavelet scale s. The additional factor $1/\sqrt{s}$ in Eq. 3.45 (and $\sqrt{s}$ in Eq.

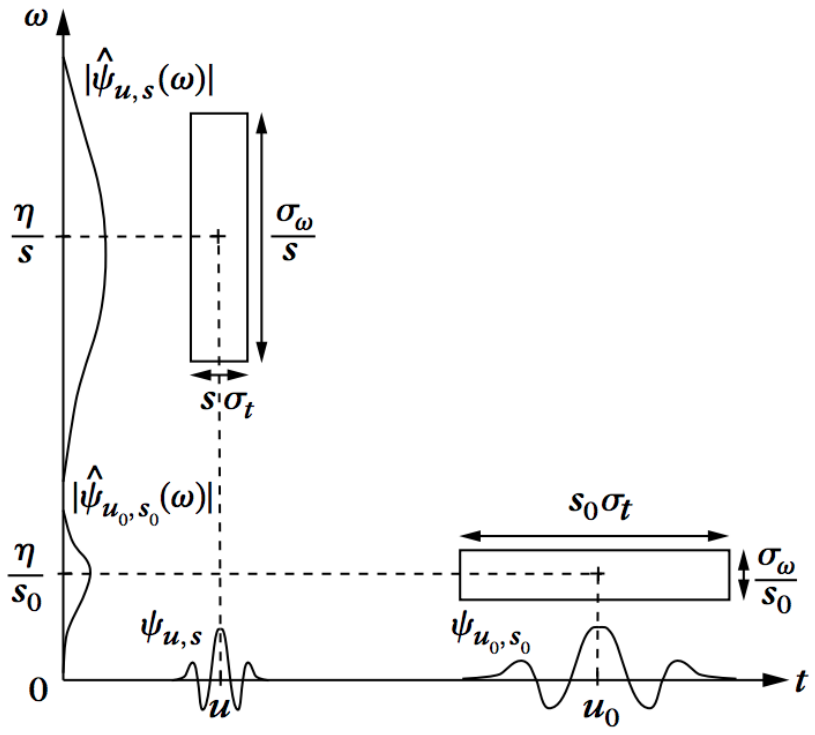

Figure 3.31: Heisenberg representation of Morlet wavelets $\Psi_\gamma = \psi$ in a time-frequency (t, ω) space [306]

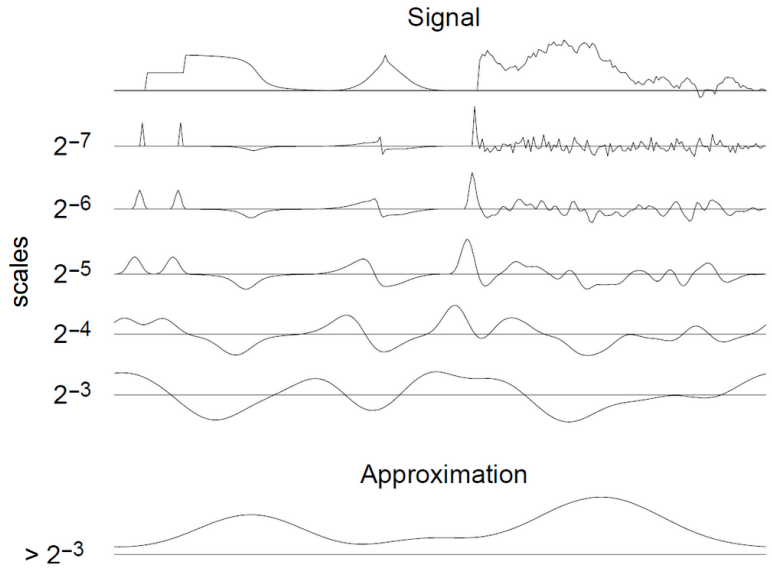

Figure 3.32: A representation of a cascade of convolutions for an arbitrary signal (top) by using wavelet transforms computed at successive dyadic scales $2^{-7} \leq 2^j \leq 2^{-3}$; the approximation curve (bottom) carries the lower frequencies corresponding to scales larger than 2^{-3} [306]

3.46) modifies the expression of the variance in Eq. 3.40 which defines the spreading box. On the time axis the scale increases with the box's width $s\sigma_t$ but decreases the box's width σ_ω/s in the frequency space. The process of a wavelet transform applied to a signal can be interpreted as a cascade of convolutions as shown in Fig. 3.32. For each scale s, a convolution of the signal with a pre-defined wavelet is computed. Then a cascade of N convolutions gives the transform coefficients $W_v(t,s)$ constructing a spectrum. The scaling acts as a moving filter on the signal able to resolve the lowest and highest frequencies. For graphical representation the wavelet spectral power or spectrogram P_ψ is defined as:

$$P_\psi(t,s) = \frac{1}{s}\left|W_v(t,s)\right|^2 \tag{3.47}$$

Note that the denominator in Eq. 3.47, *i.e.* the factor $1/s$, is a correction for restoring a bias in the spectral power when increasing frequencies [308, 309]. For simplification, the spectrogram $P_\psi(t,f)$ can be re-expressed in terms of frequencies instead of scales. For graphical representation, the spectrogram $P_\psi(t,f)$ can be normalised with spectral amplitudes between 0 and 1:

$$P_\psi(t,f) \equiv \frac{P_\psi(t,f) - P_{\psi,min}(t,f)}{P_{\psi,max}(t,f) - P_{\psi,min}(t,f)} \tag{3.48}$$

The wavelet spectrum is often referred as scalogram and the frequency bands are rescaled as function of $\log_2(s)$ instead of s. Assuming that the normalized mother wavelet has unit energy, the relationship between scale s and frequency ξ is [306]:

$$s = \frac{\omega_0}{(2\pi\xi\delta x)} \tag{3.49}$$

In this thesis the python package PyCWT [310] was used to perform wavelet transforms. The implemented functions for the spectral analysis (chapter 6) are included in the Appendix.

Chapter 4

Edge plasma conditions and shoulder formation in COMPASS

4.1 Introduction

The understanding of heat and particle transport is an important area of research in tokamak physics and plasma confinement. More specifically, predicting the SOL behaviour is crucial for ensuring the plasma stability at the edge and reducing the impact on the walls due to erosion. Transient structures (*i.e.* blobs, filaments, etc). tend to form at the separatrix and propagate radially outwards due to the cross-field transport mechanism (*i.e.* $E \times B$ drift). However, depending on the plasma conditions, density perturbations occur at the SOL which in turn causes changes in the properties of these transient structures. As mentioned in chapter 2 section 2.2.5, significant changes in the SOL decay lengths and blobs elongation are associated with the manifestation of a SOL intermediate region. This phenomenon is known as a *shoulder* because of its characteristic shape in the density profile. The motivation for analysing the evolution of blobs during shoulder formation is to understand the SOL behaviour in high density COMPASS plasmas and, to some extent, validate blob scaling laws for multi-machine theory. For that purpose the data acquired by the

probes located at the edge of COMPASS contains the signatures of filamentary structures in the SOL and the state of the plasma at the divertor. This chapter presents the work undertaken during the Fusion-CDT collaboratory project supervised by J. Adamek and K. Kovarik on COMPASS at IPP Prague. The analysed data originates from the discharges produced during the Winter Course for the Erasmus Mundus Training (EMTRAIC) in December 2017, The main goal is to analyse the edge plasma conditions in COMPASS and determine what requirements are needed for the formation of a shoulder in the SOL density profile. The structure of this chapter is as follows: in section 4.2 the description of experimental setup with the horizontal reciprocating manipulator and different probe heads and the divertor probes; in section 4.3 the application of the blob statistical algorithm and the blob propagation model; in section 4.4 the list analysed discharges; in section 4.5 the results from the data analysis applied to the selected shots; in section 4.6 the summary, discussions on results, and suggestions for the future work.

4.2 Experimental setup

4.2.1 Horizontal reciprocating manipulator and probe head

The horizontal reciprocating manipulator in COMPASS was originally conceived at UKAEA that was included with COMPASS-D when it was loaned to IPP Prague [242]. The geometry of the horizontal manipulator is presented in Fig. 4.1. At the top of the manipulator it is possible to connect interchangeable probe heads with different sets of probes depending on the aim of each experiment. When inactive in parking position the probe head is located at the vacuum window sector. When a measurement is requested the manipulator is moved by pneumatic pistons to 6 atm, accelerated by an equivalent gravitational force of 4 g, reaching 1.5 m s^{-1}. The probe head passes through a gate valve emerging into the vessel at the outer midplane. The probe head penetrates radially into the edge plasma around $R = 0.72 - 0.78$ m in the vicinity of the separatrix with an immersion time of ~ 0.1 s. The reciprocating mechanism was recently upgraded to allow the probe head to reach the pedestal region. The materials used for the probe head manipulator were stainless steel and vespel for insulation. The short immersion time and the choice of the material are chosen

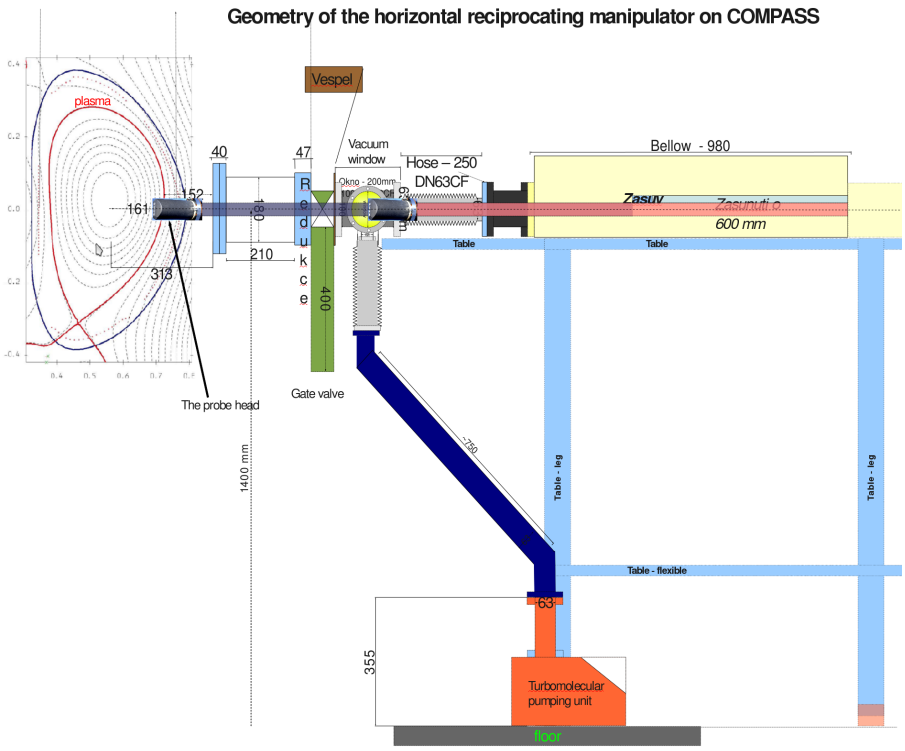

Figure 4.1: Schematics of the horizontal manipulator in COMPASS [311]

to avoid self-emission and melting of the probes as well as the release of impurities into the plasma. In order to perform this rapid measurement the data acquisition system provides a high temporal submicrosecond resolution of 5 Msamples / s [312]. The diagnostic used during EMTRAIC was the Reynolds stress probe head presented in Fig. 4.2 mounted on the horizontal reciprocating manipulator. This probe head was conceived for studying sheared flows during the L-H transition [313]. The multi-pin configuration combining LPs and BPPs allows the measurement of electric fields in different orientations and the tracking of the spatio-temporal evolution from the passing blobs. The original design was upgraded into the existing design in order to mitigate the appearance of disruptions by plasma cooling due to the probe head [314]. The upgrade included two new probes (BPP4 and BPP6) and resulted in the current arrangement as shown in Fig. 4.2. This design avoids the shadowing between probes during measurements. The probe head material, previously graphite, was replaced by boron nitride to avoid short-circuiting between probes, whereas boron nitride allows a disposition where probes can be closer to each other. A LP pin consists of a graphite cylinder with diameter of 0.9 mm a length of 1.5 mm. A BPP pin consists of a stainless-steel rod with a diameter

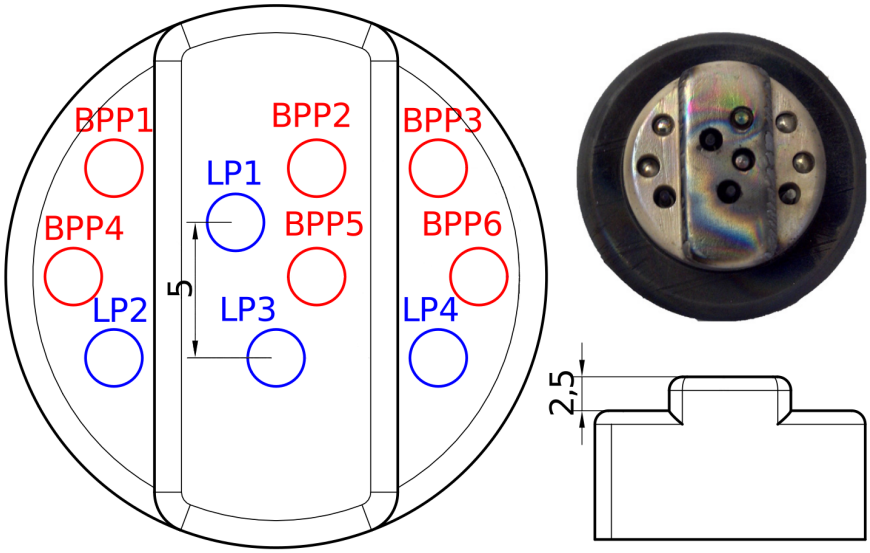

Figure 4.2: Schematics (left and bottom right) and picture (top right) of the Reynolds stress probe head used for EMTRAIC measurements. Dimensions in mm. Left view and right top view are in the poloidal/toroidal plane with respect to the tokamak, right bottom view is in the radial/toroidal plane [313].

of 2 mm, retracted by 0.5 mm in a 3 mm deep hole in the boron nitride support. The separations between the probes are approximately 2.5 mm radially and $\sim$ 4 mm poloidally. When inserted into the plasma, the head's position was maintained for 50 ms on the outer midplane at 2 cm from the Last Closed Flux Surface (LCFS). The probe head was slightly rotated with an angle of $\sim 5°$ in order to align the toroidal axis with the magnetic field lines. During the data acquisition, signals were recorded with a sampling time of 0.2 μs. All LP pins were biased with a constant voltage of -270 V in order to measure exclusively the ion saturation current $I_{i,sat}$. None of the BPP pins were considered in the analysis of this study.

4.2.2 Divertor probes

The divertor probes are positioned as shown in Fig. 4.3 with 56 BPPs and 110 roof-top shaped LPs mounted on the divertor target. The divertor setup is an upgrade from a previous design [315]. The BPPs were arranged in one array that is separated in two sections: from 1 to 25 on the High Field Side (HFS), and from 26 to 56 on the Low Field Side (LFS). The LPs were arranged in two arrays labelled LPA and LPB of 55

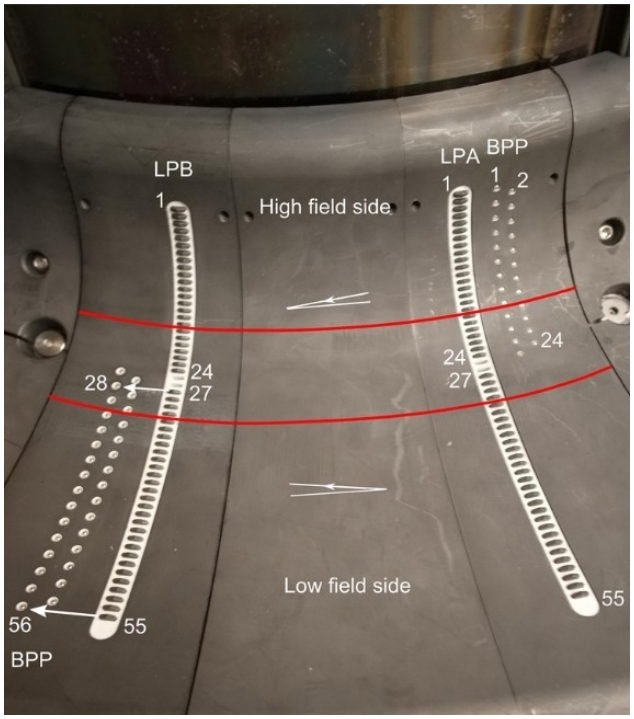

Figure 4.3: Picture of divertor probes in COMPASS [316]. Langmuir probes are mounted in two arrays (LPA and LPB) and Ball-Pen Probes are mounted in one array divided in inner (HFS) and outer (LFS) sides. The red lines indicate the inner and outer strike points of the separatrix and were calculated in the conditions of the flat-top phase of the L-mode discharge #13025. The magnetic field line orientation for a standard plasma current and toroidal magnetic field orientation are also indicated with white arrows.

probes each covering the radial extent of the target. Each BPP consisted of a boron nitride shielding tube with a diameter of 3 mm, and a stainless-steel collector with a diameter of 2 mm. All of the BPP collectors were retracted to a depth of ~ 0.4 mm within the shielding tube. Each LP had a graphite collector with a diameter of ~ 6.5 mm fixed in a boron-nitride holder which protrudes 1.5 mm above the graphite surface. The roof-top shape is characterised by a chamfer with an angle of 20° and an effective collection area of 2.8 mm^2. The dimensions of the roof-top shape LP are specified in Fig. 4.4. The rooftop-shaped design is meant to reduce the impact of the parallel heat flux on the collector surface, however, being vulnerable to sheath-expansion effects. The poloidal distance between neighboring probes is ~ 3.5 mm and the toroidal distance between neighboring BPPs and LPs is ~ 2 cm. The large separation between both LP arrays was meant to avoid mutual shadowing due to the low inclination angle of the field lines. Only data from probes

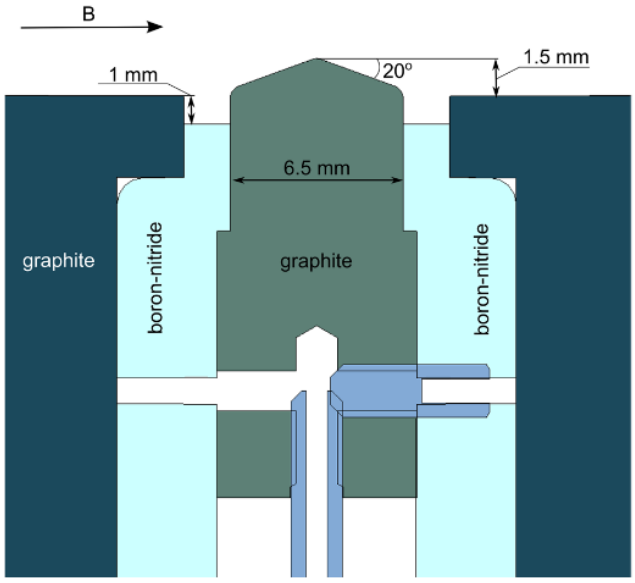

Figure 4.4: Cross-section schematic of a rooftop-shaped LP mounted in the COMPASS divertor. The probe collector, made of graphite, is fixed inside a boron-nitride holder [316]

located in the Low Field Side will be analysed. This list includes: from BPP28 to BPP56, from LPB27 to LPB55, and from LPA27 to LPA55. From Fig. 4.3 (left side) the arrays BPP28 - BPP56 and LPB27 - LPB55 were set to floating mode (*i.e.* null current) to measure Φ^{BPP} and V_f respectively. In Fig. 4.3 (right side) the probes of the array LPA27 - LPA55 were negatively biased with -270 V for I_{sat} measurements. All probe signals are acquired by the data acquisition electronics connected to 200 channels with a sampling frequency of 4 Msamples / s. Signals were recorded with a sampling time of 0.2 μs. From this probe arrangement, several parameters characterising the plasma at the divertor can be measured. The electron temperature is calculated as described in Eq. 3.20 between neighbouring (LPAs, LPBs) and BPPs with the empirical factor $\alpha_{div,deu} = \alpha_{LP} - \alpha_{BPP} = 1.4$ for deuterium plasmas at the divertor. The LPA probes evaluate the electron density assuming the plasma quasi-neutrality at the divertor by using Eq. 3.16:

$$n_e = \frac{I_{i,sat}}{e \times A \times c_s} \tag{4.1}$$

The probe surface area is $A = 2.8$ mm^2 and the ion acoustic speed takes into account the ion temperature contribution in the Bohm criterion assuming that $T_e \sim T_i$ and with m_D the mass of deuterium:

$$c_s \sim v_i \sim \sqrt{\frac{T_e + T_i}{m_D}} \sim \sqrt{\frac{2T_e}{m_D}} \tag{4.2}$$

The parallel heat flux at the divertor is defined by the following scaling:

$$q_{\parallel,div}[\mathrm{W/m^2}] = \gamma \times I_{sat}[\mathrm{A}] \times T_e[\mathrm{eV}] \tag{4.3}$$

The sheath heat transmission factor γ was predicted as ~ 11 W m^{-2} K^{-1} for COMPASS [317] and assumed to be constant along the target. This value was verified by IR thermography measurements [318]. The divertor collisionality is defined by [188]:

$$\Lambda_{div} = \frac{L_\parallel \nu_{ei}}{c_s} \frac{\omega_{c,i}}{\omega_{c,e}} \tag{4.4}$$

Here $L_\parallel$ is the connection length, $\omega_{c,e}$ and $\omega_{c,i}$ are the electron and ion gyroradius respectively, and ν_{ei} is the electron-ion collision frequency defined by [319]:

$$\nu_{ei} = \frac{\sqrt{2} e^4 n_e \ln \Lambda_c}{12\pi^{3/2}\sqrt{m_e}\epsilon_0^2 (k_B T_e)^{3/2}} \tag{4.5}$$

$\ln \Lambda_c$ is the Coulomb logarithm defined depending on the temperature range [319]:

$$\begin{aligned} \ln \Lambda_c &= 23 - \ln\left(n_e^{1/2}[\mathrm{cm^{-3}}] Z_i T_e^{-3/2}[\mathrm{eV}]\right) \qquad \frac{m_e}{m_i} T_i < T_e < 10 Z_i^2 \mathrm{eV} \\ \ln \Lambda_c &= 24 - \ln\left(n_e^{1/2}[\mathrm{cm^{-3}}] T_e^{-1}[\mathrm{eV}]\right) \qquad \frac{m_e}{m_i} T_i < 10 Z_i^2 \mathrm{eV} < T_e \end{aligned} \tag{4.6}$$

4.3 Blob statistical analysis

4.3.1 Blob detection

The probe signals are treated following the mentioned steps below in order to quantify the occurrence of blobs in the ion saturation currents. The raw signal is first smoothed with a Savitzky-Golay filter [320] using a third order polynomial fit and a filter window of 10 μs. An example of the blob detection algorithm is applied to a I_{sat} signal is shown in Fig. 4.5. The definition of the threshold I_{thres} is given by Eq. 3.34. The region below the baseline is rejected for this analysis. All regions above the baseline which exceed the threshold are denoted as exclusion zones in red. The peak maximum of an exclusion zone (*i.e.* a red triangle) represents a blob event. However, due to the structures' turbulent nature, the threshold might incorrectly identify fictitious blobs. For instance, several peaks might appear inside the same exclusion zone

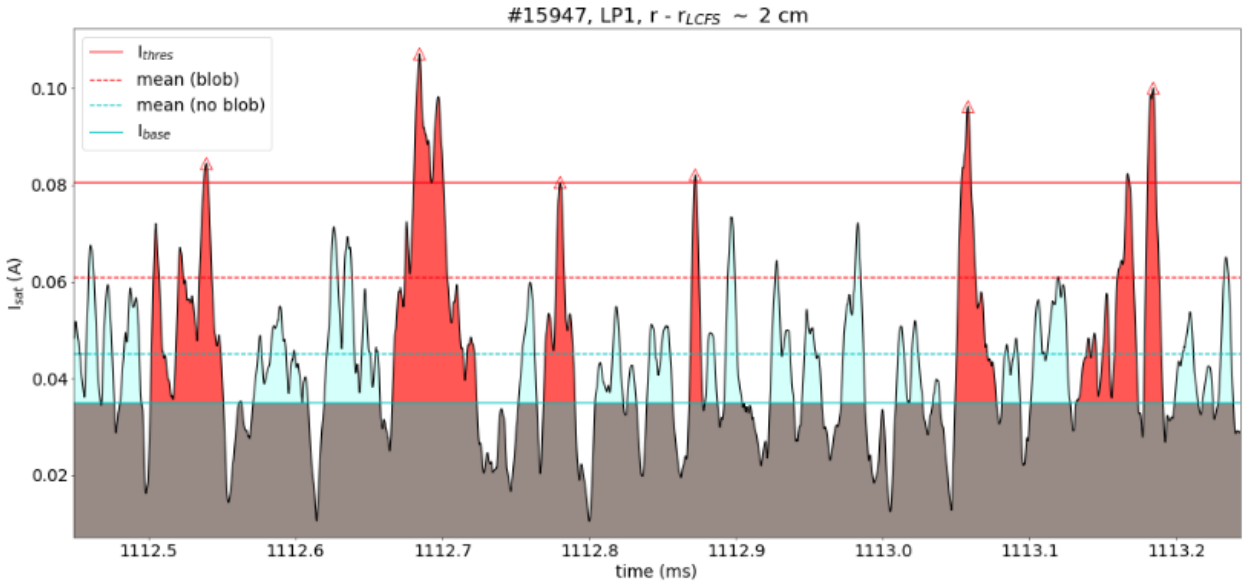

Figure 4.5: Blob detection algorithm applied to I_{sat} signal from LP1 at 2 cm from the LCFS during discharge #15947. Red triangles are *blob events*, red zones are *exclusion blob zones*, light-blue zones are *neglected non-blob zones* and the grey zone is the *background*. The red solid line is the *threshold level* I_{thres}, red (light-blue) dashed lines are the mean values of all *blob* (*non-blob*) zones, and the blue solid line is the *baseline level* I_{base}. Restriction of 25 μs is applied to the neighbouring peaks at 1113.16 and 1113.18 ms.

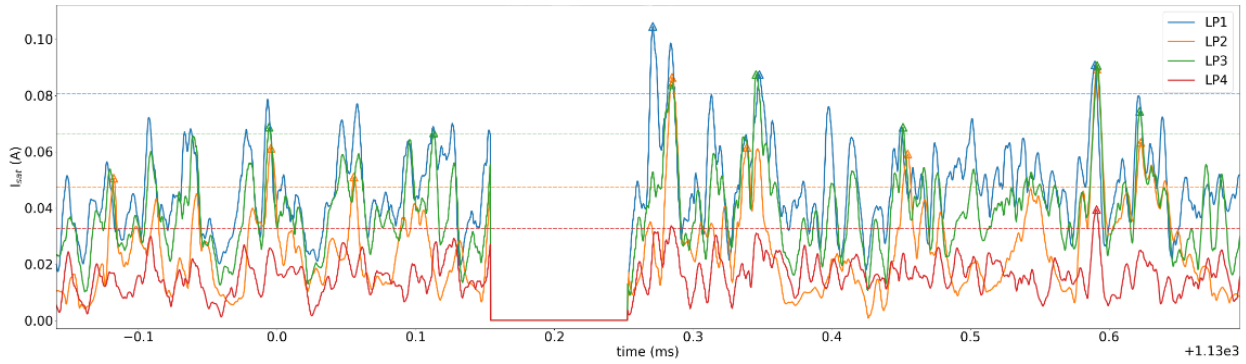

Figure 4.6: Blob detection using 4 I_{sat} signals from different probes (LP1, LP2, LP3, LP4) of the Reynolds probe head. Between $t \sim [0.15,\ 0.25]$ ms, high spikes were removed (by setting to zero) to avoid false correlations between adjacent peaks. Each dashed color line corresponds to a threshold level of a LP signal.

or adjacent exclusion zones are too close to each other representing the same blob. This is the case of the last two neighbouring exclusion zones in Fig. 4.5: these represent the same blob event. In order to ensure that individual blobs are distinguishable from each other, two consecutive blob events must be separated by at least 25 μs [321]. If several peaks are with 25 μs of each other then the peak with the highest amplitude is allocated. Additionally, in order to avoid false detections (*e.g.* unidentified peaks with extremely high and rapid currents), it is assumed that the condition $I_{sat} > I_{thres}$ must be satisfied in an exclusion zone for at least 1 μs, otherwise the peak is not considered as a blob event. Then this peak is omitted by by setting the signal value to zero. An example is exposed in Fig. 4.6. Therefore a peak is allocated to a blob if it satisfies the following criteria: it exceeds the threshold, it lies in an exclusion zone, it is the highest peak if there are several within 25 μs, and it lasts for more than 1 μs. Note that different signals from each probe manifest different amplitudes. The probe LP4 with the lowest collected current is probably located in the shadowing side of the probe head.

4.3.2 Conditionally averaged blob

A typical blob can be represented by averaging over all detected blob events to obtain a conditional averaged blob. The Conditional Average (CAV) of the I_{sat} quantity is defined by [321]:

$$\mathrm{CAV}_{I_{sat}}(t) = N_{blob}^{-1} \sum_{event=1}^{N_{blob}} I_{sat}(t_{event} + t) \tag{4.7}$$

N_{blob} is the number of blob events detected through the entire data set for one probe, t_{event} is the time of each blob event, and t is the time averaging interval. This interval is fixed at 50 μs long centered at the blob event time (*i.e.* $\pm$ 25 μs), and is long enough to capture the blob's characteristics but short enough to exclude most of the background. In Fig. 4.7 an example of conditional averaging applied to the data sets from 4 LPs is shown. Before CAV is applied each data set is subtracted to the mean value $\mu_{I_{sat}}$ and normalized to the standard deviation $\sigma_{I_{sat}}$. The average number of blobs detected is obtained by calculating the mean value of all blob events from the data set for each pin. The full width half maxima of these 4 CAV signals suggest that the characteristic blob event lifetime is around 10 μs.

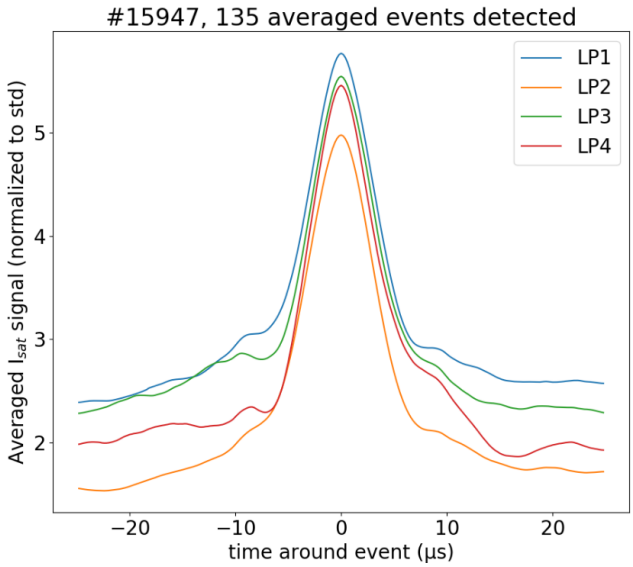

Figure 4.7: Example of conditional averaged signals from 4 LPs (discharge #15947). The average number of blob events is $\langle N_{blob} \rangle = 135$.

4.3.3 Cross correlation

The cross correlation method allows to measure the cross-correlation times *i.e.* the time delays between adjacent blob events from the different LP pins. The cross correlation between two probes, LP1 and LP2, is defined by their respective ion saturation currents:

$$C_{CC}(\tau) = \sum_t I_{sat,1}(t+\tau) \cdot I^*_{sat,2}(t) \tag{4.8}$$

τ is the time delay, and $*$ is the notation referring to the complex conjugate. The correlation time or phase shift corresponds to the angle of the complex argument of the cross correlation function. There are two possible correlations: between two separate probes which returns the cross correlation time between an event is passing between these probes; with the probe itself which returns the auto correlation time between events passing the probe. The auto-correlation times noted t_{AC} is the duration of a blob event sensed by one probe, defined as the full width at half maximum of the argument of the C_{AC} function. An example of autocorrelation times per blob event from the LP1 signal is shown in Fig. 4.8 with $t_{AC} \sim 8.5$ μs in average.

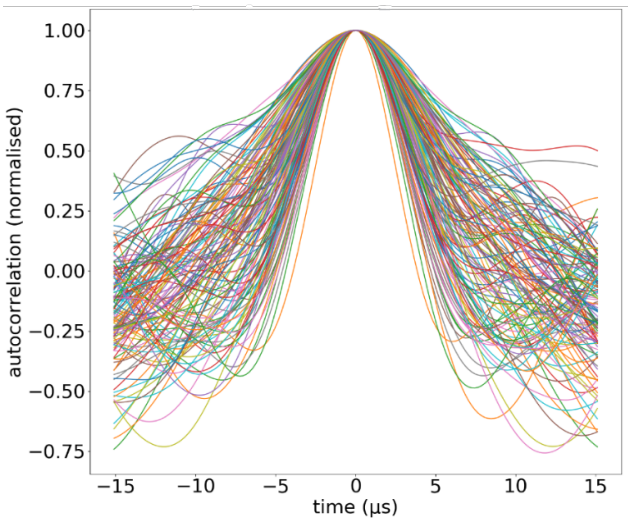

Figure 4.8: Example of auto-correlation times functions per blob event from LP1 signal (discharge #15947).

4.3.4 Blob propagation model

The propagation model used here for the determination of the blob velocity was inspired from the model proposed by Carralero *et al.* [196]. This approach was adapted to the geometry of the Reynolds stress prohe head. A schematic of the model is shown in Fig. 4.9 (a) describing the blob motion across pins in the perpendicular plane to the toroidal magnetic field. The same approximations in the model are taken here, namely: the blob density distribution is approximated as an ellipse in the perpendicular plane, the blob perpendicular size is greater than the separation between pins, and the blob is symmetric with respect to an axis parallel to the direction of propagation. The assumptions mentioned in chapter 3 section 3.4.1 are verified later when obtaining the results on the blob size. In Fig. 4.9 the propagation plane is defined by vectors $\boldsymbol{e_r}$ and $\boldsymbol{e_\theta}$ denoting radial and poloidal directions respectively. The light-blue dashed line represents the maximum peak of blob density distribution. Consequently, when the blob passes by each pin a peak is observed. The peak delays between pins correspond to the cross-correlation times. It is possible to establish a system of equations with the aim of finding the perpendicular velocity $v_\perp$ and the angle α that describe the blob propagation. The angle α is defined with respect to the poloidal direction. The cross-correlation times are defined by the subscripts: t_{12} between LP1 and LP2, and t_{13} between LP1 and LP3. Distances r_{12}, p_{12} and p_{13} are radial (r) and poloidal (p) distances as shown in Fig. 4.9 (b). The following relations

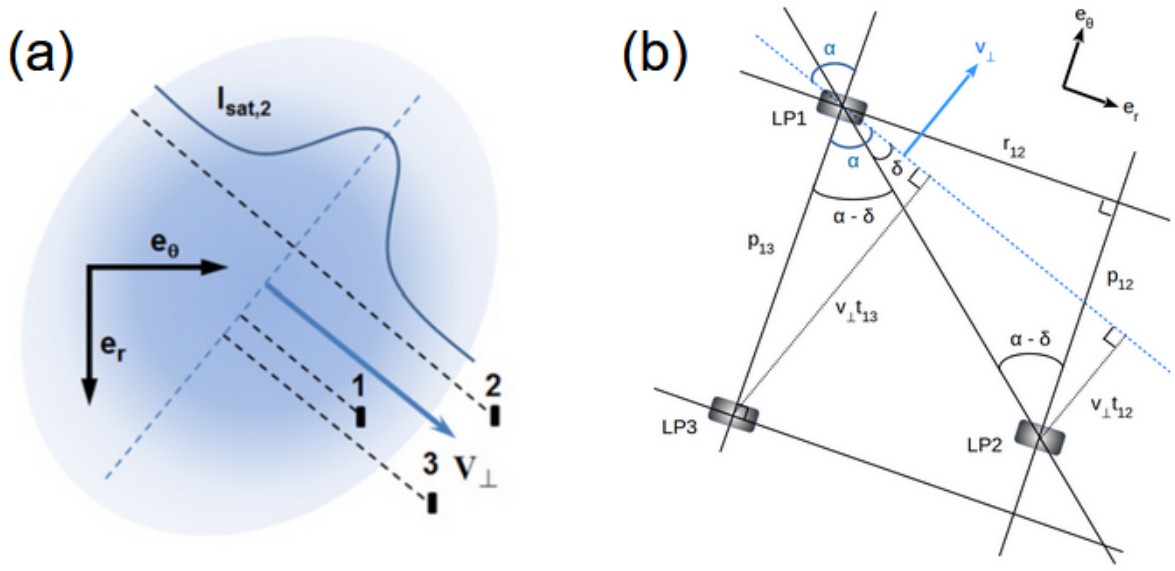

Figure 4.9: Schematics of the blob propagation model: (a) a generic blob propagating towards three I_{sat} pins of the probe head used in AUG [196]; (b) geometric description of the (LP1, LP2, LP3) pins of the Reynolds stress probe head used in COMPASS. Vectors $\boldsymbol{e_r}$ and $\boldsymbol{e_\theta}$ define the radial and poloidal directions. The light-blue dashed line indicates the blob's position being orthogonal to the propagation velocity $v_\perp$.

can be obtained using trigonometry:

$$\sin\alpha = \frac{v_\perp t_{13}}{\mathrm{p}_{13}} \tag{4.9}$$

$$\sin\delta = \frac{v_\perp t_{12}}{\sqrt{\mathrm{r}_{12}^2 + \mathrm{p}_{12}^2}} \tag{4.10}$$

$$\delta = \alpha - \arctan\left(\frac{\mathrm{r}_{12}}{\mathrm{p}_{12}}\right) \tag{4.11}$$

By combining these equations the propagation velocity $v_\perp$ is then given by the distances and the cross-correlation times between the LP pins:

$$v_\perp = \left(\left(1 + \left[\frac{\mathrm{p}_{12}}{\mathrm{r}_{12}}\right]^2\right)\left[\frac{t_{13}}{\mathrm{p}_{13}}\right]^2 + \left(\Upsilon - \frac{t_{13}}{\mathrm{p}_{13}}\frac{\mathrm{p}_{12}}{\mathrm{r}_{12}}\right)\Upsilon\right)^{-1/2} \tag{4.12}$$

$$\Upsilon = \frac{t_{12}}{\sin\left(\arctan\left(\frac{\mathrm{r}_{12}}{\mathrm{p}_{12}}\right)\right)\sqrt{\mathrm{r}_{12}^2 + \mathrm{p}_{12}^2}} \tag{4.13}$$

Additionally, the probe head was slightly rotated around the radial axis in order to align the probes with the magnetic field lines as shown in Fig. 4.10. The rotation angle of the probe head was of $\varphi \sim 5°$. The poloidal

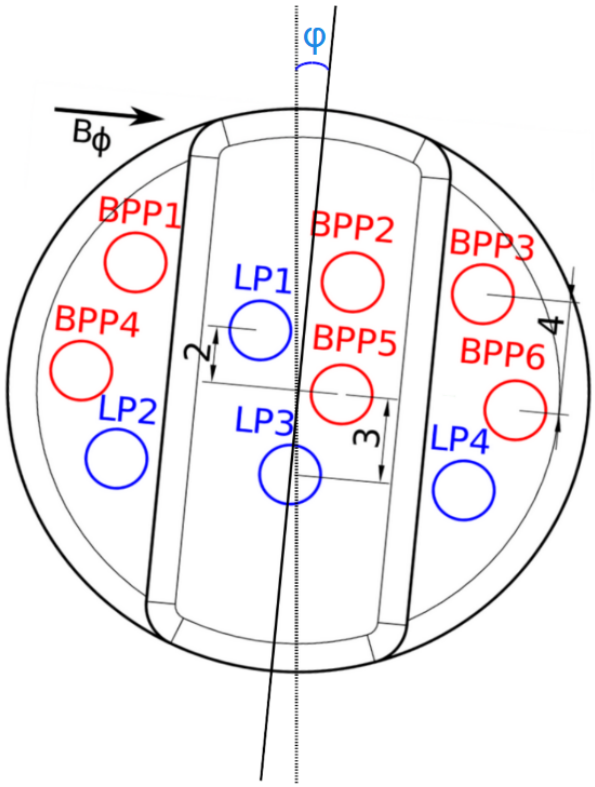

Figure 4.10: Schematics of the rotated Reynolds stress probe head during EMTRAIC measurements. Dimensions are in mm. B_Φ and φ are the toroidal magnetic field vector and the rotation angle of the probe head respectively [313].

distances p_{12}, and p_{13} in the model coordinates do not correspond to the poloidal dimensions $p_{12} = 5.0$ mm, $p_{13} = 5.0$ mm in the convention (R, θ, ϕ) coordinates. The radial distance r_{12} corresponds exactly to the radial dimension $r_{12} = 2.5$ mm. The distances in the propagation model are corrected as follows[1]:

$$\mathrm{r}_{12} = r_{12} \tag{4.14}$$

$$\mathrm{p}_{13} \simeq p_{13} \cos\left(\frac{\pi}{180}\varphi\right) \tag{4.15}$$

$$\mathrm{p}_{12} \simeq \sqrt{p_{12}^2 + p_{13}^2} \cos\left(\frac{\pi}{180}\varphi + \arctan\left(\frac{p_{12}}{p_{13}}\right)\right) \tag{4.16}$$

Radial and poloidal velocities are simply obtained by calculating their respective projections: $v_r = v_\perp \cos\alpha$, $v_\theta = v_\perp \sin\alpha$. Therefore the characteristic blob size is approximated as the length $\delta_b = v_\perp t_{AC}$ travelled by the blob during the auto-correlation time assuming a constant propagation velocity.

[1] A mistake was made in the calculations by using the expression of the radial distance: $\mathrm{r}_{12} = r_{12} \cos\left(\pi\varphi/180\right) \simeq r_{12}$

Shot #	15947	15948	15949	15950	15953	15954
I_p (kA)	160	160	160	160	160	160
B_T (T)	1.38	1.38	1.38	1.38	1.38	1.38
n ($\times 10^{19}$ m^{-3})	4.1	6.2	7.4	8.1	9.0	10.6
f_{GW}	0.226	0.341	0.407	0.446	0.495	0.583
Λ_{div} ($R - R_{sep} \sim 50$ mm)	4×10^{-3}	0.0208	0.0159	0.0708	0.2114	0.0463

Table 4.1: Selected 6 shots for shoulder formation study during EMTRAIC (2017). n is the line averaged density, f_{GW} is the Greenwald factor, and Λ_{div} is the divertor collisionallity taken at $R - R_{sep} \sim 50$ mm from the separatrix.

4.4 Analysed discharges

6 shots presented in Table 4.1 were analysed for different plasma densities. The plasma current I_p and toroidal magnetic field B_T were set to be constant, only the density n was progressively increased by means of gas puffing. The Reynolds stress probe head was mounted on the horizontal reciprocator, with probes LP1, LP2, LP3, LP4 measuring I_{sat} for applying the blob statistical method. No BPPs were considered in this analysis. The divertor probes were used for different purposes *i.e.* LPA measuring I_{sat} for calculating n_e, LPB and BPP measuring V_f and Φ_{BPP} for calculating T_e. The value of the divertor collisionality Λ_{div} at $R - R_{osp} \sim 50$ mm, from the outer strike point (osp) of the separatrix, is chosen for comparison as done in AUG [199]. The analysis time range is enclosed during the flat-top phase (1130 - 1170 ms) when I_p remains constant.

4.5 Results

The values of blobs averaged parameters obtained by conditional analysis have been correlated with the increase of the line averaged density. These are the radial velocity v_r, the poloidal velocity v_θ, the blob size δ_b, and the auto-correlation time t_{AC} as a function of the line average density $\bar{n}_e$ displayed in Fig. 4.11.

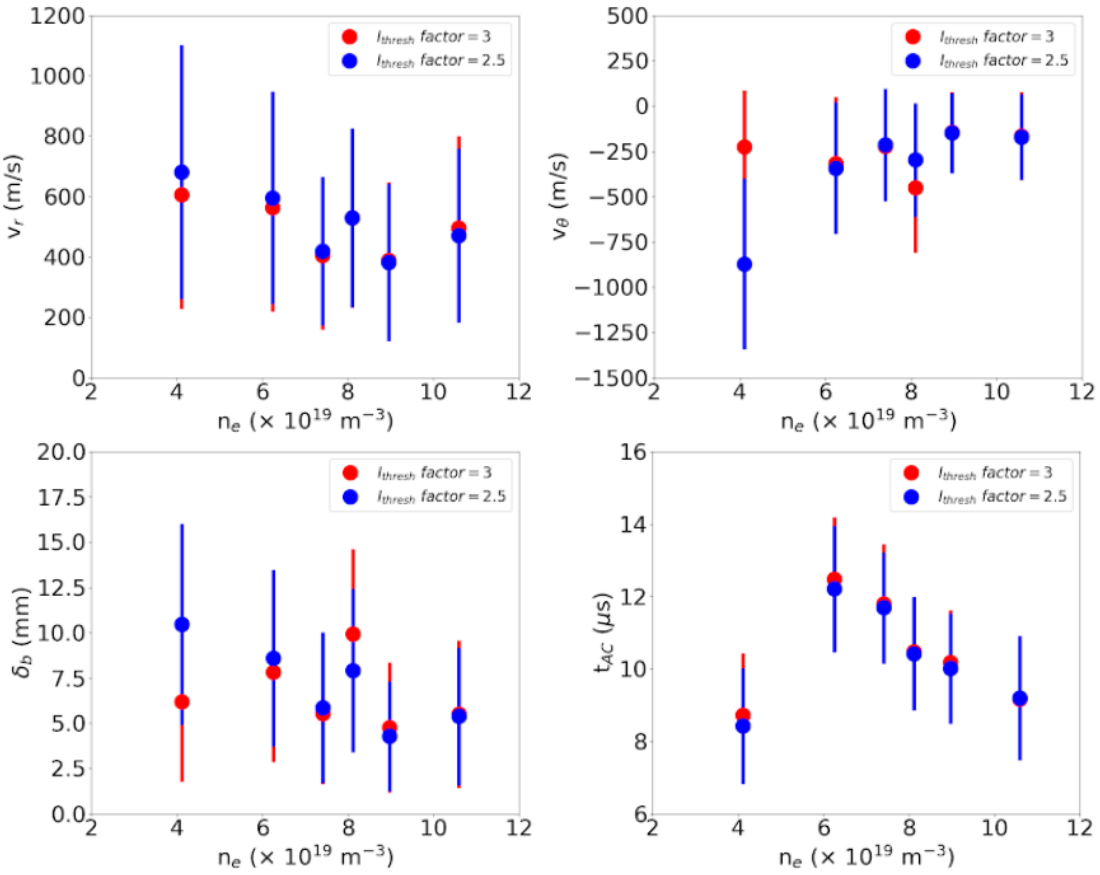

Figure 4.11: Results of the conditional analysis for EMTRAIC data: dependence of radial velocity v_r, poloidal velocity v_θ, blob size δ_b, and auto-correlation time t_{AC} on line average density $\bar{n}_e$. Data is from upstream side (LP1-LP2-LP3) of Reynolds stress probe head. Blue dots refer to a 2.5 threshold factor, red dots refer to a 3 threshold factor.

The results shown in this section correspond to the correlation between LP1-LP2-LP3 probes labelled as the upstream side. It was observed that the I_{sat} current measured by the LP4 probe was slightly lower in comparison with the other probes as shown in Fig. 4.6. This remark suggests that the LP4 was shadowed by the probe head geometry, *i.e.* it was located in the opposite side to the upcoming plasma direction, hence the LP1-LP3-LP4 probes corresponded to the downstream side. Nonetheless, downstream results do not differ significantly from the upstream ones. Complementary points are added by repeating the same data analysis procedure but replacing the threshold factor in Eq. 3.34 *i.e.* $I_{thres} = \mu_{I_{sat}} + 3\sigma_{I_{sat}}$. Thus, this corresponds to increasing the threshold level and averaging over the most dominant blobs. Overall, the

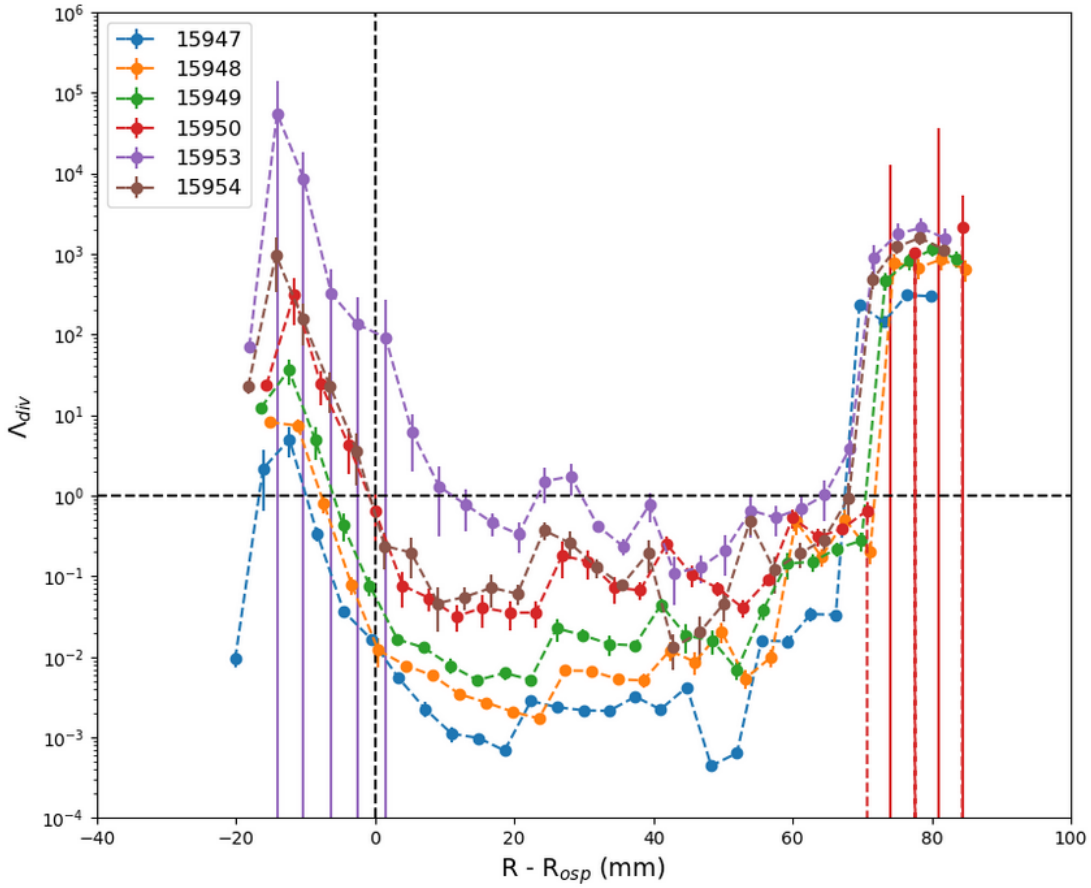

Figure 4.12: Radial $R - R_{osp}$ (mm) profiles of the divertor collisionality Λ_{div} for EMTRAIC discharges.

change of threshold factors does not vary substantially the results. As shown in Fig. 4.11 the characteristic radial blob velocity, v_r, slightly decreases with increasing plasma density. In particular, radial velocities vary between 600 m / s and 450 m / s and seem to stagnate when reaching high density values of $\sim 8 \times 10^{19}$ m^{-3}. The poloidal blob velocity, v_θ, seems to slightly increase with increasing plasma density. Negative poloidal velocities represent the opposite poloidal direction. The values of poloidal velocities tend to be less oscillating specially for predominant blobs detected with the higher threshold factor 3. However, the lower threshold of factor 2.5 results in an outlier point at a density of $\sim 4 \times 10^{19}$ m^{-3}. This is resolved when using the higher threshold of factor 3 as shown in Fig. 4.11. In that case, the poloidal velocity does not vary considerably and remains stable around ~ -250 m / s. The variation of blob size, δ_b, with plasma density is less clear. The lower threshold data shows a definite decrease of the blob size with increasing density. The higher threshold results in a significant difference with the lower threshold at a density of $\sim 4 \times 10^{19}$

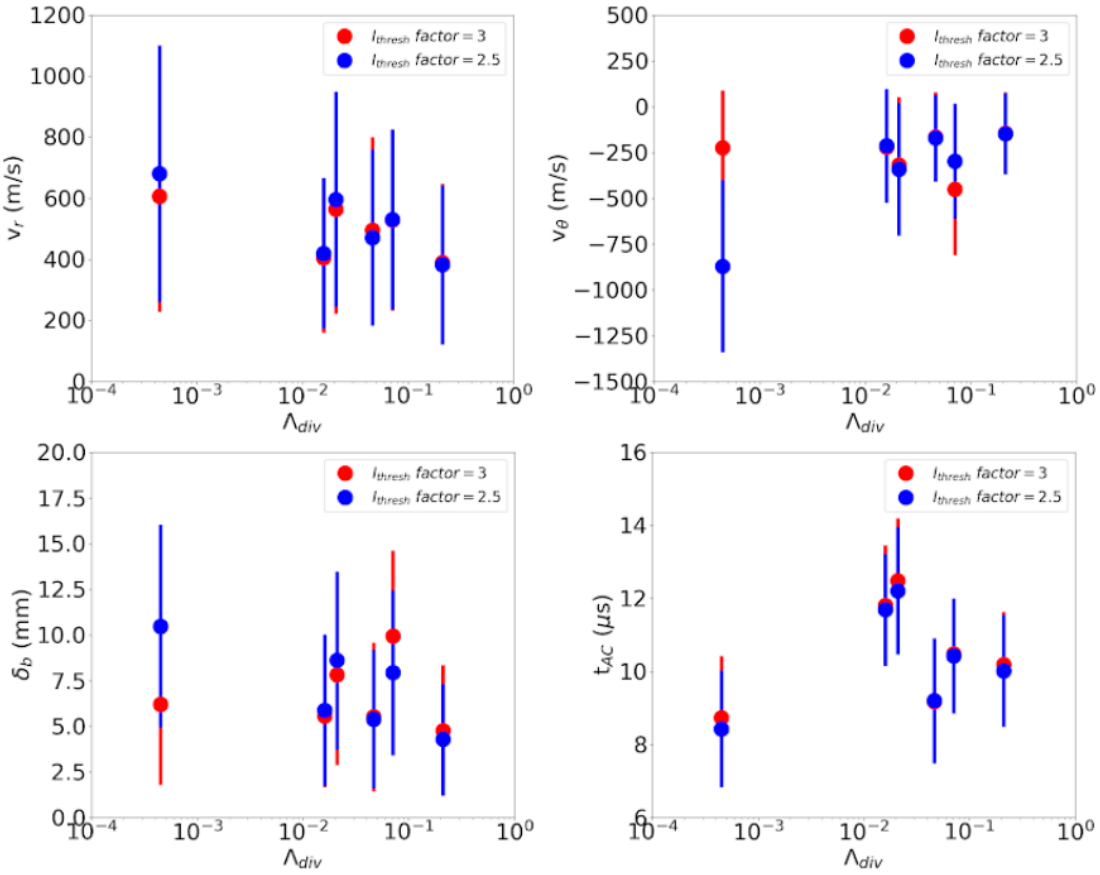

Figure 4.13: Results of the conditional analysis for EMTRAIC data: dependence of radial velocity v_r, poloidal velocity v_θ, blob size δ_b, and auto-correlation time t_{AC} on divertor collisionality Λ_{div}. Data is from upstream side (LP1-LP2-LP3) of Reynolds stress probe head. Blue dots refer to a 2.5 threshold factor, red dots refer to a 3 threshold factor.

m^{-3}. For higher densities the higher threshold points are in closer agreement with the lower threshold points as density is increased. The data indicates that the blob size decreases from around 10 mm at lower densities to around 5 mm at the higher densities. Note that the blob size values satisfies the assumption that the size must be greater than the pin separation (as discussed in section 4.3.4). At the higher densities of around 5 mm. The pin separation is 5 mm then this assumption is on the limit at the higher densities. The auto-correlation times, t_{AC}, show a clear decreasing trend with increasing density above 6×10^{19} m^{-3}. At a density of $\sim 4 \times 10^{19}$ m^{-3} both threshold values result in a significantly lower t_{AC}. The data shows the travel times over single pins are between 9 and 12 μs which is in agreement with preliminary results of

full width at half maxima from conditional averaged functions in Fig. 4.7 with a blob lifetime of ~ 10 μs. Additionally, the measurements taken by the divertor probes arrays allow to reconstruct the radial profiles of divertor plasma parameters, *e.g.* the divertor collisionality Λ_{div} as a function of the radius $R - R_{osp}$ with R_{osp} the outer strike point radius as shown in Fig. 4.12. Each dot relates to the T_e and n_e measurements performed by LP and BPP probes at the same radial position in the arrays. All values in the profiles are averaged over the flat-top phase time range. The Λ_{div} values taken at $R - R_{osp} \sim 50$ mm (as chosen in AUG for comparison) have been correlated with the blob averaged parameters taken at the midplane. These results are displayed in Fig. 4.13. Overall, these trends are very similar to the results in Fig. 4.11 since the scaling of the divertor collisionality with the density is expected to be $\Lambda_{div} \propto n_e \, T_e^{-2}$. The highest value $\Lambda_{div} \sim 0.2$ is achieved for $\bar{n_e} \sim 9 \times 10^{19}$ m^{-3}. In the highest density case with $\bar{n_e} \sim 10 \times 10^{19}$ m^{-3}, the corresponding Greenwald factor is $f_{GW} \sim 0.58$, however the collisionality is $\Lambda_{div} \sim 0.05$. Therefore, both cases were insufficient for satisfying the shoulder formation criteria during EMTRAIC discharges.

4.6 Summary and discussions

The analysis conducted previously in AUG [196] has shown that the shoulder formation is associated with a sharp increase of the blob size. However, the blob statistical analysis of COMPASS data demonstrated that the shoulder formation did not occur in EMTRAIC discharges. The observed values for COMPASS in Fig. 4.11 only match the stage before shoulder formation or pre-shoulder regime for AUG as seen in Fig. 4.14. Similar values for AUG such as $v_r \sim 300$ m/s, $v_\theta \sim -250$ m/s and $\delta_b \sim 5$ mm at a similar position $r - r_{LCFS} \sim 2$ cm are only found for low density discharges $n_e \sim 2 \times 10^{19}$ m^{-3} in the pre-shoulder regime. Nevertheless, the same general trends are observed in this stage for AUG with auto-correlation times around 15 μs being in good agreement to the values obtained in COMPASS. This suggests that both types of structures do present similar behaviours, therefore a potential threshold could be found at higher densities $n_e > 11 \times 10^{19}$ m^{-3}. For instance the AUG shoulder threshold appears at $n_e \simeq 2.5 \times 10^{19}$ m^{-3} and blobs features at $n_e \simeq 2 \times 10^{19}$ m^{-3} coincide with COMPASS values such as $\delta_b \sim 0.5$ cm. Furthermore, Λ_{div} values from this analysis have been superimposed with AUG and JET values in Fig. 4.15. COMPASS

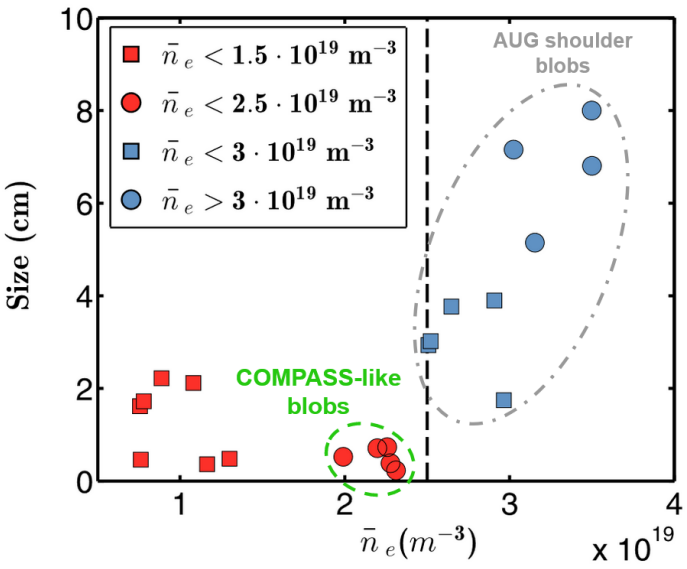

Figure 4.14: Results of the conditional analysis in AUG [196]. Points are classified in four groups of increasing densities. The vertical dashed line indicates the threshold for the shoulder formation. Two domains are defined: the AUG pre-shoulder regime with COMPASS-like blobs (green dashed circle) corresponding to the EMTRAIC results; the AUG shoulder regime (grey dashdot circle).

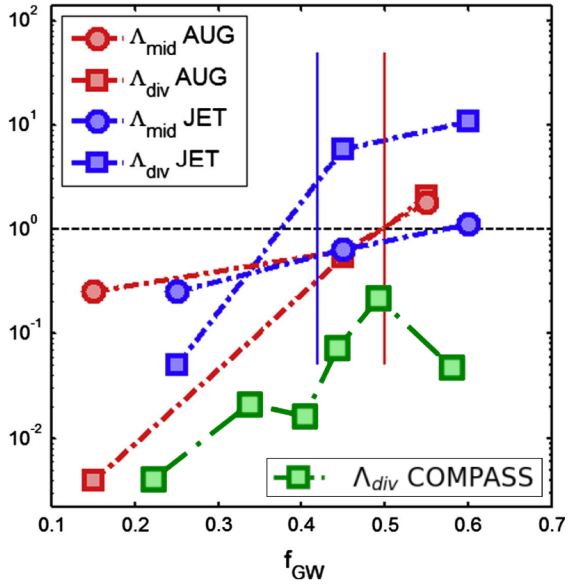

Figure 4.15: Effective collisionality parameter Λ for different f_{GW} values at AUG (red), JET (blue) and COMPASS (green). Circles/squares indicate Λ values at the midplane/divertor. COMPASS values correspond to the EMTRAIC results [199]

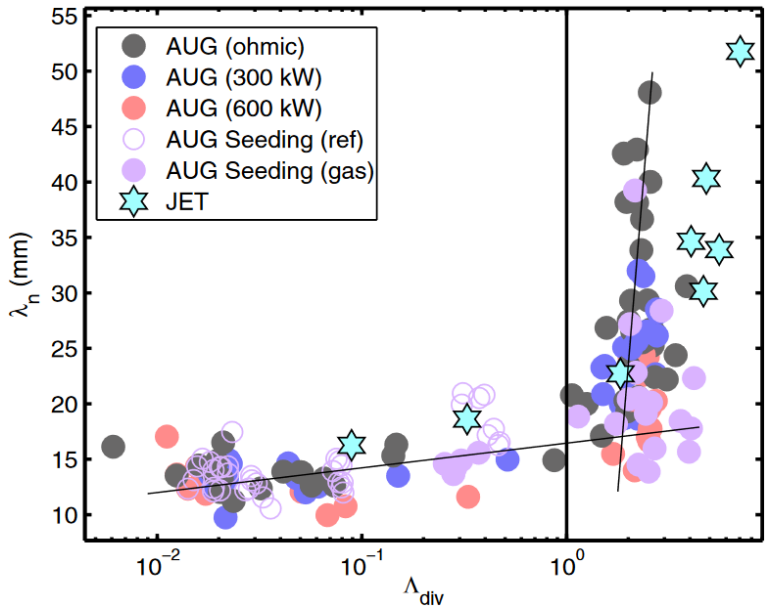

Figure 4.16: Density e-folding length λ_n versus divertor collisionality Λ_{div}. Black (ohmic), blue (300 kW), and red (600 kW) circles represent different input power values in AUG. Purple circles correspond to seeded discharges, empty (ref) and solid (gas) circles correspond to before and after N_2 puffing in AUG. Light blue stars are data points from JET [171]

values (f_{GW}, Λ_{div}) are below the AUG and JET trends for achieving shoulder formation. With EMTRAIC operations surpassing the condition $f_{GW} \geq 0.5$, the corresponding value of $\Lambda_{div} \sim 0.2$ remains inferior to the threshold. Note that the profile for the shot #15953 displayed in Fig. 4.12 presents values $\Lambda_{div} \sim 1$ satisfying the criterion, however a shoulder was not observed. In other terms, both parameters are still insufficient to explain this process. The divertor collisionallity threshold is also correlated with an increase of the density decay length $\lambda_n \sim (\nabla_r \log n)^{-1}$ at the midplane, as shown in Fig. 4.16 [171]. It is speculated that other factors such as the deuterium fuelling rates [201] or the divertor recycling and geometry [322] might also need to be taken into account. During the Summer School Training (SUMTRAIC) in 2019 several discharges were undertaken in order to address these questions. For the moment there is no agreement on releasing SUMTRAIC results before publication.

Chapter 5

Imaging analysis of ELM-filaments in MAST

5.1 Introduction

The transition between the L-mode and H-mode is characterised by the formation of a transport barrier. Due to a high steepening of edge gradients, instabilities tend to grow producing violent ejections or bursts of filamentary plasma, followed by the pedestal collapse and degrading the confinement. If the barrier is maintained with sufficient heating, the process repeats revealing that these bursts are quasi-periodic relaxation events, *i.e.* the Edge Localised Modes. Unfortunately this mechanism is not fully understood yet, nonetheless the best candidate up-to-date explaining ELMs might consist in the coupling of peeling-ballooning modes. The trigger seems to be manifested by prior oscillations known as ELM-precursors mentioned in chapter 2 section 2.3.6. The study of precursors in MAST has been focused on observing the evolution of the plasma edge using fast cameras, interferometry and beam emission spectroscopy. Furthermore, the Elzar algorithm has been recently developed. Elzar is a tomographic inversion technique that identifies filamentary structures from camera frames. Its performance was demonstrated recently for MAST discharges in L-mode.

The motivation on analysing the evolution of ELM-filaments has the aim of understanding the triggering conditions on ELMs in MAST plasmas and compare the ELM-precursors behaviour with other tokamaks. This chapter consists in a preliminary analysis supervised by P. Bryant at UoL and A. Field & F. Militello at CCFE. The aim is to evaluate if any ELM-precursor activity can be visualised from fast camera frames. Data from the campaigns including ELMy H-mode discharges taking place in 2013 were analysed. Part of the analysis involves the 2D imaging by the BES system for the identification of density fluctuations at the pedestal during inter-ELM periods. Additionally the tomographic inversion implemented in Elzar was employed with the purpose of observing the generation of filaments before the ELM ejection in MAST plasmas. The structure of this chapter is as follows: section 5.2 presents the experimental setup with the beam emission spectroscopy system and the fast camera; section 5.3 includes the summary of analysed discharges; section 5.4 corresponds to the results from the BES imaging analysis; section 5.5 shows a preliminary study of camera frames and the following Elzar analysis; and section 5.6 is the summary and discussions that will introduce chapter 6.

5.2 Experimental setup

5.2.1 Beam Emission Spectroscopy (BES)

The BES technique combines the stimulation of D_α emissions in the plasma by the beam and the collection of these emissions by the spectroscopy system. The review of the BES theory is given in chapter 3 section 3.3.3. Two BES configurations relied on two beams. The SS and SW beams corresponded to two tangentially oriented NBI systems, located at ports in the vessel named after the cardinal convention. Each beam was supported by the spectroscopy system composed by an optical setup and a detector. The position of both beams, the detectors and the B field vectors direction are illustrated in Fig. 5.1. The filled red area represents the intersection of the optics line-of-sight and the beam with a viewing direction parallel to the magnetic field. This observation area can scan radially from 0.9 m to 1.5 m which includes the outer plasma edge.

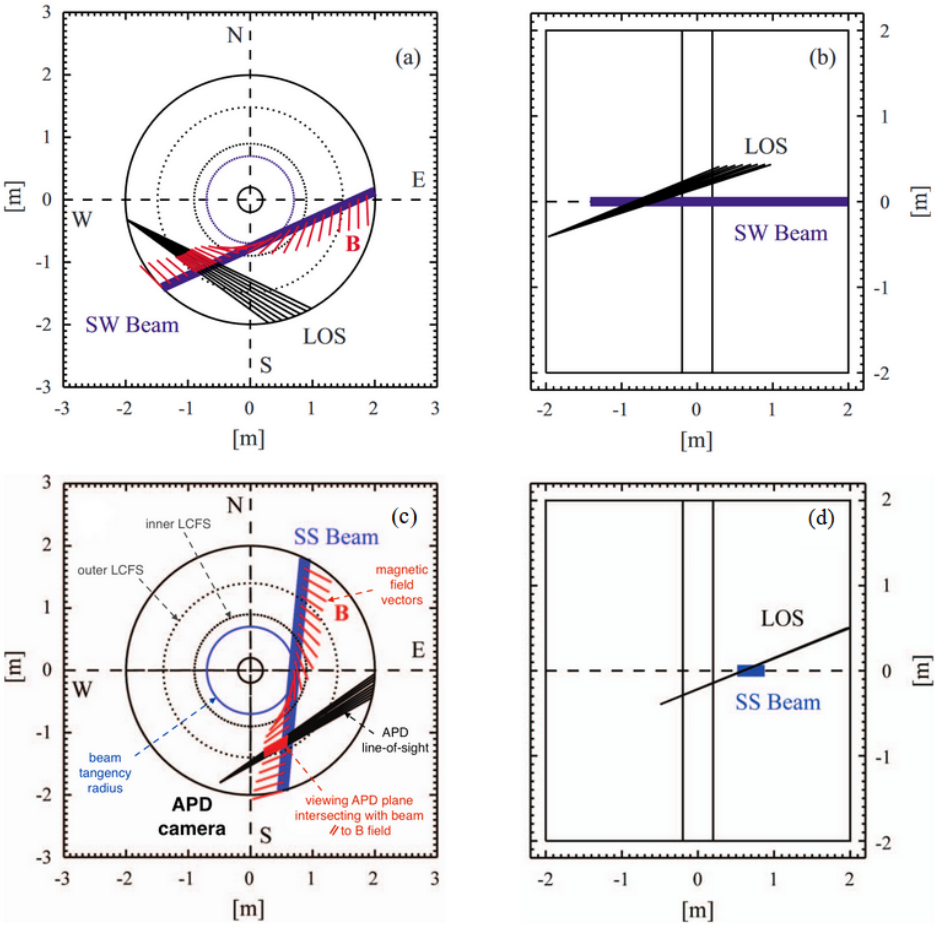

Figure 5.1: Plan (a & c) and E-W sectional (b & d) views of the observation geometry of the BES imaging system; cases (a & b) and (c & d) correspond to South-West (SW) Beam and South-South (SS) Beam ports respectively; the Line-Of-Sight (LOS) indicates the detector's location [285, 286]

5.2.2 Fast camera

The camera's location in MAST is illustrated in Fig. 5.2. The camera was installed in the port HM-10 (sector 10) located at the toroidal angle $\phi = 215°$, and slightly mounted back from the vessel to reduce the interference of the magnetic field. The distance of the camera to the centre column was of ~ 2.15 m and ~ 0.75 m to the plasma edge. Two viewing geometries of the fast camera are illustrated in Fig. 5.3 corresponding to the midplane and divertor field of views. The following analysis only concerns the midplane view. This view includes the edge of the centre column on the left and the vessel components such as poloidal field coils (P4, P5), RMP coils and the divertor at the bottom.

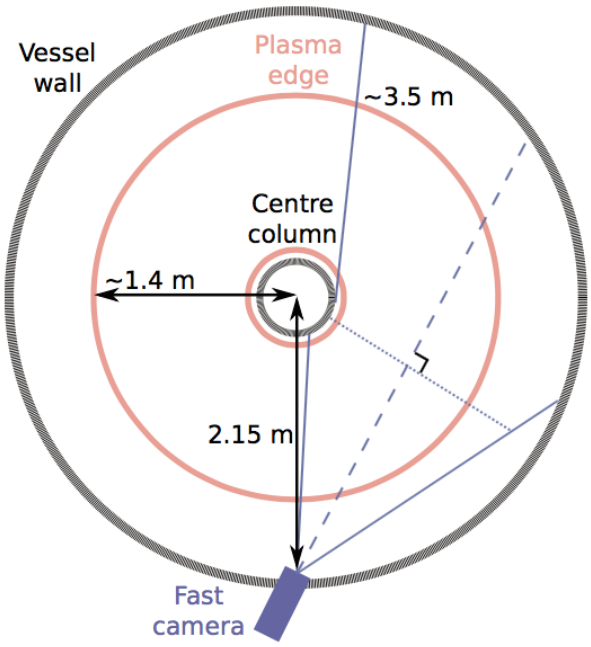

Figure 5.2: Top down view schematic of MAST showing the field of view of the midplane fast camera, sight lines in blue, dashed blue tangent to toroidal magnetic field, plasma edge in pink [297].

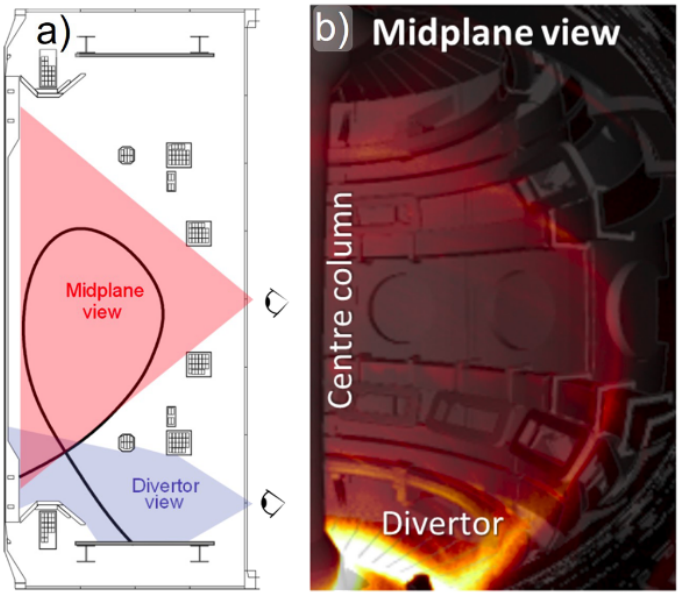

Figure 5.3: (a) Schematic of the field of view of the Photron SA-1 fast camera when installed at the midplane or divertor. (b) False color image of a MAST plasma, as viewed by the SA1 camera, with a CAD rendering of the MAST vessel components overlaid [298].

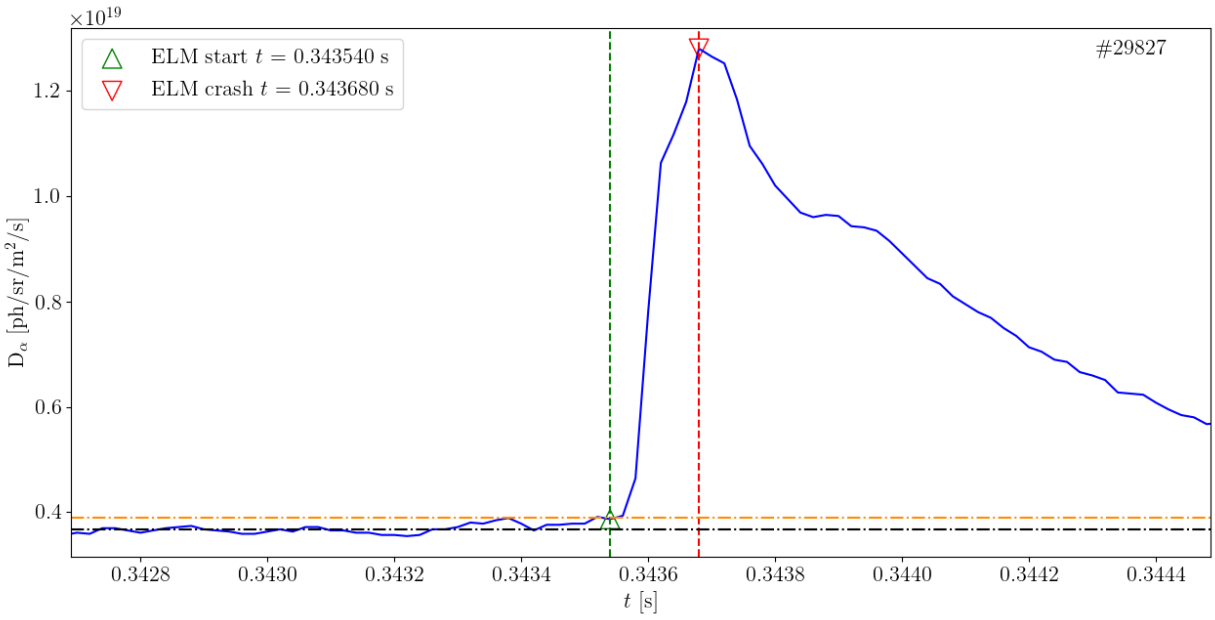

Figure 5.4: Temporal evolution of the D_α emission in time for discharge #29827. The 4th ELM of this discharge appears around $t \sim 0.3436$ s, with the ELM onset time $t \sim 0.34354$ s in green and the ELM crash time $t \sim 0.34368$ s in red.

5.3 Analysed discharges and ELMs identification

From the MAST M9 campaign in 2013, a list of selected discharges was elaborated for the imaging analysis. The main criterion for this selection was to find shots where both diagnostics, the 2D BES system and the fast camera, were operational during H-mode plasmas. The list of analysed discharges with plasma parameters is summarized in Table 5.1. From these overlapped shots the next step consisted in the identification of ELMs and reporting the respective ELM times. Fast camera frames help with the observation of the ELM crash however identifying the ELM starting time is ambiguous. The definition of the ELM start is crucial for the study of the ELM-precursor time range. An example of D_α signal and ELM identification is shown in Fig. 5.4. The start time is determined by examining the time evolution of the line emission brightness from the D_α linear camera. The D_α *Lincam* is a 2D CCD array located on port HM-10 giving a midplane plasma view. The sensors are arranged in the radial direction that allows to obtain the D_α radial profile. The ELM start time was defined as the foot of the D_α peak which is the highest value representing the emission

Shot	Time (s)	ELMs type	Magnetic config.	I_p (kA)	B_T (T)	n_e ($\times 10^{19}$ m^{-3})	P_{NBI} (MW)
29742	0.36 - 0.67	type-I	SND	450	0.35	6.02	0.0
29762	0.21 - 0.33	type-I	DND	903	0.42	4.05	2.24
29768	0.28 - 0.66	type-I	LSND	448	0.35	4.28	2.26
29786	0.21 - 0.31	type-I	DND	810	0.42	4.82	2.13
29790	0.26 - 0.34	type-I	DND	802	0.43	5.53	2.19
29808	0.21 - 0.43	type-III	DND	749	0.42	7.32	2.26
29814	0.16 - 0.57	type-III	DND	446	0.40	5.43	2.18
29826	0.26 - 0.37	type-III	LSND	438	0.29	10.04	2.40
29827	0.30 - 0.45	type-I	LSND	435	0.30	5.30	2.19
29834	0.16 - 0.26	type-III	SND	651	0.35	3.33	2.25
29843	0.15 - 0.23	type-III	DND	903	0.33	4.57	2.10
29848	0.16 - 0.21	type-III	DND	609	0.29	5.47	2.16
29849	0.15 - 0.19	type-III	DND	618	0.26	3.50	1.89
29978	0.18 - 0.25	type-I	DND	803	0.43	5.80	2.15
29992	0.22 - 0.35	type-I	DND	903	0.43	5.86	0.0

Table 5.1: List of overlapped shots with BES and fast camera showing ELMs. Parameters are: shot number, time range, ELMs type, magnetic configuration (single null diverted (SND), lower single null diverted (LSND) double null diverted (DND)), plasma current at the flat top phase (I_p), maximum toroidal magnetic field (B_T), line averaged density (n_e) and injected neutral beam power by the SS beam (P_{NBI})

from the ELM crash. A baseline is defined as the mean signal value taken over 1 ms before the ELM peak. The onset time corresponds to the closest value to the foot that surpasses the threshold. This is defined as one standard deviation obtained from the values over the 1 ms interval. The analysis of the ELM-precursor activity will be then constrained to the time range between 200 μs and the start time. The results of the data analysis presented in the following sections correspond to the discharge #29827. Complementary diagnostics help with the characterisation of the edge conditions, specially for identifying the pedestal region and the

separatrix. The electron density and temperature radial profiles come from the Thomson Scattering (TS) data. The D_α emission profile is provided by the Lincam data. Additionally, the radial profiles of the safety factor and the shear, obtained from EFIT, are also included.

5.4 BES imaging analysis

The purpose of this section is to reconstruct images of density fluctuations from the light intensity captured by the BES system. The BES imaging serves as a preliminary analysis that will determine the size and velocities of the ELM-precursor structures. First of all, each BES signal is digitally filtered with a bandwidth between frequencies 10 and 50 kHz. This range is chosen due to the fact that the ELM-precursor characteristic frequency is expected to be $\sim$ 20 kHz according to Kirk *et al.* [234]. The signals from all 32 channels are used in a linear interpolation fitting function to reconstruct the image. The resulting image shown in Fig. 5.5 reconstructs the edge density distribution in the (R, Z) viewing plane. R is the radial direction and Z is the poloidal-vertical direction. In comparison with the array sensor design (Fig. 3.15), the image is mirrored along the row channels in the R orientation. By observing different frames from -90 μs before the ELM onset time, it is noticed in Fig. 5.6 that successive high (and low) dense islands appear and propagate in the same direction. These structures can be labelled as blobs (*i.e.* with positive density above the background) and holes (*i.e.* with negative density below the background). The observed motion is mainly oriented vertically, *i.e.* in the negative poloidal direction. Structures appear periodically with new concatenated blobs/holes every $\sim$ 20 μs. These observations are in agreement with the structures seen in Fig. 2.37. However, close to the ELM crash, this behaviour is interrupted: structures stop and suddenly propagate in the opposite (*i.e.* positive) poloidal direction. The observed motion can be described as a reversal similar to a turbulent vortex. After a few tens of microseconds, the coherent motion takes the lead with the original propagating direction. This behaviour of rotating islands and holes was observed in all of the ELMs analysed. However, it is unclear to determine if the reversal motion close to the ELM onset is universal. In order to characterise these structures, some variables need to be defined: ΔR and ΔZ the radial and vertical lengths of the structure. Complementary diagnostics mentioned in section 5.4 provide

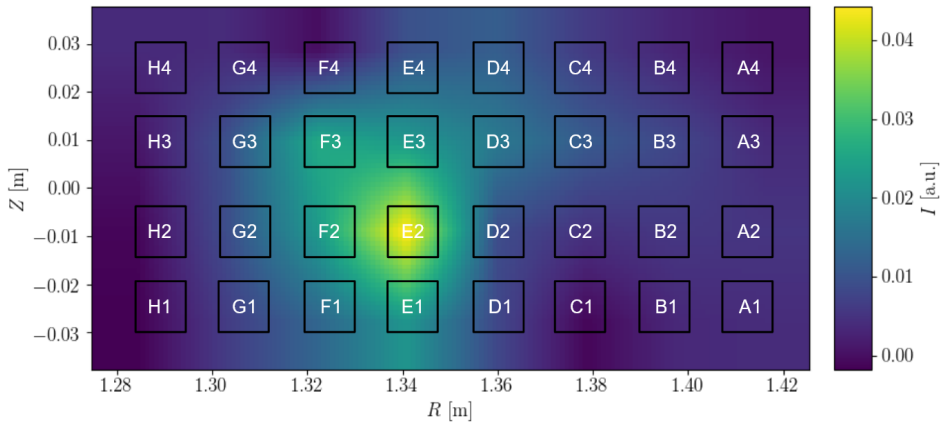

Figure 5.5: BES reconstructed image superimposed with the APD channels disposition.

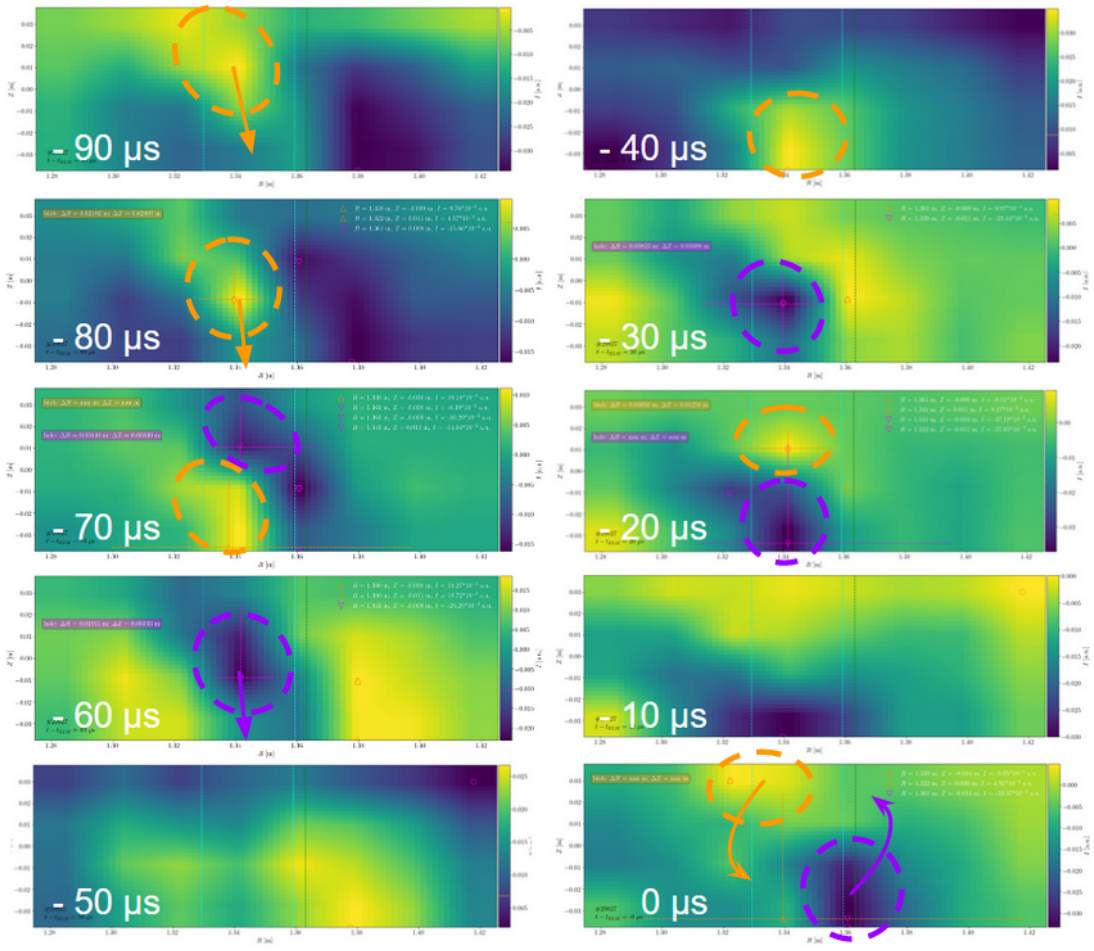

Figure 5.6: BES frames between -90 and 0 μs before the ELM onset time. *Blobs* and *holes* are highlighted with dashed circles in orange and purple respectively. Complementary arrows are added to indicate the orientation of the blob/hole propagation. The two light-blue vertical lines contain the pedestal region.

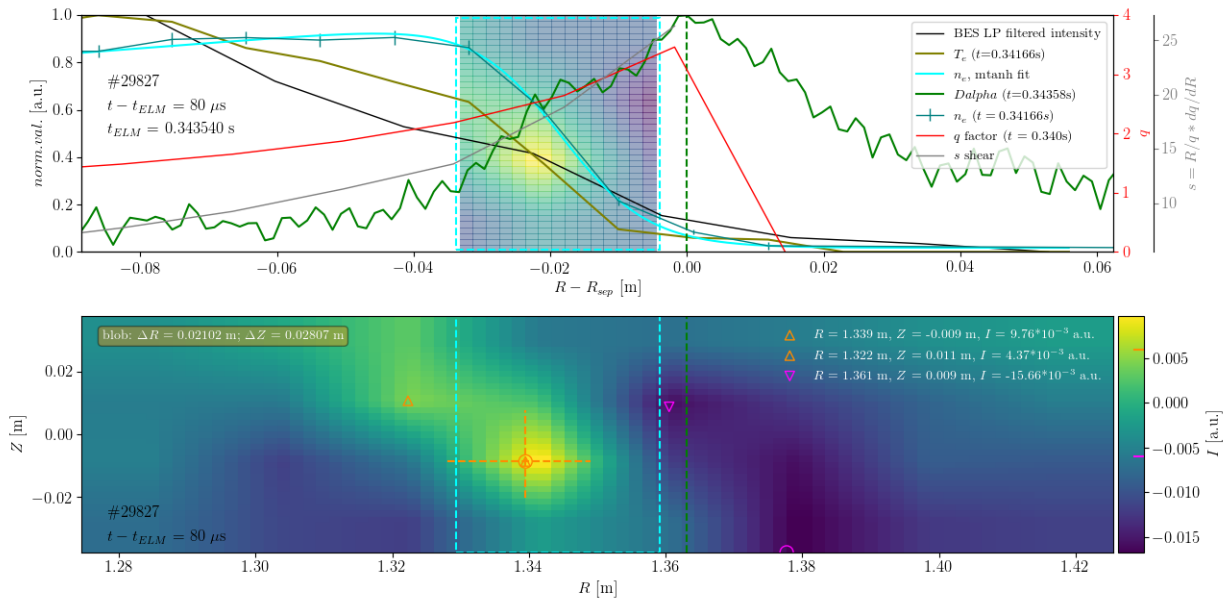

Figure 5.7: Radial parameter profiles and BES image for MAST shot 29827 at $t = 80$ μs before the ELM. (Top) Normalised radial profiles from TS, Lincam diagnostics. (Bottom) the reconstructed BES image. The cyan square containing the blob corresponds to the pedestal region defined by $R \sim [1.33, 1.36]$ m. The dashed green line corresponds to the separatrix radius $R \sim 1.36$ m. The radial and vertical widths of the blob are marked in dashed orange lines.

further information radially including density and temperature from TS, and D_α emission from Lincam. The BES image is correlated to these radial profiles in Fig. 5.7. Radial profiles values are normalised with respect to the TS values except for the safety factor and the shear profiles. The corresponding D_α peak indicates approximately the separatrix position. The contribution of the D_α emission in the pedestal corresponds to $\sim$ 20% of the Lincam peak. The TS density profile is fitted by an hyperbolic tangent function (mtanh) [323]. The mtanh fit is used to define the pedestal dimensions with 5 parameters: the pedestal position, width, height, slope, and offset. These parameters define a dashed light-blue box on BES frames in order to display the location of the pedestal. The rotating structures are located in this box *i.e.* in the pedestal region (except for times after the ELM crash). On a BES frame, local intensity peaks are detected using a local maximum filter limited to the pedestal region. The threshold detection of peaks is defined by 2.5σ with σ the standard deviation above the mean background intensity. The detections at superior ($Z > 0.03$

m) and inferior ($Z < -0.03$ m) vertical edges are considered non valid. The radial and vertical full-widths of detected structures are estimated from that local peak. Each length extends in each respective direction until reaching the threshold limit. For a large number of frames, parameters such as the peak intensity I, poloidal velocity v_Z, radial ΔR and vertical ΔZ lengths for both blobs and holes were obtained. The poloidal wavelength is estimated as twice the poloidal length *i.e.* $\lambda_Z = 2\Delta Z$, and the poloidal wavenumber is defined as $k_Z = \pi/\Delta Z$. Poloidal velocities are calculated by measuring the distance between succesive peaks (with intensities of same sign) from different frames and dividing by the time between frames. The poloidal wavelength is then normalised using $k_Z\rho_L$ with $\rho_L = \sqrt{m_i T_e}/eB$ the hybrid Larmor radius. The poloidal number is approximated as $m = R_b k_Z$ with R_b the radial position of the blob taken at the center. These characteristic parameters are shown as in function of time in Fig. 5.8. Overall, the parameters do not show much deviation in scatter before, during and after precursor times or little difference between holes/blob peaks. However some deviations are noticed in $k_Z\rho_L$ and m graphs during the precursor activity, and blob velocities v_Z sporadically increase. The peak intensity I graph shows the periodic behaviour with regular oscillations for both holes and blobs. The characteristic time between these intensity oscillations is $\sim$ 50 μs which correspond to a frequency of $\sim$ 20 kHz. The increase in intensity occurs around $\sim$ -300 μs. This might indicate an earlier onset of activity than - 200 μs. After $\sim$ -300 μs the intensity is high for two cycles then drops to values similar to those before until increases again at the ELM onset. On the v_Z graph, there is no significant difference between blob and hole velocities between pre-precursor times and during the precursor time range. No positive velocities were recorded at the ELM crash because blobs (or holes) are not regularly located at the pedestal or too close to the edges. The spread of radial widths ΔR is more difficult to interpret, but generally blobs present larger sizes in comparison with holes. The same remark can be applied to vertical widths ΔZ, but holes tend to become vertically larger than holes during the precursor time. It is possible that the structures dimension can be eventually larger than the vertical resolution of the BES frame, which makes this measurement less reliable. However the decrease of ΔZ values at the precursor range causes significantly high values of $k_Z\rho_L$ and m. In order to simplify the evaluation of typical precursor structures, this collected data needs to be re-interpreted by using statistical methods. For times before the ELM onset, all collected values are selected for further statistical analysis in order to

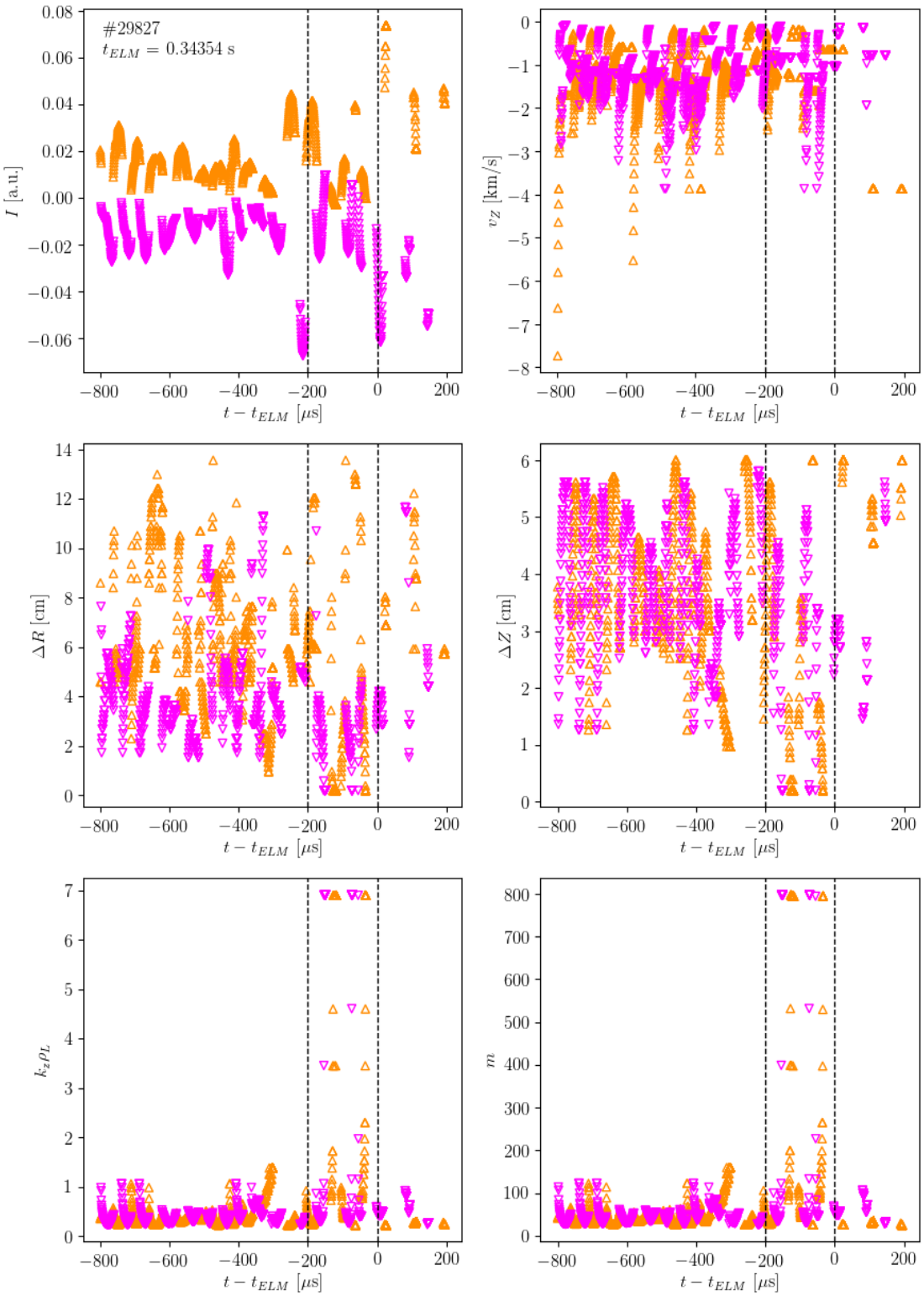

Figure 5.8: BES analysis results for MAST shot 29827 with ELM burst peaking at $t = 0.34354$ s. Vertical dashed lines indicate the ELM-precursor time range. These lines are taken at -200 μs and 0 μs relative to the ELM onset time. Orange and pink points correspond to blobs and holes respectively.

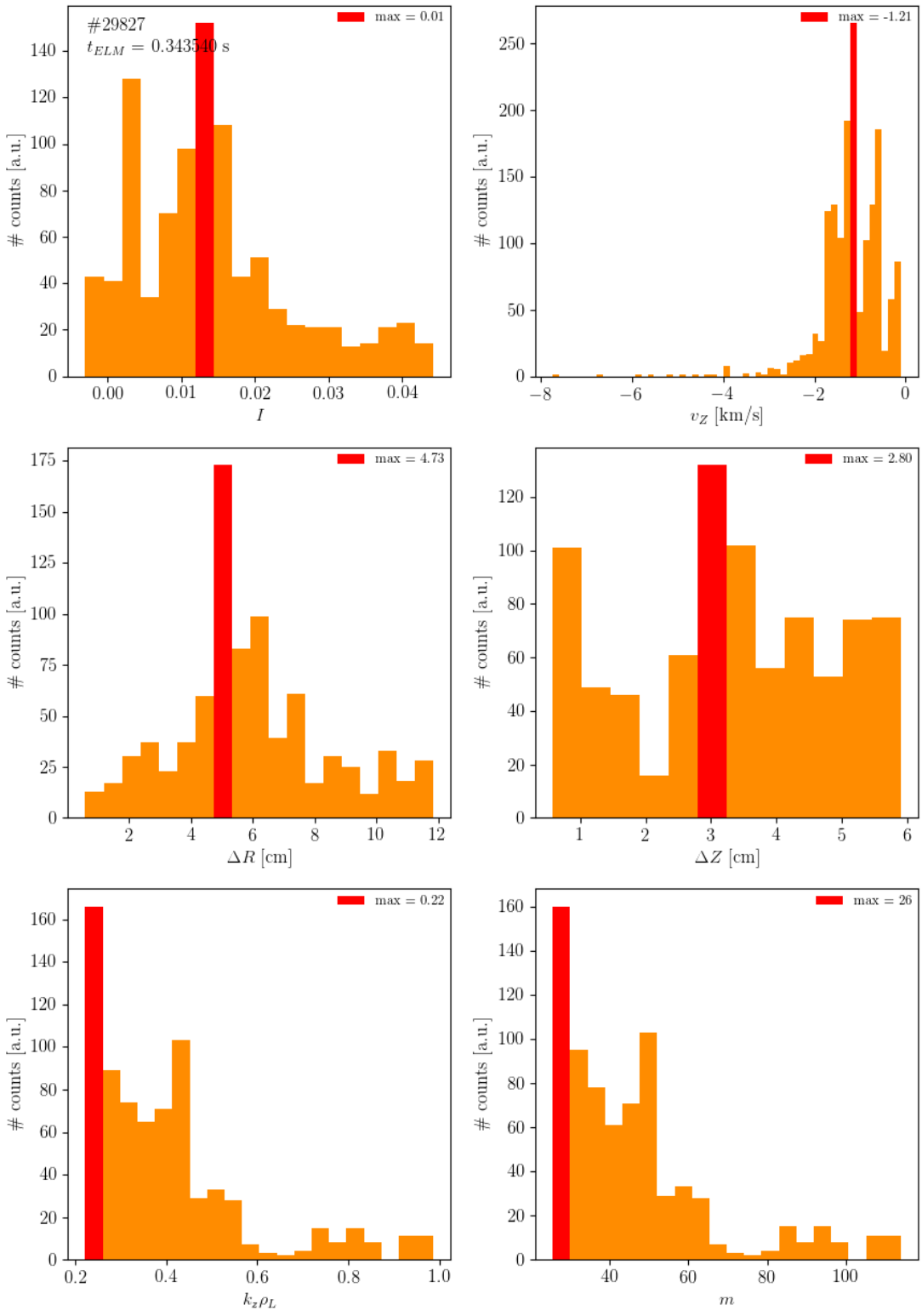

Figure 5.9: BES histograms of blob parameters before ELM burst peaking at $t = 0.34354$ s for MAST shot 29827. Red bars correspond to the mode value (highest frequency / number of data values)

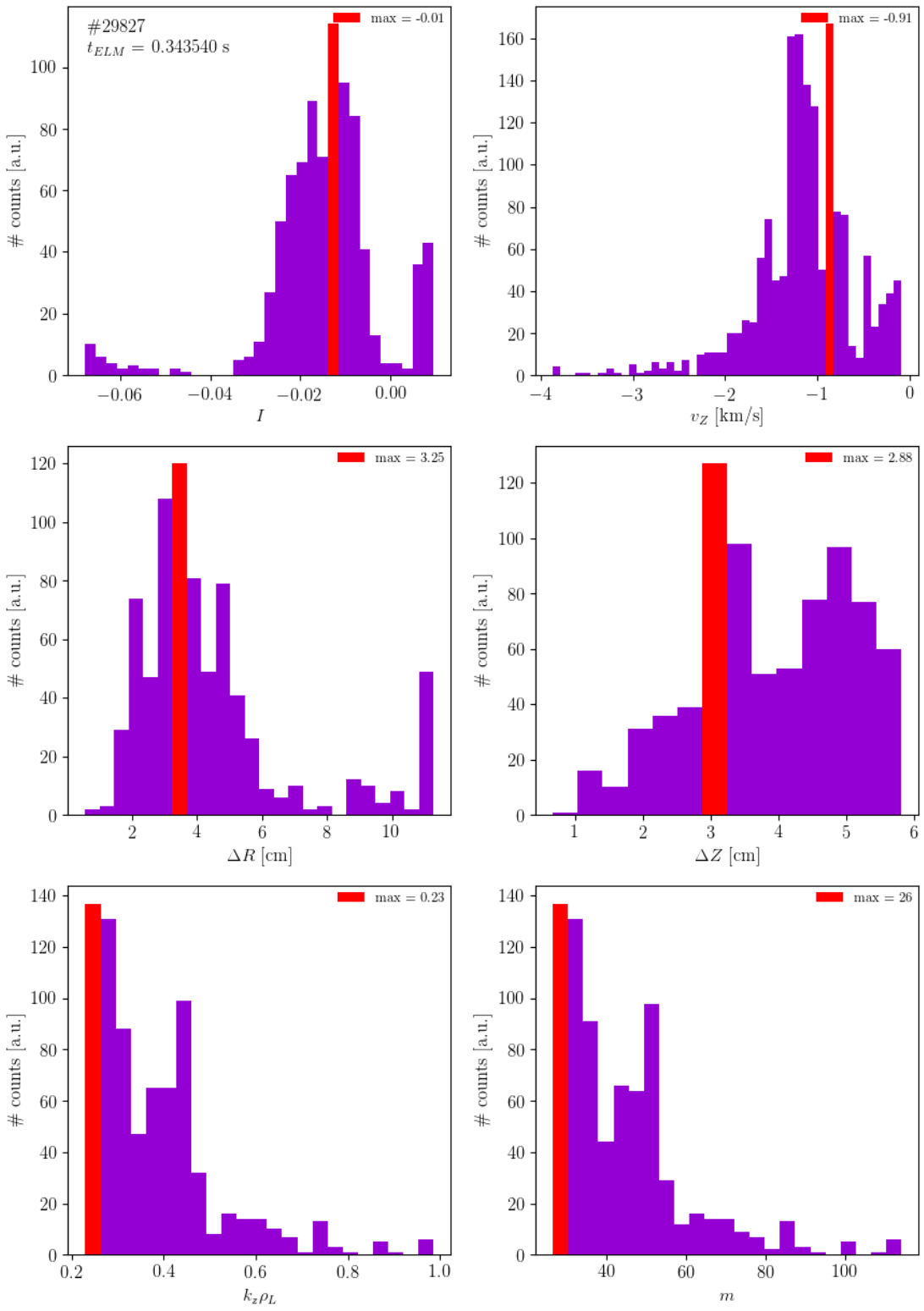

Figure 5.10: BES histograms of hole parameters with ELM burst peaking at $t = 0.34354$ s for MAST shot 29827. Red bars correspond to the mode value (highest frequency / number of data values)

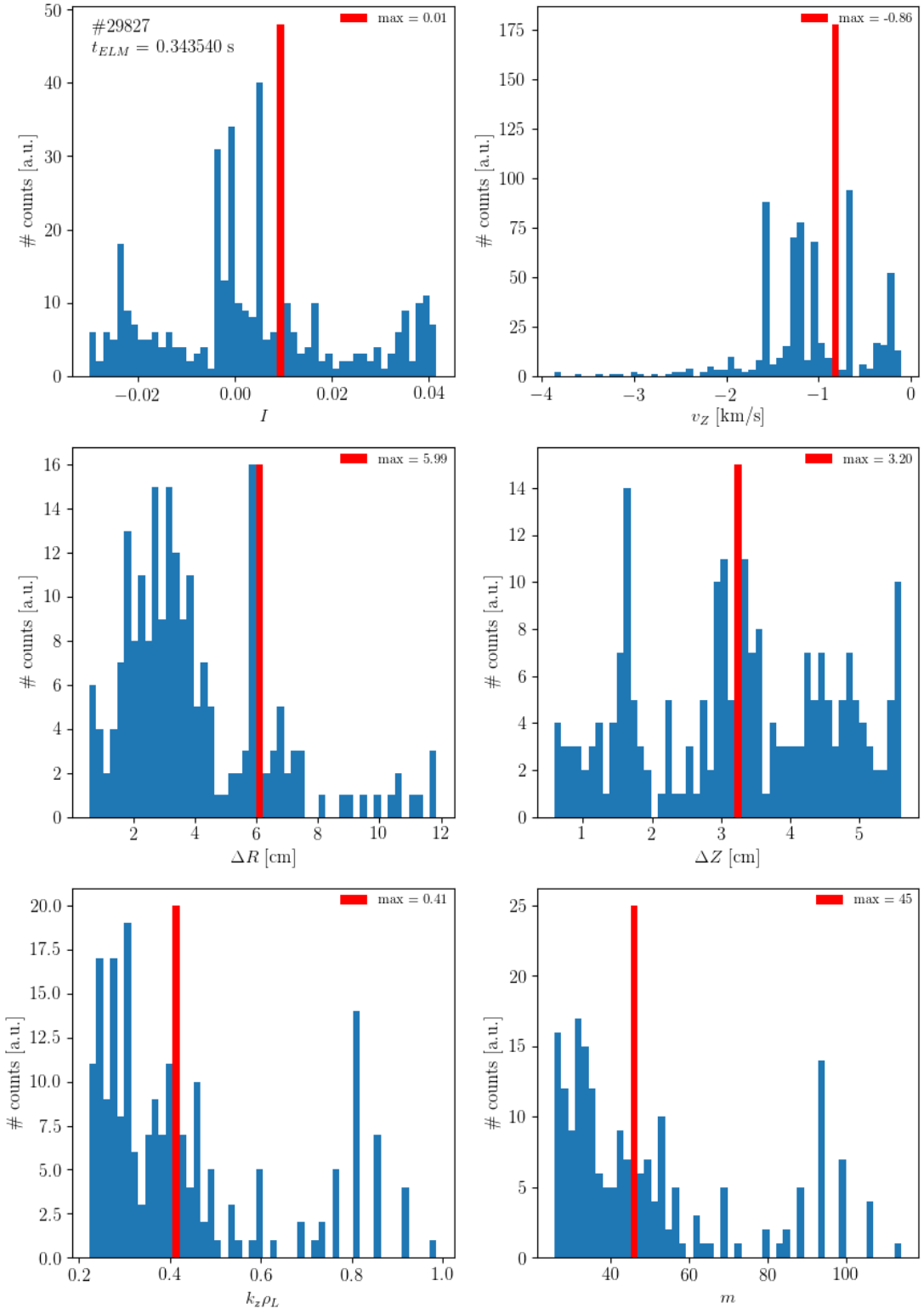

Figure 5.11: BES histograms of blob & hole parameters between -200 μs and 0 mus before the ELM burst at $t = 0.34354$ s for MAST shot 29827. Red bars correspond to the mode value (highest frequency / number of data values)

construct distribution functions. Blobs and holes values are distinguished for this analysis. The respective histograms in Figs. 5.9 and 5.10 return the characteristic features with the highest probability that occur during 800 μs before the ELM. Concerning blobs histograms, the most frequent values are: $v_Z = -1.21$ km/s, $\Delta R = 4.73$ cm, $\Delta Z = 2.80$ cm, $k_Z\rho_L = 0.22$, and $m = 26$. Concerning holes histograms, the most frequent values are: $v_Z = -0.91$ km/s, $\Delta R = 3.25$ cm, $\Delta Z = 2.88$ cm, $k_Z\rho_L = 0.23$, and $m = 26$. During the ELM-precursor time range, *i.e.* between $t = [-200, 0]$ μs, all collected values in that range are used to obtain a typical ELM-precursor structure. Unfortunately all values from blobs and holes are combined due to the reduced number of points in that range. The respective histogram is presented in Fig. 5.11. The bins correspond to the parameter values occurring at the highest frequency indicated during the ELM-precursor activity. The most frequent poloidal velocities of $v_Z = -0.86$ km/s with a range of values from -0.0 to -0.18 km/s. This wide range of values shows that the precursor structure does not repeat itself exactly with deviations occurring in each cycle. Poloidal velocities never exceed -2 km/s. The histogram of the radial width presents two peaks, one broad but at lower values and the other sharp and narrow at higher values with $\Delta R = 5.99$ cm. Since this combines both holes and blobs, the sharp value would correspond to the coherent repetitable structure *i.e.* the blob, and the wide peak corresponds to variable holes. Very few blobs are greater than this point so blobs width measures less than 8 cm. Concerning the poloidal width, it is hard to locate upper and lower limits poloidal sizes are quite irregular around $\Delta Z = 3.20$ cm with a secondary peak at $\Delta Z \sim 1.60$ cm. Histograms on $k_Z\rho_L$ and m results do not allow to extract a characteristic value. A wide range of values can be attributed *e.g.* $k_Z\rho_L < 0.5 - 0.6$ and $m < 60$ with a mode at $m = 45$.

5.5 Fast camera analysis

The purpose of this section is to investigate whether that the ELM-precursor activity can be observed from images recorded by the fast camera. Unlike the BES system, this remote approach relies on the unfiltered visible emission from the plasma to detect precursor activity. The first step is to check if there is visible emission prior to the ELM onset. Filaments move toroidally while following the helical structure of the magnetic field. The emission of the inter-ELM filaments is substantially low compared to the eruption

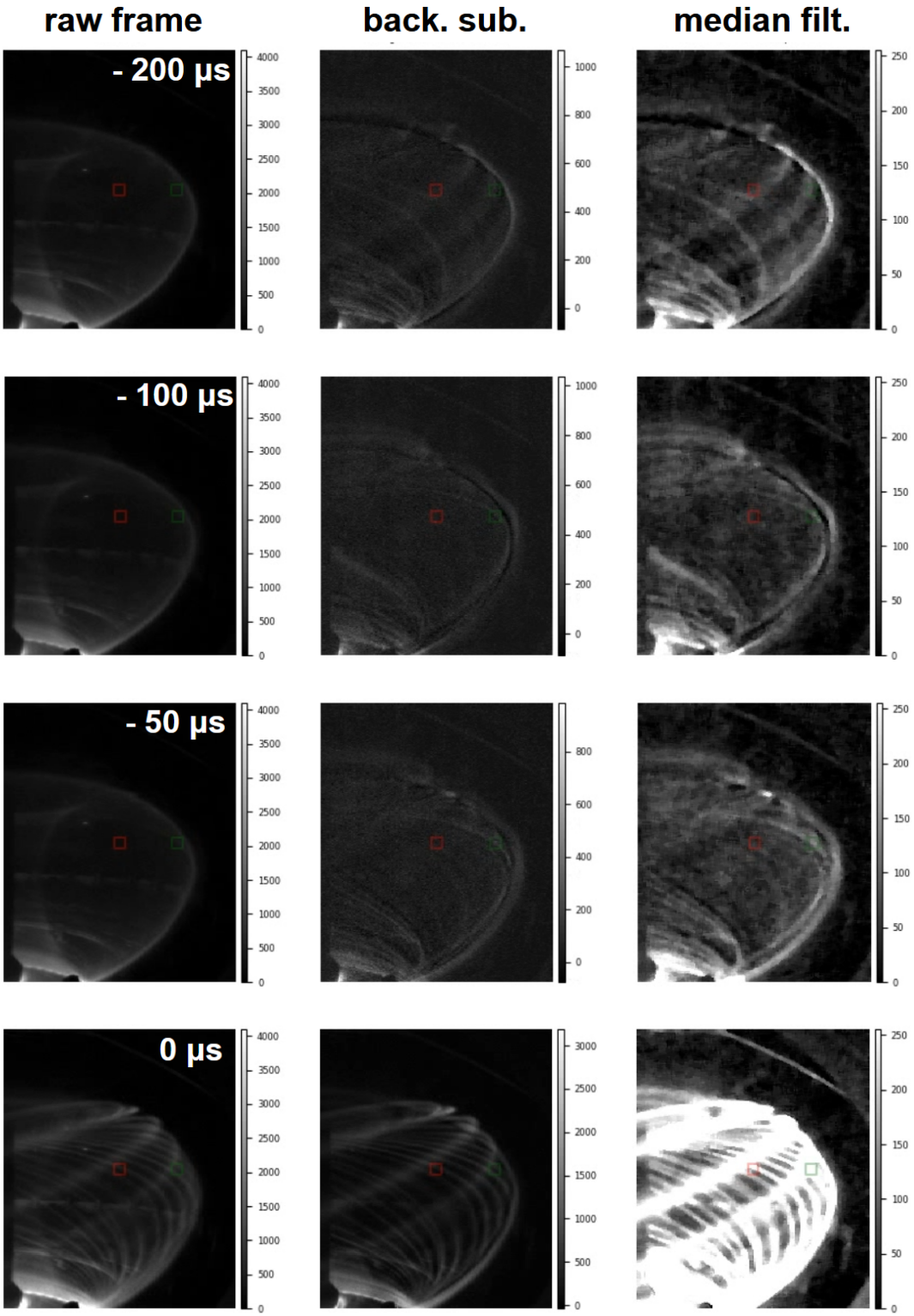

Figure 5.12: Visible camera frames for MAST discharge 29827 at 200 μs (1st row), 100 μs (2nd row), 50 μs (3rd row) and 0 μs (4th row) before the ELM onset at $t = 0.34354$ s. From left to right: raw frame (1st col.), background subtracted frame (2nd col.), median filter applied (3rd col.)

event. It is uncertain if the fast camera is capable of collecting such as low emission level. For that purpose, a background subtraction is applied before the application of the Elzar technique. Elzar performs a background subtraction as well, but this is an intermediate step and automatically returns the final inversion. A background subtraction described in Fig. 3.25 from section 3.4.2 in chapter 3 is applied here and results are shown in Fig. 5.12. Two pixels are selected for visualising the oscillations of the light emission: one is placed at the center of the frame; the other is placed at the plasma edge on the right of the frame. The observed filaments move through these pixels that serve as references for observing the evolution of the collected emission. Note that the plasma edge is ambiguously defined here and does not correspond to the pedestal. It was observed that the emission was really low and fluctuates intermittently as filaments pass through these pixels. The cause of the observed intermittency is the interference between the foreground and background filaments at the same pixel which produce intermittent peaks in the pixel signal. At times close to the ELM onset the filamentary structure becomes more regular just prior to the filament ejection outwards (see 0 μs, 3rd col in Fig. 5.12). The problem with the use of fixed pixels was the impossibility to follow the individual filament emission. Hence, a second method is performed by following one single filament before the ELM onset. In order to do this all pixels relating to the filament are manually identified. Care was taken to avoid pixels which had overlapping background filaments. Due to the existence of two different types of data frames in the archive, named "raw data" and "data" frames, both cases were analysed. All of the filament pixels intensities were then averaged and plotted as a time series. The results are shown in Fig. 5.13. The emission slightly increases before the ELM onset, however, the level remains low. There were some particular frames where it was difficult to identify the filamentary shape due to the reduced emission. The filament from frames before and at ELM onset keep the same structure and location but with different emission levels (see 0 μs, 3rd row). Due to the limited resolution of this method, the start of the ELM onset is between the baseline and dashed vertical line that establishes the onset time.

Finally several tests with Elzar were performed. Different inversion grid settings were tried with the grid being placed inside the separatrix. The inversion plane center angle was set close to the camera at $\phi_0 \sim 180°$. The wathershed amplitude threshold for the identification of blobs cross-section on the inversion plane was set as low as possible ~ 0.001 [a.u.]. As shown in Fig. 5.14 a) filaments do not follow the magnetic field lines.

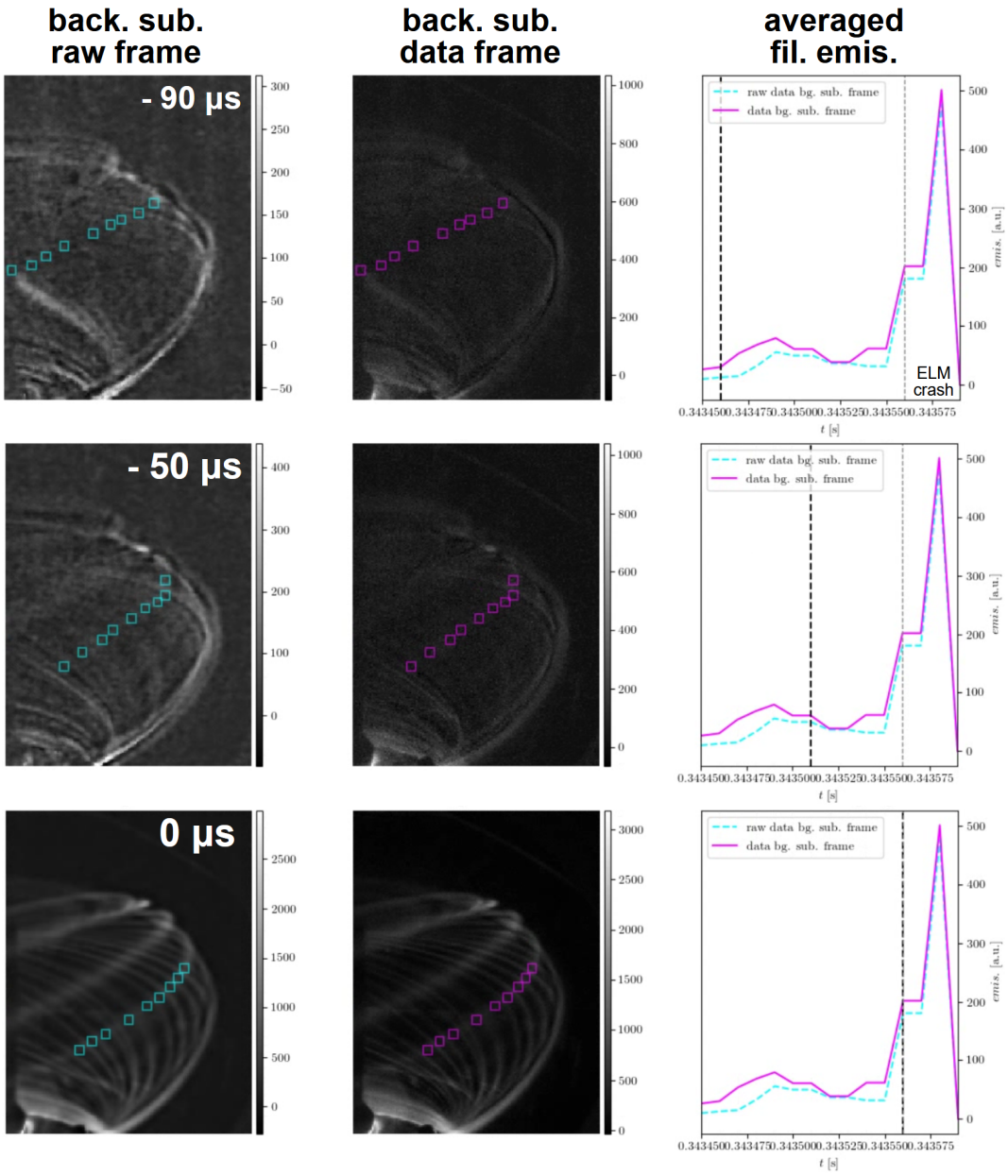

Figure 5.13: Filament emission analysis following a single filament before the ELM onset. Both frames are background subtracted from raw (cyan) and data (pink) frames. The emission of all pixels along a filament is averaged in order to obtain the emission profile (right column)

In Fig. 5.14 c) the filaments detected in the inverted plane are located too deep into the plasma core (*e.g.* -10 cm from the separatrix) or too close to the boundaries (*i.e.* outside the analysis grid). These structures were not identified, then were suspected of being "false positives". A different attempt was effectuated for

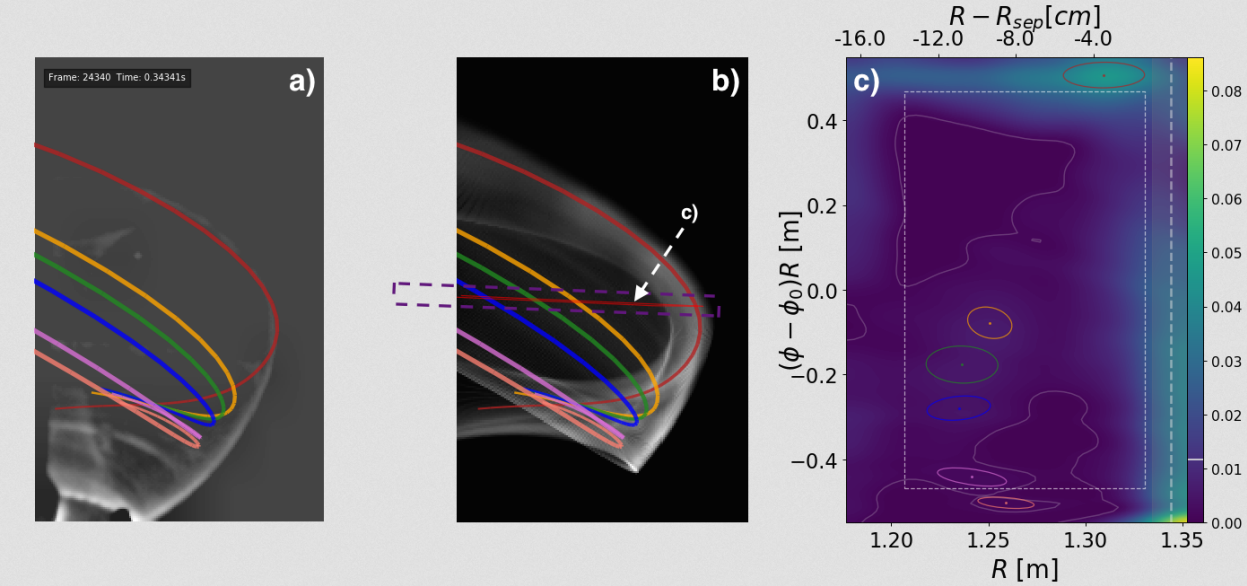

Figure 5.14: Elzar analysis results for MAST shot 29827; a) the pre-processed (raw) frame taken at $t = 0.34341$ s with superimposed field lines; b) the reprojection of emissivity data, the purple dashed box contains the inversion plane; c) inversion plane with false detections. The grid was placed in the interior of the separatrix.

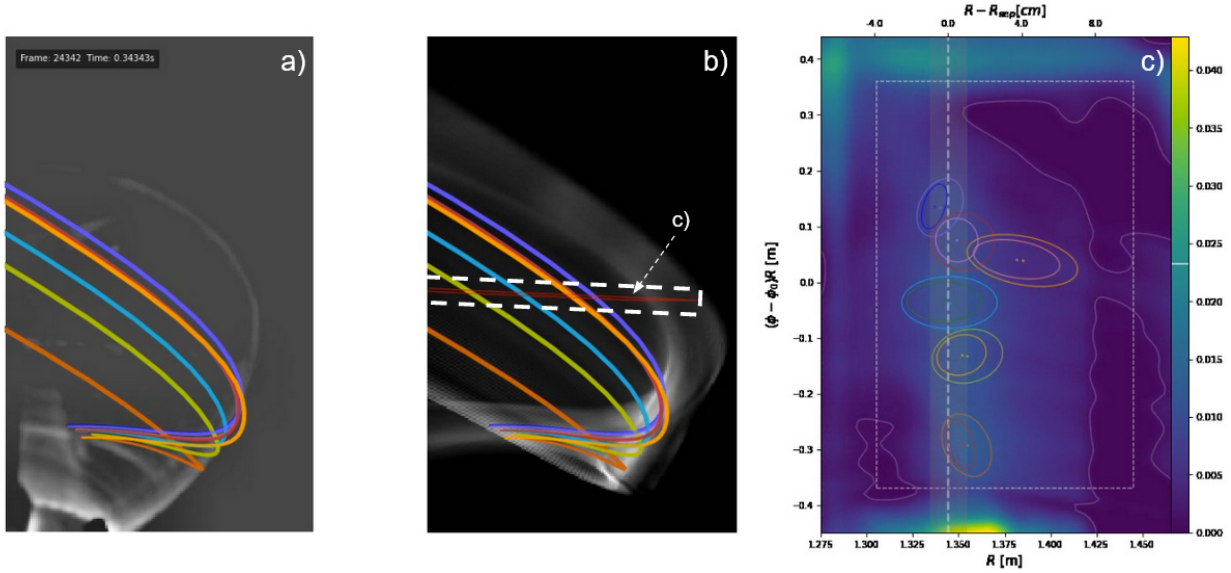

Figure 5.15: Elzar analysis results for MAST shot 29827; a) the pre-processed (raw) frame taken at $t = 0.34343$ s with superimposed field lines; b) the reprojection of emissivity data, the purple dashed box contains the inversion plane; c) inversion plane with false detections. The grid was placed in the vicinity of the separatrix.

the same ELM at a different frame, but changing the location of the grid in the vicinity of the separatrix. In Fig. 5.15 a) it is still observed that traced filaments do not follow the magnetic field lines. The inverted plane c) indicates that these filaments cross sections are located at the separatrix every $\sim 0.1m$. It is speculated that these are still false filaments. This lack of detection might be due to the line-integrated light by the fast camera. The D_α emission is more brighter in the SOL rather than in the pedestal region and interfere with the light from the transient structures.

5.6 Summary and discussions

The BES imaging technique is a powerful tool for observing ELM-precursor activity at the pedestal. Characteristic features from the detected structures at the pedestal are in reasonable good agreement with the observations reported by Kirk *et al.* [234]. Poloidal velocities are of the order of $v_Z \sim 1$ km/s and sizes are $\Delta R \sim 2-6$ cm and $\Delta Z = 2-3$ cm. Compared to different discharges and ELMs most of the cases show a negative velocity (with respect to the Z axis). However cases with opposite velocities were observed during the analysis (these were not shown in this chapter). The normalised scale $k_Z \rho_L \sim 0.4$ is lower the expected values of > 0.6. The most probable poloidal number $m \sim 45$ corresponds to the toroidal number $n \sim m/q \sim 20$ which is lower than the expected values $n \sim 30-40$. However, the statistical analysis does not return conclusive since all parameters have a distribution of values. This could be due to the approximations used in the analysis of BES data. The BES image is reconstructed from a linear interpolation using a small number of channel (32 over entire image, 8 within the pedestal region). This means that parameters derived from the reconstructed image (lengths, peak positions, etc) will have an error of the order of the pixel separation in the target area. The interpolated image therefore does not fully represent the exact shape of the precursor in detail.

The active Doppler shifted line emission from the excitation of neutrals provides more information compared to the passive D_α emission from background ionisations. The camera collects line integrated light and does not distinguish between the emissions from the SOL and the pedestal region. Elzar seemed unable to detect any structure in the pedestal region. The necessary assumptions that allow to perform a successful

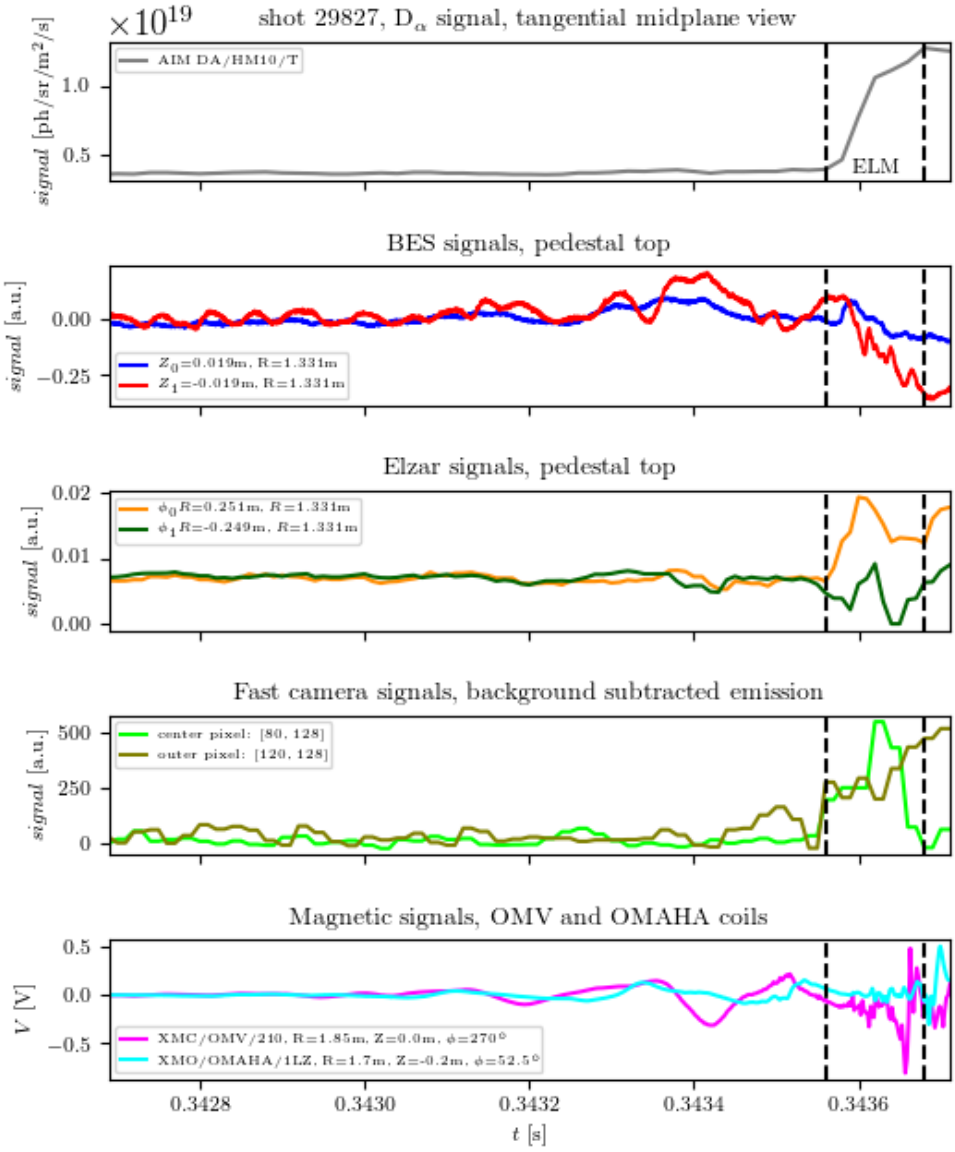

Figure 5.16: Comparison of diagnostics signals as functions of time, from top to bottom: line integrated D_α emission signal; BES signals at the pedestal top; Elzar inverted emissivity signals at the pedestal top; fast camera emission pixel-signals from background subtracted frames; Mirnov coils signals.

tomographic inversion are satisfied for L-mode plasmas with enough emission. However this is not the case with a low emission from inter-ELM filaments in H-mode plasmas. The camera has a resolution of 10 μs hence it could potentially detect fast oscillations with frequencies around 20 kHz. Another point is that an increase ion frame rate would decrease the detected light intensity (fewer photons getting collected) so with

a finite amount of gain this will make such features hard to detect. It is not a matter of resolution but other reasons need to be taken into account. The precursor activity and associated emissions are much fainter than ELM emission so are likely to be too faint to observe using line integrated line of sight camera. Applying a background subtraction at such low emission will increase the likely-hood of not detecting faint objects. Visible filaments in the background might correspond to ones already in the SOL and may overlap with the emission from transient structures inside the separatrix. Overall, visible camera based diagnostics and the analysis methodology presented severe limitations except for the BES system. This diagnostic was able to provide reasonable precursor parameters as well as a visual representation of the 2D structure and dynamics of precursors. Several signals are presented in Fig. 5.16 prior to an ELM event. The BES and Mirnov coils signals are able to show fluctuations during the ELM-precursor time range. The study of ELM-precursors requires a more reliable and solid approach that will be introduced in the next chapter.

Chapter 6

Spectral analysis of ELM-precursors in MAST

6.1 Introduction

Spectral methods can be used for extracting information from structures in the time domain. The trace recorded by a diagnostic in the form of a time series can be separated into frequency components representing the oscillations in the plasma. In this way the wavenumbers and directions (if multiple detectors are used) of the detected structures can be inferred. However, fast fluctuations cannot be analysed accurately by using techniques such as the Fourier transform. This method is ideal for studying turbulence that is stationary and homogeneous *i.e.* exhibiting a periodic behaviour [324]. However, this method is not applicable to non-linear and non-periodic modes. The origin of the problem comes from the locality in time and space of turbulence *i.e.* the interaction between large and small eddies as seen in chapter 2 section 2.1.1. The Fourier components are no longer independent of each other due to the mixing nature of turbulent flows. The Fourier transform spreads the information of locality (*i.e.* positions and times) to all scales of the coefficients unable to seize the inter-scale interactions. This means that the coefficients containing information from the whole time series

and any local information (*i.e.* locality in time and space) is smoothed out. The wavelet transform became an alternative in order to avoid the drawbacks of the Fourier transform as shown in chapter 3 section 3.4.3. This method is a generalisation of Fourier's theorem that improves the space/time resolution by constructing a particular local or windowed sinusoidal function (*i.e.* wavelet) which can be adjusted (*i.e.* zoom feature) to fit into each frequency band (*i.e.* scale). In this way the wavelet transform can independently measure the localised non-linear dynamics in a turbulent signal. The use of a type of wavelet, *e.g.* the Morlet wavelet, was proposed by Farge and Rabreau [325] for analysing two-dimensional turbulent flows, later applied to the study of diverse phenomena in plasma turbulence [326]. The combination of wavelet transforms with analysis tools such as cross-correlation and bicoherence allows to measure the rapid phase shifts and the non-linear coupling of intermittent short-lived modes in plasmas. The motivation of this chapter is demonstrating the utility of the wavelet transform applied to ELM-precursors in MAST. The aim is to confirm these precursors share similar characteristics found in others tokamaks, especially to the results of NSTX which has the same spherical configuration. The same discharges studied in chapter 5 (*i.e.* 2013 campaign) will be studied here. The mentioned studies in chapter 2 section 2.3.6 have shown that the ELM-precursor nature can be measured as edge intensity fluctuations and as electromagnetic perturbations *i.e.* it originates from a MHD instability. Hence, in this chapter the BES data will be compared to the magnetic coil data using the wavelet transform technique. Data from fast camera is not used as it is unable to capture the fast fluctuations due to its low temporal resolution (as seen in Fig. 5.16 in section 5.6). The structure of this chapter is as follows: in section 6.2 the experimental setup is described including the BES and OMAHA diagnostics; section 6.3 explains the wavelet analysis method; section 6.4 is the summary of the discharges dataset; section 6.5 presents the results of the cross correlation analysis and section 6.6 presents the bispectral analysis; section 6.7 summarises the main results.

6.2 Experimental setup

The BES signals are analysed in this chapter in order to extract the spectral features of pedestal density fluctuations before the ELM crash. The specifications of the BES system were described in section 3.3.3.

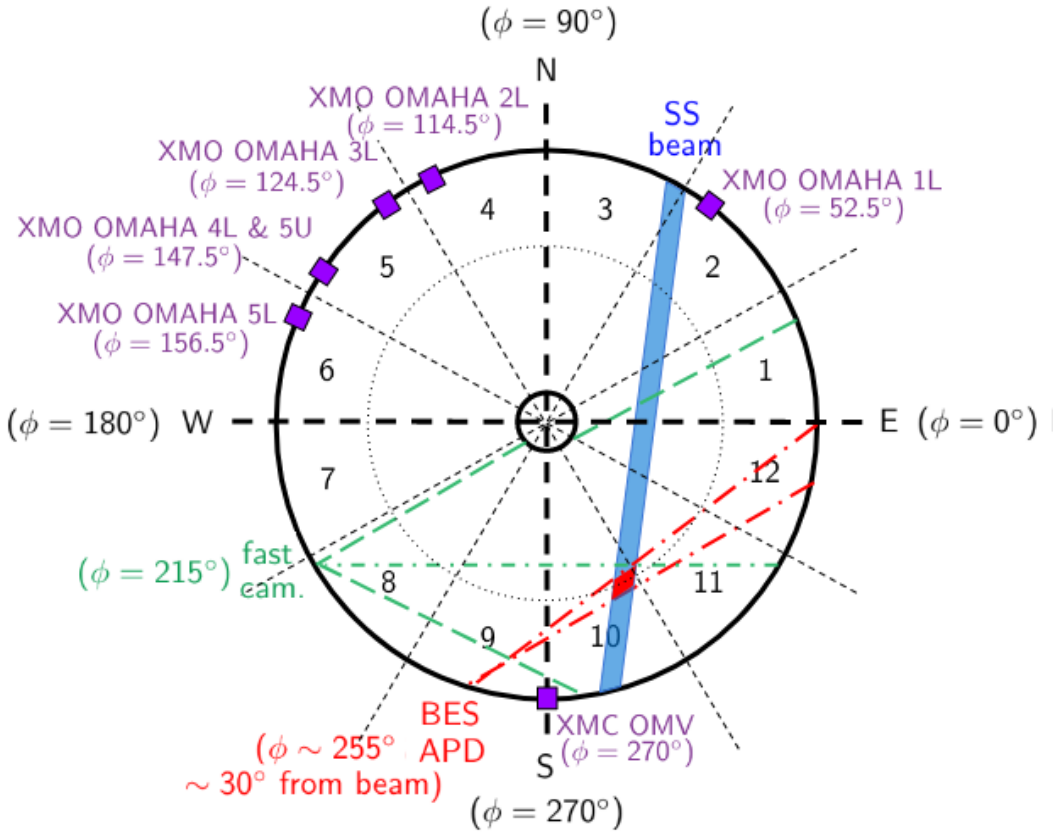

Figure 6.1: MAST top down cross-sectional view in the (R, ϕ) plane. Each diagnostic instrument is indicated: BES APD (red), NBI SS beam (blue), fast camera (green), and OMV, OMAHA coils (violet). Sectors are numbered from 1 to 12.

Name	1LZ	2LT	2LZ	3LT	3LZ	4LR	4LT	4LZ	5UR	5UT	5UZ	5LT	5LZ
Orientation	B_Z	B_ϕ	B_Z	B_ϕ	B_Z	B_R	B_ϕ	B_Z	B_R	B_ϕ	B_Z	B_ϕ	B_Z
R (m)	1.7	1.7	1.7	1.7	1.7	1.7	1.7	1.7	1.7	1.7	1.7	1.7	1.7
Z (m)	-0.2	-0.2	-0.2	-0.2	-0.2	-0.2	-0.2	-0.2	0.2	0.2	0.2	-0.2	-0.2
ϕ (°)	52.5	114.5	114.5	124.5	124.5	147.5	147.5	147.5	147.5	147.5	147.5	156.5	156.5

Table 6.1: OMAHA coils names, orientations, radial, vertical, and toroidal positions in MAST. L (lower) and U (upper) refer to the vertical position Z = -0.2 m and 0.2 m respectively. R, T, Z refer to the coils orientations B_R, B_ϕ, B_Z respectively [327]

The location of the different diagnostics used in this chapter are shown in the MAST top down view in Fig. 6.1. The analysis includes exclusively the data from the BES and OMAHA diagnostics. The position of the fast camera and the Outboard Mirnov Vertical (OMV) coils are also reported. The OMV arrays consisted of 19 pairs of coils mounted vertically at sector 9. However, several problems were reported in the CCFE log book: the swapping of signal names due to the limited number of channels and problematic recordings with null output signals. For these reasons the OMAHA coils were chosen instead of the OMV coils with different bandwidths of 2 MHz and 500 kHz respectively. Six OMAHA probe heads are located in different sectors of the torus as shown in Fig. 6.1. The name for each OMAHA coil designates its orientation (R, T, Z) and vertical position (U, L). The orientations and coordinates of the OMAHA coils are given in Table 6.1.

6.3 Wavelet transform

6.3.1 Wavelet spectral envelope

From chapter 3 section 3.4.6, the wavelet spectrum or spectrogram $P_\psi(t,f)$ is defined as the square of the wavelet coefficients $W(t,f)$ of a time signal according to Eq. 3.47. The bias correction by the normalisation of scales is included. The definition of the computed coefficients $W(t,f)$ is given by Eq. 3.45. The growth rate γ is approximated as the normalised derivative of the envelope of $P_\psi(t,f)$:

$$\gamma(t,f) = \frac{1}{\left|H[P_\psi(t,f)]_f\right|}\frac{\partial\left|H[P_\psi(t,f)]_f\right|}{\partial t} \tag{6.1}$$

The envelope corresponds to the absolute value of the Hilbert transform $\mathcal{H}[\,]_f$ applied along the time axis at each frequency f_j of the spectrogram such as:

$$\mathcal{H}[P_\psi(t,f)]_f = \left\{\frac{1}{\pi t} * P_\psi(t,f_j)\right\}_{j=0,1,\ldots,J} \tag{6.2}$$

Here $*$ is the binary convolution operator. The octave index j indicates the values of P_ψ in time at each scale s_j (*i.e.* frequency f_j).

6.3.2 Wavelet cross-correlation

The output of the wavelet transform corresponds to the spectral energy coefficients containing the information of any detected mode present in the original signal. These coefficients represent the amplitudes and the phases of these modes. In general the cross-correlation of two sinusoidal signals (shifted in time or space) gives the phase shift between these signals. The phase shift δ is calculated from the angle of the argument between two computed wavelet spectral components at different positions (in time or space) indicated by the subscripts 0 and 1:

$$\delta_{0,1} = \arg\left[W_0^*(t,f)W_1(t,f)\right] \tag{6.3}$$

Here arg refers to the argument and $*$ refers to the complex conjugate. At JET, large spurious phase jumps were measured during ELMs using Fourier transforms. Wrapped phases are enclosed in the $[-\pi, \pi]$ interval. Unwrapping methods consist in correcting any eventual discontinuities by adding or subtracting multiples of 2π to the phase angle. By using wavelet transforms, the possible effect of phase jumps are neglected for variations related to coherent spectral components [239]. In this thesis this assumption is incorporated. Two BES signals from different APD channels corresponding to two vertical positions (Z_0, Z_1) at the same radius (located at the top pedestal position R_{ped}) are used to estimate the poloidal mode number:

$$m(t,f) = \frac{\delta_{Z_0,Z_1}}{\Delta\theta} = \frac{1}{\Delta\theta}\arg\left[W_{Z_0}^*(t,f)W_{Z_1}(t,f)\right] \tag{6.4}$$

The poloidal arc for a spherical tokamak is approximated as $\Delta\theta \simeq \Delta Z/R_{ped}$ with $\Delta Z = |Z_0 - Z_1|$ the vertical distance between both channels. Assuming that the mode propagates in rational surfaces, the toroidal n modal number can be approximately calculated from:

$$n(t,f) \simeq \frac{m(t,f)}{q_{ped}} \tag{6.5}$$

Here q_{ped} is the safety factor taken at the top pedestal radius R_{ped}. The safety factor q is obtained by using EFIT. The corresponding wavevector and velocity are given by:

$$k_Z = \frac{\delta_{Z_0,Z_1}}{\Delta Z} = \frac{\delta_{Z_0,Z_1}}{R_{ped}\Delta\theta} \qquad\qquad v_Z = \frac{2\pi f}{k_Z} \tag{6.6}$$

OMAHA coils are separated in the toroidal direction but located at the same radial distance from the centre *i.e.* at $R_O = 1.7$ m. The wavelet cross correlation of two OMAHA time signals at two toroidal positions (ϕ_0,

ϕ_1) gives the toroidal mode number:

$$n(t,f) = \frac{\delta_{\phi_0,\phi_1}}{\Delta\phi} = \frac{1}{\Delta\phi}\arg\left[W^*_{\phi_0}(t,f)W_{\phi_1}(t,f)\right] \tag{6.7}$$

The toroidal arc is calculated as $\Delta\phi = |\phi_0 - \phi_1|$ in radians. Note that the correlation is performed between coils oriented toroidally and at the same poloidal position. In the toroidal orientation, the corresponding wavevector[1] and velocity are given by:

$$k_\phi = \frac{\delta_{\phi_0,\phi_1}}{R_{ped}\Delta\phi} \qquad\qquad v_\phi = \frac{2\pi f}{k_\phi} \tag{6.8}$$

For all diagnostics, the normalised scale $k\rho_L$ is the characteristic size of the coherent structures dimensions and is used for comparison between different tokamaks [328]. The hybrid Larmor radius is given by:

$$\rho_L = \frac{\sqrt{m_i T_e}}{eB} \tag{6.9}$$

Finally, the cross coherence is defined by the amplitude [329]:

$$\Gamma(t,f) = \frac{\left|W^*_0(t,f)W_1(t,f)\right|}{\sqrt{W^*_0(t,f)W_0(t,f)W^*_1(t,f)W_1(t,f)}} \tag{6.10}$$

The subscripts (0, 1) refer to the Z or ϕ positions. The cross coherence measures the degree of correlation between both wavelet spectra: when $\Gamma \sim 1$ wavelet coefficients are in phase, when $\Gamma \sim 0$ wavelet coefficients are uncorrelated.

6.3.3 Wavelet bispectrum and bicoherence

In order to analyse the intermittent non-linear coupling between interacting modes the wavelet transform can be combined with the bispectral analysis. The phase coupling is defined to occur when three frequencies (f, f_1, f_2) are simultaneously present in the signal, and the sum of the phases of these frequencies remains constant [330]. The wavelet bispectrum computed between $t_1 = \tau_1\delta t$ and $t_2 = (\tau_1 + T)\delta t$ is given by:

$$B_\psi(t,f_1,f_2) = \frac{1}{T}\sum_{\tau=\tau_1}^{\tau_1+T} W(t,f_1)W(t,f_2)W^*(t,f_1+f_2) \tag{6.11}$$

[1]Instead of using the radius of the OMAHA location $R_O = 1.7$ m, the chosen radius was the location of the ELM-precursor *i.e.* at the pedestal R_{ped} in the range $\sim [1.2, 1.4]$ m.

and respectively the wavelet bicoherence is the normalized bispectrum:

$$b^2_\psi(t, f_1, f_2) = \frac{\left|\sum_\tau W(t, f_1)W(t, f_2)W^*(t, f_1 + f_2)\right|^2}{\sum_\tau \left|W(t, f_1)W(t, f_2)\right|^2 \sum_\tau \left|W^*(t, f_1 + f_2)\right|^2} \tag{6.12}$$

Here τ_1 is the sampling start time and T the sampling index which must be longer than the wave period of interest. The bispectrum B_ψ indicates the degree of non-linear coupling between modes of frequencies (f, f_1, f_2) in the spectrogram. Any interaction must satisfy the three-wave coupling criterion: $f = f_1 + f_2$. As T is increased, both bispectra converge to higher-order spectral areas unveiling the presence of non-linear interactions in the original signal. In comparison with the cross coherence, the bispectrum measures the phase coherence of quadratically correlated modes. The bicoherence b_ψ is the normalised bispectrum: when $b^2_\psi \sim 1$ modes are strongly coupled whereas when $b^2_\psi \sim 0$ modes are uncorrelated. In plasma physics the squared form b^2_ψ is used instead of b_ψ. The integrated bispectrum and bicoherence are respectively given by:

$$B_\psi(t, f) = \sum_{f_1, f_2} \left|B_\psi(t, f_1, f_2)\right| \qquad\qquad b^2_\psi(t, f) = \sum_{f_1, f_2} b^2_\psi(t, f_1, f_2) \tag{6.13}$$

The integrated bispectrum represents the contribution of nonlinear interactions at each frequency f due to phase coupling of all spectral components summing over the frequencies f_1 and f_2 satisfying the resonance condition. The integrated bicoherence is defined likewise with values between 0 and 1.

6.4 Discharges dataset

The Table 6.2 summarises the set of discharges studied. The shot #29827 was previously studied in the BES imaging analysis and the 4th ELM once more used as an example for guidance. Additionally, ELMs from 7 supplementary discharges are also analysed. In total, the analysis covered an ensemble of 60 ELMs in total: this amounts to 52 type-I ELMs and 6 type-III ELMs. Two "failed" ELMs (indicated by a "(+1)" in shots #29442 and #29786) are characterised with an interrupted D_α peak and no observed plasma ejection. The same proceeding for identifying the inter-ELM period, the ELM-precursor and the ELM onset is detailed in chapter 5 and repeated in this chapter. An example of D_α signal and ELM identification is shown in Fig. 5.4. Several ELMs are contained in a particular time range for each discharge.

Shot #	type	amount	t(s)	B_ϕ(T)	I_p(kA)	$P_{nbi,ss}$(MW)
29442	III	6 (+1)	0.22-0.24	0.44	503	2.42
29504	I	6	0.27-0.35	0.41	383	2.21
29762	I	7	0.28-0.33	0.43	657	2.24
29768	I	9	0.40-0.50	0.35	384	2.26
29786	I	9 (+1)	0.23-0.30	0.42	627	2.13
29790	I	10	0.28-0.32	0.43	622	2.19
29827	I	8	0.30-0.40	0.29	384	2.19
29978	I	3	0.24-0.25	0.43	631	2.15

Table 6.2: Shot used in for the study of ELM-precursors using BES data. Columns from left to right: shot number, ELM type, amount of ELMs, time range containing ELMs, maximum toroidal magnetic field, average plasma current, and maximum heating power of the NBI south beam.

6.5 Results

6.5.1 Wavelet spectral analysis

The wavelet analysis is applied to BES and OMAHA signals. A typical example (in this case shot #29827) of the raw signals from BES, OMV and OMAHA diagnostics and the corresponding spectrograms is shown in Fig. 6.2. The foot of the D_α peak in Fig. 6.2 (a) is taken as the ELM onset reference time. The time window of analysis is wide enough covering 6 ms centered at the ELM onset time in order to avoid boundary errors. The analysis window corresponds to $N = 12000$ data points with a time step $dt = 0.5$ μs for BES and OMAHA signals. The analysis window corresponds to $N = 3000$ data points with a time step $dt = 2$ μs for OMV signals. The subplots only show the spectral power inside the cone of influence 1 ms before

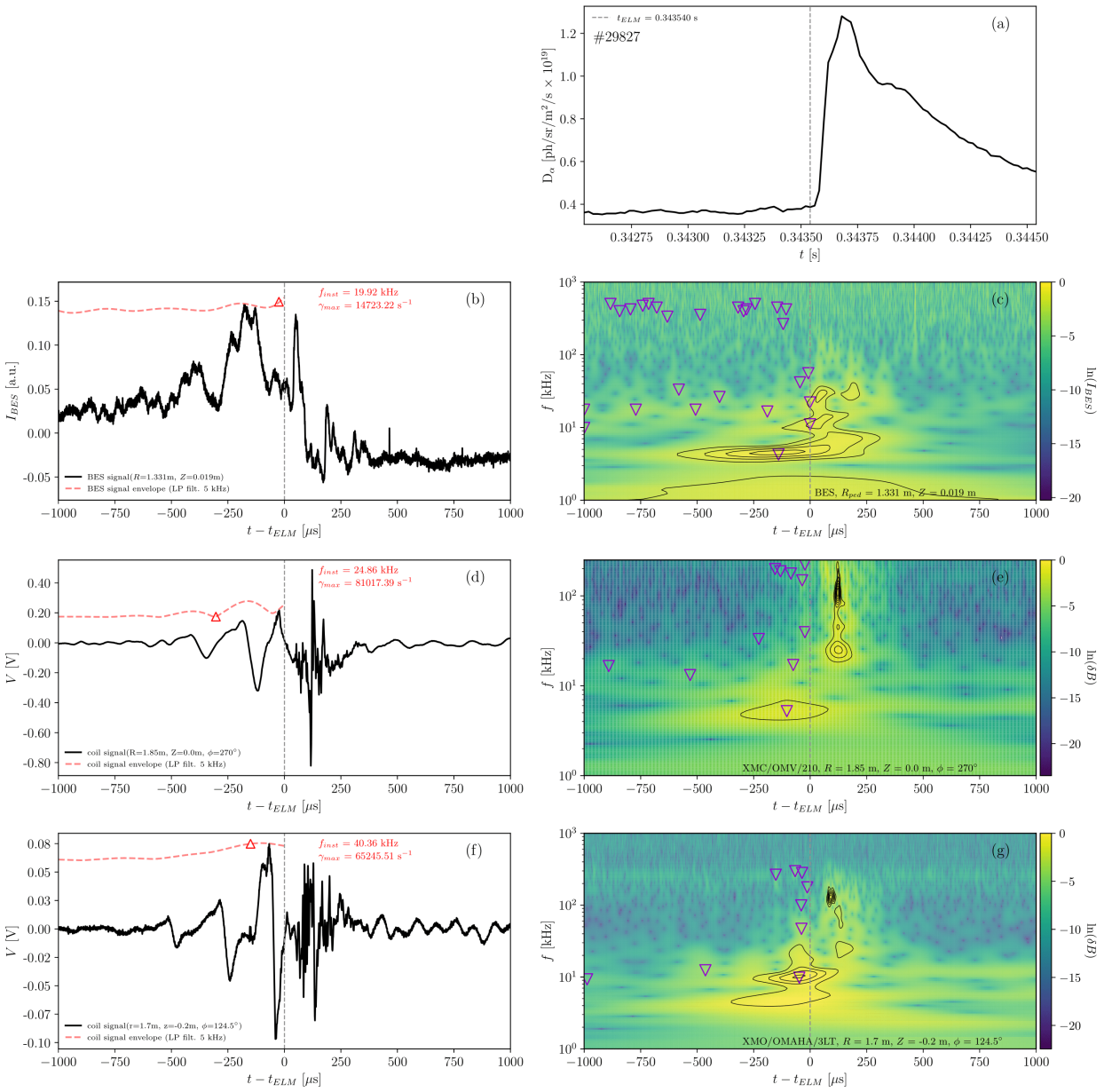

Figure 6.2: MAST shot #29827. In (a) D_α peak marking the ELM onset at $t = 0.34354$ s (dashed vertical line). Subplots in (b), (d) and (f) correspond to BES, OMV and OMAHA raw signals (black) respectively plus the envelopes of low-pass filtered signals (dashed red); the red triangle marks the maximum growth rate time. Subplots in (c), (e) and (f) correspond to the raw signals' respective wavelet spectrograms $\ln P_\psi(t, f)$ in logarithmic scale; black contours correspond to the 95% significance level; upside-down purple triangles mark the local peaks above the standard deviation of the spectral power and detected before the ELM onset.

and after the ELM onset. In the case of the OMAHA signal the transfer function was applied for each computed frequencies by the wavelet routine. Instead of correcting the raw signal which is consuming, the resulting spectrogram was corrected for each frequency in amplitude attenuation and phase shift [295]. In a preliminary analysis, envelopes are calculated using the Hilbert transform of low-pass filtered signals $x_{LP}(t)$ with a cut-off frequency of 5 kHz. The choice of this cut-off frequency is meant to exclude the low frequency modes in order to detect the dominant high frequency components. The instantaneous frequency f_{inst} and growth rate γ are respectively defined as:

$$f_{inst}(t) = \frac{1}{2\pi}\frac{d\Phi}{dt} \qquad \gamma(t) = \frac{1}{A}\frac{dA}{dt} \tag{6.14}$$

The phase angle Φ and the envelope amplitude A are defined as the argument and the absolute value of the applied Hilbert transform to the low-pass filtered signal:

$$\Phi = \arg[\mathcal{H}[x_{LP}(t)]_t] \qquad A = \left|\mathcal{H}[x_{LP}(t)]_t\right| \tag{6.15}$$

In Figs. 6.2 (b), (d) and (f), amplifying oscillations are clearly observed starting before the ELM onset. The instantaneous frequency tends to be of the order of $20 - 40$ kHz. The maxima of the growth rates remain in the range of $10^4 - 10^5$ s^{-1}. In Figs. 6.2 (c), (e) and (g), the respective spectrograms show similar spectral features across all diagnostics. Despite detecting several modes in the range of 5 to 250 kHz prior to the ELM onset, the highest spectral power areas are located inside the 95% significance contours for frequencies between $5 - 30$ kHz. For all diagnostics, around 100 μs before the ELM onset the 5 kHz mode is decaying while the $10 - 30$ kHz modes start to increase reaching their maxima just before the ELM onset at $t - t_{ELM} \simeq 0$ μs. In order to follow a more refined approach, a 2D peak detection method helps to highlight isolated, but less significant, peaks above a variable threshold proportional to the standard deviation of the spectral power before the ELM crash. In the case of the BES signal, some regular intermittency is visible for the 18 kHz mode (*i.e.* slightly below 20 kHz) that peaks in amplitude every $(-250, -200)$ μs until reaching the ELM crash. Note that no modes are detected above $>$ 20 kHz up to the ELM onset until reaching frequencies around $\sim$ 500 kHz with irregular peaks. Furthermore, near to the ELM onset such as $>$ - 50 μs the intermittent mode diverges and several components appear in a narrowed area: peaks appear at $\sim$ 10, $\sim$ 20, and $\sim$ 40 kHz. In the case of both Mirnov coils signals, activity can be detected for a large range

of frequencies between $5 - 250$ kHz during 100 μs before the ELM crash. Due to its lower bandwidth of 1 MHz, the OMV coil has lower resolution and the spectrum can only highlight the 5 kHz mode. This can be seen in Figs. 6.2 (d)-(e) and (f)-(g) when comparing the OMV and OMAHA time series and spectrograms: high frequency components observed in the OMAHA signal and spectrum are not present in the OMV signal and spectrum. For these reasons and for the following analysis the data from the OMV coils are not used. By analysing different discharges, it was noticed that there is not a clear pattern in the arrangement of spectral features. For instance, for shots #29442 and #29504 the 5 kHz mode was not detected whereas spectral peaks around 20 kHz were identified. Some ELMs for shot #29442 include intermittent peaks around $80 - 90$ kHz. Differently, for shot #29992 some peaks were associated with frequencies around 50 kHz. This diversity of spectrograms, in between ELMs and shots, could indicate the existence of different types of precursors. The amount of data and information contained in one spectrogram meant that a more targeted approach was needed. A complementary analysis of OMAHA signals and wavelet spectra was undertaken to find patterns in the precursor activity. The aim was to isolate different frequencies identified in the spectrogram and extract characteristic parameters. These are the onset times, envelope's maximum peak times, envelope's maximum amplitudes and maximum growth rates. In Fig. 6.3 the signal from the OMAHA 4LT coil is used as an example. Here only the last 1 ms before the ELM crash is analysed by applying a bandpass filter to the raw signal for each frequency: 5, 10, 20 kHz. The choice of these frequencies is due to their association with the instabilities involved in the ELM mechanism *i.e.* the ballooning mode (low frequency mode) and the ELM-precursor (high frequency mode). The filtered signals were then corrected for amplitude attenuation and phase shift. The onset time corresponds to the starting point of the amplifying oscillations: this is calculated as the time at which the signal exceeds the standard deviation computed over a longer time. The Hilbert transform was applied to the signal to obtain the signal's envelope. It was noticed that signals variations tend to evolve from a linear to a non-linear behaviour when increasing to higher frequencies. More specifically, the 5 kHz case shows a linear growth whereas the 20 kHz case present a regular beating distinguished by three local peaks. These "beatings" (or peaks on the signal or spectral areas on spectrograms) intermittently occur every 200 μs which corresponds to a beating frequency of 5 kHz. It is deduced that there might be indicative of a coupling between both modes. Furthermore, the

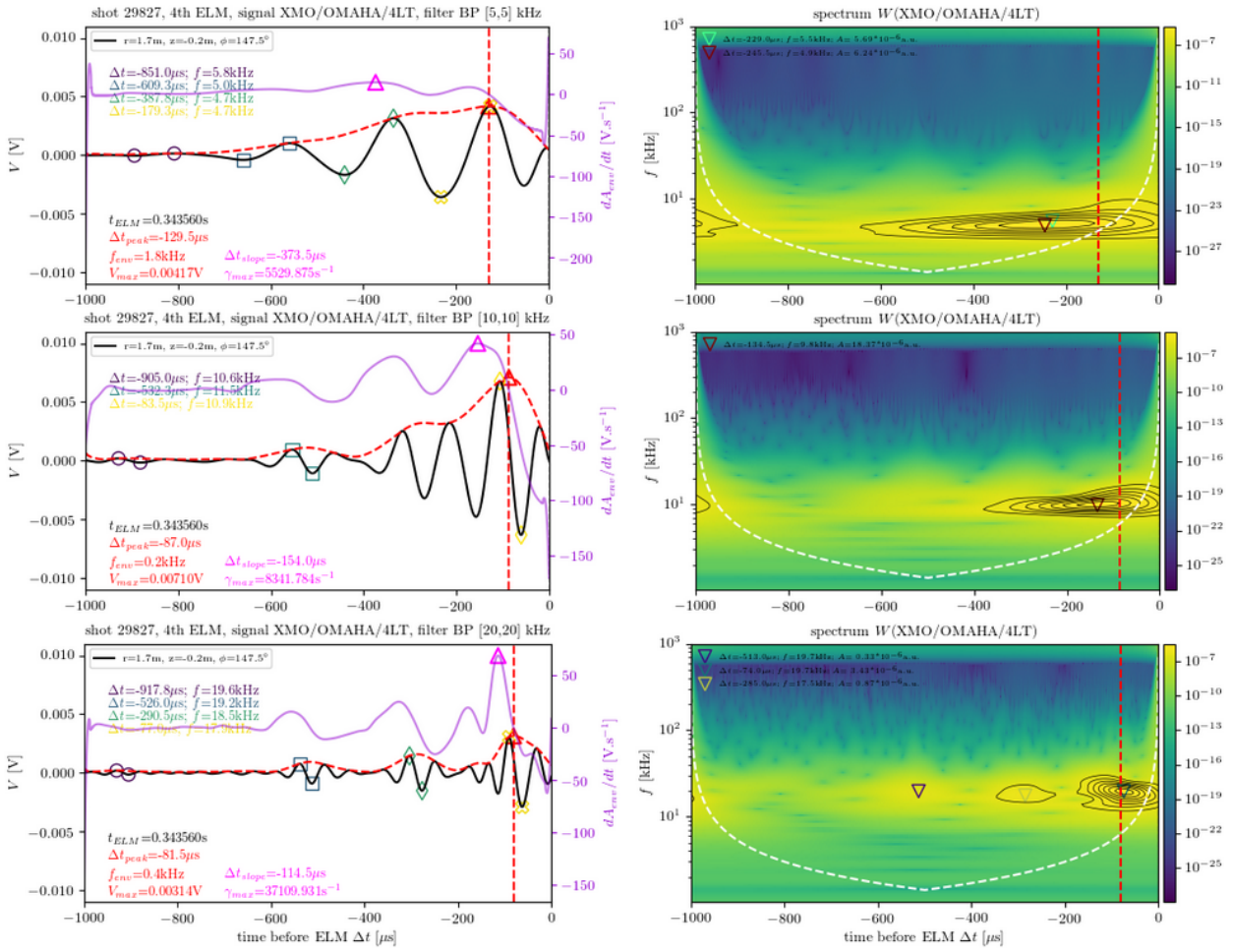

Figure 6.3: MAST shot #29827; ELM at $t = 0.34354$ s. (left) OMAHA/4LT signals filtered at 5, 10, 20 kHz respectively; (right) corresponding wavelet spectra. On the left: the red dashed line indicates the envelope peak A_{max}, the magenta line indicates the envelope gradient dA/dt with triangle markers indicating the maxima. On the right: the white dashed line indicated the cone of influence, upside-down triangle markers indicate the local spectral maxima.

envelope peaks for each frequency correspond to $\Delta t_5 \sim -130$ μs, $\Delta t_{10} \sim -87$ μs, and $\Delta t_{20} \sim -81$ μs and their respective spectral peaks correspond to $\Delta t_5 \sim -230$ μs, $\Delta t_{10} \sim -120$ μs, and $\Delta t_{20} \sim -75$ μs. Note that there is always a decay between the envelope peak and the ELM onset of the order of 50 μs which decreases with increasing frequency. This analysis is applied to 12 ELMs that occur during the shot #29827. All characteristic parameters are reported in function of ELM crash times in Fig. 6.4. Some points are absent indicating there was no clear feature to extract. The onset times (top left) decrease with increasing

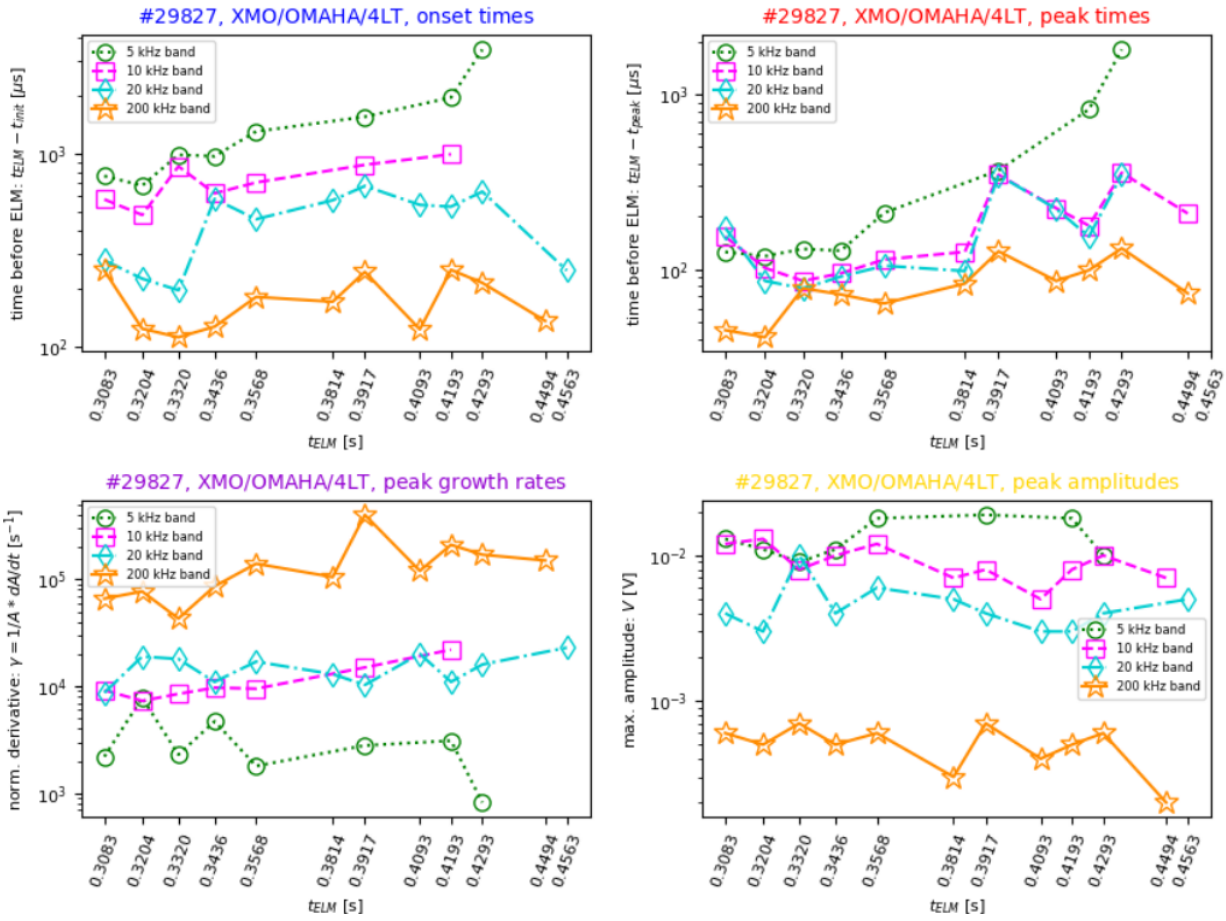

Figure 6.4: MAST shot #29827; 12 ELMs times are indicated along the x axis. Analysed parameters are: onset times (top left), envelope peak times (top right), peak growth rates (bottom left) and amplitudes (bottom right) for frequency bands: 5, 10, 20 and 200 kHz.

frequency, with a range from the order of the ms (for 5 kHz) to the order of hundreds of μs (for 200 kHz). As long as the discharge continues, there seems to be an increase trend with lower frequencies on setting earlier with later elms but the onset is approximately same at higher frequencies. A similar trend is observed in the envelope peak times (top right) with the envelope peaking closer to the ELM the higher the frequency. This correlates with the onset times since earlier onset times lead to earlier envelope peaks. Also, as the ELM number increases the envelope peaks at increasingly early times. This is especially clear for the 5 kHz mode but less clear for the higher frequencies. The peak amplitude (bottom right) is proportional to the inverse of the frequency therefore lower frequencies have more energy. Concerning the normalized growth rate (bottom left), assuming that the peak of the envelope gradient is close to the peak (might not be), the decrease in the

growth rate with decreasing frequency is due to the increase in the amplitude. These remarks do not fully help to predict the manifestation of precursors. It was noticed that events of coupling take place in between the different modes as seen in Fig 6.3. By linearly decomposing the signals per frequency, by computing their corresponding spectrogram and then extracting characteristic features, leads to an incomplete analysis because these exclude the non-linear dynamics of the precursor. The next sections employ diverse methods that take into account these components.

6.5.2 Cross correlation analysis

The correlation of different BES channels or two OMAHA coils signals allows to estimate the characteristic parameters of precursors (see section 5.3.2). Using the raw data in Fig. 6.2, two examples are shown in Fig. 6.5 for two BES signals originating from the pedestal region at two vertical positions Z_0 = -0.02 and Z_1 = 0.02 m, and Fig. 6.7 for two OMAHA signals at two toroidal positions $\phi_0 = 124.5°$ and $\phi_1 = 147.5°$. The convention for determining the chosen APD channels is based on the results obtained in the previous chapter. According to the BES images, visible structures have vertical lengths of $\Delta Z \simeq 3$ cm in average. In order to detect the same structure the correlation of both signals must analyse the same oscillation. In this case channels need to be as close as possible in this configuration. Besides, the choice of both coils OMAHA/3LT and OMAHA/4LT was in part arbitrary (OMAHA/2LT have shown recording errors; OMAHA/1LT was to close to the beam). In order to help the visualisation the frequency range has been restrained to an interval of interest between 1 and 55 kHz. From the correlation between the wavelet spectra computed from the two BES signals according to Eq. 6.3 the phase is plotted in Fig. 6.5 (a). A common feature that was found for different spectra and ELMs cases is the change of phase at the ELM onset where a plasma rotation reversal is taking place (see Fig. 5.6). In the case of Fig. 6.6 it is noticeable the transition from positive (π) to negative ($-\pi$) values or frequencies above 5 kHz. Low frequency modes close to 5 kHz present a rapid sign change before the ELM crash. High frequency modes seem to revert back to the original phase just before the ELM. Right after the crash, there is a recovery period of ~ 500 μs where phases are negative, then the phase reverts back to positive values. This trend is less obvious in the OMAHA cross spectra in Fig. 6.5 (a)

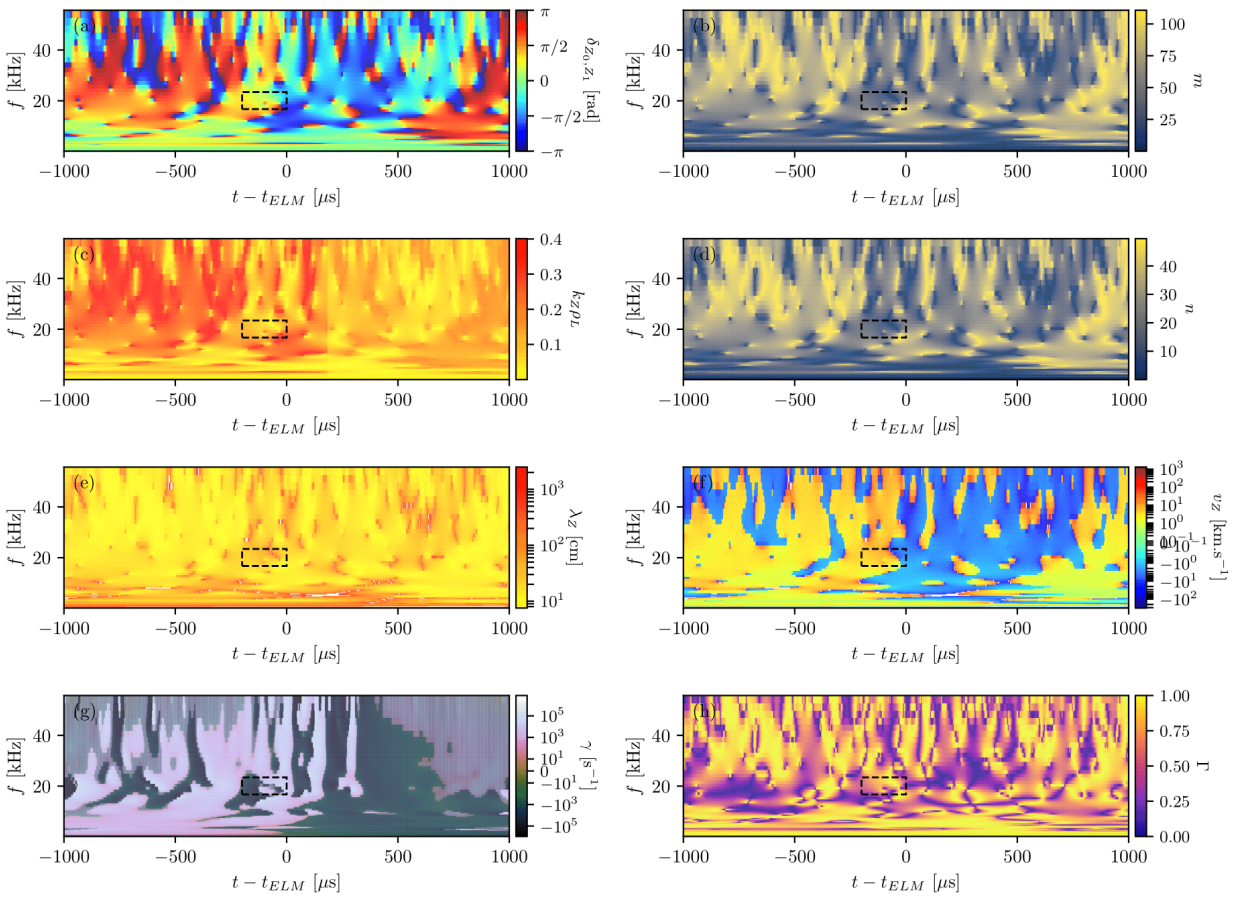

Figure 6.5: MAST shot #29827; ELM onset at $t = 0.34354$ s; cross spectra of two BES signals at pedestal: (a) phase δ_{Z_0,Z_1}; (b) poloidal number m; (c) normalised scale $k_Z\rho_L$; (d) toroidal number n; (e) vertical wavelength λ_Z; (f) vertical velocity v_Z; (g) average growth rate γ; (h) cross coherence Γ. Dashed black grids indicate the sampling area for computing histograms in Fig. 6.9.

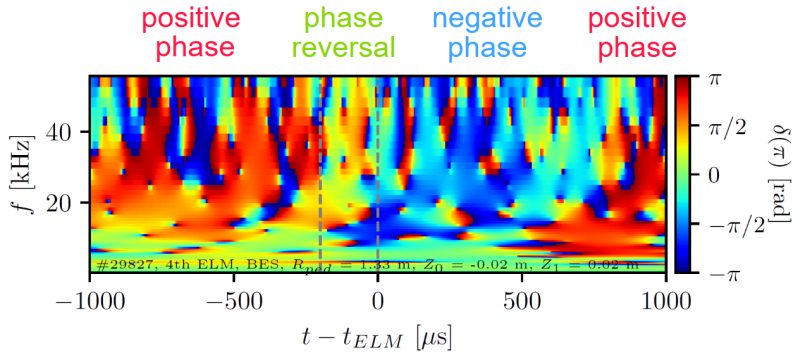

Figure 6.6: Phase $\delta(\pi)$ from Fig. 6.5 divided in stages before, during and after the ELM. The phase reversal from (π) to $(-\pi)$ passing through 0 occurs during the ELM-precursor time range (-200, 0) μs.

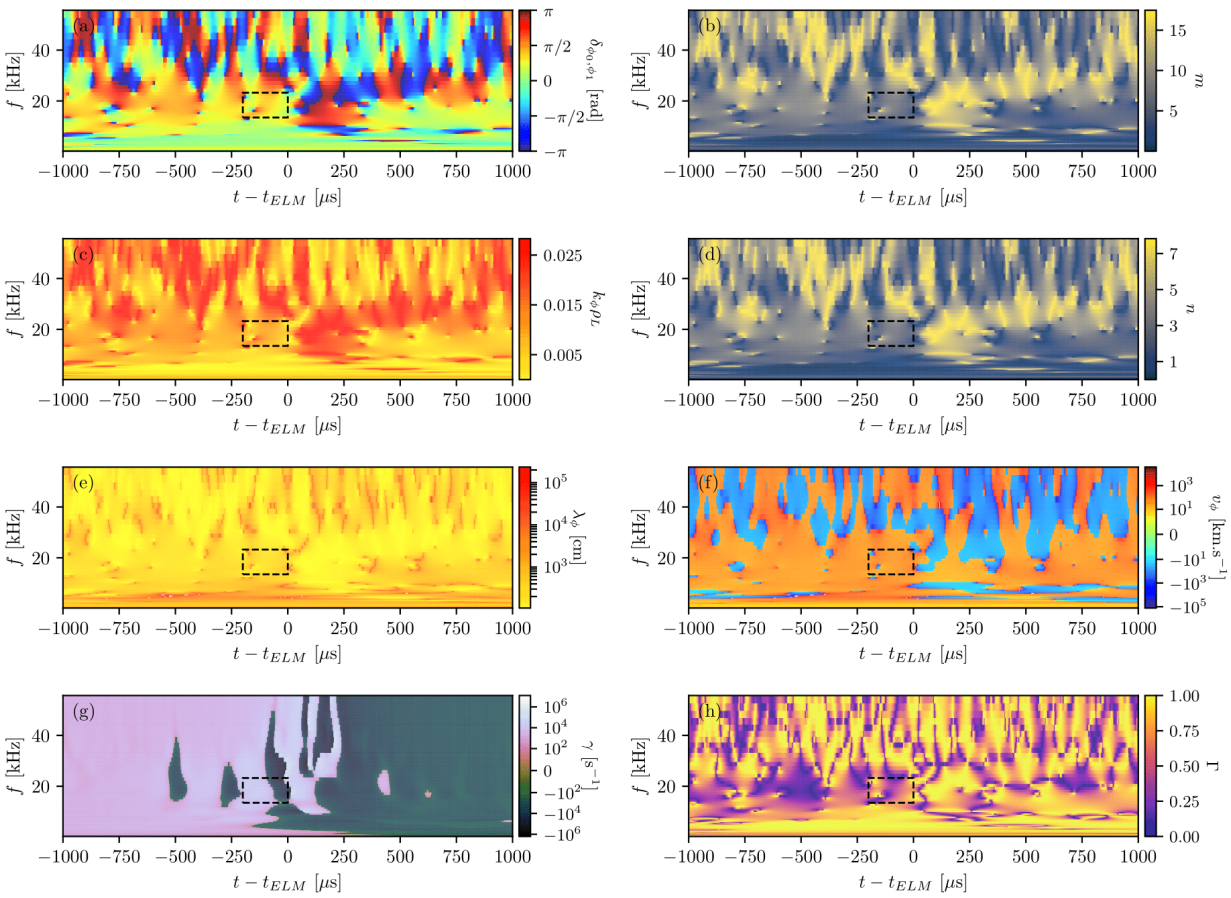

Figure 6.7: MAST shot #29827; ELM onset at $t = 0.34354$ s; cross spectra of two OMAHA 3LT & 4LT coils signals: (a) phase δ_{ϕ_0,ϕ_1}; (b) poloidal number m; (c) normalised scale $k_\phi \rho_L$; (d) toroidal number n; (e) toroidal wavelength λ_ϕ; (f) toroidal velocity v_ϕ; (g) average growth rate γ; (h) cross coherence Γ. Dashed black grids indicate the sampling area for computing histograms in Fig. 6.10.

with intermittent changes on the phase after the ELM. It can be inferred that the reversal of the poloidal flow is more affected by the pedestal collapse than the toroidal flow. Note that the behaviour described by the phase subplot determines the rest of the cross spectral parameters, except for the growth rate subplot. All these different spectra are difficult to interpret: each subplot contains too much information and/or noise that rapidly varies to the point it is impossible to identify a clear pattern. Plotting each subplot serves as an intermediate step to treat the data. In order to solve this issue an area of interest on the cross spectra is selected for a statistical analysis. This sampling area is delimited by a dashed black box in Figs 6.2 and 6.5 with dimensions such as time, frequency and cross power intensity. The time dimensions correspond to a

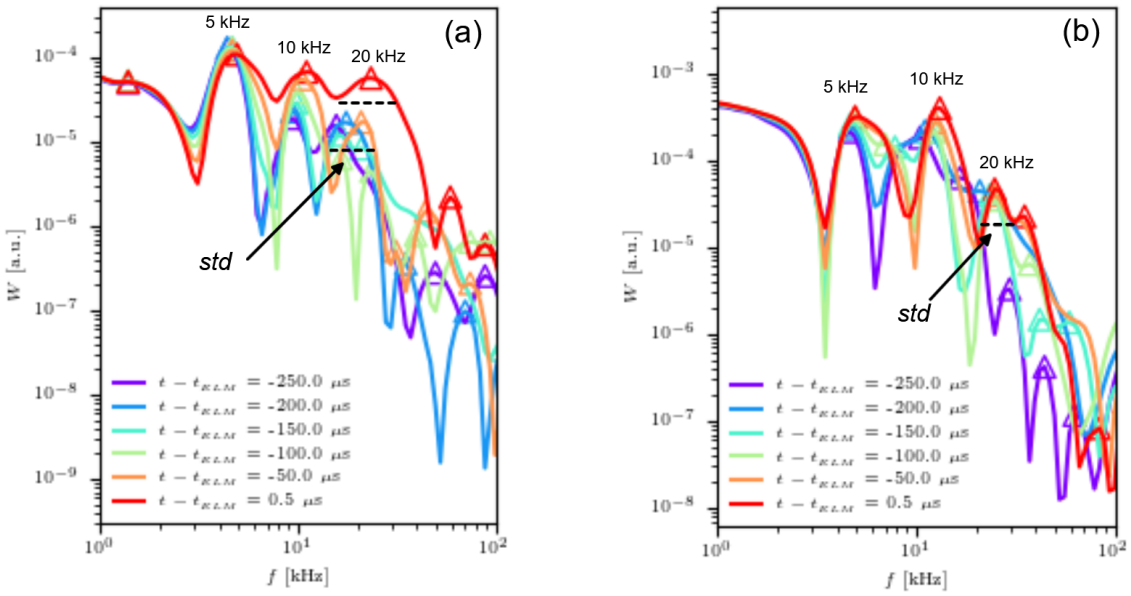

Figure 6.8: MAST shot #29827; ELM onset at $t = 0.34354$ s; BES wavelet spectral amplitude in function of frequency for channels at $Z = 0.02$ m (a) and $Z = -0.02$ m (b). Several curves correspond to different times between [-250, 0] μs. Three main peaks are highlighted corresponding to 5, 10 and 20 kHz modes. Dashed lines draw the approximated width of 20 kHz peaks representing the standard deviation (std).

fixed range of 200 μs before the ELM onset, which is the expected duration of the precursor. The frequency dimensions correspond to a varying interval case by case, centered at the closest peak to 20 kHz which is the expected frequency of the precursor. An example is shown in Fig. 6.8. For a given mode the frequency corresponding to the peak power is not constant and it evolves as the time gets close to the ELM crash. An average peak over the time interval ((-200, 0) μs) of this area is calculated, then the frequency interval is defined by the standard deviation of each average peak slice. The extracted power intensity within that area of interest is plotted as a histogram. This statistical representation allows to identify the most frequent number in a set. For each distribution a primary maximum and a second local maximum are reported. Each distribution is fitted with a Gaussian function centered at each histogram primary maximum. Two examples are shown in Fig. 6.9 for BES data and Fig. 6.10 for OMAHA data. In the case of BES, the frequency range was limited to (16, 23) kHz. Representative values are considered to be associated suitably with the Gaussian peaks. The phase is centered at $\delta_{Z_0,Z_1} \sim \pi/4$. By observing the grid in Fig. 6.5 (a), this value corresponds to the earlier times of the analysis area and then decreases when times is close to the ELM crash. Poloidal and

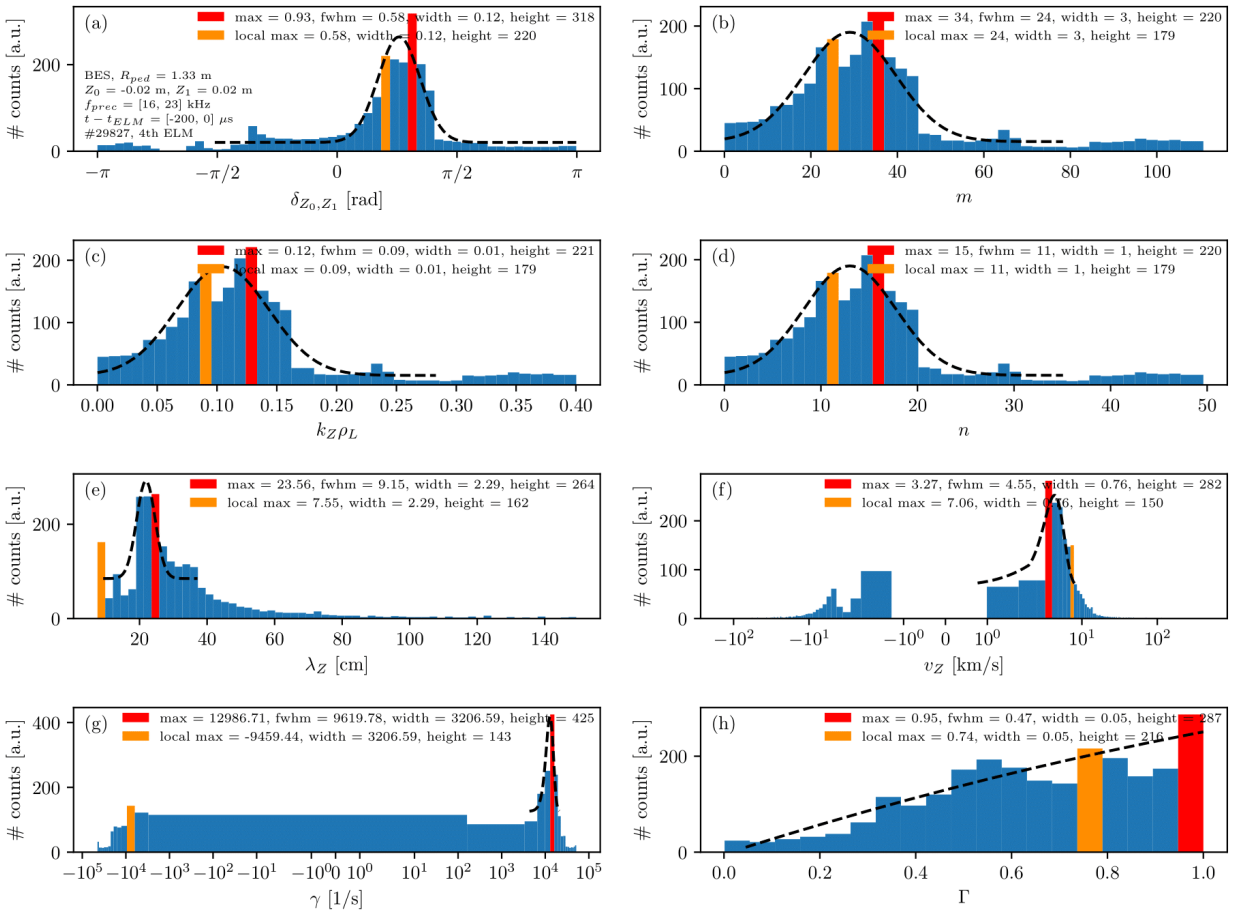

Figure 6.9: MAST shot #29827; ELM onset at $t = 0.34354$ s; BES histograms from Fig. 6.5: (a) vertical phase δ_{Z_0,Z_1}; (b) poloidal number m; (c) normalised scale $k_Z\rho_L$; (d) toroidal number n; (e) vertical wavelength λ_Z; (f) vertical velocity v_Z; (g) average growth rate γ; (h) cross coherence Γ. Red and orange bars indicate the primary maximum and second local maximum. Dashed black curves correspond to the Gaussian fit.

toroidal numbers peaks are located around $m \sim 30 \pm 10$ and $n \sim 12 \pm 5$. Poloidal wavelengths presents two peaks at 8 cm (early stage in the grid) and 20 cm (late stage in the grid). These results correlate with the observations from the last chapter: inter-ELM stages of the precursor present structures of length $\Delta Z \sim 3$ cm, whereas the stage close to the crash presents irregular structures that exceed the window of the BES imaging system and these would measure $\Delta Z \sim 10$ cm. The normalised scale is centered at $k_Z\rho_L \sim 0.1 \pm 0.05$ for early stages, which is in the same order of magnitude of BES imaging results. The poloidal velocity peak

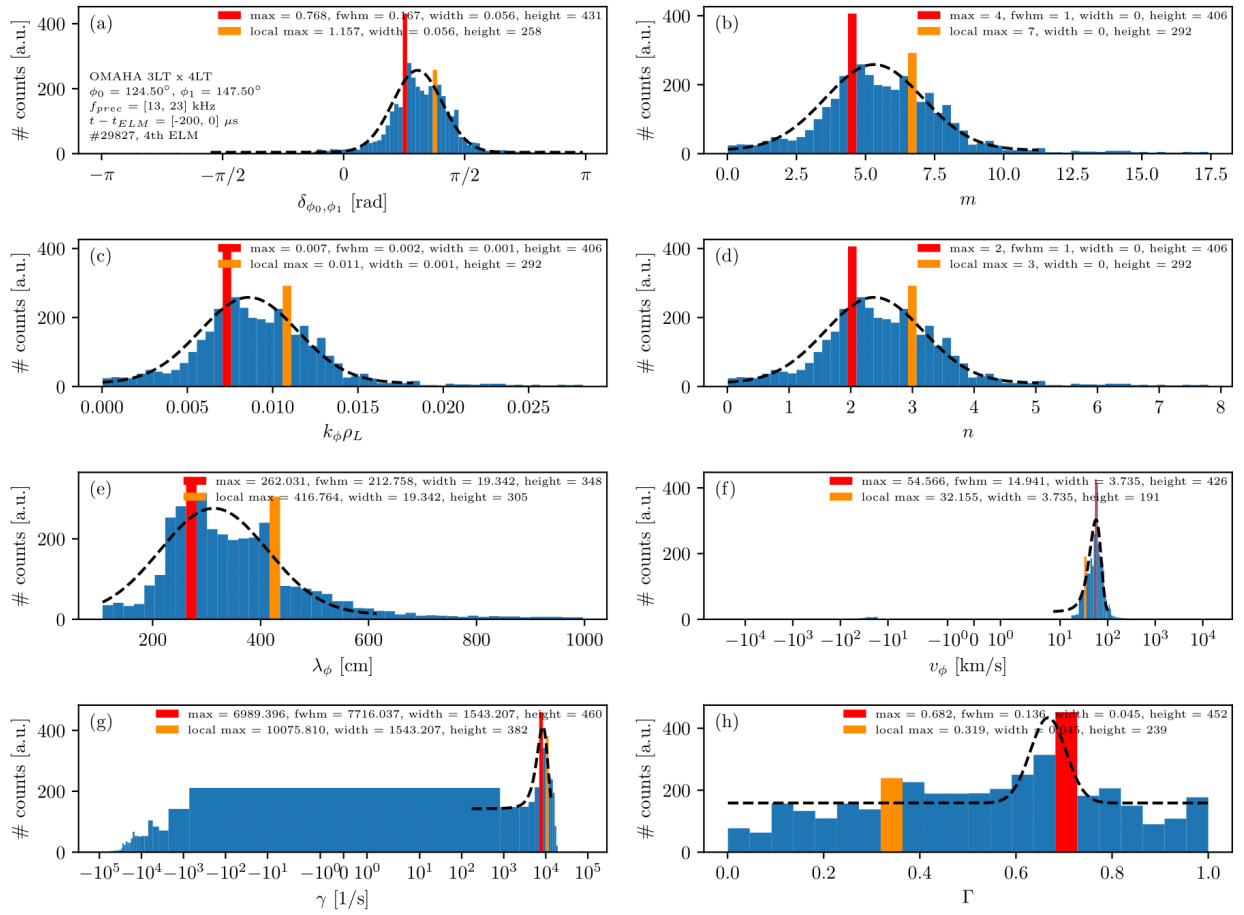

Figure 6.10: MAST shot #29827; ELM onset at $t = 0.34354$ s; OMAHA 3LT $\times$ 4LT histograms from Fig. 6.7: (a) toroidal phase δ_{ϕ_0,ϕ_1}; (b) poloidal number m; (c) normalised scale $k_\phi \rho_L$; (d) toroidal number n; (e) toroidal wavelength λ_Z; (f) toroidal velocity v_ϕ; (g) average growth rate γ; (h) cross coherence Γ. Red and orange bars indicate the primary maximum and second local maximum. Dashed black curves correspond to the Gaussian fit.

is $v_Z \sim 3 \pm 2$ km/s which correspond to the early stage of the precursor, whereas the negative component is correlated to the ELM crash and the reversal motion seen in BES images. The maximum growth rate is $\gamma \sim 10^4$ which was expected. The cross coherence shows a tendency to increase with peak around $\Gamma \sim 1$ when getting closer to the ELM crash. In the case of OMAHA, the frequency range was broaden to (13, 23) kHz. The phase is centered at $\delta_{\phi_0,\phi_1} \sim \pi/4$ that is predominant in the grid in Fig. 6.7 (a). Poloidal and toroidal numbers peaks are located around $m \sim 5 \pm 2$ and $n \sim 2 \pm 2$. Toroidal wavelengths presents a peak

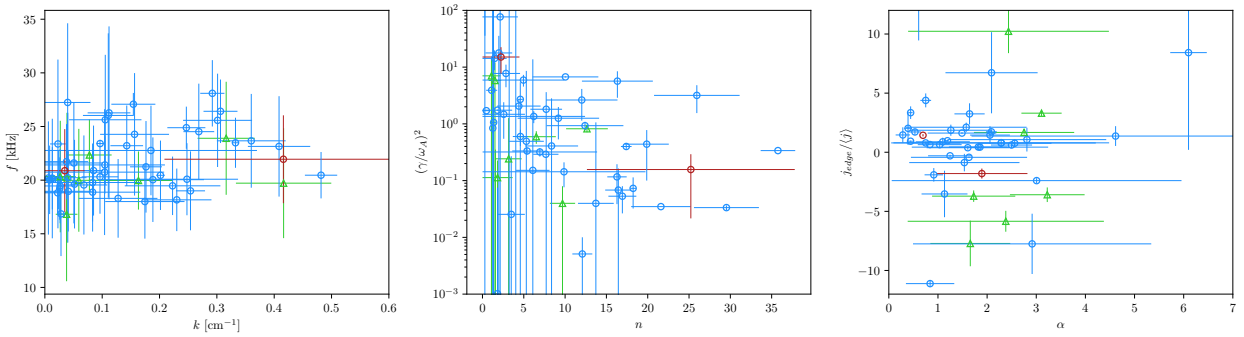

Figure 6.11: Results from BES data from Table 6.2; (left) precursor frequency f against poloidal wavenumber k; (center) normalised growth rate $(\gamma/\omega_A)^2$ against the toroidal number n; (right) $(j_{edge}/\langle j\rangle, \alpha)$ diagram; blue, green and red markers indicate type-I, type-III, and 'quasi' failed ELMs respectively.

at 300 cm with an large uncertainty of ± 100 cm. The normalised scale peak is around $k_Z\rho_L \sim 0.008 \pm 0.003$ for early stages, which is in the same order of magnitude of BES imaging results. The toroidal velocity peak is $v_\phi \sim 54 \pm 15$ km/s with no negative reverse velocity. Observing the corresponding grid, a reversal motion takes place once the ELM crash time is surpassed. The maximum growth rate is at $\gamma \sim 10^4$, in agreement with previous results. The cross coherence highlights the value $\Gamma \sim 0.7$ but a fit fails due to the spread of many bins across. In order to distinguish patterns of the above mentioned parameters, the cross correlation analysis is repeated exclusively with BES data for all ELMs in the discharges enumerated in Table 6.2. These results are presented in Fig. 6.11. This analysis was undertaken using BES data, instead of OMAHA data, in order to focus on the poloidal dynamics of the plasma. Scatter markers and error bars correspond to the peaks and widths of Gaussian fits. Characteristic ranges of parameters are such as $n \sim 1 - 30$ and $k \sim 0.01 - 0.5$ cm^{-1}. On the other hand, normalised scales for poloidal wavevectors k tend to typically vary over the range $k\rho_L \leq 0.1$. The normalised scales $k\rho_L < 0.1$ are associated with the peeling-ballooning instability according to gyrokinetic simulations [331], while $k\rho_L \sim 0.1$ are associated with kinetic ballooning modes [332]. The relation between the normalised growth rate $(\gamma/\omega_A)^2$, with ω_A, the Alfven frequency, and the toroidal number is associated with the flow shear which stabilizes the plasma edge [333]. However, the Gaussian fit was not ideal for the growth rate histograms: bins were spread among several ranges which complicated the performance of the fitting method. The theory predicts a decrease of the

growth rates when increasing toroidal n numbers. However, the computed results are far from a describing a tendency. Furthermore, the diagram $(j_{edge}/\langle j\rangle, \alpha)$ is also plotted. $j_{edge} = n_{ped} q v_Z$ is the edge current density, $\langle j\rangle = n_{ped} q \langle v_Z\rangle$ is the averaged current density during the inter-ELM period and $\alpha = -(2\mu_0 R q^2/B^2)\ dp/dr$ is the normalised pressure gradient. The diagram is associated with the destabilisation regions of the peeling and ballooning instabilities [334] (see chapter 2, section 2.3.3). A problematic feature is the velocity changing sign case by case. In the vertical convention, the majority of results show a preference for positive values which correspond to an upward rotation, *i.e.* in the electron diamagnetic direction. Prior to the ELM onset values are concentrated around $(j_{edge}/\langle j\rangle, \alpha) \sim (1-2, 1-3)$ which could define the stable area. Other ELMs, specially the case of type-III ELMs, seem to be located out of that area related to unstable regions.

6.5.3 Bicoherence analysis

The study of precursors and possible triggering mechanisms for ELMS requires the study of mode coupling. Bicoherence analysis is able to identify which modes are coupled and is therefore ideally suited for this purpose. As a typical example, the bispectrum and bicoherence is computed from a BES signal and an OMAHA signal for the same ELM (4th ELM of shot #29827) are computed according to Eqs. 6.11 and 6.12. The averaging time defined by the sampling index T is restricted to 400 samples corresponding to a time interval of 200 μs. The averaging is performed during the precursor range before the ELM onset *i.e.* (-200, 0.5) μs. The resulting bispectra and bicoherence plots are shown in Figs. 6.12 and 6.13 respectively. The most prominent bispectrum feature is localised in the lowest frequencies between $(1, 5)$ kHz. Several features are common to both BES and OMAHA bicoherence. First, the horizontal red area at $f_2 \sim 1-5$ kHz indicates the coupling of all f_1 frequencies with a sheared zonal flow. Second, diagonal spots such as $f_1 = f_2 = 10$ kHz are self-resonant modes. Third, an area of strong coupling ($b^2 \sim 1.0$) enclosed in between $(f_1, f_2) \leq (20, 10)$ with several harmonics for higher frequencies with amplitudes $b^2 \sim 0.5 \pm 0.1$. Fourth, a high component $(f_1, f_2) \sim (30, 30)$ kHz of strong bicoherence amplitude. An extended bicoherence analysis was performed with BES data for each ELM appearing in the same discharge. For each ELM, areas with high bicoherence were identified by using the 2D peak detection method. The detected local maxima were

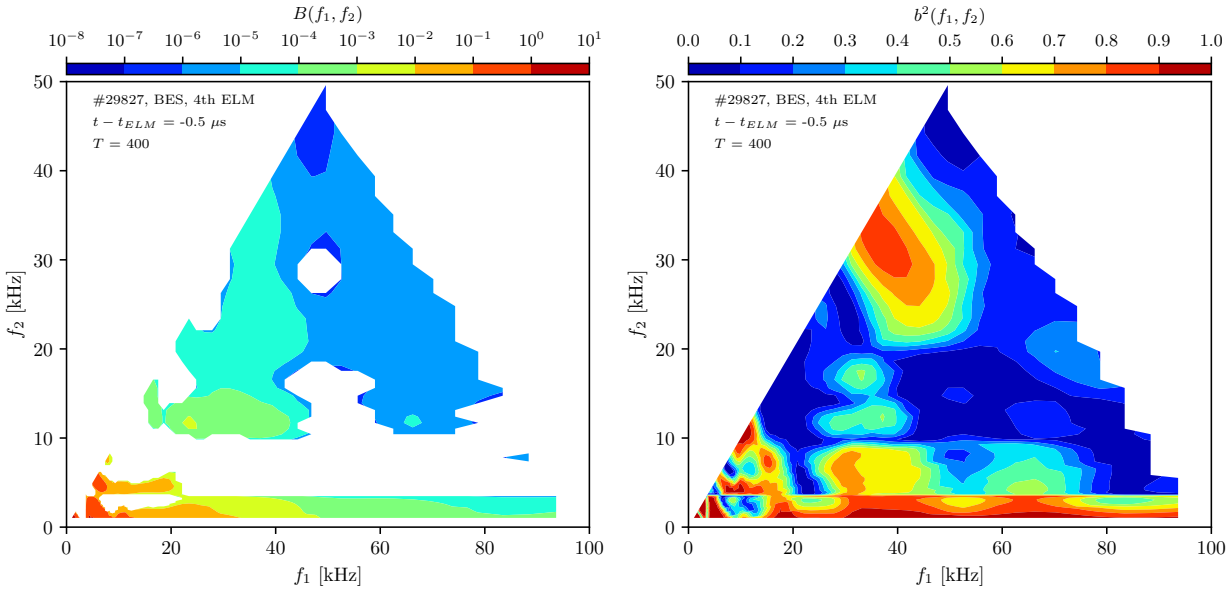

Figure 6.12: MAST shot #29827; BES bispectrum and bicoherence computed over the time range (-200, -0.5) μs equivalent to a sampling index of $T = 400$. Empty areas on the bispectrum correspond to complex values.

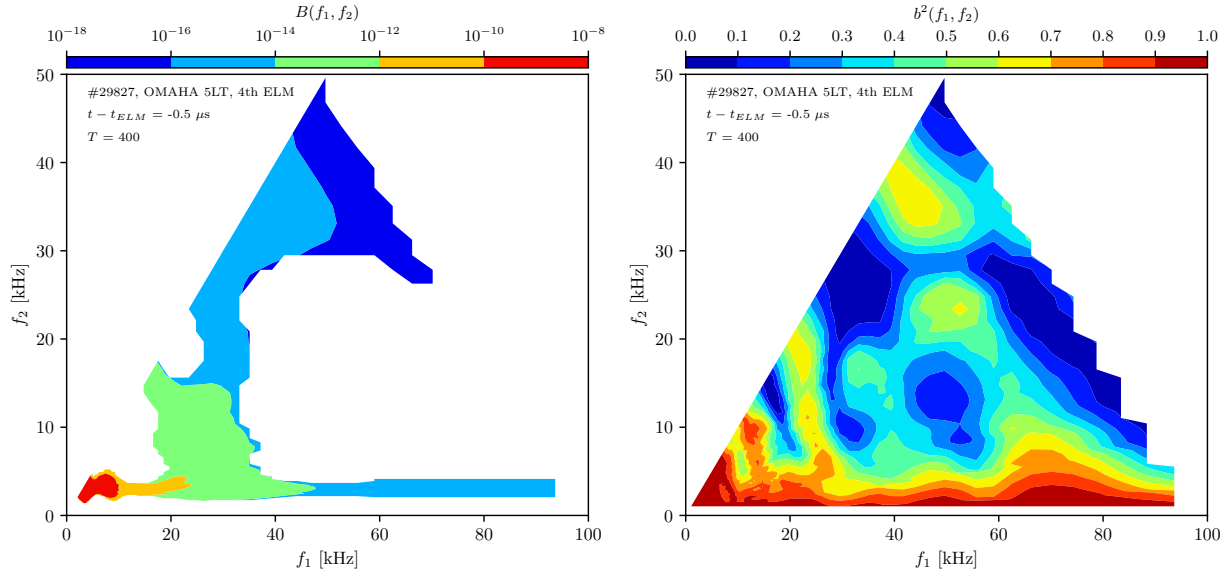

Figure 6.13: MAST shot #29827; OMAHA 5LT bispectrum and bicoherence computed over the time range (-200, -0.5) μs equivalent to a sampling index of $T = 400$. Empty areas on the bispectrum correspond to complex values.

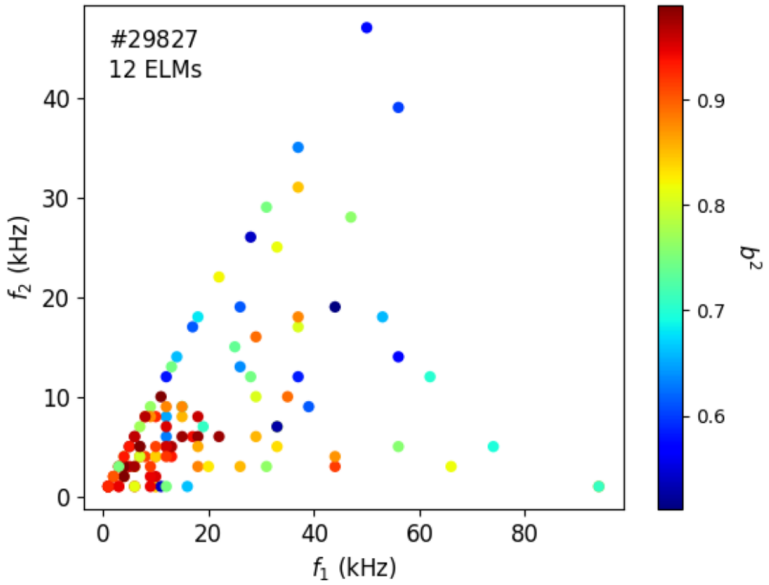

Figure 6.14: Results from BES bicoherence analysis for 12 ELMs in MAST shot #29827

collected for and gathered in Fig. 6.14. A vast majority of non-linear coupling is concentrated for frequencies between $f_1 = 1-20$ kHz and $f_2 = 1-10$ kHz. The ELM trigger could come from that area of strong coupling with an interplay between low f_2 mode and intermediate f_1 mode. This multiplicity of peaks imply that these modes are not fixed frequencies but respond to the plasma conditions of different ELMs and discharges.

6.6 Summary and discussions

The wavelet analysis have shown there is an extensive variety of modes located at the pedestal region during the inter-ELM and ELM-precursors periods. The spectrograms highlighted the presence of five different modes: a low frequency mode ($f \leq 5$ kHz), an intermediate mode ($f \sim 10$ kHz), the ELM-precursor mode ($f \sim 20$ kHz), washboard modes ($f \sim 30 - 150$ kHz), and a high frequency mode ($f \geq 200$ kHz). It was also noticed that the ELM-precursor frequency is not fixed but can be intermittent during the inter-ELM period. The precursor frequency can slightly decrease to $15 - 19$ kHz while other lower modes decay in amplitude when approaching the ELM crash moment. This hierarchy of modes is in agreement with the Laggner model [231] in addition with $f \sim 5$ kHz and $f \sim 10$ kHz modes. All these modes co-exist and

interact with each other causing the ELM trigger. The wavelet cross correlation analysis allowed to identify several parameters of ELM-precursors. BES and OMAHA results seem to be consistent to some extent. The discrepancies of these results can be due to the difference of location of both diagnostics. Note that the precursor mode rotates poloidally because its main contribution comes from the poloidal shear flow. The BES diagnostic focuses on the observation of that particular motion. Nonetheless the OMAHA analysis allows to better assess the toroidal number of the mode. The summary plots in Fig. 6.11 point out that ELM-precursors in MAST are not different to other machines' precursors enumerated in Table 2.2 in chapter 2. Characteristic ranges of parameters are such as $n \sim 1 - 30$ and $k \sim 0.01 - 0.5$ cm^{-1}. Nevertheless, the MAST ELM-precursors seem to share similar features with the spherical tokamak NSTX results with $n \sim 5 - 10$ and $k \sim 0.05 - 0.2$ cm^{-1} [233]. Toroidal mode numbers were lower than the expected values of $n \sim 30 - 40$ predicted by Kirk *et al.* for MAST [234]. On one hand, it is possible that the assumption used for rational surfaces (*i.e.* $n \sim m/q$) is not valid and overvalues the result. On the other hand, the existence of different types of precursors has been proposed to explain this broad range from intermediate $n \sim 10$ to $n \sim 1$ modes [335]. Moreover, the values regarding the normalised scales $k\rho_L \sim 0.1$ are in agreement with the peeling-ballooning and/or kinetic ballooning instabilities [331, 332]. Additionally, at the zero crossing point, when the phase $\delta \sim 0$, the mode grows in size, from $\lambda_Z \sim 8$ cm to $\lambda_Z \sim 20$ cm, which is in agreement with the imaging analysis. The measured upward motion, *i.e.* $j_{edge}/\langle j \rangle > 0$, corresponds to a expected rotation in the counter-current or electron diamagnetic direction [234]. However, some cases infer the ion diamagnetic direction was dominant. The ELM crash time might not always be defined accurately by the D_α peak foot. The grid for computing histograms can be often misplaced, noticing both peaks that represent the transition from the electron to the ion diamagnetic motion. The reversal onset time must be a fluctuating point that depends on a non-linear combination of parameters. Despite that, the D_α peak foot remains a pragmatic reference in order to perform the analysis. In the wavelet bicoherence analysis, the ELM trigger is inferred as the coupling of multiple modes. The 5 kHz mode is associated with a ballooning-like mode with a cross-phase being close to zero at the ELM onset, while the peeling mode can develop in all sorts of frequencies. The coupling related to the ELM-precursor would be an interplay transferring energy from the 5 kHz (ballooning-like) mode to the $\sim 20 - 30$ kHz (tearing-like) mode [232]. Micro-tearing modes are

characterised by normalised scales such as $k\rho_L \lesssim 0.1$ in the spherical tokamak configuration [336] which matches with the BES cross-correlation results. Most of these interpretations need to be taken with caution. Markers tend to be scattered in Figs. 6.11 and 6.14, and any observed tendency is not definitive. Therefore more data points, *i.e.* more analysed ELMs, are needed in order to confirm these conclusions.

Chapter 7

Conclusions and future work

Self-organisation remains a challenge for the comprehension of magnetised plasmas. The observation of coherent structures in nature under different conditions led to speculate that an universal mechanism was responsible for these phenomena. The process of vorticity is deeply connected with the self-generation of these structures [124]. Turbulence is characterised by a ubiquitous decorrelated nature of creating small-scale vortices that degrade any form of organisation. Nonetheless, under some unknown conditions, the turbulence can stabilize the plasma in the presence of sheared flows [134, 137]. The self-regulating capability of the plasma can be beneficial by bringing regimes with improved performances, such as the H-mode in tokamaks [119]. Several phenomena considered anomalous or intermittent in the fusion research area are still poorly understood. Filamentary structures in tokamak plasmas remain an active topic of research as these filaments reflect the status of the Scrape-Off Layer [182, 183]. Furthermore, the appearance of explosive events ejecting filaments outwards, eroding the vessel components, is a problem that requires to be tackled in the short term for ITER. The theory of Edge-Localised Modes remains a complex subject with no definitive model. For the moment, simulations present limitations to fully describe non-linear phenomena in plasma turbulence. Pragmatically, the computational results are compared with the findings from experiments in order to establish empirical scalings. These laws would allow to predict the plasma behaviour in future machines [217, 202].

In this thesis, the intention was to analyse the conditions that trigger events or transitions at the edge of tokamak plasmas. The two main contributions of this work are the study of edge plasma conditions and shoulder formation in COMPASS, and the imaging plus spectral analysis of ELM-precursors in MAST.

The probe measurements in COMPASS were focused on determining the requirements for triggering shoulder formation. Different sets of probes were tested including the Ball-Pen probe, a novel tool adapted for magnetised plasmas. A statistical analysis and a propagation model were implemented similarly to the approach proposed in AUG [199]. This methodology, applied to the probe data from EMTRAIC measurements, gave the typical characteristics of blobs in COMPASS. Complementary parameters such as the Greenwald criterion and the divertor collisionality were correlated to the blob results. However, all parameters indicated that a shoulder was not formed. This implied that supplementary requirements might be necessary to fulfill the shoulder trigger. A set of discharges was planned during the Summer School Training (SUMTRAIC) in 2019. The goal was to reproduce the conditions to observe the shoulder formation by increasing the heating power and density. Midplane density profiles using the Li-BES system reported the formation of a shoulder for some of these shots. Unfortunately, the measurements were interrupted due to the failure of the probe and blob data could not be recorded. Since COMPASS was dismantled, there is no possibility of repeating these experiments. No continuation will follow this work. Nonetheless, additional factors such as the deuterium fuelling rates [201], *e.g.* seeding and impurities level, and the divertor recycling and geometry [322] have been neglected in this analysis. It will be worth studying these features' impact on the plasma edge and divertor.

The analysis of ELM-filaments in MAST was motivated by the development of a recent tomographic technique from camera frames known as Elzar [298]. Elzar was able to track L-mode filaments, hence its application was contemplated to H-mode plasmas prior to a plasma eruption. The initial attempt was to combine Elzar and BES in order to correlate the activity observed on the BES radial/vertical frames and the Elzar inverted radial/toroidal plane. However, the Elzar performance with inter-ELM filaments is inefficient, introducing false filament identifications. The resolution of the fast camera was rapid enough to collect emissions from ELM-precursors. It was considered the emissions from the ELM-precursors were much fainter than the ELM ejection emission. The line integration of the camera line of sight widely observing the ensemble of the

plasma does not allow to distinguish between SOL and pedestal emission as both overlap. Furthermore, D_α signals do not show peaks during ELM-precursor oscillations. Therefore these cannot be observed unless an active method such as the neutral beam enhances the amount of emissions at the pedestal. The BES system [286] can visualise blob-like structures corresponding to the ELM-precursor activity. Previous works mentioned some characteristics of ELM-precursors found in MAST without specifying the applied methodology [234]. The first attempt at analysing 2D reconstructed images consisted in measuring straightforwardly the structures' dimensions and velocities with relatively good agreement with the literature. However, this method relies on a linear interpolation that gives an inaccurate approximation of the ELM-precursor.

An alternative method of analysis was required to describe precursors correctly. Applying wavelet transforms to BES and OMAHA signals was fruitful for analysing short-lived structures [239, 232]. Magnetic coils signals detecting fluctuations during ELM-precursors lifetimes became a convenient replacement for the fast camera. Compared with the previous method of analysis, the wavelet transform is a powerful tool that reveals a considerable amount of details from the original signals. A complex combination of spectral features were highlighted in the wavelet spectra: several inter-ELM fluctuations were detected in agreement with theoretical models [231]. The cross correlation results from the precursor time range, then re-interpreted using histograms, provided an estimation of characteristic parameters. Results demonstrated that the ELM-precursors in MAST are similar to the typically observed precursors in other tokamaks. In particular, the characteristic features found in MAST align with NSTX findings [233]. Moreover, the obtained values for toroidal mode numbers and normalised wavenumbers were associated with peeling-ballooning or kinetic ballooning modes [215]. Finally, a bispectral analysis was undertaken in order to quantify the non-linear coupling between modes. Results could suggest there was a non-linear coupling between a high frequency mode (*i.e.* the precursor) and a lower frequency mode (*i.e.* the ballooning). The micro-tearing mode could also satisfy the conditions stated in the cross correlation analysis and be responsible for the energy transfer for the low frequency mode in agreement with AUG results [232]. However, these results are not fully conclusive as most detected features seem to be self-resonant from low frequencies. A more extensive study with magnetic coils data and additional ELMs from different discharges will be necessary to confirm the observed trends from the BES data analysis.

Appendix

Python code for wavelet analysis

This appendix includes the key functions to run the wavelet analysis. This functions are: get_cwt (*i.e.* computes the wavelet transform), get_xwt (*i.e.* computes the cross wavelet spectra) and get_bwt (*i.e.* computes the wavelet bispectra). Additionally, the 2D peak detection function get_2d_peaks is also included at the end. We will distinguish between the "time" array and the raw "signal" array (with its mean value previously removed). Libraries such as PyCWT [310] were previously installed.

```
#libraries:
import pycwt
import numpy as np
import scipy.ndimage.filters as filters
from scipy.ndimage import center_of_mass, label



#wavelet transform function:
def get_cwt(time, signal, trend):
    N = signal.size
```

```
dt = time[1] - time[0]
#detrending if dataset has a well defined trend:
if trend == True:
    p = np.polyfit(time, signal, 1)
    signal_no_trend = signal - np.polyval(p, time)
    std_signal = sig_no_trend.std()
    var_signal = std_signal ** 2
    signal_norm = signal_no_trend / std_signal
else:
    signal_no_trend = signal
#define mother wavelet:
omega_0 = 2 * np.pi
mother_cwt = pycwt.Morlet(omega_0)
s_0 = 2 * dt
dj = 1 / 12
J = -1 #default value, will be computed by pycwt
#compute wavelet transform coefficients and spectral power:
coeffs_cwt, scales, freqs_cwt, cone_infl, fft, freqs_fft = pycwt.cwt(signal_norm, dt, dj, s_0, J, mother_cwt)
power_cwt = (np.abs(coeffs_cwt)) ** 2
#bias correction (Liu et al. 2007):
power_cwt /= scales[:, None]
#power spectra significance contours:
signif, fft_theor = pycwt.significance(1.0, dt, scales, 0, 0, significance_level=0.95, wavelet=mother_cwt)
sig95 = np.ones([1, N]) * signif[:, None]
sig95 = power_cwt / sig95
return coeffs_cwt, scales, freqs_cwt, power_cwt, cone_infl, sig95
```

```
#cross wavelet function:
def get_xwt(coeffs_cwt_0, coeffs_cwt_1):
    #compute auto-correlation coefficients:
    coeffs_auto_0 = coeffs_cwt_0.conj() * coeffs_cwt_0
    coeffs_auto_1 = coeffs_cwt_1.conj() * coeffs_cwt_1
    #compute cross-correlation coefficients:
    coeffs_xwt = coeffs_cwt_0.conj() * coeffs_cwt_1
    phase_xwt = np.angle(coeffs_xwt)
    #compute cross coherence:
    coh_xwt = np.abs(np.real(coeffs_xwt)) / np.sqrt(coeffs_auto_0 * coeffs_auto_1)
    return coeffs_xwt, phase_xwt, coh_xwt



#bispectral, bicoherence wavelet function:
def get_bwt(time, freqs_cwt, coeffs_cwt, dtype, T):
    coeffs_cwt = np.transpose(coeffs_cwt, [1, 0])
    T_dict, bispec_dict, bicoh_dict = [dict() for _ in range(3)]
    bikeys_dict = ['t', 'T', 't-add', 'f-sum']
    for key in bikeys_dict:
        T_dict[key], bispec_dict[key], bicoh_dict[key] = [dict() for _ in range(3)]
    B_num_T, B_spec_T, B_num_t_add, B_spec_t_add = [np.zeros([len(freqs_cwt), len(freqs_cwt)], dtype=dtype)
for _ in range(4)]
    B_denum_1_T, B_denum_2_T, B_denum_1_t_add, B_denum_2_t_add = [np.zeros([len(freqs_cwt), len(freqs_cwt)])
for _ in range(4)]
    B_num_f = np.zeros([len(time), len(freqs_cwt)], dtype=dtype)
    B_sum_f, B_denum_1_f, B_denum_2_f, bicoh_sum_f = [np.zeros([len(time), len(freqs_cwt)]) for _ in range(4)]
```

```
    T_counter, t_counter = 1, 1
    for id_t in range(len(time)):
        B_num_t, B_denum_1_t, B_denum_2_t = [np.zeros([len(freqs_cwt), len(freqs_cwt)], dtype=dtype) for _
in range(3)]
        for id_f1 in range(len(freqs_cwt)):
            for id_f2 in range(len(freqs_cwt)):
                f3 = freqs_cwt[id_f1] + freqs_cwt[id_f2] #resonance condition
                if f3 > max(freqs_cwt) or freqs_cwt[id_f1] > freqs_cwt[id_f2]:
                    B_num_t[id_f1, id_f2], B_denum_1_t[id_f1, id_f2], B_denum_2_t[id_f1, id_f2] = None, None,
None
                else:
                    id_f3 = (np.abs(freqs_cwt - f3)).argmin()
                    B_num_t[id_f1, id_f2] = coeffs_cwt[id_t, id_f1] * coeffs_cwt[id_t, id_f2] * np.conjugate(coeffs_cwt[id_t,
id_f3])
                    B_denum_1_t[id_f1, id_f2] = coeffs_cwt[id_t, id_f1] * coeffs_cwt[id_t, id_f2]
                    B_denum_2_t[id_f1, id_f2] = np.conjugate(coeffs_cwt[id_t, id_f3])
                    B_sum_f[id_t, id_f3] += 1/(len(time)+1)*np.abs(B_num_t[id_f1, id_f2])
                    B_num_f[id_t, id_f3] += B_num_t[id_f1, id_f2]
                    B_denum_left_f[id_t, id_f3] += np.abs(coeffs_cwt[id_t, id_f1] * coeffs_cwt[id_t, id_f2]) ** 2
                    B_denum_2_f[id_t, id_f3] += np.abs(np.conjugate(coeffs_cwt[id_t, id_f3])) ** 2
                    bicoh_sum_f[id_t, id_f3] = (np.abs(B_num_f[id_t, id_f3])**2) / (B_denum_1_f[id_t, id_f3]*B_denum_2_f[id_t,
id_f3])
        if T is not None:
            B_spec_T += 1 / T * B_num_t
            B_num_T += B_num_t
            B_denum_1_T += np.abs(B_denum_1_t) ** 2
            B_denum_2_T += np.abs(B_denum_2_t) ** 2
```

```
            T_dict['T'][str(time[id_t])] = T_counter
            bispec_dict['T'][str(time[id_t])] = B_spec_T
            bicoh_dict['T'][str(time[id_t])] = (np.abs(B_num_T) ** 2) / (B_denum_1_T * B_denum_2_T)
            if T_counter == T: # reaching sampling limit to stop computing bicoherence
                B_num_T, B_spec_T = [np.zeros([len(freqs_cwt), len(freqs_cwt)], dtype=dtype) for _ in range(2)]
                B_denum_1_T, B_denum_2_T = [np.zeros([len(freqs_cwt), len(freqs_cwt)]) for _ in range(2)]
                T_counter = 0
        else:
            B_spec_t_add += 1 / (len(time)+1) * B_num_t
            B_num_t_add += B_num_t
            B_denum_1_t_add += np.abs(B_denum_1_t) ** 2
            B_denum_2_t_add += np.abs(B_denum_2_t) ** 2
            bispec_dict['t-add'][str(time[id_t])] = B_spec_t_add
            bicoh_dict['t-add'][str(time[id_t])] = (np.abs(B_num_t_add) ** 2) / (B_denum_1_t_add * B_denum_2_t_add)
        T_counter += 1
        t_counter += 1
        bispec_dict['f-sum'] = np.transpose(B_sum_f)
        bicoh_dict['f-sum'] = np.transpose(bicoh_sum_f)
    return time, freqs_cwt, T_dict, bispec_dict, bicoh_dict, bikeys_dict



#2d peak detection function:
def get_peaks(power, size, factor_thresh):
    threshold = factor_thresh * np.std(power)
    power_max = filters.maximum_filter(power, size)
    maxima = (power == power_max)
    power_min = filters.minimum_filter(power, size)
```

```
    diff = ((power_max - power_min) > threshold)

    maxima[diff == 0] = 0

    labeled, num_objects = label(maxima)

    xy_coordinates = np.array(center_of_mass(power, labeled, range(1, num_objects + 1)))

    return xy_coordinates
```

Bibliography

[1] Global Footprint Network. National Footprint Accounts, 2018th ed., Global Footprint Network: Oakland, CA, USA, 2018.

[2] Z. Liu, P. Ciais, Z. Deng, R. Lei, S. J. Davis, S. Feng, B. Zheng, D. Cui, X. Dou, B. Zhu, R. Guo, P. Ke, T. Sun, C. Lu, P. He, Y. Wang, X. Yue, Y. Wang, Y. Lei, H. Zhou, Z. Cai, Y. Wu, R. Guo, T. Han, J. Xue, O. Boucher, E. Boucher, F. Chevallier, K. Tanaka, Y. Wei, H. Zhong, C. Kang, N. Zhang, B. Chen, F. Xi, M. Liu, F.-M. Breon, Y. Lu, Q. Zhang, D. Guan, P. Gong, D. M. Kammen, K. He, and H. J. Schellnhuber, Nat. Commun. 11 (1), 1-12, 2020.

[3] IEA, World Energy Outlook, 2021: `https://www.iea.org/reports/world-energy-outlook-2021`.

[4] J. Wesson, Tokamaks, 3rd ed., Clarendon Press, Oxford, 2004.

[5] H. S. Bosch and G. M. Hale. Nucl. Fusion, 32 (4), 611, 1992.

[6] Wikimedia Commons, Archive: Binding energy curve - common isotopes.svg, 2008: `https://commons.wikimedia.org/w/index.php?curid=1540082`.

[7] National Minerals Information Center, Lithium Statistics and Information, United States Geological Survey, 2016: `https://www.usgs.gov/centers/national-minerals-information-center/lithium-statistics-and-information`.

[8] S. Atzeni and J. Meyer-ter-Vehn, Physics of Inertial Fusion: Beam Plasma Interaction, Hydrodynamics, Hot Dense Matter, Cambridge University Press, 2005.

[9] H. G. Liddell and R. Scott, A Greek English Lexicon, Oxford, Clarendon Press, 1940: http://www.perseus.tufts.edu/hopper/text?doc=Perseus:text:1999.04.0057:entry=pla/sma.

[10] I. Langmuir, Proc. Natl. Acad. Sci. U S A., 14 (8), 627–637, 1928.

[11] L. Tonks and I. Langmuir, Phys. Rev., 33 (2), 195–210, 1929.

[12] L. Tonks, Am. J. Phys., 35 (9), 857-858, 1967.

[13] J. A. Bittencourt, Fundamentals of Plasma Physics, 3rd ed., Springer, 2004.

[14] A. I. Morozov, Introduction to plasma dynamics, CRC Press, 2013.

[15] F. F. Chen, Introduction to Plasma Physics, 3rd ed., Springer, 2016.

[16] J.-M. Rax and B. Bigot, Physique des Plasmas: Cours et applications, Dunod, 2015.

[17] D. R. Nicholson, Introduction to Plasma Theory, John Wiley & Sons Inc., 1983.

[18] S. I. Braginskii. Transport processes in a plasma. Rev. Mod. Phys., Ed. M. A. Leontovich, 1:205, 1965.

[19] H. Alfven, Nature, 150 (3805), 405-406, 1942.

[20] J. P. Freidberg, Rev. Mod. Phys., 54 (3), 801–902, 1982.

[21] V. D. Shafranov, Phys.-Usp., 44 (8), 835–865, 2001.

[22] V. P. Smirnov, Nucl. Fusion, 50 (1), 014003, 2009.

[23] IAEA, Establishment of ITER: Relevant Documents. ITER Documentation Series No.1, 1988: https://inis.iaea.org/collection/NCLCollectionStore/_Public/21/068/21068957.pdf?r=1.

[24] R. Aymar, P. Barabaschi, and Y. Shimomura (for the ITER Team), Plasma Phys. Control. Fusion, 44 (5), 519-565, 2002.

[25] B. Bigot, Fusion Eng. Des., 164, 112207, 2021.

[26] EUROfusion, The tokamak: https://www.euro-fusion.org/fileadmin/user$_$upload/Archive/wp-content/uploads/2011/09/jg05-537-1c.jpg

[27] K. Miyamoto, Plasma Physics and Controlled Nuclear Fusion, Springer Science & Business Media. (Vol. 38), 2005.

[28] L. Spitzer Jr. and R. Harm, Phys. Rev. 89 (5), 977-981, 1953.

[29] J. D. Lawson, Proc. Phys. Soc. B 70(1), 6, 1957.

[30] ITER Physics Expert Groups on Confinement and Transport and Confinement Modelling and Database, ITER Physics Basis Editors, ITER EDA, Naka Joint Work Site, Mukouyama, Naka-machi, Naka-gun, Ibaraki-ken, Japan, Nucl. Fusion, 39, 2175, 1999.

[31] C. D. Challis, J. Garcia, M. Beurskens, P. Buratti, E. Delabie, P. Drewelow, L. Frassinetti, C. Giroud, N. Hawkes, J. Hobirk, E. Joffrin, D. Keeling, D. B. King, C. F. Maggi, J. Mailloux, C. Marchetto, D. McDonald, I. Nunes, G. Pucella, S. Saarelma, J. Simpson and JET Contributors, Nucl. Fusion, 55 (5), 053031, 2015.

[32] M. Keilhacker and ASDEX Team, Nucl. Fusion, 25 (9), 1045, 1985.

[33] D. Ryutov, Phys. Plasmas, 14 (6), 064502, 2007.

[34] M. Kotschenreuther, P. M. Valanju, S. M. Mahajan, and J. C. Wiley, Phys. Plasmas, 14 (7), 072502, 2007.

[35] P. M. Valanju, M. Kotschenreuther, S. M. Mahajan, and J. Canik, Phys. Plasmas, 16 (5), 056110, 2009.

[36] EFDA-JET, 2011: `www.jet.efda.org`.

[37] G. F. Matthews, P. Edwards, T. Hirai, M. Kear, A. Lioure, P. Lomas, A. Loving, C. Lungu, H. Maier, P. Mertens, D. Neilson, R. Neu, J. Pamela, V. Philipps, G. Piazza, V. Riccardo, M. Rubel, C. Rusel, E. Villedieu, M. Way and on behalf of the ITER-like Wall Project Team, Phys. Scr., T128, 137, 2007.

[38] P. C. Stangeby, Phys. Plasmas, 9 (8), 3489-3507, 2002.

[39] A. H. Boozer, Rev. Mod. Phys., 76 (4), 1071-1141, 2005.

[40] T. M. Antonsen Jr., J. F. Drake, P. N. Guzdar, A. B. Hassam, Y. T. Lau, C. S. Liu, and S. V. Novakovskii, Phys. Plasmas, 3 (6), 2221–2223, 1996.

[41] F. Troyon, R. Gruber, H. Sauremann, S. Semenzato, and S. Succi, Plasma Phys. Control. Fusion, 26 (1A), 209, 1984.

[42] M. Greenwald, J. L. Terry, S. M. Wolfe, S. Ejima, M. G. Bell, S. M. Kaye, and G. H. Neilson, Nucl. Fusion, 28 (12), 2199, 1988.

[43] D. A. Gates and L. Delgado-Aparicio, Phys. Rev. Lett., 108 (16), 165004, 2012.

[44] R. J. Goldston and P. H. Rutherford, Introduction to Plasma Physics, The Rayleigh-Taylor and flute instabilities, Institute of Physics Press, Bristol, 1995.

[45] C. Ham, A. Kirk, S. Pamela, and H. Wilson, Nat. Rev. Phys., 2 (3), 159-167, 2020.

[46] M. Kruskal and J. L. Tuck, Proc. R. Soc. A: Math, Phys. Eng. Sci., 245 (1241), 222–237, 1958.

[47] Y. Nishimura and M. Azumi, Phys. Plasmas, 4 (7), 2365-2375, 1997.

[48] Event Horizon Telescope Collaboration, Akiyama, K. *et al.* Astrophys. J. Lett. 930 (2), L12, 2022.

[49] Legacy Astronomical Images, Radio Galaxy 3C31, NRAO Archives: `https://www.nrao.edu/archives/items/show/33372`.

[50] Bellan Plasma Group, Division of Engineering and Applied Science, California Institute of Technology: `http://www.bellanplasmagroup.caltech.edu/index.html`.

[51] J. Held, Andor, Oxford Instruments, 2022: `https://andor.oxinst.com/learning/view/article/measuring-the-phase-velocity-of-plasma-waves-using-the-double-image-mode-of-the-istar-scmos`.

[52] Transition Region and Coronal Explorer (TRACE) Image Archive, November 6, 1999, at 02:30 UT: `https://sdowww.lmsal.com/TRACE/POD/TRACEpodarchive.html`.

[53] G P. Williams, Planetary circulations: 1. Barotropic representation of Jovian and terrestrial turbulence, J. Atmos. Sci., 35 (8), 1399-1426, 1978.

[54] A. L. Peratt, J. McGovern, A. H. Qoyawayma, M. A. Van der Sluijs and M. G. Peratt, IEEE Trans. Plasma Sci, 35 (4), 778-807, 2007.

[55] A. L. Peratt and C. M. Snell, Phys. Rev. Lett., 54 (11), 1167-1170, 1985.

[56] B. D. Dudson, N. Ben Ayed, A. Kirk, H. R. Wilson, G. Counsell, X. Xu, M. Umansky, P. B. Snyder, B. LLoyd and the MAST team, Plasma Phys. Control. Fusion, 50 (12), 124012, 2008.

[57] Theodore von Karman, Aerodynamics, McGraw-Hill, 1963: ISBN 978-0-07-067602-2, Dover, 1994: ISBN 978-0-486-43485-8.

[58] A. N. Kolmogorov - Cr Acad. Sci. URSS, 1941.

[59] U. Frisch, Turbulence: The Legacy of A. N. Kolmogorov, Cambridge University Press, 1995.

[60] L. F. Richardson, Proc. Roy. Soc. London, Ser. A, 110 (756), 709-737, 1926.

[61] P. H. Diamond, S.-I. Itoh and K. Itoh, A Tutorial on Basic Concepts in MHD Turbulence and Turbulent Transport, Reviews of the Theory of Magnetized Plasmas Volume 1, Relaxation Dynamics in Laboratory and Astrophysical Plasmas, Pages: 119–150, World Scientific Publishing Co Pte Ltd (Verlag), ISBN 9814291544, 9789814291545, 2009.

[62] P. S. Iroshnikov, Astron. J. SSSR, 40, 742-750, 1963 (Soviet Astron. 7, 566, 1963).

[63] R. H. Kraichnan, Phys. Fluids, 8 (7), 1385, 1965.

[64] R. H. Kraichnan, Phys. Fluids, 10 (7), 1417, 1967.

[65] W.-C. Muller and R. Grappin, Nonlinear Cascades and Spatial Structure of Magnetohydrodynamic Turbulence, Reviews of the Theory of Magnetized Plasmas Volume 1, Relaxation Dynamics in Laboratory and Astrophysical Plasmas, Pages:187–217, World Scientific Publishing Co Pte Ltd (Verlag), ISBN 9814291544, 9789814291545, 2009.

[66] R. H. Kraichnan, J. Fluid Mech., 47 (3), 525-535, 1971.

[67] R. H. Cohen and R. M. Kulsrud, Phys. Fluids, 17 (12), 2215-2225, 1974.

[68] P. Goldreich and S. Sridhar, Astrophys. J., 438, 763–775, 1995.

[69] P. C. Thonemann, E. P. Butt, R. Carruthers, A. N. Dellis, D. W. Fry, A. Gibson, G. N. Harding, D. J. Lees, R. W. P. McWhirter, R. S. Pease, S. A. Ramsden, and S. Ward, Nature, 181 (4604), 217–220, 1958.

[70] J. B. Taylor, Phys. Rev. Lett., 33 (19), 1139–1141, 1974.

[71] L. Woltjer, Proc. Nat. Acad. Sci., 44 (6), 489-491, 1958.

[72] A. J. L. Verhage, A. S. Furzer and D. C. Robinson, Nucl. Fusion, 18 (4), 457–473, 1978.

[73] D. F. Escande, S. Cappello, F. D'Angelo, P. Martin, S. Ortolani and R. Paccagnella, Plasma Phys. Control. Fusion, 42 (12B), B243–B253, 2000.

[74] D. Bonfiglio, S. Cappello, and D. F. Escande, Phys. Rev. Lett., 94 (14), 145001, 2005.

[75] R. Lorenzini, E. Martines, P. Piovesan, D. Terranova, P. Zanca, M. Zuin, A. Alfier, D. Bonfiglio, F. Bonomo, A. Canton, S. Cappello, L. Carraro, R. Cavazzana, D. F. Escande, A. Fassina, P. Franz, M. Gobbin, P. Innocente, L. Marrelli, R. Pasqualotto, M. E. Puiatti, M. Spolaore, M. Valisa, N. Vianello, RFX-mod team and collaborators, Nat. Phys., 5 (8), 570–574, 2009.

[76] C. D. Cothran, M. R. Brown, T. Gray, M. J. Schaffer, and G. Marklin, Phys. Rev. Lett., 103 (21), 215002, 2009.

[77] M. Gobbin, D. Bonfiglio, A. H. Boozer, A. W. Cooper, D. F. Escande, S. P. Hirshman, J. Lore, R. Lorenzini, L. Marrelli, P. Martin, E. Martines, B. Momo, N. Pomphrey, I. Predebon, M. E. Puiatti, R. Sanchez, G. Spizzo, D. A. Spong, D. Terranova, and RFX-mod Team, Phys. Plasmas, 18 (6), 062505, 2011.

[78] S. C. Jardin, N. Ferraro, and I. Krebs, Phys. Rev. Lett., 115 (21), 215001, 2015.

[79] D. F. Escande, What is a reversed field pinch, Rotation and momentum transport in magnetized plasmas, Reviews of the Theory of Magnetized Plasmas Volume 2, Rotation and Momentum Transport in Magnetized Plasmas, Pages: 247-286, World Scientific Publishing Co Pte Ltd (Verlag), ISBN 9814644846, 9789814644846, 2015.

[80] S. C. Hsu and P. M. Bellan, Phys. Rev. Lett., 90 (21), 215002, 2003.

[81] P. Bellan, J. Plasma Phys., 84 (5), 755840501, 2018.

[82] A. Simon, Phys. Fluids, 6 (3), 382, 1963.

[83] F. C. Hoh, Phys. Fluids, 6 (8), 1184, 1963.

[84] F. F. Chen and A. W. Cooper, Phys. Rev. Lett., 9 (8), 333, 1962.

[85] J. F. Bonnal, G. Briffod, M. Gregoire, and C. Manus, Nucl. Fusion, Suppl., 3, 995, 1962: `http://www-naweb.iaea.org/napc/physics/FEC/1961.pdf`.

[86] G. Briffod, M. Gregoire, and C. Manus, Phys. Lett., 2 (4), 201-203, 1962.

[87] D. L. Morse, Phys. Fluids, 8 (3), 516, 1965.

[88] G. S. Janes and R. S. Lowder, Phys. Fluids, 9 (6), 1115-1123, 1966.

[89] P. B. Barber, D. A. Swift and B. A. Tozer, J. Phys. D: Appl. Phys., 5 (4), 693, 1972.

[90] Himmel, G., E. Mobius, and A. Piel, Z. Naturforschung A, 31 (8), 934-941, 1976.

[91] H. Alfven, On the Origin of the Solar System, Clarendon Press, Oxford, 1954.

[92] A. Piel, E. Mobius, and G. Himmel, Astrophys. Space Sci., 72 (1), 211–221, 1980.

[93] W. Biel, A. Abou-El Magd, H. Kempkens and J. Uhlenbusch, Plasma Phys. Control. Fusion, 37 (6), 599, 1995.

[94] W. Biel, H. Kempkens and J. Uhlenbusch, Plasma Phys. Control. Fusion, 40 (11), 1845, 1998.

[95] E. M. Oks, A. Anders, I. G. Brown, I. A. Soloshenko and A. I. Shchedrin, 31 (11), 978–983, 2005.

[96] A. V. Nedospasov, Sov. Phys. Usp., 18 (8), 588-599, 1975.

[97] V. V. Vladimirov, Sov. Phys. Usp. 18 (1), 37–50, 1975.

[98] E. Y. Choueiri, Phys. Plasmas, 8 (4), 1411–26, 2001.

[99] E. Chesta, C. M. Lam, N. B. Meezan, D. P. Schmidt, M. A. Cappelli, IEEE Trans. Plasma Sci., 29 (4), 582–591, 2001.

[100] J. B. Parker, Y. Raitses, and N. J. Fisch, Appl. Phys. Lett., 97 (9), 091501, (2010).

[101] E. Martines, M. Zuin, V. Antoni, R. Cavazzana, G. Serianni, M. Spolaore, and C. Nakashima, Phys. Plasmas, 11 (5), 1938–1946, (2004).

[102] A. V. Kozyrev, N. S. Sochugov, K. V. Oskomov, A. N. Zakharov, and A. N. Odivanova, Plasma Phys. Rep., 37 (7), 621–627, 2011.

[103] A. Anders, P. Ni, and A. Rauch, J. Appl. Phys., 111 (5), 053304, 2012.

[104] Y. Yang, J. Liu, L. Liu, and A. Anders, Appl. Phys. Lett., 105 (25), 254101, 2014.

[105] P. A. Ni, C. Hornschuch, M. Panjan, and A. Anders, Appl. Phys. Lett., 101 (22), 224102, 2012.

[106] A. P. Ehiasarian, A. Hecimovic, T. de los Arcos, R. New, V. Schulz-von der Gathen, M. Boke, and J. Winter, Appl. Phys. Lett., 100 (11), 114101, 2012.

[107] A. Anders, Appl. Phys. Lett., 100 (22), 224104, 2012.

[108] T. de los Arcos, V. Layes, Y. Aranda Gonzalvo, V. Schulz-von der Gathen, A. Hecimovic and J. Winter, J. Phys. D: Appl. Phys., 46 (33), 335201, 2013.

[109] N. Brenning, D. Lundin, T. Minea, C. Costin and C. Vitelaru, J. Phys. D: Appl. Phys., 46 (8), 084005, 2013.

[110] D. Lundin, U. Helmersson, S. Kirkpatrick, S. Rohde, and N. Brenning, Plasma Sources Sci. Technol., 17 (2), 025007, 2008.

[111] M. Panjan, S. Loquai, J. E. Klemberg-Sapieha and L. Martinu, Plasma Sources Sci. Technol., 24 (6), 065010, 2015.

[112] A. Hecimovic and A. von Keudell, J. Phys. D: Appl. Phys., 51, 453001, 2018.

[113] J. Held and A. von Keudell, Plasma Chem. Plasma Process., 40, 643–660, 2020.

[114] J. P. Boeuf and M. Takahashi, Phys. Plasmas, 27 (8), 083520, 2020.

[115] A. I. Smolyakov, O. Chapurin, W. Frias, O. Koshkarov, I. Romadanov, T. Tang, M. Umansky, Y. Raitses, I. D. Kaganovich, and V. P. Lakhin, Plasma Phys. Control. Fusion, 59 (1), 014041, 2016.

[116] A. Hasegawa and K. Mima, Phys. Fluids, 21 (1), 87, 1978.

[117] A. Hasegawa, C. G. Maclennan, and Y. Kodama, Phys. Fluids, 22 (11), 2122, 1979.

[118] F. Wagner, G. Becker, K. Behringer, D. Campbell, A. Eberhagen, W. Engelhardt, G. Fussmann, O. Gehre, J. Gernhardt, G. v. Gierke, G. Haas, M. Huang, F. Karger, M. Keilhacker, Q. Kluber, M. Kornherr, K. Lackner, G. Lisitano, G. G. Lister, H. M. Mayer, D. Meisel, E. R. Muller, H. Murmann, H. Niedermeyer, W. Poschenrieder, H. Rapp, H. Rohr, F. Schneider, G. Siller, E. Speth, A. Stabler, K. H. Steuer, G. Venus, O. Vollmer, and Z. Yu, Phys. Rev. Lett., 49 (19), 1408–1412, 1982.

[119] F. Wagner, G. Fussmann, T. Grave, M. Keilhacker, M. Kornherr, K. Lackner, K. McCormick, E. R. Muller, A. Stabler, G. Becker, K. Bernhardi, U. Ditte, A. Eberhagen, O. Gehre, J. Gernhardt, G. v. Gierke, E. Glock, O. Gruber, G. Haas, M. Hesse, G. Janeschitz, F. Karger, S. Kissel, O. Kluber, G. Lisitano, H. M. Mayer, D. Meisel, V. Mertens, H. Murmann, W. Poschenrieder, H. Rapp, H. Rohr, F. Ryter, F. Schneider, G. Siller, P. Smeulders, F. Soldner, E. Speth, K.-H. Steuer, Z. Szymanski, and O. Vollmer, Phys. Rev. Lett., 53 (15), 1453–1456, 1984.

[120] ASDEX Team, Nucl. Fusion, 29, 1959, 1989.

[121] A. Hasegawa and M. Wakatani, Phys. Rev. Lett., 50 (9), 682–686, 1983.

[122] M. Wakatani and A. Hasegawa, Phys Fluids, 27 (3), 611, 1984.

[123] A. Hasegawa, Self-organization processes in continuous media, Adv. Phys., 34 (1), 1–42, 1985.

[124] A. Hasegawa and M. Wakatani, Phys. Rev. Lett., 59 (14), 1581–1584, 1987.

[125] R. J. Groebner, K. H. Burrell, and R. P. Seraydarian, Phys. Rev. Lett., 64 (25), 3015–3018, 1990.

[126] K. C. Shaing and E. C. Crume Jr., Phys. Rev. Lett., 63 (21), 2369–2372, 1989.

[127] H. Biglari, P. H. Diamond, and P. W. Terry, Phys. Fluids B, 2 (1), 1–4, 1990.

[128] P. H. Diamond and Y.-B. Kim, Phys. Fluids B, 3 (7), 1626–1633, 1991.

[129] Diamond, P. H., Y.-M. Liang, B. A. Carreras, and P. W. Terry, Phys. Rev. Lett., 72 (16), 2565–2568, 1994.

[130] T. S. Hahm and K. H. Burrell, Phys. Plasmas, 2 (5), 1648–1651, 1995.

[131] R. A. Moyer, K. H. Burrell, T. N. Carlstrom, S. Coda, R. W. Conn, E. J. Doyle, P. Gohil, R. J. Groebner, J. Kim, R. Lehmer, W. A. Peebles, M. Porkolab, C. L. Rettig, T. L. Rhodes, R. P. Seraydarian, R. Stockdale, D. M. Thomas, G. R. Tynan, and J. G. Watkins, Phys. Plasmas, 2 (6), 2397–2407, 1995.

[132] P. H. Diamond and T. S. Hahm, Phys. Plasmas, 2 (10), 3640–3649, 1995.

[133] D. E. Newman, B. A. Carreras, P. H. Diamond, and T. S. Hahm, Phys. Plasmas, 3 (5), 1858–1866, 1996.

[134] Z. Lin, T. S. Hahm, W. W. Lee, W. M. Tang, and R. B. White, Science, 281 (5384), 1835–1837, 1998.

[135] A. E. Hubbard, B. A. Carreras, R. L. Boivin, J. W. Hughes, E. S. Marmar, D. Mossessian, and S. J. Wukitch, Plasma Phys. Control. Fusion, 42, A15, 2000.

[136] Z. Lin, T. S. Hahm, W. W. Lee, W. M. Tang, and P. H. Diamond, Phys. Rev. Lett., 83 (18), 3645–3648, 1999.

[137] A. Fujisawa, K. Itoh, H. Iguchi, K. Matsuoka, S. Okamura, A. Shimizu, T. Minami, Y. Yoshimura, K. Nagaoka, C. Takahashi, M. Kojima, H. Nakano, S. Ohsima, S. Nishimura, M. Isobe, C. Suzuki, T Akiyama, K. Ida, K. Toi, S.-I. Itoh, and P. H. Diamond, Phys. Rev. Lett., 93 (16), 165002, 2004.

[138] P. Manz, M. Ramisch, and U. Stroth, Phys. Rev. Lett., 103 (16), 165004, 2009.

[139] N. Winsor, J. L. Johnson, and J. M. Dawson, Phys. Fluids, 11 (11), 2448, 1968.

[140] M. Jakubowski, R. J. Fonck, and G. R. McKee, Phys. Rev. Lett., 89 (26), 265003, 2002.

[141] G. D. Conway, B. Scott, J. Schirmer, M. Reich, A. Kendl and the ASDEX Upgrade Team, Plasma Phys. Control. Fusion, 47 (8), 1165-1185, 2005.

[142] P. W. Terry, Rev. Mod. Phys., 72 (1), 109–165, 2000.

[143] P. H. Diamond, S.-I. Itoh, K. Itoh and T. S. Hahm, Plasma Phys. Control. Fusion 47, R35, 2005.

[144] L. Kelvin, Phil. Mag, 42 (281), 362-377, 1871.

[145] W. Knauer, J. Appl. Phys., 37(2), 602–611, 1966.

[146] NASA's Solar Dynamics Observatory Catches Surfer Waves on the Sun, Astrophys. J. Lett., 2011: `https://www.nasa.gov/mission$_$pages/sunearth/news/sun-surfing.html`.

[147] P. W. Gingell, S. C. Chapman and R. O. Dendy, Plasma Phys. Control. Fusion, 56 (3), 035012, 2014.

[148] L.-X. Li and R. Narayan, R., Astrophys. J., 601 (1), 414–427, 2004.

[149] X. Garbet, C. Fenzi, H. Capes, P. Devynck, and G. Antar, Phys. Plasmas, 6 (10), 3955–3965, 1999.

[150] E. C. Harding, J. F. Hansen, O. A. Hurricane, R. P. Drake, H. F. Robey, C. C. Kuranz, B. A. Remington, M. J. Bono, M. J. Grosskopf, and R. S. Gillespie, Phys. Rev. Lett., 103 (4), 045005, 2009.

[151] I.T. Chapman, S. Brown, R. Kemp and N.R. Walkden, Nucl. Fusion, 52 (4), 042005, 2012.

[152] D. W. Hughes and S. M. Tobias, An Introduction to Mean Field Dynamo Theory, Reviews of the Theory of Magnetized Plasmas Volume 1, Relaxation Dynamics in Laboratory and Astrophysical Plasmas, Pages: 15–48, World Scientific Publishing Co Pte Ltd (Verlag), ISBN 9814291544, 9789814291545, 2009.

[153] E. N. Parker, Cosmical Magnetic Fields: Their Origin and Their Activity, Clarendon Press, Oxford, 1979.

[154] J. B. Taylor, and B. McNamara, Phys. Fluids, 14 (7), 1492, 1971.

[155] A. Das, P. Kaw and R. Jha, Intermittency Like Phenomena in Plasma Turbulence, Reviews of the Theory of Magnetized Plasmas Volume 1, Relaxation Dynamics in Laboratory and Astrophysical Plasmas,

Pages: 151–185, World Scientific Publishing Co Pte Ltd (Verlag), ISBN 9814291544, 9789814291545, 2009.

[156] E. A. Novikov and R. W. Stewart, Izv. Geophys. Ser, 3, 408-413, 1964.

[157] U. Frisch, P. L. Sulem, and M. Nelkin, J. Fluid Mech., 87(4), 719-736, 1978.

[158] Z.-S, She and E. Leveque, Phys. Rev. Lett., 72 (3), 336–339, 1994.

[159] R. H. Kraichnan, Phys. Rev. Lett., 65 (5), 575–578, 1990.

[160] G. Y. Antar, P. Devynck, X. Garbet, and S. C. Luckhardt, Phys. Plasmas, 8 (5), 1612–1624, 2001.

[161] G. Y. Antar, G. Counsell, Y. Yu, B. Labombard, and P. Devynck, Phys. Plasmas, 10 (2), 419–428, 2003.

[162] D. A. D'Ippolito, J. R. Myra, and S. J. Zweben, Phys. Plasmas, 18 (6), 060501, 2011.

[163] S. J. Zweben, Phys. Fluids, 28 (3), 974, 1985.

[164] N. Katz, J. Egedal, W. Fox, A. Le, and M. Porkolab, Phys. Rev. Lett., 101 (1), 015003, 2008.

[165] D. H. J. Goodall, J. Nucl. Mater. 111-112, 11–22, 1982.

[166] N. R. Walkden, B. Labit, H. Reimerdes, J. Harrison, T. Farley, P. Innocente, F. Militello, the TCV Team and the MST1 Team, Plasma Phys. Control. Fusion, 60 (11), 115008, 2018.

[167] J. Cavalier, N. Lemoine, F. Brochard, V. Weinzettl, J. Seidl, S. Silburn, P. Tamain, R. Dejarnac, J. Adamek and R. Panek, Nucl. Fusion, 59 (5), 056025, 2019.

[168] A. Kirk, N. Ben Ayed, G. Counsell, B. Dudson, T. Eich, A. Herrmann, B. Koch, R. Martin, A. Meakins, S. Saarelma, R. Scannell, S. Tallents, M. Walsh, H. . R. Wilson and the MAST team, Plasma Phys. Control. Fusion, 48 (12B), B433–B441, 2006.

[169] S. J. Zweben, R. J. Maqueda, D. P. Stotler, A. Keesee, J. Boedo, C. E. Bush, S. M. Kaye, B. LeBlanc, J. L. Lowrance, V. J. Mastrocola, R. Maingi, N. Nishino, G. Renda, D. W. Swain, J. B. Wilgen and the NSTX Team, Nucl. Fusion, 44 (1), 134–153, 2004.

[170] J. A. Boedo, D. Rudakov, R. Moyer, S. Krasheninnikov, D. Whyte, G. McKee, G. Tynan, M. Schaffer, P. Stangeby, P. West, S. Allen, T. Evans, R. Fonck, E. Hollmann, A. M. A. Leonard, G. Porter, M. Tillack, and G. Antar, Phys. Plasmas, 8 (11), 4826–4833, 2001.

[171] D. Carralero, P. Manz, L. Aho-Mantila, G. Birkenmeier, M. Brix, M. Groth, H. W. Muller, U. Stroth, N. Vianello, E. Wolfrum, ASDEX Upgrade team, JET Contributors, and EUROfusion MST1 Team, Phys. Rev. Lett., 115 (21), 215002, 2015.

[172] G. S. Xu, V. Naulin, W. Fundamenski, J. Juul Rasmussen, A. H. Nielsen, and B. N. Wan, Phys. Plasmas, 17 (2), 022501, 2010.

[173] J. L. Terry, S. J. Zweben, K. Hallatschek, B. LaBombard, R. J. Maqueda, B. Bai, C. J. Boswell, M. Greenwald, D. Kopon, W. M. Nevins, C. S. Pitcher, B. N. Rogers, D. P. Stotler, and X. Q. Xu, Phys. Plasmas, 10 (5), 1739–1747, 2003.

[174] M. Agostini, P. Scarin, R. Cavazzana, F. Sattin, G. Serianni, M. Spolaore, and N. Vianello, Plasma Phys. Control. Fusion, 51 (10), 105003, 2009.

[175] R. J. Maqueda, D. P. Stotler, and the NSTX Team, Nucl. Fusion, 50 (7), 075002, 2010.

[176] R.J. Maqueda, D.P. Stotler, S.J. Zweben, and the NSTX team, J. Nucl. Mater., 415 (1), S459–S462, 2011.

[177] J. A. Boedo, D. L. Rudakov, R. A. Moyer, G. R. McKee, R. J. Colchin, M. J. Schaffer, P. G. Stangeby, W. P. West, S. L. Allen, T. E. Evans, R. J. Fonck, E. M. Hollmann, S. Krasheninnikov, A. W. Leonard, W. Nevins, M. A. Mahdavi, G. D. Porter, G. R. Tynan, D. G. Whyte, and X. Xu, Phys. Plasma, 10 (5), 1670–1677, 2003.

[178] Y. Sechrest, D. Smith, D. P. Stotler, T. Munsat, and S. J. Zweben, Phys. Plasmas, 22 (5), 052310, 2015.

[179] A. Huber, U. Samm, B. Schweer and Ph. Mertens, Plasma Phys. Control. Fusion, 47 (3), 409–440, 2005.

[180] A. V. Nedospasov, Sov. J. Plasma Phys. 15, 659, 1989.

[181] X. Garbet, L. Laurent, J.P. Roubin, and A. Samain, Nucl. Fusion, 31 (5), 967–972, 1991.

[182] S. I. Krasheninnikov, Phys. Lett. A, 283 (5-6), 368–370, 2001.

[183] D. A. D'Ippolito, J. R. Myra, S. I. Krasheninnikov, Phys. Plasmas, 9 (1), 222–233, 2002.

[184] S. I. Krasheninnikov, D. A. D'Ippolito, and J. R. Myra, J. Plasma Phys., 74 (5), 679-717, 2008.

[185] O. E. Garcia, N. H. Bian, V. Naulin, A. H. Nielsen, and J. J. Rasmussen, Phys. Plasmas, 12 (9), 090701, 2005.

[186] J. R. Myra and D. A. D'Ippolito, Phys. Plasmas, 12 (9), 092511, 2005.

[187] D. D. Ryutov and R. H. Cohen, Contrib. Plasma Phys., 44 (13), 168–175, 2004.

[188] J. R. Myra, D. A. Russell, and D. A. D'Ippolito, Phys. Plasmas, 13 (11), 112502, 2006.

[189] D. A. Russell, J. R. Myra, and D. A. D'Ippolito. Phys. Plasmas, 14 (10), 102307, 2007.

[190] D. A. D'Ippolito and J. R. Myra, Phys. Plasmas, 13 (6), 062503, 2006.

[191] S. I. Krasheninnikov, D. D. Ryutov and G. Yu, J. Plasma Fusion Res., 6, 139, 2004.

[192] F. Militello and J. T. Omotani, Nucl. Fusion, 56 (10), 104004, 2016.

[193] B. LaBombard, R. L. Boivin, M. Greenwald, J. Hughes, B. Lipschultz, D. Mossessian, C. S. Pitcher, J. L. Terry, S. J. Zweben, and Alcator Group, Phys. Plasmas, 8 (5), 2107–2117, 2001.

[194] D. L. Rudakov, J. A. Boedo, R. A. Moyer, P. C. Stangeby, J. G. Watkins, D. G. Whyte, L. Zeng, N. H. Brooks, R. P. Doerner, T. E. Evans, M. E. Fenstermacher, M. Groth, E. M. Hollmann, S. I. Krasheninnikov, C. J. Lasnier, A. W. Leonard, M. A. Mahdavi, G. R. McKee, A. G. McLean, A. Yu. Pigarov, W. R. Wampler, G. Wang, W. P. West and C. P. C. Wong, Nucl. Fusion, 45 (12), 1589–1599, 2005.

[195] O. E. Garcia, J. Horacek, R. A. Pitts, A. H. Nielsen, W. Fundamenski, V. Naulin and J. Juul Rasmussen, Nucl. Fusion, 47 (7), 667–676, 2007.

[196] D. Carralero, G. Birkenmeier, H. W. Muller, P. Manz, P. de Marne, S. H. Muller, F. Reimold, U. Stroth, M. Wischmeier, E. Wolfrum, and The ASDEX Upgrade Team, Nucl. Fusion, 54 (12), 123005, 2014.

[197] F. Militello, L. Garzotti, J. Harrison, J. T. Omotani, R. Scannell, S. Allan, A. Kirk, I. Lupelli, A. J. Thornton and the MAST team, Nucl. Fusion, 56 (1), 016006, 2016.

[198] B. Lipschultz, D. Whyte and B. LaBombard, Plasma Phys. Control. Fusion, 47 (10), 1559–1578, 2005.

[199] D. Carralero, H. W. Muller, M. Groth, M. Komm, J. Adamek, G. Birkenmeier, M. Brix, F. Janky, P. Hacek, S. Marsen, F. Reimold, C. Silva, U. Stroth, M. Wischmeier, E. Wolfrum, ASDEX Upgrade Team, COMPASS Team, and JET-EFDA Contributors, J. Nucl. Mater., 463, 123–127, 2015.

[200] N. Asakura, Y. Koide, K. Itami, N. Hosogane, K. Shimizu, S. Tsuji-Iio, S. Sakurai, and A. Sakasai, J. Nucl. Mater., 241-243, 559-563, 1997.

[201] D. Carralero, J. Madsen, S. A. Artene, M. Bernert, G. Birkenmeier, T. Eich, G. Fuchert, F. Laggner, V. Naulin, P. Manz, N. Vianello, E. Wolfrum, the EUROfusion MST1 team, and the ASDEX Upgrade Team, J. Nucl. Mater., 12, 1189–1193, 2017.

[202] A. W. Leonard, Phys. Plasmas, 21 (9), 090501, 2014.

[203] K. H. Burrell, S. L. Allen, G. Bramson, N. H. Brooks, R. W. Callis, T. N. Carlstrom, M. S. Chu, A. P. Colleraine, D. Content, J. C. DeBoo, R. R. Dominguez, J. R. Ferron, R. L. Freeman, P. Gohil, C. M. Greenfield, R. J. Groebner, G. Haas, W. W. Heidbrink, D. N. Hill, F. L. Hinton, R. -M. Hong, W. Howl, C. L. Hsieh, G. L. Jackson, G. L. Jahns, R. A. James, A. G. Kellman, J. Kim, L. L. Lao, E. A. Lazarus, T. Lehecka, J. Lister, J. Lohr, T. C. Luce, J. L. Luxon, M. A. Mahdavi, H. Matsumoto, M. Mayberry, C. P. Moeller, Y. Neyatani, T. Ohkawa, N. Ohyabu, T. Okazaki, T. H. Osborne, D. O. Overskei, T. Ozeki, A. Peebles, S. Perkins, M. Perry, P. I. Petersen, T. W. Petrie, R. Philipona, J. C. Phillips, R. Pinsker, P. A. Politzer, G. D. Porter, R. Prater, M. E. Rensink, M. J. Schaffer, D. P. Schissel, J. T. Scoville, R. P. Seraydarian, M. Shimada, T. C. Simonen, R. T. Snider, G. M. Staebler, B. W. Stallard, R. D. Stambaugh, R. D. Stav, H. St John, R. E. Stockdale, E. J. Strait, P. L. Taylor, T. S. Taylor, P. K. Trost,

U. Stroth, R. E. Waltz, S. M. Wolfe, R. D. Wood and D. Wroblewski, Plasma Phys. Control. Fusion, 31 (10), 1649–1664, 1989.

[204] A. Loarte, G. Saibene, R. Sartori, D. Campbell, M. Becoulet, L. Horton, T. Eich, A. Herrmann, G. Matthews, N. Asakura, A. Chankin, A. Leonard, G. Porter, G. Federici, G. Janeschitz, M. Shimada and M. Sugihara, Plasma Phys. Control. Fusion, 45 (9), 1549–1569, 2003.

[205] N. Ben Ayed, A. Kirk, B. Dudson, S. Tallents, R. G. L. Vann, H. R. Wilson and the MAST team, Plasma Phys. Control. Fusion, 51 (3), 035016, 2009.

[206] H. R. Wilson, P. B. Snyder, G. T. A. Huysmans, and R. L. Miller, Phys. Plasmas, 9 (4), 1277–1286, 2002.

[207] Association EURATOM-CEA, Commissariat à l'Énergie Atomique et aux Énergies Alternatives, 2018: `http://www-fusion-magnetique.cea.fr`

[208] J. W. Connor, Plasma Phys. Control. Fusion, 40 (2), 191–213, 1998.

[209] J. W. Connor, R. J. Hastie, and J. B. Taylor, Proc. R. Soc. A: Math. Phys. Eng. Sci., 365 (1720), 1–17, 1979.

[210] C. F. Kennel, Convention and Substorms: Paradigms of Magentospheric Phenomenology, Oxford University Press, New York, 1995.

[211] S. Cowley, M. Artun, and B. Albright, Phys. Plasmas, 3 (5), 1848–1852, 1996.

[212] H. R. Wilson and S. C. Cowley, Phys. Rev. Lett., 92 (17), 175006, 2004.

[213] T. H. Osborne, J. R. Ferron, R. J. Groebner, L. L. Lao, A. W. Leonard, M. A. Mahdavi, R. Maingi, R. L. Miller, A. D. Turnbull, M. Wade and J. Watkins, Plasma Phys. Control. Fusion, 42 (5A), A175–A184, 2000.

[214] J. L. Luxon and L. G. Davis, Fusion Technol., 8 (1P2A), 441–449, 1985.

[215] P. B. Snyder, H. R. Wilson, J. R. Ferron, L. L. Lao, A. W. Leonard, T. H. Osborne, A. D. Turnbull, D. Mossessian, M. Murakami, and X. Q. Xu, Phys. Plasmas, 9 (5), 2037–2043, 2002.

[216] P. B. Snyder, H. R. Wilson, J. R. Ferron, L. L. Lao, A. W. Leonard, D. Mossessian, M. Murakami, T. H. Osborne, A. D. Turnbull, and X. Q. Xu, Nucl. Fusion, 44 (2), 320–328, 2004.

[217] H. Zohm, Plasma Phys. Control. Fusion, 38 (2), 105–128, 1996.

[218] E. J. Doyle, R. J. Groebner, K. H. Burrell, P. Gohil, T. Lehecka, N. C. Luhmann Jr., H. Matsumoto, T. H. Osborne, W. A. Peebles, and R. Philipona, Phys. Fluids B 3: Plasma Physics, 3 (8), 2300–2307, 1991.

[219] T. Ozeki, M. S. Chu, L. L. Lao, T. S. Taylor, M. S. Chance, S. Kinoshita, K .H. Burrell, R. D. Stambaugh, Nucl. Fusion, 30 (8), 1425–1432, 1990.

[220] C. P. Perez, H. R. Koslowski, G. T. A. Huysmans, T. C. Hender, P. Smeulders, B. Alper, E. de la Luna, R. J. Hastie, L. Meneses, M. F. F. Nave, V. Parail, M. Zerbini and JET-EFDA Contributors, Nucl. Fusion, 44 (5), 609–623, 2004.

[221] M. Valovic *et al.*, Proc. 21st Euro. Conf. Controlled Fusion and Plasma Physics (Montpellier) vol I p 318, 1994.

[222] H. Weisen *et al.*, Proc. 22nd Euro. Conf. Controlled Fusion and Plasma Physics (Bournemouth, UK), 1995.

[223] J. A. Snipes, R. S. Granetz, M. Greenwald, A. E. Hubbard, I. H. Hutchinson, J. Irby, J. Kesner, S. Migliuolo, T. Sunn Pedersen, J. Ramos, J. Rice, P. C. Stekd, Y. Takase and S. M. Wolfe, Plasma Phys. Control. Fusion, 40 (5), 765–770, 1998.

[224] H. Zohm, T. H. Osborne, K. H. Burrell, M. S. Chu, E. J. Doyle, P. Gohil, D. N. Hill, L. L. Lao, A. W. Leonard, and T. S. Taylor, Nucl. Fusion, 35 (5), 543–550, 1995.

[225] T. E. Evans, A. Moyer, J. G. Watkins, P. R. Thomas, T. H. Osborne, J. A. Boedo, M. E. Fenstermacher, K. H. Finken, R. J. Groebner, M. Groth. J. Harris, G. L. Jackson, R. J. LaHaye, C. J. Lasnier, M. J. Schaffer, G. Wang, and L. Zeng, J. Nucl. Mater. 337-339, 691-696, 2005.

[226] P. T. Langa, G. D. Conway, T. Eich, L. Fattorini, O. Gruber, S. Gunter, L. D. Horton, S. Kalvin, A. Kallenbach, M. Kaufmann, G. Kocsis, A. Lorenz, M. E. Manso, M. Maraschek, V. Mertens, J. Neuhauser,

I. Nunes, W. Schneider, W. Suttrop, H. Urano and the ASDEX Upgrade Team, Nucl. Fusion, 44 (5), 665–677, 2004.

[227] The JET Team (presented by D. Stork), Plasma Phys. Control. Fusion, 36 (7A), A23–A38, 1994.

[228] M. Keilhacker, A. Gibson, C. Gormezano, P. J. Lomas, P. R. Thomas, M. L. Watkins, P. Andrew, B. Balet, D. Borba, C. D. Challis, I. Coffey, G. A. Cottrell, H. P. L. De Esch, N. Deliyanakis, A. Fasoli, C. W. Gowers, H. Y. Guo, G. T. A. Huysmans, T. T. C. Jones, W. Kerner, R. W. T. Konig, M. J. Loughlin, A. Maas, F. B. Marcus, M. F. F. Nave, F. G. Rimini, G. J. Sadler, S. E. Sharapov, G. Sips, P. Smeulders, F. X. Soldner, A. Taroni, B. J. D. Tubbing, M. G. von Hellermann, D. J. Ward, and the JET Team, Nucl. Fusion, 39 (2), 209–234, 1999.

[229] A. Cathey, M. Hoelzl, G. Harrer, M. G. Dunne, G. T. A. Huijsmans, K. Lackner, S. J. P. Pamela, E. Wolfrum, S. Gunter and the JOREK Team, the ASDEX Upgrade Team and the EUROfusion MST1 Team, Plasma Phys. Control. Fusion, 64 (5), 054011, 2022.

[230] O. Sauter, C. Angioni, and Y. R. Lin-Liu, Phys. Plasmas 6 (7), 2834-2839, 1999.

[231] F. M. Laggner, A. Diallo, M. Cavedon, and E. Kolemen, Nucl. Mater. Energy, 19, 479-486, 2019.

[232] P. Manz, J. E. Boom, E. Wolfrum, G. Birkenmeier, I. G. J. Classen, N. C. Luhmann Jr., U. Stroth and the ASDEX Upgrade Team, Plasma Phys. Control. Fusion, 56 (3), 035010, 2014.

[233] Y. Sechrest, T. Munsat, D. J. Battaglia and S. J. Zweben, Nucl. Fusion, 52 (12), 123009, 2012.

[234] A. Kirk, D. Dunai, M. Dunne, G. Huijsmans, S. Pamela1, M. Becoulet, J. R. Harrison, J. Hillesheim, C. Roach, and S. Saarelma, Nucl. Fusion, 54 (11), 114012, 2014.

[235] G. S. Yun, W. Lee, M. J. Choi, J. Lee, H. K. Park, B. Tobias, C. W. Domier, N. C. Luhmann, Jr., A. J. H. Donne, J. H. Lee, and KSTAR Team, Phys. Rev. Lett., 107 (4), 045004, 2011.

[236] N. Oyama, N. Hayashi, N. Aiba, A. Isayama, H. Urano, Y. Sakamoto, Y. Kamada, T. Takizuka and the JT-60 Team, Nucl. Fusion, 51 (3), 033009, 2011.

[237] R.P. Wenninger, H. Reimerdes, O. Sauter and H. Zohm, Nucl. Fusion, 53 (11), 113004, 2013.

[238] R. Scannell, A. Kirk, N. Ben Ayed, P. G. Carolan, G. Cunningham, J. McCone, S. L. Prunty, and M. J. Walsh, Plasma Phys. Control. Fusion, 49 (9), 1431, 2007.

[239] F. M. Poli, S. E. Sharapov, and S. C. Chapman, Plasma Phys. Control. Fusion, 50 (9), 095009, 2008.

[240] J.-W. Ahn, H.-S. Kim, Y. S. Park, L. Terzolo, W. H. Ko, J.-K. Park, A. C. England, S. W. Yoon, Y. M. Jeon, S. A. Sabbagh, Y. S. Bae, J. G. Bak, S. H. Hahn, D. L. Hillis, J. Kim, W. C. Kim, J. G. Kwak, K. D. Lee, Y. S. Na, Y. U. Nam, Y. K. Oh and S. I. Park, Nucl. Fusion, 52 (11), 114001, 2012.

[241] R. Panek, O. Bilykova, V. Fuchs, M. Hron, P. Chraska, P. Pavlo, J. Stockel, J. Urban, V. Weinzettl, J. Zajac, and F. Zacek, Czechoslov. J. Phys., 56 (2), B125–B137, 2006.

[242] V. Weinzettl, R. Panek, M. Hron, J. Stockel, F. Zacek, J. Havlicek, P. Bilkova, D. I. Naydenkova, P. Hacek, J. Zajac, R. Dejarnac, J. Horacek, J. Adamek, J. Mlynar, F. Janky, M. Aftanas, P. Bohm, J. Brotankova, D. Sestak, I. Duran, R. Melich, D. Jares, J. Ghosh, G. Anda, G. Veres, A. Szappanos, S. Zoletnik, M. Berta, V. F. Shevchenko, R. Scannell, M. Walsh, H. W. Muller, V. Igochine, A. Silva, M. Manso, R. Gomes, Tsv. Popov, D. Sarychev, V. K. Kiselov, and S. Nanobashvili, Fusion Eng. Des., 86 (6-8), 1227–1231, 2011.

[243] R. Panek, J. Adamek, M. Aftanas, P. Bilkova, P. Bohm, F. Brochard, P. Cahyna, J. Cavalier, R. Dejarnac, M. Dimitrova, O. Grover, J. Harrison, P. Hacek, J. Havlicek, A. Havranek, J. Horacek, M. Hron, M. Imrisek, F. Janky, A. Kirk, M. Komm, K. Kovarik, J. Krbec, L. Kripner, T. Markovic, K. Mitosinkova, J. Mlynar, D. Naydenkova, M. Peterka, J. Seidl, J. Stockel, E. Stefanikova, M. Tomes, J. Urban, P. Vondracek, M. Varavin, J. Varju, V. Weinzettl, J. Zajac and the COMPASS team, Plasma Phys. Control. Fusion, 58 (1), 014015, 2015.

[244] IPP Prague: `http://www.ipp.cas.cz/vedecka_struktura_ufp/tokamak/COMPASS/`

[245] R. Panek, T. Markovic, P. Cahyna, R. Dejarnac, J. Havlicek, J. Horacek, M. Hron, M. Imrisek, P. Junek, M. Komm, D. Sestak, J. Urban, J. Varju, V. Weinzettl, J. Adamek, P. Bilkova, P. Bohm, M. Dimitrova, P. Hacek, K. Kovarik, J. Krbec, J. Mlynar, A. Podolnik, J. Seidl, J. Stockel, M. Tomes, F.

Zajac, K. Mitosinkova, M. Peterka, P. Vondracek, and the COMPASS team, Fusion Eng. Des., 123, 11–16, 2017.

[246] A. Sykes, E. Del Bosco, R.J. Colchin, G. Cunningham, R. Duck, T. Edlington, D.H.J. Goodall, M.P. Gryaznevich, J. Holt, J. Hugill, Nucl. Fusion, 32 (4), 694, 1992.

[247] Y.-K. M. Peng, D. J. Strickler, Nucl. Fusion, 26 (6), 769, 1986.

[248] H. Bruhns, R. Brendel, G. Raupp and J. Steiger, Nucl. Fusion, 27 (12), 2178, 1987.

[249] A. E. Costley, Phil. Trans. R. Soc. A, 377 (2141), 20170439, 2019.

[250] M. Gryaznevich, R. Akers, P. G. Carolan, N. J. Conway, D. Gates, A. R. Field, T. C. Hender, I. Jenkins, R. Martin, M. P. S. Nightingale, C. Ribeiro, D. C. Robinson, A. Sykes, M. Tournianski, M. Valovic, and M. J. Walsh, Phys. Rev. Lett., 80 (18), 3972-3975, 1998.

[251] A. Sykes, R. J. Akers, L. C. Appel, P. G. Carolan, J. W. Connor, N. J. Conway, G. F. Counsell, A. Dnestrovskij, Yu. N. Dnestrovskij, M. Gryaznevich, P. Helander, M. P. S. Nightingale, C. Ribeiro, C. M. Roach, M. Tournianski, M. J. Walsh, H. R. Wilson, The START Team, and The NBI Team, Phys. Rev. Lett., 84 (3), 495-498, 2000.

[252] Cox, M. and the MAST team, Fusion Eng. Des., 46 (2-4), 397-404, 1999.

[253] A. Kirk, J. Adamek, R. J. Akers, S. Allan, L. Appel, F. Arese Lucini, M. Barnes, T. Barrett, N. Ben Ayed, W. Boeglin, J. Bradley, P. K. Browning, J. Brunner, P. Cahyna, S. Cardnell, M. Carr, F. Casson, M. Cecconello, C. Challis, I. T. Chapman, S. Chapman, J. Chorley, S. Conroy, N. Conway, W. A. Cooper, M. Cox, N. Crocker, B. Crowley, G. Cunningham, A. Danilov, D. Darrow, R. Dendy, D. Dickinson, W. Dorland, B. Dudson, D. Dunai, L. Easy, S. Elmore, M. Evans, T. Farley, N. Fedorczak, A. Field, G. Fishpool, I. Fitzgerald, M. Fox, S. Freethy, L. Garzotti, Y. C. Ghim, K. Gi, K. Gibson, M. Gorelenkova, W. Gracias, C. Gurl, W. Guttenfelder, C. Ham, J. Harrison, D. Harting, E. Havlickova, N. Hawkes, T. Hender, S. Henderson, E. Highcock, J. Hillesheim, B. Hnat, J. Horacek, J. Howard, D. Howell, B. Huang, K. Imada, M. Inomoto, R. Imazawa, O. Jones, K. Kadowaki, S. Kaye, D. Keeling, I. Klimek, M. Kocan, L. Kogan, M. Komm, W. Lai, J. Leddy, H. Leggate, J. Hollocombe, B. Lipschultz, S.

Lisgo, Y.Q. Liu, B. Lloyd, B. Lomanowski, V. Lukin, I. Lupelli, G. Maddison, J. Madsen, J. Mailloux, R. Martin, G. McArdle, K. McClements, B. McMillan, A. Meakins, H. Meyer, C. Michael, F. Militello, J. Milnes, A.W. Morris, G. Motojima, D. Muir, G. Naylor, A. Nielsen, M. O'Brien, T. O'Gorman, M. O'Mullane, J. Olsen, J. Omotani, Y. Ono, S. Pamela, L. Pangione, F. Parra, A. Patel, W. Peebles, R. Perez, S. Pinches, L. Piron, M. Price, M. Reinke, P. Ricci, F. Riva, C. Roach, M. Romanelli, D. Ryan, S. Saarelma, A. Saveliev, R. Scannell, A. Schekochihin, S. Sharapov, R. Sharples, V. Shevchenko, K. Shinohara, S. Silburn, J. Simpson, A. Stanier, J. Storrs, H. Summers, Y. Takase, P. Tamain, H. Tanabe, H. Tanaka, K. Tani, D. Taylor, D. Thomas, N. Thomas-Davies, A. Thornton, M. Turnyanskiy, M. Valovic, R. Vann, F. Van Wyk, N. Walkden, T. Watanabe, H. Wilson, M. Wischmeier, T. Yamada, J. Young, S. Zoletnik and the MAST Team and the EUROfusion MST1 Team, Nucl. Fusion, 57 (10), 102007, 2017.

[254] B. Lloyd, J-W. Ahn, R. J. Akers, L. C. Appel, E. R. Arends, K. B. Axon, R. J. Buttery, C. Byrom, P. G. Carolan, C. Challis, D. Ciric, N. J. Conway, M. Cox, G. F. Counsell, G. Cunningham, A. Darke, A. Dnestrovskij, J. Dowling, M. R. Dunstan, A. R. Field, S. J. Fielding, S. Gee, M. P. Gryaznevich, P. Helander, M. Hole, M. B. Hood, P. A. Jones, A. Kirk, I. P. Lehane, G. P. Maddison, S. J. Manhood, R. Martin, G. J. McArdle, K. G. McClements, M. A. McGrath, H. Meyer, A. W. Morris, S. K. Nielsen, M. Nightingale, A. Patel, T. Pinfold, M. N. Price, J. Qin, C. Ribeiro, C. M. Roach, D. C. Robinson, O. Sauter, V. Shevchenko, S. Shibaev, K. Stammers, A. Sykes, A. Tabasso, D. Taylor, M. R. Tournianski, G. Turri, M. Valovic, G. Voss, M. J. Walsh, S. Warder, J. R. Watkins, H. R. Wilson, Y. Yang, S. You and the MAST and NBI teams, Nucl. Fusion 43 (12), 1665, 2003.

[255] A. Sykes, R. J. Akers, L. C. Appel, E. R. Arendsa, P. G. Carolan, N. J. Conway, G. F. Counsell, G. Cunningham, A. Dnestrovskijb, Yu. N. Dnestrovskijb, A. R. Field, S. J. Fielding, M. P. Gryaznevich, S. Korsholmc, E. Lairdd, R. Martin, M. P. S. Nightingale, C. M. Roach, M. R. Tournianski, M. J. Walshe, C. D. Warrick, H. R. Wilson, S. You, MAST Team and NBI Team, Nucl. Fusion, 41 (10), 1423-1433, 2001.

[256] M. Gryaznevich, R. J. Akers, G. F. Counsell, G. Cunningham, A. Dnestrovskij, A. R. Field, T. C. Hender, A. Kirk, B. Lloyd, H. Meyer, A. W. Morris, A. Sykes, A. Tabasso, M. Valovic, G. M. Voss, H.

R. Wilson, and the MAST and NBI teams, Phys. Plasmas, 10 (5), 1803-1808, 2003.

[257] A. W. Morris, IEEE Trans. Plasma Sci., 40 (3), 682–691, 2012.

[258] I. Katramados, G. Fishpool, M. Fursdon, G. Whitfield, V. Thompson, and H. Meyer, Fusion Eng. Des., 86 (9-11), 1595-1598, 2011.

[259] MAST Upgrade Research Plan, Culham Centre for Fusion Energy, November 2019: `https://ccfe.ukaea.uk/wp-content/uploads/2019/12/MAST-U_RP_2019_v1.pdf`

[260] H. M. Mott-Smith and I. Langmuir, Phys. Rev., 28 (4), 727–763, 1926.

[261] I. H. Hutchinson, Principles of Plasma Diagnostics, Cambridge University Press, 2nd Ed., 2005.

[262] D. Bohm, The Characteristics of Electrical Discharge in Magnetic Fields, McGraw-Hill, New York, 1949.

[263] Adamek, J. Stockel, M. Hron, J. Ryszawy, M. Tichy , R. Schrittwieser, C. Ionita, P. Balan, E. Martines, and G. Van Oost, Czech. J. Phys., 54 (3), C95-C99, 2004.

[264] I. Katsumata and M. Okazaki, Jpn. J. Appl. Phys., 6 (1), 123–124, 1967.

[265] M. Komm, J. Adamek, R. Dejarnac, J. P. Gunn and Z. Pekarek, Plasma Phys. Control. Fusion, 53 (1), 015005, 2010.

[266] J. P. Sheehan and N. Hershkowitz, Plasma Sources Sci. Technol., 20 (6), 063001, 2011.

[267] F. C. Jobes and R. L. Hickok, Nucl. Fusion, 10 (2), 195–197, 1970.

[268] J. Adamek, J. Stockel, I. Duran, M. Hron, R. Panek, M. Tichy , R. Schrittwieser, C. Ionita, P. Balan, E. Martines, and G. Van Oost, Czech. J. Phys., 55 (3), 235-242, 2005.

[269] J. Adamek, M. Peterka, T. Gyergyek, P. Kudrna, M. Ramisch, U. Stroth, J. Cavalier, and M. Tichy, Contrib. Plasma Phys., 53 (1), 39–44, 2013.

[270] B. J. Harris, M. Smith, S. Murphy-Sugrue, J. Harrison, J. W. Bradley and P. M. Bryant, Plasma Sources Sci. Technol., 28 (5), 055018, 2019.

[271] J. Adamek, J. Horacek, H. W. Muller, V. Rohde, C. Ionita, R. Schrittwieser, F. Mehlmann, B. Kurzan, J. Stockel, R. Dejarnac, V. Weinzettl, J. Seidl, M. Peterka, and the ASDEX Upgrade Team, Contrib. Plasma Phys., 50 (9), 854-859, 2010.

[272] J. Adamek, V. Rohde, H. W. Muller, A. Herrmann, C. Ionita, R. Schrittwieser, F. Mehlmann, J. Stockel, J. Horacek, J. Brotankova, and the ASDEX Upgrade Team, J. Nucl. Mater., 390-391, 1114–1117, 2009.

[273] N. R. Walkden, J. Adamek, S. Allan, B. D. Dudson, S. Elmore, G. Fishpool, J. Harrison, A. Kirk, and M. Komm, Rev. Sci. Instrum., 86 (2), 023510, 2015.

[274] C. Silva, J. Adamek, H. Fernandes and H. Figueiredo, Plasma Phys. Control. Fusion, 57 (2), 025003, 2015.

[275] J. Adamek, H. W. Muller, C. Silva, R. Schrittwieser, C. Ionita, F. Mehlmann, S. Costea, J. Horacek, B. Kurzan, P. Bilkova, P. Bohm, M. Aftanas, P. Vondracek, J. Stockel, R. Panek, H. Fernandes, and H. Figueiredo, Rev. Sci. Instrum., 87 (4), 043510, 2016.

[276] R. M. Sullivan, R. Ochoukov, and D. G. Whyte, J. Nucl. Mater., 438, S1253-S1256, 2013.

[277] D. Brunner, B. LaBombard, R. Ochoukov, R. Sullivan, and D. Whyte, Plasma Phys. Control. Fusion, 55 (12), 125004, 2013.

[278] S. Murphy-Sugrue, J. Harrison, N. R. Walkden, P. Bryant and J. W. Bradley, Plasma Phys. Control. Fusion, 59 (5), 055007, 2017.

[279] R. P. Seraydarian, K. H. Burrell, R. J. Groebner, Rev. Sci. Instrum., 59 (8), 1530-1532, 1988.

[280] A. Boileau, M. von Hellerman, W. Mandl, H. P. Summers, H. Weisen and A. Zinoviev, J. Phys. B: At. Mol. Opt. Phys., 22 (7), L145-L152, 1989.

[281] M. G. von Hellermann, W. Mandl, H. P. Summers, H. Weisen, A. Boileau, P. D. Morgan, H. Morsi, R. Koenig, M. F. Stamp, and R. Wolf, Rev. Sci. Instrum., 61 (11), 3479-3486, 1990.

[282] R. J. Fonck, P. A. Duperrex and S. F. Paul, Rev. Sci. Instrum., 61 (11), 3487-3495, 1990.

[283] R. D. Durst, R. J. Fonck, G. Cosby, H. Evensen and S. F. Paul, Rev. Sci. Instrum., 63 (10), 4907-4912, 1992.

[284] W. Mandl, R. C. Wolf, M. G. von Hellermann and H. P. Summers, Plasma Phys. Control. Fusion, 35 (10), 1373-1394, 1993.

[285] A. R. Field, D. Dunai, N. J. Conway, S. Zoletnik, and J. Sarkozi, Rev. Sci. Instrum., 80 (7), 073503, 2009.

[286] A. R. Field, D. Dunai, R. Gaffka, Y.-c. Ghim, I. Kiss, B. Meszaros, T. Krizsanoczi, S. Shibaev, and S. Zoletnik, Rev. Sci. Instrum. 83 (1), 013508, 2012.

[287] N. J. Conway, P. G. Carolan, J. McCone, M. J. Walsh, and M. Wisse, Rev. Sci. Instrum., 77 (10), 10F131, 2006.

[288] G. McKee, R. Ashley, R. Durst, R. Fonck, M. Jakubowski, K. Tritz, K. Burrell, C. Greenfield, and J. Robinson, Rev. Sci. Instrum. 70 (1), 913-916, 1999.

[289] Hamamatsu: `https://www.hamamatsu.com/eu/en/product/optical-sensors/apd/si-apd-array/S8550-02.html`.

[290] D. Dunai, S. Zoletnik, J. Sarkozi, and A. R. Field, Rev. Sci. Instrum., 81 (10), 103503, 2010.

[291] S. J. Zweben and S. S. Medley, Phys. Fluids B: Plasma Physics, 1 (10), 2058-2065, 1989.

[292] Photron FastCam SA1.1 hardware manual: `www.highspeedimaging.com/media/photron_manuals/FASTCAM_SA1_1&SA1_1RV_HW_Manual.pdf`.

[293] A. Kirk, A. J. Thornton, J. R. Harrison, F. Militello, N. R. Walkden and the MAST Team and the EUROfusion MST1 Team, Plasma Phys. Control. Fusion, 58 (8), 085008, 2016.

[294] S. V. Mirnov, J. Nucl. Energy Part C, Plasma Physics, Accelerators, Thermonuclear Research, 7 (3), 325, 1965.

[295] M. J. Hole, L. C. Appel, and R. Martin, Rev. Sci. Instrum., 80 (12), 123507, 2009.

[296] B. Dudson, Edge turbulence in the Mega-Amp Spherical Tokamak, PhD thesis, Trinity College, University of Oxford, 2007: `http://www-users.york.ac.uk/~bd512/dudson_thesis.pdf`.

[297] T. Farley, Analysis of Plasma Filaments with Fast Visible Imaging in the Mega Ampère Spherical Tokamak. PhD thesis, University of Liverpool, 10.17638/03066785, 2019.

[298] T. Farley, N. R. Walkden, F. Militello, M. Sanna, J. Young, S. S. Silburn, J. Harrison, L. Kogan, I. Lupelli, S. S. Henderson, A. Kirk, and J. W. Bradley, Rev. Sci. Instrum., 90 (9), 093502, 2019.

[299] R. Nguyen van yen, N. Fedorczak, F. Brochard, G. Bonhomme, K. Schneider, M. Farge and P. Monier-Garbet, Nucl. Fusion, 52 (1), 013005, 2011.

[300] Calcam software: `https://euratom-software.github.io/calcam`.

[301] L. C. Appel, I. Lupelli and JET Contributors, Comput. Phys. Commun., 223, 1-17, 2018.

[302] L. C. Appel, G. T. A. Huysmans, L. L. Lao, P. J. McCarthy, D. G. Muir, E. R. Solano, J. Storrs, D. Taylor, and W. Zwingmann, 33rd EPS Conference on Plasma Physics, 2, 1235–1238, 2006.

[303] R. C. Aster, B. Borchers, and C. H. Thurber, Parameter Estimation and Inverse Problems, 3rd ed., ISBN: 9780128046517, Elsevier, 2018.

[304] T. Hobiger, T. Kondo, and Y. Koyama, Earth, Planets and Space, 60, 727–735, 2008.

[305] A. Grossmann and J. Morlet, SIAM J. Math. Anal., 15 (4), 723-736, 1984.

[306] S. Mallat, A Wavelet Tour of Signal Processing, Academic Press, Elsevier, 2001.

[307] C. Torrence and G. P. Compo, Bull. Am. Meteorol. Soc., 79 (1), 61–78, 1998.

[308] Y. Liu, X. S. Liang, and R .H. Weisberg, J. Atmos. Ocean. Technol., 24 (12), 2093-2102, 2007.

[309] D. Veleda, R. Montagne, and M. Araujo, J. Atmos. Ocean. Technol., 29 (9), 1401-1408, 2012.

[310] S. Krieger, N. Freij, A. Brazhe, C. Torrence, G. P. Compo and contributors, Python PyCWT 0.3.0a22 module documentation: `https://pypi.org/project/pycwt/`, `https://pycwt.readthedocs.io/`.

[311] IPP Prague: http://www.ipp.cas.cz/miranda2/export/sitesavcr/ufp/vedecka_struktura_ufp/tokamak/COMPASS/systemy/img/rec_probe_1.png.

[312] V. Weinzettl, J. Adamek, M. Berta, P. Bilkova, O. Bogar, P. Bohm, J. Cavalier, R. Dejarnac, M. Dimitrova, O. Ficker, D. Fridrich, O. Grover, P. Hacek, J. Havlicek, A. Havranek, J. Horacek, M. Hron, M. Imrisek, M. Komm, K. Kovarik, J. Krbec, T. Markovic, E. Matveeva, K. Mitosinkova, J. Mlynar, D. Naydenkova, R. Panek, R. Paprok, M. Peterka, A. Podolnik, J. Seidl, M. Sos, J. Stockel, M. Tomes, M. Varavin, J. Varju, M. Vlainic, P. Vondracek, J. Zajac, F. Zacek, M. Stano, G. Anda, D. Dunai, T. Krizsanoczi, D. Refy, S. Zoletnik, A. Silva, R. Gomes, T. Pereira, Tsv. Popov, D. Sarychev, G. P. Ermak, J. Zebrowski, M. Jakubowski, M. Rabinski, K. Malinowski, S. Nanobashvili, M. Spolaore, N. Vianello, E. Gauthier, J. P. Gunn and A. Devitre, J. Instrum., 12 (12), C12015-C12015, 2017.

[313] O. Grover, J. Seidl, D. Refy, J. Adamek, P. Vondracek, M. Tomes, P. Junek, P. Hacek, J. Krbec, V. Weinzettl, M. Hron, S. Zoletnik, and The COMPASS Team, Nucl. Fusion, 58 (11), 112010, 2018.

[314] O. Grover, J. Adamek, J. Seidl, A. Devitre, M. Sos, P. Vondracek, P. Bilkova, and M. Hron, Rev. Sci. Instrum., 88 (6), 063501, 2017.

[315] J. Adamek, J. Seidl, M. Komm, V. Weinzettl, R. Panek, J. Stockel, M. Hron, P. Hacek, M. Imrisek, P. Vondracek, J. Horacek, A. Devitre and the COMPASS Team, Nucl. Fusion, 57 (2), 022010, 2016.

[316] J. Adamek, J. Seidl, J. Horacek, M. Komm, T. Eich, R. Panek, J. Cavalier, A. Devitre, M. Peterka, P. Vondracek, J. Stockel, D. Sestak, O. Grover, P. Bilkova, P. Bohm, J. Varju, A. Havranek, V. Weinzett, J. Lovell, M. Dimitrova, K. Mitosinkova, R. Dejarnac, M. Hron, The COMPASS Team and The EUROfusion MST1 Team, Nucl. Fusion, 57 (11), 116017, 2017.

[317] P. Vondracek, Plasma Heat Flux to Solid Structures in Tokamaks, Dissertation PhD thesis, Charles University Prague, 2018: https://is.cuni.cz/webapps/zzp/detail/123000/.

[318] P. Vondracek, E. Gauthier, M. Grof, M. Hron, M. Komm, and R. Panek, Fusion Eng. Des., 146, 1003-1006, 2019.

[319] R. Fitzpatrick, Plasma Physics: An Introduction, CRC Press, ISBN 1466594268, 9781466594265, 2014.

[320] A. Savitzky and M. J. E. Golay, Anal. Chem., 36 (8), 1627-1639, 1964.

[321] J. Horacek, J. Adamek, H. W. Muller, J. Seidl, A. H. Nielsen, V. Rohde, F. Mehlmann, C. Ionita, E. Havlickova, and the ASDEX Upgrade Team, Nucl. Fusion, 50 (10), 105001, 2010.

[322] A. Wynn, B. Lipschultz, I. Cziegler, J. Harrison, A. Jaervinen, G. F. Matthews, J. Schmitz, B. Tal, M. Brix, C. Guillemaut, D. Frigione, A. Huber, E. Joffrin, U. Kruzei, F. Militello, A. Nielsen, N. R. Walkden, S. Wiesen and JET Contributors, Nucl. Fusion, 58 (5), 056001, 2018.

[323] R. J. Groebner and T. N. Carlstrom, Plasma Phys. Control. Fusion, 40 (5), 673, 1998.

[324] G. K. Batchelor, The Theory of Homogeneous Turbulence. Cambridge University Press, 1982.

[325] M. Farge and G. Rabreau, C. R. Acad. Sci. Paris 307, 1479-1486, 1988.

[326] M. Farge and K. Schneider, J. Plasma Phys., 81 (6), 2015.

[327] CCFE FusionWiki, MAST Magnetics: `http://fusweb1.fusion.ccfe.ac.uk/~nben/html/omahaDiagnosticSummary.html#omahaDiagnosticSummary`.

[328] P. Hennequin, Comptes Rendus Physique, Elsevier, 7 (6), 670-678, 2006.

[329] Z. Ge, Annales Geophysicae, 26 (12), 3819-3829, 2008.

[330] B. Ph. van Milligen, E. Sanchez, T. Estrada, C. Hidalgo, B. Brañas, B. Carreras, and L. Garcia, Phys. Plasmas, 2 (8), 3017-3032, 1995.

[331] W. Wan, S. E. Parker, Y. Chen, Z. Yan, R. J. Groebner, and P. B. Snyder, Phys. Rev. Lett., 109 (18), 185004, 2012.

[332] Z. Yan, G. R. McKee, R. J. Groebner, P. B. Snyder, T. H. Osborne, M. N. Beurskens, and K. H. Burrell, Phys. Plasmas, 18 (5), 056117, 2011.

[333] H. R. Wilson, S. C. Cowley, A. Kirk and P. B. Snyder, Plasma Phys. Control. Fusion, 48 (5A), A71–A84, 2006.

[334] S. J. P. Pamela, G. T. A. Huijsmans, T. Eich, S. Saarelma, I. Lupelli, C. F. Maggi, C. Giroud, I. T. Chapman, S. F. Smith, L. Frassinetti, M. Becoulet, M. Hoelzl, F. Orain, S. Futatani and JET Contributors, Nucl. Fusion, 57 (7), 076006, 2017.

[335] I. Krebs, M. Holzl, K. Lackner, and S. Gunter, Phys. Plasmas, 20 (8), 082506, 2013.

[336] W. Guttenfelder, J. Candy, S. M. Kaye, W. M. Nevins, E. Wang, J. Zhang, R. E. Bell, N. A. Crocker, G. W. Hammett, B. P. LeBlanc, D. R. Mikkelsen, Y. Ren, and H. Yuh, Phys. Plasmas, 19 (5), 056119, 2012.

List of Figures

List of Tables